UNIVERSITY OF SOUTHAMPTON

FACULTY OF PHYSICAL SCIENCES AND ENGINEERING

SCHOOL OF ELECTRONICS AND COMPUTER SCIENCE

Optical Wireless Communication Systems

by

Junyi Jiang

B. Eng., MSc.

A PhD. final thesis

the requirements for the award of Doctor of Philosophy

at the University of Southampton

October 2015

Professor Lajos Hanzo

FREng, FIEEE, FIEE, DSc, EIC IEEE Press

Chair of Communications, Signal Processing and Control Group

and

SUPERVISOR:

Dr. Rong Zhang

PhD,

Department of Electronics and Computer Science

University of Southampton

Southampton SO17 1BJ

United Kingdom

Dedicated to my family

UNIVERSITY OF SOUTHAMPTON

ABSTRACT

FACULTY OF ENGINEERING AND APPLIED SCIENCE
School OF ELECTRONICS AND COMPUTER SCIENCE

Doctor of Philosophy

Optical Wireless Communication Systems

by Junyi Jiang

In recent years, Optical Wireless (OW) communication techniques have attracted substantial attention as a benefit of their abundant spectral resources in the optical domain, which is a potential solution for satisfying the ever-increasing demand for increased wireless capacity in the conventional Radio Frequency (RF) band. Motivated by the emerging techniques and applications of OW communication, the Institute of Electrical and Electronics Engineers (IEEE) had released the IEEE standard 802.15.7 for short-range optical wireless communications, which categorised the Physical layer (PHY) of the OW communication into three candidate-solutions according to their advantages in different applications and environments: 1) Physical-layer I (PHY I): Free Space Optical (FSO) communication employs high-intensity Light Emitting Diodes (LEDs) or Laser Diodes (LDs) as its transmitter. 2) Physical-layer II (PHY II) uses cost-effective, low-power directional white LEDs for the dual function of illumination and communication. 3) Physical III (PHY-III) relies on the so-called Colour-Shift Keying (CSK) modulation scheme for supporting high-rate communication.

Our investigations can be classified into three major categories, namely Optical Orthogonal Frequency Division Multiplexing (OFDM) based Multiple-Input Multiple-Output (MIMO) techniques for FSO communications in the context of PHY-I, video streaming in PHY-II and the analysis and design of CSK for PHY-III. To be more explicit, in Chapter 2 we first construct a novel ACO-OFDM based MIMO system and investigate its performance under various FSO turbulence channel conditions. However, MIMO systems require multiple optical chains, hence their power consumption and hardware costs become substantial. Hence, we introduced the concept of Aperture Selection (ApS) to mitigate these problems with the aid of a simple yet efficient ApS algorithm for assisting our ACO-OFDM based MIMO system.

Since the channel conditions of indoor Visible Light Communication (VLC) environments are more benign than the FSO-channels of Chapter 2, directional white LEDs are used to create an "attocell" in Chapter 3. More specifically, we investigate video streaming in a multi-Mobile Terminals (MTs) indoor VLC system relying on Unity Frequency Reuse (UFR) as well as on Higher Frequency Reuse Factor based Transmission (HFRFT) and on Vectored Transmission (VT) schemes. We minimise the distortion of video streaming, while satisfying the rate constraints as well as opti-

cal constraints of all the MTs.

In Chapter 4 we analyse the performance of CSK relying both on joint Maximum Likelihood (ML) Hard-Detection (HD), as well as on the the Maximum *A posteriori* (MAP) criterion-based Soft-Detection (SD) of CSK. Finally, we conceive both two-stage and three-stage concatenated iterative receivers capable of achieving a substantial iteration gain, leading to a vanishingly low BER.

Declaration of Authorship

I, **Junyi Jiang**, declare that the thesis entitled **Optical Wireless Communication Systems** and the work presented in it are my own and has been generated by me as the result of my own original research. I confirm that:

- This work was done wholly or mainly while in candidature for a research degree at this University;
- Where any part of this thesis has previously been submitted for a degree or any other qualification at this University or any other institution, this has been clearly stated;
- Where I have consulted the published work of others, this is always clearly attributed;
- Where I have quoted from the work of others, the source is always given. With the exception of such quotations, this thesis is entirely my own work;
- I have acknowledged all main sources of help;
- Where the thesis is based on work done by myself jointly with others, I have made clear exactly what was done by others and what I have contributed myself;
- Parts of this work have been published.

Signed: ..... Date: .....

Acknowledgements

Firstly, I would like to thank my supervisor Professor Lajos Hanzo and Dr. Rong Zhang for their generous support and insightful guidance and just because of their wise advices that allowed this work to become reality. Their guidance and encouragement have greatly benefited me and I really appreciate this invaluable friendship.

I would also like to thank all my teachers and colleagues for their supports and helps. Special thanks to Dr. Peichang Zhang, Dr. Fan Jin, Dr. Yongkai Huo, Dr. Chao Xu, Dr. Shaoshi Yang and Dr. Li Li for their kindly and helpful advice on my work.

Finally, my sincere thanks to my parents for their endless love, support and understanding.

List of Publications

Journal Papers (4):

1. **J. Jiang, P. Zhang, R. Zhang, S. Chen, and L. Hanzo**, "Aperture Selection for ACO-OFDM in Free-Space Optical Turbulence Channel", *IEEE Transactions on Vehicular Technology (Early Access)*, 2015.

2. **J. Jiang, F. Jin, Y. Huo, R. Zhang, and L. Hanzo**, "Video Streaming in the Multiuser Indoor Visible Downlink", *Submitted to IEEE Access*.

3. **J. Jiang, R. Zhang and L. Hanzo**, "Analysis and Design of Three-stage Concatenated Colour-Shift Keying", *IEEE Transactions on Vehicular Technology*, vol. 64, no. 11, pp. 5126–5136, November, 2015.

4. **J. Jiang, R. Zhang, and L. Hanzo**, "Visible Light Communication Systems: Challenges and Opportunities", *To be submitted to IEEE Communications Survey and Tutorials*.

Contents

Glossary

μ-LEDs	Micro-LEDs
2D	2-Dimensional
5G	Fifth Generation
ACO-OFDM	Asymmetrically Clipped OOFDM
ADO-OFDM	Asymmetrically Clipped DC-bias OOFDM
ApS	Aperture Selection
AS	Antenna Selection
AWGN	Additive White Gaussian Noise
BER	Bit Error Ratio
BPSK	Binary Phase Shift Keying
CIR	Channel Impulse Response
COWA	Centre on Optical Wireless Applications
CP	Cyclic Prefix
CSI	Channel State Information
CSK	Colour-Shift Keying
DCO-OFDM	DC-biased OOFDM
DD	Direct Detection
DFE	Decision Feedback
DL	Down Link
DPIM	Digital Pulse Interval Modulation
DPPM	Differential PPM
E/O	Electronic to Optical

EGC Equal-Gain Combining

EXIT EXtrinsic Information Transfer

FD Frequency Domain

FDCTF Frequency Domain Channel Transfer Function

FEC Forward-Error Correction

FEDC Free squared Euclidean Distance Conditioned

FFR Fractional Frequency Reuse

FFT Fast Fourier Transform

FOV Field-of-View

FPS Frame per Second

FSO Free Space Optical

GOPs Group-of-Pictures

GSSK Generalised Space Shift Keying

HD Hard-Detection

HetNet Heterogeneous Networks

HFRFT Higher Frequency Reuse Factor based Transmission

IBI Inter-Band Interference

IFFT Inverse Fast Fourier Transform

IIR Infinite Impulse Response

IM Intensity Modulation

IR Infrared

IrCC Irregular Convolutional Code

ISI Inter-Symbol Interference

JTRApS Joint Transmit/Receive Aperture Selection

JTRAS Joint Transmit/Receive Antenna Selection

LDPC Low-Density Parity Check

LDs Laser Diodes

LEDs Light Emitting Diodes

LLRs Log-Likelihood Ratios

LOS Line-of-Sight

LTE Long Term Evolution

MAP Maximum A posteriori Probability
MC-LEDs Multi-Chip LEDs
MIMO Multiple-Input Multiple-Output
MISO Multiple-Input Single-Output
ML Maximum Likelihood
MMSE Minimum Mean Square Error
MMW Millimeter-Wave
MPPM Multipulse PPM
MRC Maximal-Ratio Combining
MSE Mean Square Error
MT Mobile Terminal
MWC Millimetre Wave Communications

NB Norm-Based
NOMAD Nonlinear Optimization by Mesh Adaptive Direct Search

O/E Optical to Electronic
OFDM Orthogonal Frequency Division Multiplexing
OLEDs Organic LEDs
OMEGA hOME Gigabit Access
OOFDM Optical-OFDM
OOK On-Off Keying
OPPM Overlapping PPM
OSM Optical Spatial Modulation
OW Optical Wireless

PAM Pulse Amplitude Modulation
PAM-DMT PAM based Discrete Multitone
PAPR Peak-to-Average Power Ratio
PC-LEDs Phosphor Converted LEDs
PD Photodetector
PDF Probability Density Function
PEP Pairwise Error Probability
PHY I PHYsical layer I
PHY II PHYsical layer II
PHY III PHYsical layer III

PLR Packet Loss Ratio
PolSK Polarization Shift Keying
PPM Pulse Position Modulation
PSNR Peak Signal-to-Noise Ratio
PWM Pulse Width Modulation

QAM Quadrature Amplitude Modulation
QoS Quality of Service

RApS Receive Aperture Selection
RAps Receive Apertures
RAT Radio Access Technologies
RF Radio Frequency
RGB Red Green Blue
RS Reed Solomon
RSC Recursive Systematic Convolutional
RVs Random Variables
RxAS Receive Antenna Selection

SC Selection Combining
SD Soft-Detection
SIM Subcarrier Intensity Modulation
SIMO Single-Input Multiple-Output
SINR Signal-to-Interference-plus-Noise-Ratio
SISO Single-Input Single-Output
SLERC Smart Lighting Engineering Research Center
SNR Signal-to-Noise Ratio
STBC Space-Time Block Code
STC Space-Time Coding
STSK Space-Time Shift Keying

TApS Transmit Aperture Selection
TAps Transmit Apertures
TCM Trellis Coded Modulation
TD Time Domain
TPC Transmission Precoding
TTCM Turbo Trellis Coded Modulation

TxAS	Transmit Antenna Selection
UC-Light	Ubiquitous Communication by Light
UFR	Unity Frequency Reuse
URC	Unity Rate Code
V-BLAST	Vertical-Bell Laboratories Space-Time
VLC	Visible Light Communication
VLCC	VLC Consortium
VT	Vectored Transmission
WB	White Balanced
WCDMA	Wideband Code Division Multiple Access
WPANs	Wireless Personal Area Networks
ZF	Zero-Forcing

List of Symbols

Special Symbols

Generic Symbols

α_g: Large scale scattering of the Gamma-Gamma distribution.

β_g: Small scale scattering of the Gamma-Gamma distribution.

β_{r1}: The irradiance angle to a reflected point.

β_{r2}: The irradiance angle to the receiver.

$\Gamma(\cdot)$: Gamma function.

Γ_{FET}: The FET channel noise factor.

κ: The Boltzmann's constant.

λ: Wavelength.

ϕ_d: The irradiance angle of the direct link.

ϕ_r: The irradiance angle of the reflected link.

$\Phi_{\frac{1}{2}}$: The semi-angle at half illumination power.

ψ_d: The incidence angle of the direct link.

ψ_r: The incidence angle of the reflected link.

Ψ_c: The Field-of-View (FOV).

ρ_r: The reflectance factor.

η: The fixed capacitance of the PD per unit area.

ξ: The responsivity of the Photodetector (PD).

σ_{r}^2: The Rytov variance.

σ_{shot}^2: The shot noise variance.

$\sigma_{\mathrm{thermal}}^2$: The thermal noise variance.

A_{r}: The physical area of the PD at receiver.

A_{wall}: The physical area of the reflected point.

C_n^2: Refractive index.

d_{g}: A diameter-related factor of the Gamma-Gamma distribution.

D_{aper}: Diameter of the aperture.

D_{r1}: The distance from Light Emitting Diode (LED) to the reflected point.

D_{r2}: The distance from the reflected point to the receiver.

f_{d}: Normalised Doppler shift.

g_{c}: The factor of the optical concentrator.

g_{FET}: The FET transconductance.

G: The open-loop voltage gain.

$\mathcal{G}_{\mathrm{d}}$: A factor of the direct link.

$\mathcal{G}_{\mathrm{r}}$: A factor of the reflected link.

H: Channel State Information (CSI).

H_{d}: The channel gain of the direct link.

H_{r}: The channel gain of the reflected link.

$\mathbf{H}$: MIMO channel CSI.

I_{bg}: The background current.

I_{nb1}: The noise bandwidth factor 1.

I_{nb2}: The noise bandwidth factor 2.

$\mathcal{J}$: The substitute factor for the irradiance angles.

k_{g}: Number of optical waves.

$K_\nu(\cdot)$: Modified Bessel function of the second kind.

l_{lam}: The Lambertian order.

L_{dis}: Propagated distance of light.

M_{sym}: Modulation order.

n_{re}: Refractive index of a lens at a PD.

N_{b}: Number of bits per symbol.

p_{GG}: PDF of the Gamma-Gamma distribution.

q: The electronic charge.

T_{k}: The absolute temperature (Kelvin).

T_{s}: The gain of the optical filter.

v: Complex-valued AWGN noise.

x: A transmitted symbol.

$\mathbf{x}$: Transmitted symbol vector.

y: A received symbol.

$\mathbf{y}$: The received symbol vector.

Specific Symbols in Chapter 2

γ_{equ}: Equivalent Signal-to-Noise Ratio (SNR).

$\mathbf{\Lambda}^{(n,m)}$: Eigenvalue of $\mathbf{H}^{(n,m)}$.

$\mathbf{A}$: Dispersion matrix.

$\mathcal{A}_{\text{det}}$: Normalised achievable rate of the EXIT characteristics.

$\boldsymbol{\mathcal{A}}$: All legitimate matrices candidates.

f_{ApS}: Aperture Selection factor.

$\mathbf{F}$: The Fast Fourier Transform (FFT) matrix.

G_{RSC}: Generate polynomial of Recursive Systematic Convolutional (RSC) code.

G_{URC}: Generate polynomial of URC.

$\mathbf{H}_{i_\mathrm{r}}$: The i_rth 'row'-block based candidate submatrix.

$\mathbf{H}^{(n,m)}$: Circulant convolutional channel matrix between the mth TAp and the nth RAp.

$\mathbf{H}_{\mathrm{sub}}$: Selected channel matrix candidate in Aperture Selection (ApS).

$\mathbf{H}_{\mathrm{sub}}^{\mathrm{opt}}$: Optimal selected channel matrix candidate in Aperture Selection (ApS).

$\bar{\mathbf{H}}^{(n,m)}$: Linear channel matrix between the mth TAp and the nth RAp.

I_{inner}: Number of inner iterations.

I_{outer}: Number of outer iterations.

$I_{\mathrm{out,a}}$: Mutual information of $\boldsymbol{\mathcal{L}}_{\mathrm{out,a}}$ and corresponding bits.

$I_{\mathrm{out,e}}$: Mutual information of $\boldsymbol{\mathcal{L}}_{\mathrm{out,e}}$ and corresponding bits.

$\mathcal{J}_{\mathrm{ES}}$: Complexity order of exhaustively search.

$\mathcal{J}_{\mathrm{JTRApS}}$: Complexity order of Joint Transmit/Receive Aperture Scheme (JTRApS).

$\mathbf{l}_{i_\mathrm{r}}$: The column indices of the L_T blocks index vector.

L_R: Number of receive optical chains.

L_T: Number of transmit optical chains.

$\boldsymbol{\mathcal{L}}_{\mathrm{det,a}}$: *A priori* Log-Likelihood Ratios (LLRs) vector of the detection block.

$\boldsymbol{\mathcal{L}}_{\mathrm{det,p}}$: *A posteriori* LLRs vector of the detection block.

$\boldsymbol{\mathcal{L}}_{\mathrm{det,e}}$: *Extrinsic* LLRs vector of the detection block.

$\boldsymbol{\mathcal{L}}_{\mathrm{dec,a}}$: *A priori* LLRs vector of the decoding block.

$\boldsymbol{\mathcal{L}}_{\mathrm{dec,p}}$: *A posteriori* LLRs vector of the decoding block.

$\boldsymbol{\mathcal{L}}_{\mathrm{dec,e}}$: *Extrinsic* LLRs vector of the decoding block.

$\boldsymbol{\mathcal{L}}_{\mathrm{in,a}}$: *A priori* LLRs vector of the inner iteration.

$\boldsymbol{\mathcal{L}}_{\mathrm{in,p}}$: *A posteriori* LLRs vector of the inner iteration.

$\boldsymbol{\mathcal{L}}_{\mathrm{in,e}}$: *Extrinsic* LLRs vector of the inner iteration.

$\boldsymbol{\mathcal{L}}_{\mathrm{out,a}}$: *A priori* LLRs vector of the outer iteration.

$\boldsymbol{\mathcal{L}}_{\mathrm{out,p}}$: *A posteriori* LLRs vector of the outer iteration.

$\boldsymbol{\mathcal{L}}_{\mathrm{out,e}}$: *Extrinsic* LLRs vector of the outer iteration.

$m_{i_r}^{(x)}$: The norm of the xth column-block in $\mathbf{H}_{i_r}$.

$\mathbf{m}^{\max}$: The max-magnitude metric vector.

M: Number of Transmit Apertures (TAps).

N: Number of Receive Apertures (RAps).

N_F: The length of OFDM.

N_{CP}: Number of Cyclic Prefix (CP).

$\mathbf{p}$: Unit Rate Code (URC) bits sequence.

r_τ: Achievable throughput.

$\mathbf{S}$: Complex-value symbol vector.

$\tilde{\mathbf{S}}$: Possible legitimate complex-valued symbol matrix.

$\hat{\mathbf{S}}$: Recovered complex-valued symbol matrix.

$\boldsymbol{\mathcal{S}}$: All legitimate set of symbol combinations.

T_{slot}: The slot duration.

$\mathbf{v}$: Complex-valued AWGN noise vector in Time Domain (TD).

$\mathbf{V}$: Complex-valued AWGN noise vector in Frequency Domain (FD).

$\mathbf{V}_{ACO}$: Equivalent FD noise matrix.

W_N: The FFT factor.

$\mathbf{x}_m$: The Optical OFDM modulated symbols vector at TD.

$\mathbf{X}$: The FD OFDM symbols matrix of OFDM.

$\mathbf{X}_{ACO}$: Complex-valued symbols for ACO-OFDM modulation.

$\mathbf{X}_o$: Clipped ACO-OFDM symbol matrix.

$\mathbf{Y}_o$: Recovered ACO-OFDM demodulated symbol matrix.

$\mathbf{Y}_{ACO}$: Extracted symbol matrix from $\mathbf{Y}_o$.

Specific Symbols in Chapter 3

γ: Signal-to-Interference-plus-Noise Ratio (SINR).

γ_{p}: Peak Signal-to-Noise Ratio (PSNR).

γ_{UFR}: SINR of UFR scenario.

γ_{HFRFT}: SINR of HFRFT scenario.

γ_{VT2}: SINR of VT-2 scenario.

$\Delta^{(i,j)}$: Video distortion of the ith MT's jth frame.

θ: Video frame status.

B: Bandwidth.

B_{avb}: Available bandwidth of different scheme.

$\mathbf{c}_{\mathrm{v}}$: Virtual cell.

C_{ACO}: Throughput of ACO-OFDM modulation.

$\mathcal{C}$: Transmission cells.

$\mathcal{D}$: Total distortion of a MT's video stream.

$f^{(i,j)}$: The jth video frame of the ith MT.

$f'^{(i,j)}$: Recovered the jth video frame of the ith MT.

$\mathcal{F}$: Set of video frames.

$\mathbf{G}$: Pseudo-inverse of channel matrix $\mathbf{H}$.

$\mathcal{I}$: Interference.

$\mathcal{I}_{\mathrm{sch}}$: Interference of different scheme.

$\mathcal{I}_{\mathrm{UFR}}$: Interference of Unit Frequency Reuse (UFR) scheme.

$\mathcal{I}_{\mathrm{HFRFT}}$: Interference of High Frequency Reuse Factor based Transmission (HFRFT) scheme.

$\mathcal{I}_{\mathrm{VT2}}$: Interference of Vectored Transmission 2 (VT-2) scheme.

n_{f}: Length of the estimation window.

N_{cell}: Number of cells.

N_{LED}: Numer of LEDs.

N_{MT}: Number of MTs.

$P_{\mathrm{r,o}}^{\max}$: Maximum received optical power.

$P_{\mathrm{r,e}}^{\max}$: Maximum received electronic power.

$P_{\mathrm{r_e,e}}$: Equivalent received electronic power.

$P_{\mathrm{t,o}}^{\max}$: Maximum transmitted optical power.

$P_{\mathrm{t,e}}^{\max}$: Maximum transmitted electronic power.

$\mathcal{P}_{n_{\mathrm{p}}}$: The n_{p}th serving pair.

$\mathbf{P}_{\mathrm{r,e}}$: Received electronic power of all MTs' all video frames.

$\mathbf{P}_{\mathrm{r,o}}$: Received optical power of all MTs' all video frames.

$\mathbf{P}_{\mathrm{t,e}}$: Transmitted electronic power of all MTs' all video frames.

$\mathbf{P}_{\mathrm{t,o}}$: Transmitted optical power of all Mobile Terminals' (MTs) all video frames.

r_{req}: Required video rate of a MT to transmit a video frame.

r_{UFR}: Achievable VLC rate of UFR scheme.

r_{HFRFT}: Achievable VLC rate of HFRFT scheme.

r_{VT2}: Achievable VLC rate of VT-2 scheme.

$\mathcal{R}$: Total achieved video rate of a MT.

Specific Symbols in Chapter 4

γ_{e}: Electronic SNR.

γ_{o}: Optical SNR.

$\eta_{\mathrm{FEC}}^{(j)}$: The weight of the jth RSC code.

ε_0: Inter-band interference percentage.

μ_{I}: Mapping strategy for **Criterion I**.

μ_{II}: Mapping strategy for **Criterion II**.

ρ_c: Electronic to optical SNR conversion factor.

σ_0^2: Noise variance of a band per bit.

ω_{avg}: The probability of intensity vector.

$\mathcal{A}_{\text{diff}}$: Area difference of two EXIT curves.

$\mathbf{b}$: Binary bits vector.

c_{τ}: Colour constellation point.

$\mathcal{C}_{\text{avg}}$: Average perceived colour.

d_{adj}: The Hamming distance of a pair of adjacent symbols.

$d_{\text{adj}}(\cdot\,,\cdot)$: The Hamming distance between a pair of legitimate intensity vectors.

d_{h}^2: *Harmonic mean* of the minimum squared Euclidean distance after the feedback.

$E_{\text{b}_{\text{elec.}}}$: Electronic bit power.

$\mathbb{M}_{\text{sym}}$: All possible legitimate labelling map.

$\mathcal{N}_{\text{Gau}}$: The Gaussian distribution.

N_{p}: Number of different RSC components for Irregular Convolutional Code (IrCC).

P_{e}: Error probability.

$r_{\text{sub}}^{(j)}$: The code rate of the jth RSC code.

R_{FEC}: Total rate of FEC code.

s_{h}: Horizontal colour coordinate.

s_{v}: Vertical colour coordinate.

$\mathbf{s}_{\text{h,c}}$: Centre horizontal colour coordinate vector.

$\mathbf{s}_{\text{v,c}}$: Centre vertical colour coordinate vector.

$\mathbf{S}$: Colour coordinates of Colour Shift Keying (CSK) modulation.

x_{i}: Light intensity of the ith band.

x_{j}: Light intensity of the jth band.

x_{k}: Light intensity of the kth band.

$\mathbf{x}^{(n)}$: The nth intensity vector.

$\boldsymbol{\mathcal{X}}$: All legitimate intensity vector combinations.

Special operations

$||\cdot||^2$: The Euclidean norm operation.

$(\cdot)^{\mathrm{T}}$: The transpose.

$(\cdot)^*$: The conjugate of a complex symbol/vector/matrix.

$\sum$: The summation of all elements.

$\prod$: The product of all elements.

$\forall$: For all elements within a certain range.

$\int$: The integration operation.

$\bigotimes$: The Knonecker product.

$\mathsf{C}_{(\cdot)}^{(\cdot)}$: The combination operation.

$\mathrm{erf}(\cdot)$: Error function operation.

$\mathbb{E}(\cdot)$: The expectation operation.

$\mathcal{F}_{\mathrm{STBC}}(\cdot)$: STBC mapping operation.

$\mathcal{F}_{\mathrm{STSK}}(\cdot)$: STSK mapping operation.

$\exp(\cdot)$: The exponential operation.

$\log(\cdot)$: The logarithm operation.

$\ln(\cdot)$: The natural logarithm.

$\mathbb{L}(\cdot)$: Lagrangian operation.

$\max[\cdot]$: The maximum value of a vector/matrix.

$\min[\cdot]$: The minimum value of a vector/matrix.

$\mathcal{O}(\cdot)$: Order operation.

$Pr(\cdot)$: The probability operation.

$\mathcal{Q}(\cdot)$: The Q-function operation.

$\mathbb{T}(\cdot)$: Transfer function of soft detection.

Chapter 1

Introduction

In ancient times, the Optical Wireless (OW) communication had been used for conveying information in different cultures [1], which predates wireless Radio Frequency (RF) communications by centuries. Explicitly, OW communication refers to the transmission of information via unguided propagation media in the 3×10^{11} to 7.9×10^{14} [Hz] range which, includes the Infrared (IR) and visible light bands, as shown in Fig. 1.1. As an innovative technology, OW communication has attracted substantial research attention because of the ever-increasing demand for increased wireless capacity. This is because the RF band is rather limited. By contrast, there are abundant spectral resources in the optical domain. Furthermore, OW communication is capable of supporting flexible networking solutions for cost-effective, high-speed and secure license-free wireless broadband connectivity. The family of OW communication systems incorporates both Free Space Optical (FSO) systems conceived for outdoor applications as well as IR and Visible Light Communication (VLC) systems designed for indoor environments. More specifically, OW communications may be divided

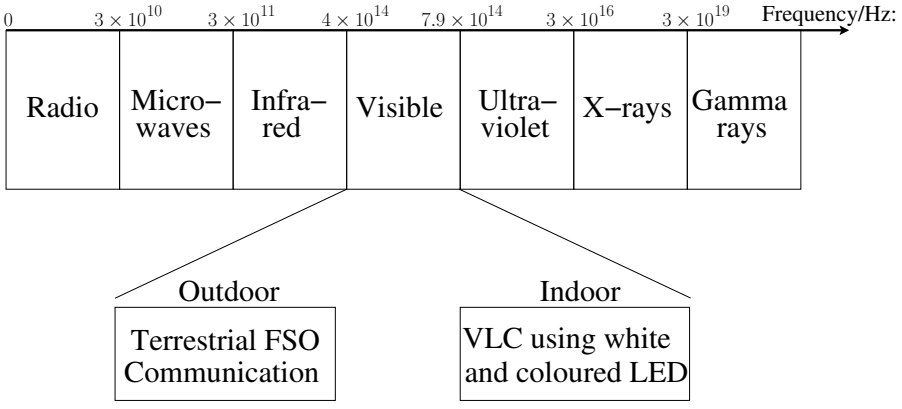

Figure 1.1: Stylised partitioning of the electromagnetic spectrum.

into five categories, according to the different transmission ranges, as follows:

- Ultra-short range OW communication, i.e. inter-chip communications in closely-packed and stacked multi-chip packages [2, 3].

- Short range OW communication, i.e. wireless body area networks and wireless personal area networks [4].
- Medium range OW communication, i.e. indoor IR communication and VLC for wireless local area networks [5, 6], vehicle-to-infrastructure and inter-vehicle communications [7].
- Long range OW communication, i.e. FSO inter-building connections [8].
- Ultra-long range OW communication, i.e. FSO inter-satellite links [9].

In this treatise, we will mainly focus our attention on medium-range OW communication, namely on VLC and Long Range OW communication, which includes both indoor and outdoor environments.

1.1 Overview of Outdoor Free-Space Optical Communication System

FSO systems have been developed for data transmission over a pair of fixed points. They typically have a high optical bandwidth, which supports a high data rate. For terrestrial FSO, the highest data rate that a product in the market has achieved is 10 [Gbps] [10]. For relatively short-range FSO transmissions designed for a modest Quality of Service (QoS), usually high-power Light Emitting Diodes (LEDs) are employed, which are equipped with a collimator for narrowing the stream of the light. However, most of the products use Laser Diodes (LDs) as the light source for the sake of achieving a high QoS. The focussed angular confinement of light ensures that FSO systems exhibit inherent security and robustness to electromagnetic interference. Additionally, thanks to their specific operating frequency, which falls in the visible light range in the vicinity of the IR band around 300 [GHz], the users do not have to purchase an operating license. Given these attractive advantages, Chan systematically described the specific challenges and the corresponding FSO solutions in [8]. Hence FSO communications technologies have been widely applied for different commercial and military systems, for campus connectivity, video surveillance, for the back-haul of cellular systems, disaster recovery, security and broadcasting [11, 12]. Let us now continue by reviewing the family of FSO systems from different perspectives.

1.1.1 FSO Channel Model

For a terrestrial FSO system, after the optical power has been launched from the Transmit Apertures (TAps), the light will be affected by various factors before its arrival at the Receive Apertures (RAps), including factors like the so-called system loss [13] characterising the implementation induced impairment, geometric loss [14], misalignment loss [15], atmospheric loss [16] and atmospheric turbulence-induced fading [17]. Here we will briefly summarise the literature.

The implementation-induced imperfections are mainly determined by the cost-constraints of the manufactures, as detailed in [13]. As for the geometric loss, its main reasons may be attributed to the channel-induced divergence of the beam. A good approximation can be found in [14], where a Gaussian profile is considered for the beam-intensity. If the beam is wide, then the wavefront may be approximated by a plane or by a spherical wavefront [18]. Another source of beam-divergence is constituted by the transmitter versus receiver misalignment and beam-tracking imperfections. The misalignment losses are mainly caused by either beam-wander or building-sway. Explicitly, the beam-wander is owing to atmosphere eddies[1] caused by random deflections, diverting the beam from its original path [15]. On the other hand, the building-sway is mainly caused by the external physical environment, such as thermal expansions, earth tremors, vibration etc. [19]. When we have a narrow beam departing from the TAps and a small Field-of-View (FOV) at the RAps, the building-sway is capable of severely effecting the QoS or might even lead to communication drop-outs [13].

A potential approach of alleviating the misalignment is that of increasing the beam-divergence at TAp. However, this method is only effective in short-range FSO systems, which is up to a couple of hundred metres. Employing the above-mentioned spatially partially coherent Gaussian beams is another option [20]. On the other hand, in long-distance FSO communication, we would need a beam-tracking system for eliminating this problem, since the system requires a narrow beam width for avoiding a high geometric loss [13]. The statistical model of misalignment-induced pointing errors has been investigated for example in [21–24]. In [21, 22], the pointing error is modelled by a Rayleigh distribution, which is based on the assumption of the horizontal building sway obeying a Gaussian distribution. In [23], the Channel Impulse Response (CIR) is modelled as a product of the geometric loss, path loss, misalignment loss and atmospheric turbulence. Furthermore, the link capacity is evaluated as a function of the pointing error in [24], where the channel model took into account the aperture diameter, the beam-width and the jitter-related factors. On the other hand, the system's Bit Error Ratio (BER) performance as a function of the pointing error both with and without channel coding was studied in [25–27].

The most straightforward effect of atmospheric loss manifests itself in terms of a reduced visibility, and it is widely recognised that FSO communication is highly dependent on the presence of a Line-of-Sight (LOS) link. Explicitly, the weather conditions directly affect the channel quality. This is, because under different weather or environmental conditions, the particles in the air include not only the rain, snow, haze and fog, but also dust, aerosols and smoke. All these particles in the air will absorb and scatter the laser light, since the FSO systems' operating frequency is near the IR light band, where the absorption would attenuate the received optical power, while scattering may deviate the beam from its original fixed transmit direction. This may interrupt the communications all together. Since the particle size of rain and snow is much larger than the wavelength of light,

[1] atmospheric disturbances extending from the surface through the troposphere.

the scattering effects are relatively low [28]. By contrast, in fog or haze, the scattering effects are much more severe [29]. In [30, 31], the effects of rain, fog and haze are characterised based on measurement results, while a range of other models can be found in [16, 32, 33].

Apart from the geometric loss, misalignment loss and atmospheric loss, the most dominant factor affecting the FSO channel is the turbulence-induced fading. Under a calm atmosphere, all these weather-related losses are negligible. The only factor we have to consider is the scintillation, which is mainly caused by the inhomogeneities in the temperature and the pressure of the atmosphere. The effect of these causes may be different in different seasons, since the inhomogeneities are induced by the solar heat and wind, which would affect the refractive index along the transmission link [15]. To model this scintillation, several models have been proposed. The most widely recognised and accepted model is the log-normal model, which is based on the first-order approximation of weakly and moderately turbulent channels [34]. This model was applied to FSO channels in [35, 36]. An appealing approach of generating the log-normal distributed Random Variables (RVs) was proposed in [37]. However, this model is only appropriate for short range transmission. Upon increasing the transmission distance, experimentally measured data has shown that this model becomes inaccurate for strongly turbulent channels [17, 38]. Instead, in this scenario, the negative exponential distribution should be employed for modelling the channel [39]. Furthermore, the K-distribution can also be used for modelling the channel characteristics of strongly turbulent conditions [40]. By contrast, the so-called I-K distribution was proposed for weak turbulence in [41]. Based on all these models, the most appropriate model for characterising the scintillation was proposed in [17], where the doubly-stochastic distribution[2] was modelled by a pair of independent Gamma distributions, which is hence known as the Gamma-Gamma distribution. This model is widely used in the literature, for the accurate characterisation of the FSO turbulence channel. Similar to the log-normal distribution, a simple Gamma-Gamma distributed RV generation approach was introduced in [42], where two independent Gamma distributed RVs are multiplied in order to produce the Gamma-Gamma distribution. We have summarised the above-mentioned channel-modelling studies in Table 1.1.

1.1.2 FSO Transceiver

In a conventional FSO system, the information is modulated onto an optical carrier, which propagates over the turbulence channel and impinges on a Photodetector (PD). The received optical signal is then converted to an electronic signal, which can be conveniently detected. The most widely used FSO system operates in the near-IR frequency band, spanning from 750 [nm] to 1550 [nm] [13, 43]. However, the 10 [μm] and UV wavelengths are also often considered for FSO transmissions owing to their better propagation characteristics in fog and due to their robustness against pointing errors as well as against background interference caused by solar radiations [13, 43]. Based

[2]The distribution constituted by two randomly generated variables

Table 1.1: A brief summary of major contributions on FSO channel modelling

Year	Authors	Contributions
1953	A. M. Obukhov [34]	Proposed log-normal distribution
1978	E. Jakeman *et al.* [40]	Proposed and applied K-distribution for strong turbulence channel
1986	L. C. Andrews *et al.* [41]	Proposed and applied I-K distribution for weak turbulence channel
2001	M. A. Al-Habash *et al.* [17]	Proposed and applied Gamma-Gamma distribution for all turbulence channels
2001	I. I. Kim *et al.* [29]	Discussed the scattering effects caused by fog and haze
2002	M. Achour [30, 31]	Proposed rainy, foggy and hazy weather model based on experimental measurement
2003	S. Bloom *et al.* [13]	Discussed the effects of system loss, geometric loss and misalignment loss
2005	H. Yuksel *et al.* [18]	Proposed an approximation for beam divergence induced geometric loss
2005	S. G. Wilson *et al.* [35]	Applied log-normal distribution to FSO channel modelling
2007	A. A. Farid *et al.* [23]	Characterised the effect of geometric loss, path loss, misalignment loss, and scintillation on FSO channel
2007	A. Garcia-Zambrana *et al.* [39]	Applied negative exponential distribution for strong turbulence channel
2009	D. K. Borah *et al.* [24]	Discussed the link capacity under the affection of pointing errors
2010	B. Epple *et al.* [37]	Proposed a technique of generating log-normal distributed RVs
2011	H. G. Sanalidis *et al.* [27]	Analysed the BER performance of coded FSO system under pointing errors
2015	M. R. Bhatnagar *et al.* [25]	Performance analysis of Alamouti code under FSO Gamma-Gamma channel affected by pointing errors

on these features, we will briefly review the family of FSO transceivers.

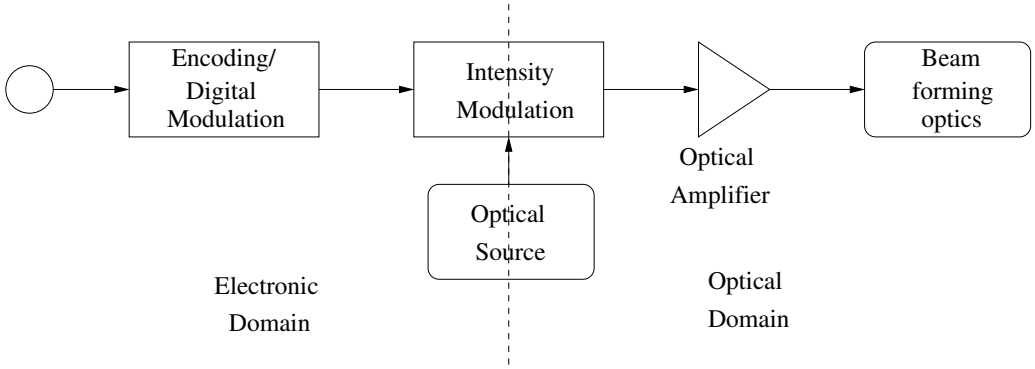

Figure 1.2: A general block diagram of FSO transmitter.

As shown in Fig. 1.2, the FSO transmitter consists of a digital modulation block, an Intensity Modulation (IM) block and an optical amplifier block, where the source bits are firstly encoded and modulated in the electronic domain. Then after IM, the electronic signals are converted to optical signals, which are amplified and finally emitted after the beam was refocused by the beam-forming optics. The most widely-used optical source is a semiconductor LD [5], although some products use high-power LEDs combined with so-called beam-collimator for the sake of creating a narrow beam [44].

There are two types of receivers. During the early stages of FSO communication, the so-called coherent FSO receivers were employed [8], but at the time of writing the Direct Detection (DD) receiver is more popular [8]. As seen by comparing Fig. 1.3 and Fig. 1.4, the structure of the DD receiver is slightly simpler.

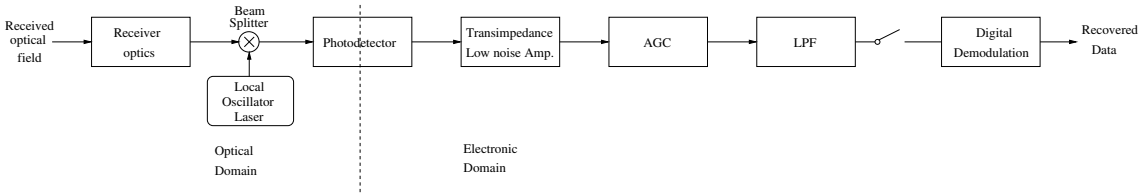

Figure 1.3: A general block diagram of the coherent FSO receiver.

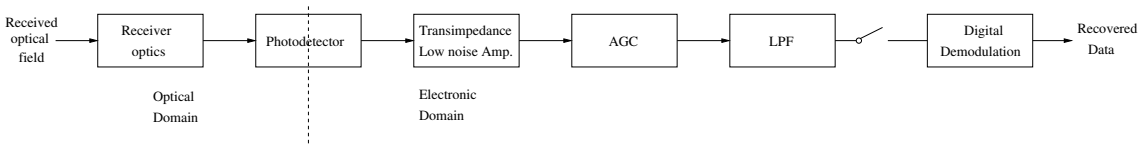

Figure 1.4: A general block diagram of the FSO Direct Detector.

More specifically, when a coherent receiver is used, various modulation types may be employed at the transmitter, including amplitude, frequency or phase modulation. The received optical signal is mixed with the local optical oscillator's signal. By contrast, when the DD receiver is used, the PD directly detects the light intensity, hence the optical local oscillator is no longer necessary. However,

this DD method constrains the choice of the modulation types, because only amplitude modulation is possible. The comparison of these two types of receivers has been provided in [8,45]. Explicitly, the coherent receiver outperforms the DD receiver, because it is capable of rejecting the background noise, of mitigating the turbulence fading, exhibits a higher receiver sensitivity and it can invoke diverse modulation types. However, the most attractive characteristics of the IM/DD system are its simplicity and low cost, which outweigh the benefits of coherent reception in terrestrial FSO systems.

The background noise of FSO systems may be modelled by a Poisson process [46], albeit when the background noise level increases, then it can be modelled by a Gaussian distribution [46]. Furthermore, when the background illumination level is relatively low, the noise process is dominated by the shot noise and thermal noise. The shot noise originates from the random current flow fluctuations through the PD, which may be modelled by the Poisson process. By contrast, the thermal noise is mainly contributed by the receiver's electronic circuitry, which is classically modelled by the zero mean Additive White Gaussian Noise (AWGN). Hence, the combined noise at the receiver may be modelled by an AWGN process [47].

1.1.3 Applicable Modulation Schemes

Like in all other OW communication scenarios, the most commonly used modulation scheme in FSO communication system is constituted by On-Off Keying (OOK), which is a binary amplitude modulation scheme. The OOK modulation scheme use the presence ("on") and absence ("off") of a light pulse for each OOK symbol. During the detection process, the knowledge of Channel State Information (CSI) is required for finding a CSI-dependent dynamic decision threshold [48], where the CSI could be estimated by using a set of pilot symbols [49]. Instead of invoking a dynamic decision threshold, other design options are constituted either by symbol-based Maximum Likelihood (ML) detection [50] or ML sequence detection based on the knowledge of the joint temporal statistics of the atmospheric turbulence [51]. Furthermore, as an improved modulation arrangement, multi-level Pulse Amplitude Modulation (PAM) was employed in [52, 53], which relies on modulating the instantaneous intensity. The advantage of PAM is its increased bandwidth efficiency, albeit, its BER performance is degraded compared to OOK.

Although OOK is appealingly simple, it requires a dynamic threshold and its bandwidth-efficiency is low, hence we need more advanced modulation schemes. Pulse Position Modulation (PPM) constitutes another appealing solution [35]. It was claimed in [54] that the PPM scheme is capable of approaching the channel capacity, and this prediction was confirmed in 1995 [55]. In contrast to OOK, PPM does not require any dynamic threshold [56,57]. Furthermore, PPM achieves 3 [dB] Signal-to-Noise Ratio (SNR) improvement over OOK [58] by using 2-PPM. However, PPM suffers from having a high Peak-to-Average Power Ratio (PAPR). As a remedy, the so-called Mul-

tipulse PPM (MPPM) technique was proposed in [59–61]. Moreover, there are several other modified PPM schemes, such as the Overlapping PPM (OPPM) and Differential PPM (DPPM) arrangements, where OPPM constrains the multiple pulses to occupy adjacent slots [62]. The DPPM scheme of [63,64] further improves the attainable spectral efficiency by eliminating the empty slots inevitably following the presence of a non-zero pulse. Since this technique results in more zero-crossings, it is also beneficial in terms of improved symbol synchronisation. In 2011, both OOK and PPM have been proposed for the PHYsical layer I (PHY I) and PHYsical layer II (PHY II) operating modes of the IEEE standard 802.15.7 [4].

Apart from these three main modulation schemes, the slightly less popular Pulse Width Modulation (PWM) [65], Digital Pulse Interval Modulation (DPIM) [66], Subcarrier Intensity Modulation (SIM) [67] and Polarization Shift Keying (PolSK) [68] may also be invoked. We have briefly summarised the modulation-related studies in Table 1.2.

Table 1.2: A brief summary of major contributions on FSO channel modelling

Year	**Authors**	**Contributions**
1983	J. G. Proakis *et al.* [52]	Introduced OOK and PAM
1988	M. H. A. Davis [54]	Predicted that PPM is capable of approaching the channel capacity
1989	H. Sugiyama *et al.* [59]	Proposed power efficient MPPM
1993	H. M. H. Shalaby [62]	Proposed OPPM
1995	R. M. Gagliardi *et al.* [55]	Proved that PPM is capable of approaching the channel capacity
1998	Z. Ghassemlooy *et al.* [66]	Proposed DPIM
1999	D. Shiu *et al.* [63]	Proposed spectral-efficient DPPM
2002	X. Zhu *et al.* [50]	Employed ML detection for OOK symbol detection
2003	X. Zhu *et al.* [51]	Employed ML sequence detection in FSO communication
2003	T. Ohtsuki [67]	Proposed SIM
2005	T. H. Chan *et al.* [53]	Capacity analysis on PAM modulation
2005	S. G. Wilson *et al.* [35,56]	Stated that PPM dose not requires a dynamic thresholds in FSO MIMO channels
2007	Y. Fan *et al.* [65]	Proposed PWM
2009	F. Xu *et al.* [57]	Analysed the performance of coded PPM in FSO channels
2009	W. Gappmair *et al.* [58]	Concluded that 2-PPM outperforms OOK by 3 [dB]
2009	X. Zhao *et al.* [68]	Proposed PolSK
2015	M. Biagi *et al.* [69]	Investigated the MIMO PPM scheme in VLC system under rate constraints

1.1.4 Information Theoretical Limits

The classical Shannon-Hartley theorem [70] stipulates the maximum data rate that can be achieved at an arbitrarily small BER over a channel for a given average signal power, which is also known as the channel capacity. Several early contributions have investigated the OW capacity. The Poisson channel's capacity was firstly studied for the quantum-noise-limited receiver in [71]. The capacity of this photon counting receiver is unbounded under a specific average optical power constraint. In this channel, the PPM modulation scheme is capable of achieving an arbitrarily low error probability [72], even when approaching the channel capacity [54], if the peak optical power is limited.

In practical OW communications, the FSO channel imposes atmospheric turbulence. Consequently, the channel capacity is a random variable [73]. Furthermore, when the channel's coherence time is high, its outage probability[3] may be increased [74]. Naturally, the transmission rate has to be lower than the mutual information between the channel's input and output, otherwise an outage event is declared [74]. Another channel capacity definition has been proposed in [75], which is known as the delay-limited capacity. The delay-limited capacity tends to zero, when no spatial diversity is achieved; whilst for an infinite diversity order this delay-limited capacity tends to the ergodic capacity [76].

As a further contribution, the ergodic capacity of an FSO channel was studied in [77, 78] under the assumptions of log-normal, Gamma-Gamma, negative exponential and I-K distributed models. On the other hand, the outage capacity of the I-K-distributed model was studied in [79]. As for the log-normal fading channel and for the Gamma-Gamma fading channel, their outage capacity was studied in [17] and [38], respectively. Furthermore, the capacity was also considered in Multiple-Input Multiple-Output (MIMO) scenarios. In [74], the outage capacity of the Gamma-Gamma channel was analysed with the aid of multiple RAps at the receiver side. The outage probability of MIMO schemes was characterised under various channel models in [80], while the ergodic and outage capacities of a MIMO Poisson channel were investigated in [81]. Furthermore, when pointing errors are involved, the FSO capacity was studied in [23]. The capacity-related studies of FSO systems are summarised in Table 1.3.

1.1.5 Channel Coding

The attainable system performance of OW systems is considerably degraded by the intensity fluctuations imposed by the atmospheric turbulence-induced fading. The optical turbulence channel has a long memory, hence the channel fades tend to result in numerous consecutive errors at the receive side. Mitigating the errors imposed by the turbulence-induced fading has been an intensive research direction [38, 83–85]. Both spatial diversity [84] and Forward-Error Correction (FEC) codes [83]

[3]The outage event is when the signal drops below the noise power level, and the probability of this event is the so-called outage probability

Table 1.3: A brief summary of the major contributions on the FSO channel capacity

Year	Authors	Contributions
2001	M. A. Al-Habash *et al.* [17]	Studied the outage capacity of Gamma-Gamma fading channels
2001	M. H. A. Davis [54]	Studied the outage capacity of log-normal fading channels
2002	M. A. Khalighi *et al.* [75]	Proposed the delay-limited capacity, which tends to the ergodic capacity, when no diversity is employed
2003	S. M. Haas *et al.* [81]	Analysed the ergodic and outage capacity in a MIMO-based Poisson channel experiencing log-normal fading
2007	A. A. Farid *et al.* [23]	Analysed the outage and ergodic capacities of FSO channels in the presence of pointing errors
2009	M. A. Khalighi *et al.* [74]	Studied the outage capacity when considering receive diversity
2009	N. Letzepis *et al.* [76]	Studied the outage capacity of a PPM-based MIMO system
2009	H. E. Nistazakis *et al.* [78]	Studied the ergodic capacity of various FSO channel models
2011	H. E. Nistazakis *et al.* [79]	Studied the ergodic capacity of FSO I-K fading channel
2012	K. P. Peppas *et al.* [77]	Studied the ergodic capacity of FSO Gamma-Gamma fading channels
2015	I. S. Ansari *et al.* [82]	Studied the ergodic capacity of FSO Gamma-Gamma fading channels considering boresight pointing errors

have been advocated as effective solutions. In this subsection we briefly review the FEC-related activities. According to [38], introducing FEC codes is beneficial, almost regardless of the turbulence level of the channel.

Convolutional codes have been studied in [83, 86]. Low-Density Parity Check (LDPC) codes have also found employment in FSO systems during the past decade [87–89]. More specifically, the achievable capacity of coded FSO systems using LDPC codes was studied in [87] while video transmission was analysed in [88]. As a further development, LDPC coded FSO MIMO investigations in [89]. Additionally, the LDPC coded Orthogonal Frequency Division Multiplexing (OFDM) was studied in [90].

The performance bounds of coded FSO systems were investigated in [58, 91–93]. Explicitly, in [91], the BER performance of a coded Single-Input Single-Output (SISO) system was analysed. The BER upper bound of block codes, convolutional codes and turbo codes in weak turbulence FSO channels were also discussed. The BER union bound of coded FSO systems communicating over a strong turbulence channel modelled by the K-distribution was analysed in [92], where the authors used the Pairwise Error Probability (PEP) based upper bound. Furthermore, in [58, 93], the performance upper bounds of Gamma-Gamma fading channels were characterised. However, these contributions were based on the assumption of having sufficiently long interleavers, which is not

always feasible in practice [94, 95]. A powerful concatenated coding scheme using turbo coding, Reed Solomon (RS) coding and convolutional coding has been proposed in [57], where somewhat surprisingly the convolutional code was found to strike the most compelling compromise under all turbulence conditions. Apart from these classical codes, rateless codes, also known as fountain codes have been further investigated in the context of FSO systems [96], where rateless Raptor codes were compared to a punctured LDPC code. We note that all the above-mentioned coding-related contributions have been based on binary modulation. For non-binary modulation such as PPM, similar FEC coding arrangements, including convolutional codes, RS codes and turbo codes have also been studied in [49, 97, 98]. We have summarised the channel coding related studies in Table 1.4.

Table 1.4: A brief summary of major contributions on FSO channel coding

Year	**Authors**	**Contributions**
1982	V. W. S. Chan [83]	Employed convolutional codes in FSO systems for transmission over atmospheric turbulence channels
1988	F. M. Davidson *et al.* [86]	Designed interleavers for coded FSO systems communicating over atmospheric turbulence channels
2003	X. M. Zhu *et al.* [91]	Analysed a coded SISO system communicating over FSO turbulence channels
2004	M. Uysal *et al.* [92]	Evaluated the BER performance of block codes, convolutional codes and Turbo codes in K-distributed channels
2005	J. A. Anguita *et al.* [87]	Discussed the Shannon capacity of LDPC coded FSO systems
2006	M. Uysal *et al.* [93]	Derived the union upper bound of coded FSO systems operating in atmospheric turbulence channels
2007	I. B. Djordevic *et al.* [90]	Employed LDPC codes in an OFDM modulated FSO system
2008	I. B. Djordevic *et al.* [89]	Employed LDPC codes in an FSO MIMO system using PPM
2009	W. Gappmair *et al.* [58]	Derived the union bound of an FSO system in Gamma-Gamma strongly-fading channels
2010	J. A. Anguita *et al.* [96]	Employed rateless coding to FSO systems
2013	A. L. Puryeara *et al.* [95]	Exploited the FSO channel's reciprocity to reduce the redundancy required by channel coding
2015	A. Gupta *et al.* [99]	Analysed the outage capacity of a coded cooperative FSO system

1.1.6 MIMO Techniques

As mentioned in Sec. 1.1.5, to mitigate the detrimental effects of turbulence-induced fading, spatial diversity relying on MIMO techniques has been widely exploited in FSO communication systems [84, 85, 100–102]. To elaborate, a spatial diversity gain may be attained using either Multiple-Input Single-Output (MISO) or Single-Input Multiple-Output (SIMO) arrangements, or alternatively by the combination of these two approaches leading to the classic concept of MIMO techniques. We will briefly discuss them in the following.

A simple technique of realising a MISO solution may rely on transmitting the same signal on different beams via different TAps [84]. This redundant transmission based regime was also referred to as 'repetition coding'. Assuming perfect CSI knowledge at the receiver, using this MISO scheme is indeed capable of achieving the maximum attainable diversity order determined by the number of TAps, as shown in [85, 103]. A more sophisticated technique of achieving transmit diversity is constituted by Space-Time Coding (STC), as detailed in [104], where the conventional Alamouti STC was appropriately modified by using real-valued positive signals for transmission over the turbulent FSO channel. As concluded in [105], the modified Space-Time Block Code (STBC) was capable of achieving the maximum attainable diversity order. Then in [39], the STC concept was generalised to OOK modulation combined with pulse shaping. The effects of imperfect CSI at receiver were considered in [106, 107].

Again, a spatial diversity gain may also be gleaned from receive diversity. Indeed, at a given transmit power, the achievable performance improvement of transmit diversity may become lower than the receive diversity, because when the total transmit power is fixed it must be shared by the antennas. This results in a relatively low power for each transmit antenna [101, 108]. A simple technique of obtaining receive diversity to mitigate the turbulence-induced fading effect is referred to as aperture-averaging [109]. This method employs a relatively large lens at the receiver in order to average the intensity fluctuations. This approach was shown to be efficient [102], especially when the aperture of the lens is larger than the spatial fading correlation length. According to [74, 102, 110], the aperture-averaging approach is capable of substantially reducing the scintillation, especially under moderate or strong turbulence channel conditions. Another straightforward approach of realising receive diversity is that of employing multiple RAps at the receiver side, where instead of using a single large RAp, we opt for using multiple small apertures at the receiver. Although the complexity of the aperture-averaging technique of [102, 110] is lower than that of the SIMO scheme of [101], the performance of the latter is better in the presence of uncorrelated MIMO channels, as demonstrated in [74]. The SIMO scheme also has a small effective aperture area and it performs well even in a strong turbulence regime. Furthermore, for a SIMO system, there are multiple receiver-diversity combining methods, such as Equal-Gain Combining (EGC), Maximal-Ratio Combining (MRC) and Selection Combining (SC). The EGC and MRC methods were discussed

in [108, 111], where the performance of MRC was shown to be slightly better. However, its performance improvement compared to EGC was relatively small. Hence, if we also consider the associated complexity issues, the EGC method may be deemed more advantageous.

As a combination of MISO and SIMO techniques, MIMO solutions were conceived for FSO systems in [35, 56, 112–116], where typically OOK and PPM modulation schemes were considered. More specifically, a MIMO system adopting MPPM is studied in log-normal fading channels in [35], while MIMO PPM systems operating in Gamma-Gamma fading channels were studied in [56, 116, 117]. The analytical BER performance of a MIMO OOK system was investigated in both weak and moderate log-normal fading channels [112, 113], while that of a negative exponentially distributed strong turbulence channel was documented in [115]. Furthermore, based on the Gamma-Gamma fading channel, the analytical performance of a MIMO-aided OOK systems was investigated in [114]. The concept of multiple symbol detection was proposed in [36, 118].

Finally, the Vertical-Bell Laboratories Space-Time (V-BLAST) scheme and Optical Spatial Modulation (OSM) were proposed in [113] and [119], respectively. The iterative decoding of LDPC coded FSO MIMO systems was conceived and studied in [89], while in [120] the diversity-multiplexing trade-off of FSO MIMO systems was discussed. We have summarised the FSO MIMO related studies in Table 1.5 at a glance.

1.2 Overview of Indoor Visible Light Communication Systems

Having considered the family of FSO systems, let us now focus our attention on VLC systems relying on cutting-edge LED devices for transmitting data in the downlink as a potential solution to circumvent the spectrum shortage of RF communication systems. By combining the illumination and communication functions, VLC offers ubiquitous communication in indoor environments. If we revisit Fig. 1.1, VLC systems mainly operate in the 4×10^{14} to 7.9×10^{14} [Hz] frequency bands. As in most OW communication systems, the information is transmitted by modulating the intensity of the signal at a rate substantially faster than the human eye's fusion frequency. Typically, photo-diode transmitters and DD receivers are employed. As a predominant optical source, the LED lights are exploited due to their unique advantages of high switching rate, energy efficiency and long-life characteristics. LEDs were developed in 1998 for transmitting modulated optical signals [122]. In the early 2000s, the indoor VLC pioneers of Japan started to utilise white LEDs for both illumination and communication functions [123, 124]. The rapid development of VLC was supported by the VLC Consortium (VLCC) and it was also standardised [125]. In Europe, the hOME Gigabit Access (OMEGA) project was founded by a number of industrial partners aiming for transmitting at Gigabit data rates for domestic users [126, 127]. Additionally, a number of other research groups, including the Centre for Ubiquitous Communication by Light (UC-Light) [128],

Table 1.5: A brief summary of major contributions on FSO MIMO techniques

Year	Authors	Contributions
1991	J. H. Churnside [109]	Proposed aperture averaging for mitigating the turbulence of the atmosphere
2003	E. Bayaki *et al.* [114]	Characterised the analytical performance of FSO MIMO system in Gamma-Gamma fading channels
2004	E. J. Lee *et al.* [108]	Analysed different SIMO receiver combining schemes
2005	S. G. Wilson *et al.* [35]	Employed an MPPM scheme in FSO MIMO systems
2005	H. Yuksel *et al.* [110]	Optimised the aperture averaging technique designed for FSO channels
2005	M. K. Simons *et al.* [104]	Modified Space-Time coding for FSO MIMO systems adopting OOK and PPM
2006	D. Bushuev *et al.* [113]	Studied the analytical performance of MIMO systems conceived both for diversity and multiplexing purposes
2007	S. M.Navidpour *et al.* [111]	Analysed the BER performance of EGC and MRC schemes
2008	M. B. Riediger *et al.* [118]	Employed multi-symbol detection in FSO MIMO systems
2008	M. Safari *et al.* [100]	Compared repetition coding aided MISO and STBC schemes, where the STBC scheme is outperformed by the former
2009	A. García-Zambrana *et al.* [103]	Discussed repetition coding aided MISO schemes, and further enhanced the performance using aperture selection
2010	S. M. Aghajanzadeh *et al.* [120]	Analysed the diversity-multiplexing gain trade-off in FSO systems
2011	R. Mesleh *et al.* [119]	Proposed and analysed OSM MIMO schemes
2015	C. Abou-Rjeily *et al.* [121]	Analysed the diversity and aperture allocation over Gamma-Gamma fading channels in a serial relaying aided system

Centre on Optical Wireless Applications (COWA) [129], the Smart Lighting Engineering Research Center (SLERC) [130] have also contributed substantially. The first IEEE 802.15.7 VLC standard was published in 2011 for Wireless Personal Area Networks (WPANs) [4]. Hence in this section, we briefly review the indoor VLC concept.

1.2.1 Light Emitting Diodes

In indoor VLC links, due to their short distance, the SNR of the system is typically high. The electromagnetic spectrum available in each room may be readily reused, thanks to the low penetration of external visible light. Given the wide availability of white LEDs [131–133], the indoor environments such as homes and offices constitute ideal scenarios for combining indoor illumination with

VLC.

Naturally, illumination remains the prime function of LEDs, which have the following advantages over traditional lighting:

- *Energy efficient*: Compared to the obsolete incandescent bulbs, LEDs save up to 80% of energy, since they generate less heat [134].
- *Long lifetime*: Compared to the 6,000 to 15,000 hours lifetime of conventional incandescent bulbs, LEDs ensure a longer service time of 25,000 to 50,000 hours [135].
- *High luminous efficacy*: Compared to the average luminous efficacy level of incandescent light bulbs (14 [lm/W]) and fluorescent lamps (75 [lm/W]), the novel InGaN based LEDs achieved a luminous efficacy of up to 254 [lm/W] in 2012 [136].
- *Moderately high bandwidth*: LEDs have been developed to have up to 100 [MHz] bandwidth that could be invoked to support communication [126].
- *Multi-functional operation*: LEDs have the versatility to control the radiated spectrum, hence they are capable of producing high-intensity multi-coloured light [137].

Given the above impressive characteristics of LED lighting, it has drawn considerable attention in both the academic and industrial research communities in terms of indoor illumination, traffic lights and other light-related infrastructures.

In the current commercial market, there are diverse types of LEDs, such as the Phosphor Converted LEDs (PC-LEDs) [138], Multi-Chip LEDs (MC-LEDs) [139], Organic LEDs (OLEDs) [140] and Micro-LEDs (μ-LEDs) [141]. Brief descriptions of the different types of LEDs are provided below and a simple comparison among these LEDs is shown in Table 1.6.

PC-LEDs: A white LED primarily using a single blue InGaN LED chip, where a layer of phosphor transforms blue light into green, yellow and red, which jointly produce white light [138]. To elaborate, the white light produced by the PC-LED can be classified into warm-white, neutral-white and cool-white, as determined by the thickness of phosphor. The bandwidth of PC-LEDs is relatively low.

MC-LEDs: They are constituted by three or more LEDs, individually emitting differently coloured light, usually red, green and blue to produce white light [139]. Colour control is achieved by adjusting the different intensities of the different colours. Compared to PC-LEDs, their complexity and cost is lower. Despite this, the MC-LED does not have a higher bandwidth than the PC-LED.

OLEDs: They are based on an organic layer sandwiched between positive and negative carriers in order to stimulate light emission. This LED is commonly used for panel displays. The limited

frequency response of OLEDs makes them unsuitable for high-speed applications [140].

μ-LEDs: An AlGaN based LED array is typically used in VLC and optical fibre applications, which has great potential to be used for panel displays for the sake of supporting high-speed parallel communication. Additionally, they are capable of handling high light output densities, as a benefit of their substantial heat-sinking ability [141].

Table 1.6: A brief comparison of different types of LEDs

Parameter	PC-LED	MC-LED	OLED	μ-LED
Bandwidth	3-5 [MHz]	10-20 [MHz]	$\leq$1 [MHz]	$\geq$300 [MHz]
Efficacy	130 [lm/W]	65 [lm/W]	45 [lm/W]	N/A
Cost	Low	High	Low	High
Complexity	Low	Moderate	High	High
Application	Illumination	Illumination	Display	Bio-sensor

There are numerous contributions on LEDs [131–133, 142, 143]. In [131], the advances in LED materials and devices are detailed, while a white LED-based hardware prototype was designed for short range broadcasting in [132], where the authors focus their attention on the physical layer. In [133], various techniques compensating for the non-linear distortions are analysed and compared in a channel-coded soft detection aided VLC system. A novel clipping distortion reduction method was also proposed. The TRIAC-dimmable LED driver of [142] supports a wide dimming range. The LED development-related studies have been summarised in Table 1.7.

Table 1.7: A brief summary of major contributions on LED techniques

Year	**Authors**	**Contributions**
2009	M. H. Crawford [131]	Described the advances in LED materials and novel devices
2009	H. Elgala *et al.* [132]	Proposed a novel VLC hardware prototype
2012	R. Mesleh *et al.* [133]	Proposed techniques of eliminating the non-linear distortion in a coded soft detection aided VLC system
2014	R. Zhang *et al.* [142]	Presented a wide range TRIAC-dimmable LED drivers
2015	T.-J. Liang *et al.* [143]	Proposed a novel LED driver having a current-limiting mechanism

1.2.2 Applicable Modulation

In VLC, the modulated signals can be used to switch the LEDs at a given frequency, which conveys the on-off pattern-based binary information to the receiver. Similar to the modulation schemes used for FSO communications systems, most of the modulation schemes were elaborated on in Sec. 1.1.3 can be directly invoked in indoor VLC systems. Furthermore, by exploiting the more

benign channel conditions of indoor VLC systems, some unique modulation schemes such as Generalised Space Shift Keying (GSSK) [144], Colour-Shift Keying (CSK) [145, 146] and Optical-OFDM (OOFDM), representing both DC-biased OOFDM (DCO-OFDM) [147] and Asymmetrically Clipped OOFDM (ACO-OFDM) [148] may be also used. In this subsection we will brief summarise the contributions that developed these three modulation schemes.

OFDM relies on multiple orthogonal subcarriers for the transmission of numerous low-rate parallel data stream, for the sake of eliminating the dispersion-induced Inter-Symbol Interference (ISI) imposed by multipath propagation effects. Again, in VLC systems, the transmitted signals must be real and positive. To appropriately modify the OFDM scheme for employment in VLC systems, the concept of DCO-OFDM inspired by [149] may be employed, where a DC-bias is used for shifting the OOFDM modulated signal above zero. However, the disadvantages of DCO-OFDM, such as its undesired negative peak-clipping and its DC-related energy inefficiency motivated the design of ACO-OFDM, which does not suffer from the above-mentioned clipping problem [150]. The ACO-OFDM concept was proposed in [148], while its BER performance and capacity for transmission over AWGN channels were evaluated in [151, 152] respectively. In [147], DCO-OFDM and ACO-OFDM were compared both in terms of their BER performance and bandwidth efficiency. As a further development, a synchronisation method was proposed for ACO-OFDM in [153]. A brief survey of OOFDM was provided in [154]. In [155], a novel sub-carrier-loading based constellation design was proposed for ACO-OFDM. In [156], various modulation schemes suitable for IM/DD were compared, including the OOK, DCO-OFDM, ACO-OFDM and PAM based Discrete Multitone (PAM-DMT) techniques. Diversity-combing assisted ACO-OFDM was advocated in [157]. The information theoretic characteristics of ACO-OFDM subject to a range of different constraints were analysed in [158]. In [159], ACO-OFDM and PAM relying on a Minimum Mean Square Error (MMSE)-Decision Feedback (DFE) equaliser for eliminating the dispersion were compared. Multiple superimposed and spread layers of information were mapped to the subcarriers of both ACO-OFDM and DCO-OFDM in [160], which were detected with the aid of a sophisticated turbo receiver. The system was capable of striking a flexible throughput versus robustness trade-off as a function of the number of superimposed layers. A hybrid OOFDM system combining some elements of both DC-biased and asymmetrically clipped techniques was conceived, which was hence referred to as Asymmetrically Clipped DC-bias OOFDM (ADO-OFDM) [161]. Another hybrid combination of ACO-OFDM and of PAM-DMT was proposed in [162], which struck a compromise. The OOFDM-related studies have been summarised in Table 1.8.

GSSK is a unique subset of the Spatial Modulation family [144], where $\log_2 M_{\text{sym}}$ bits may be conveyed by activating one out of M_{sym} signalling elements, as exemplified by an LED [164]. Compared to the conventional OOK and PPM modulation schemes, the GSSK technique exhibits a higher spectral efficiency [165]. Viewing them from a different perspectives, given the same spectral efficiency, the complexity of GSSK may be deemed to be lower than that of PAM. How-

Table 1.8: A brief summary of major contributions on OOFDM techniques

Year	Authors	Contributions
2006	J. Armstrong *et al.* [148, 151]	Proposed ACO-OFDM and analysed its performance
2007	X. Li *et al.* [152]	Investigated the channel capacity of ACO-OFDM
2008	J. Armstrong *et al.* [147]	Characterised the analytical and simulation-based performance of both ACO-OFDM and DCO-OFDM
2008	S. Tian *et al.* [153]	Proposed a synchronisation method for ACO-OFDM
2009	J. Armstrong [154]	Presented a survey of OOFDM
2009	S. K. Wilson *et al.* [155]	Proposed a new constellation design for ACO-OFDM
2011	D. J. F. Barros *et al.* [156]	Compared the performance of various modulation schemes including ACO-OFDM and DCO-OFDM
2012	X. Li *et al.* [158]	Analysed ACO-OFDM from information theoretical perspective subject to various constraints
2012	R. Zhang *et al.* [160]	Multiple superimposed and spread layers of information were mapped to the subcarriers of ACO-OFDM and DCO-OFDM
2015	J. Jiang *et al.* [163]	Proposed an aperture selection aided ACO-OFDM based MIMO system

ever, a specific impediment of GSSK is that its BER performance is highly channel-dependent, as demonstrated in [165]. The suite of CSK modulation schemes will be detailed in Chapter 4.

1.2.3 MIMO-aided Indoor VLC

Based on the maturing VLC studies [124, 166, 167] and on indoor channel modelling [123, 168, 169], the MIMO concept was introduced also into the family of VLC systems [170, 171], where multiple transmitters and receivers supported a parallel transmission scheme for the sake of linearly increasing the achievable throughput with the number of channels in an idealised crosstalk-free configuration.

Inspired by the concept of [170], numerous MIMO VLC system solutions were proposed in [171–179]. Explicitly, in [179], the experimental demonstration of an indoor VLC MIMO system relying on a 2-by-2 white LED transmitter and a 3-by-3 receiver was presented, which operated at 2 [Mbps]. A substantially higher-speed 1 [Gbps] VLC MIMO system was demonstrated in [171], albeit its BER was as high as 10^{-3}. In [172], the MIMO receiver was improved with the aid of a hemispherical lens, which improved both the FOV and the receiver diversity gain. As a further substantial development, a multi-user transmit precoding assisted MIMO system was presented in [173], where the multi-user interference was eliminated by this transmit precoding scheme. The system operated at a data rate of 100 [Mbps] and a BER level of 10^{-6}. The associated resource

Table 1.9: A brief summary of major contributions on indoor VLC MIMO techniques

Year	Authors	Contributions
2009	L. Zeng [170]	Proposed a MIMO scheme relying on an image receiver for enhancing they system throughput
2013	A. H. Azhar *et al.* [171]	Constituted an MIMO-OFDM scheme on operating at 1 [Gbps] at a BER level of 10^{-3}
2013	T. Q. Wang *et al.* [172]	Employed a hemispherical lens in an indoor VLC MIMO arrangement for improving both FOV and the diversity gain
2013	Y. Hong *et al.* [173]	Proposed a multi-user transmit precoding aided MIMO system operating at 100 [Mbps] and a BER of 10^{-6}
2013	K.-H. Park *et al.* [174]	Conceived sophisticated resource allocation for indoor VLC MIMO
2013	T. Fath *et al.* [175]	Analysed the BER performance of indoor VLC MIMO schemes, including repetition coded MIMO and spatial multiplexing
2014	Y. Wang *et al.* [176]	Employed frequency domain equalisation in a indoor MIMO system
2014	T. Chen *et al.* [177]	Employed an ultra-wide fisheye lens for indoor VLC MIMOs capable of near-omnidirectional reception
2015	M. Biagi *et al.* [69]	Proposed an orthogonal PPM-STBC scheme under a rate constraint

allocation problems were first considered in the context of a VLC MIMO system in [174]. In [175], the BER performance analysis of diverse VLC MIMOs was studied, including both spatial diversity which mapped the same signal to several LEDs, using the above-mentioned concept of repetition coding and spatial multiplexing. The theoretical results were also confirmed by simulations. Again, a 2-by-2 LED VLC MIMO scheme relying on an image receiver[4] was also considered in [176], where a frequency domain equalisation method based on two pairs of time-multiplexed training symbols was proposed. Similar to [172], a novel fisheye lens was advocated in [177] for a VLC MIMO scheme relying on an image receiver, which achieved near-omnidirectional reception with the aid of an ultra-wide-angle fisheye lens. In [69], an orthogonal PPM-STBC scheme operating under specific rate constraints was proposed for VLC. We have summarised the indoor MIMO related studies in Table 1.9.

[4]Compared to the conventional MIMO receiver, the image receiver exploits a lens above the PDs to enhance difference of the the MIMO channels.

1.3 Novel Contributions

The novel research aspects provided by this treatise are summarised as follows:

- We propose a novel ACO-OFDM based FSO MIMO system adopting various MIMO schemes, including: STBC and Space-Time Shift Keying (STSK). Furthermore, we investigate the ACO-OFDM based MIMO system relying on JTRApS for transmission over FSO turbulence channels, which employs joint ML Hard-Detection (HD) for uncoded systems and joint Maximum A posteriori Probability (MAP) Soft-Detection (SD) for FEC coded systems. Additionally, we design a novel JTRApS scheme based on exploiting the FSO channel characteristics for assisting our ACO-OFDM based MIMO system, which is capable of significantly improving both the achievable BER and throughput, while imposing a reduced power consumption and hardware complexity. We will show that the performance gain of our JTRApS scheme becomes more significant under hostile turbulence conditions. **These novel contributions were proposed in paper "Journal 1" in the publication list.**

- We carefully adapt some concepts from classical RF communication to formulate beneficial multiuser transmission scenarios relying on Unity Frequency Reuse (UFR) as well as on Higher Frequency Reuse Factor based Transmission (HFRFT) and on Vectored Transmission (VT). We investigate both the video degradation and the achieved video rate of the above three resource allocation algorithms in a video-streaming application. The results show that the VT scenario is capable of providing the best performance under all circumstances. **These novel contributions were proposed in paper "Journal 2" in the publication list.**

- We conceive the MAP-based SD of CSK and characterise its *extrinsic* mutual information improvement achieved by our iterative receiver with the aid of EXtrinsic Information Transfer (EXIT) charts. We first characterise the performance-limitations of the IEEE standard's constellation labelling and circumvent them by designing improved signal labelling strategies with the aid of EXIT charts. As a result, we demonstrate that the power gain attained by this signal labelling improves the achievable transmission distance, and/or enhances the link's reliability in VLC applications. **These novel contributions were proposed in paper "Journal 3" in the publication list.**

1.4 Thesis Outline

Let us now highlight the outline of this thesis, which is organised as shown in Fig. 1.5.

Chapter 2: OOFDM Based MIMO System

In Chapter 2, an OOFDM based MIMO system is proposed for transmission over outdoor FSO

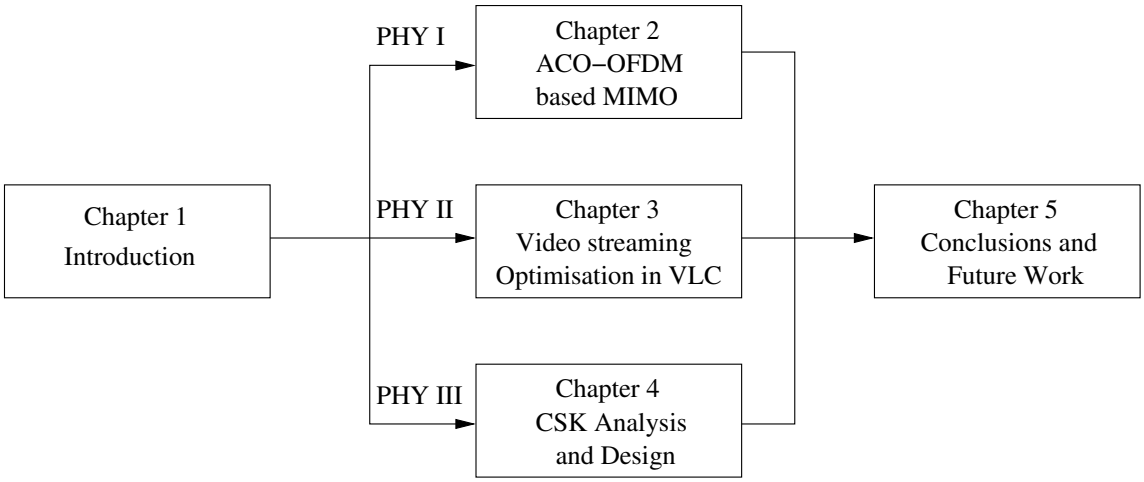

Figure 1.5: Organisation of the thesis.

turbulence channels. MIMO schemes, such as STBC and STSK will be investigated. In Sec. 2.2, the performance of an ACO-OFDM based MIMO system will be studied both in non-dispersive and in dispersive channels. In Sec. 2.3, three different Aperture Selection (ApS) scenarios will be discussed, and a novel Joint Transmit/Receive Aperture Selection (JTRApS) scheme will be proposed. The performance of this JTRApS aided ACO-OFDM based uncoded MIMO system will be characterised in Sec. 2.4. Furthermore, a three-stage concatenated Recursive Systematic Convolutional (RSC) coded and Unity Rate Code (URC) system will be conceived in Sec. 2.5.

Chapter 3: Video Streaming in the Multiuser Indoor Visible Light Downlink

In Chapter 3, we will design a video streaming system for diverse transmission scenarios. In Sec. 3.2, the different transmission scenarios, such as the UFR, HFRFT and VT-2 regime will be described. In Sec. 3.3, we will firstly introduce the video traffic model, where the transmission priority of different types of video frames will also be discussed. In Sec. 3.4, the system performance will be analysed, demonstrating that the VT-2 scenario suffers from the lowest video degradation.

Chapter 4: Analysis and Design of CSK

In Chapter 4, we mainly focus our attention on the performance analysis of CSK modulation schemes in the context of an indoor VLC system. Based on the results we propose a pair of algorithms for finding the best bit-to-symbol mapping for different detection schemes. In Sec. 4.2, we will introduce the CSK system and the associated channel model. The detection performance of different system configurations is detailed in Sec. 4.3, where a union bound aided BER performance analysis is provided. In Sec. 4.4, the performance of the system is characterised by EXIT charts. Finally,in Sec. 4.5, a pair of bit-to-symbol mapping algorithms is proposed.

Chapter 5: Conclusions and Future Research

In Sec. 5.1, we summarise the major findings and contributions of this treatise, while in Sec. 5.2 we outline a range potential future research topics.

Chapter 2

PHY I: Optical Orthogonal Frequency Division Multiplexing Based MIMO Systems

2.1 Introduction

In recent years, the availability of spectral resources in classical RF communication is lagging behind the ever-increasing user demands. Hence FSO [8, 24, 180, 181] has attracted considerable attention, as its benefits include license-free operation and high data rate. According to the IEEE standard [4] conceived for short range optical wireless communication, owing to the specific nature of optical wireless communication, the transmitted symbols must be unipolar, namely real and non-negative. Thus in the so-called PHY I of outdoor optical wireless communication, the early modulation techniques employed were restricted to low-complexity schemes, such as OOK, PPM and PAM.

2.1.1 MIMO in FSO Communication

FSO communication mainly operates in turbulent outdoor channel conditions, where it suffers from scintillation, geometric loss, atmospheric loss, pointing errors and other adverse propagation factors. Fortunately, FSO devices typically support point-to-multipoint transmissions. Hence, MIMO techniques, which are capable of increasing the system's throughput as well as acquiring a diversity gain and/or offering an improved BER performance, can be invoked for mitigating these detrimental effects in FSO communication. More specifically, both spatial diversity as well as time diversity can be attained at both the transmitter and receiver for combating the short-term loss of signal strength as proposed in [108]. Alamouti-type space-time coding was conceived for optical communication in [104], while STBCs were designed for FSO communication in [39]. Although

FSO MIMO techniques are capable of enhancing the system's reliability and capacity, they require a large number of transceiver devices, which may lead to a high power consumption and high costly hardware. This situation is similar to that in conventional RF MIMO systems which require multiple optical chains. Actually, the situation in the optical case is more serious than the RF case, because the signals in electronic domain are transformed to and recovered from the optical domain and therefore more processing components are involved than in conventional RF communications, so that every optical transmit or receive link also includes an entire optical chain in RF domain correspondingly. If we exploit a large-dimensional MIMO scheme, not only the hardware expense would be excessive, but also the MIMO design complexity could be another problem we have to carefully consider.

2.1.2 ACO-OFDM in OW Communication

As mentioned above, at the early stage of development, the modulation techniques were limited to simple OOK, PPM and PAM. The development of optical OFDM has changed the entire situation. The DCO-OFDM [149] adopts the method of 'Hermitian symmetry' to enable the employment of complex-valued modulation schemes and it uses a DC-bias to shift the negative values of modulated symbols up above the zero value, whilst simultaneously clipping the excessive negative peaks. However, this DC-bias lifting operation introduces non-linear distortion known as 'clipping noise'. As a further disadvantage, the DC-bias required leads to additional undesirable power-dissipation. Hence, the authors of [148] proposed a novel optical OFDM method, known as the ACO-OFDM, which provides an alternative way of converting complex-valued signals into unipolar ones. Similar to DCO-OFDM, ACO-OFDM also exploits the Hermitian symmetry. However, since no DC-bias is introduced, ACO-OFDM is more power-efficient at the expense of a reduced bandwidth efficiency [147, 151], as discussed in Chapter 1. More specifically, ACO-OFDM only uses the odd-indexed subcarriers of OFDM symbols to transmit useful information, while letting the 'clipping noise' fall on the even-indexed subcarriers [158]. This arrangement, which obviously sacrifices the bandwidth efficiency, requires no DC-bias and, therefore, circumvents the above-mentioned clipping distortion and power-inefficiency problem.

2.1.3 Brief Introduction to Aperture Selection

In RF MIMO communication, Antenna Selection (AS) offers a low-cost, low-complexity means of reducing the number of optical chains utilised at the transmitter and/or receiver, while retaining the significant advantages of MIMO.

Generally, AS in RF MIMO can be classified into three categories, namely, Transmit Antenna Selection (TxAS), Receive Antenna Selection (RxAS), as well as Joint Transmit/Receive Antenna Selection (JTRAS) [182]. The TxAS schemes conceived for MIMO systems employing different

criteria were studied in [183–185], while several RxAS schemes designed for MIMO systems were investigated in [186–189]. As a hybrid version of TxAS and RxAS, many JTRAS schemes were proposed in [190–198], where it was observed that employing JTRAS schemes was capable of improving the system's performance, while maintaining a low system complexity. Moreover, it is well-known that the maximum capacity based AS usually requires exhaustive search over all the possible subsets of the full MIMO channel matrix, which becomes impractical for systems having a large number of transmit and/or receive antennas [198]. Sub-optimal capacity-based AS techniques were proposed in [194, 195, 198], which were capable of reducing the AS complexity at the cost of a certain performance loss. As another promising, yet low-complexity category of AS algorithms, the Norm-Based (NB) AS techniques were investigated in [193, 196, 197], where it was shown that NB AS algorithms are capable of approaching the performance of capacity based AS techniques, while imposing a lower complexity. Recently, we have developed a simple yet efficient NB JTRAS scheme [199].

These beneficial AS techniques developed for RF MIMO may also provide valuable tools for improving the appeal of optical MIMOs, by efficiently exploiting the available optical chains. Furthermore, at a modest extra cost imposed on FSO system design and optical alignment, the system becomes capable of providing a high performance. Due to the system-level similarity between RF MIMOs and FSO MIMOs, the philosophy of AS techniques originally conceived for conventional RF MIMOs [182, 197, 198] may also be applied to FSO MIMOs, leading to the concept of Aperture Selection (ApS) [103, 200–202], which inherits the low-cost and low-complexity benefits of the classic RF AS. In [103], the concept of transmit AS was introduced to FSO communication, and it was shown to be capable of achieving full diversity, whilst AS applied both at the transmit and receive sides for multi-element FSO was comprehensively studied in [201]. In [200] a practical application of ApS in mobile FSO nodes was characterised. Furthermore, as an extension of ApS, relay selection based on channel quality information was portrayed in [202]. Hence, in FSO MIMO systems, given a fixed number of optical chains[1], employing ApS is capable of significantly improving the system's achievable performance. Furthermore, as the average channel variance increases with the turbulence level of the FSO channel, adopting ApS in FSO MIMO become beneficial, since the specific links exhibiting the highest power will be activated.

2.1.4 Novel Contribution

Against the above background, in this chapter, we propose a novel ACO-OFDM [148] based FSO MIMO system relying on JTRApS for transmission over FSO turbulence channels, which employs joint ML HD for uncoded systems and joint MAP SD for FEC coded systems. Our contributions are as follows.

[1] In this case, we define an entire set of electronic hardware components at transmit/receive end, including electronic-to-optical conversion or optical-to-electronic conversion, as an optical chain.

- We construct a novel ACO-OFDM based MIMO system and investigate its performance under various FSO turbulence channel conditions. We will demonstrate that the resultant BER curves corresponding to different levels of turbulence reveal an intriguing performance curve-crossing phenomenon.

- We design a novel ApS scheme based on exploiting the FSO channel characteristics for assisting our ACO-OFDM based MIMO system, which is capable of significantly improving both the achievable BER and throughput, while imposing a reduced power consumption and hardware complexity. We will show that the performance gain of our ApS scheme becomes more significant under hostile turbulence channel conditions.

2.2 ACO-OFDM Based MIMO System

We refer to the number of optical chains at the transmitter and receiver as the number of Transmit Apertures (TAps) and Receive Apertures (RAps) denoted by $L_{\mathrm{T}} = M$ and $L_{\mathrm{R}} = N$, which form an $(M \times N)$-aperture MIMO-aided OW system, as seen in Fig. 2.1.

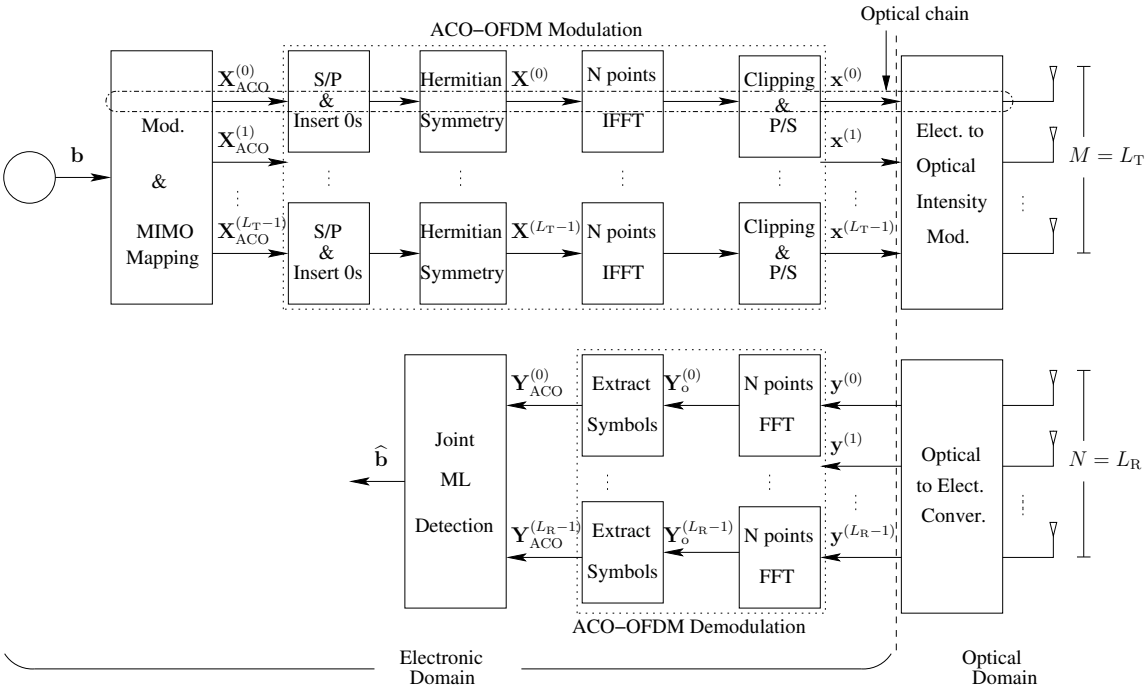

Figure 2.1: Schematic of the proposed ACO-OFDM based MIMO system, where L_{T} and L_{R} are the numbers of optical chains at the transmitter and receiver, respectively, while M and N represent the numbers of transmit and receive apertures, respectively. We have $L_{\mathrm{T}} = M$ and $L_{\mathrm{R}} = N$.

2.2.1 ACO-OFDM Modulation in MIMO System

The ACO-OFDM input vector of the mth MIMO sub-stream $0 \leq m \leq L_{\mathrm{T}} - 1$ is constituted by the $N_{\mathrm{F}}/4$ Frequency Domain (FD) data symbols given by $\mathbf{X}_{\mathrm{ACO}}^{(m)} = \left[X_0^{(m)}\ X_1^{(m)} \cdots X_{N_{\mathrm{F}}/4-1}^{(m)}\right]^{\mathrm{T}}$, where N_{F} represents the length of OFDM symbols Quadrature Amplitude Modulation (QAM) signalling is employed here. ACO-OFDM only uses the odd-indexed subcarriers to carry data, while assigning '0s' to the even-indexed subcarriers as well as simultaneously adopting a Hermitian-symmetric symbol arrangement. If we let $\bar{X}^{(m)}$ represent the elements of the input vector at the Hermitian symmetric block, then $\mathbf{X}_{\mathrm{ACO}}^{(m)}$ is first expanded into the form

$$\begin{aligned}\mathbf{X}^{(m)} &= \left[0\ X_0^{(m)} \cdots 0\ X_{N_{\mathrm{F}}/4-1}^{(m)}\ 0\ \left(X_{N_{\mathrm{F}}/4-1}^{(m)}\right)^* \cdots 0\ \left(X_0^{(m)}\right)^*\right]^{\mathrm{T}} \\ &= \left[\bar{X}_0^{(m)}\ \bar{X}_1^{(m)} \cdots \bar{X}_{N_{\mathrm{F}}-1}^{(m)}\right]^{\mathrm{T}}. \end{aligned} \tag{2.1}$$

By defining the N_F-point Inverse Fast Fourier Transform (IFFT) matrix as

$$\mathbf{F} = \frac{1}{\sqrt{N_F}} \begin{bmatrix} 1 & 1 & \cdots & 1 \\ 1 & e^{\mathrm{j}2\pi/N_F} & \cdots & e^{\mathrm{j}2\pi(N_F-1)/N_F} \\ \vdots & \vdots & \ddots & \vdots \\ 1 & e^{\mathrm{j}2\pi(N_F-1)/N_F} & \cdots & e^{\mathrm{j}2\pi(N_F-1)^2/N_F} \end{bmatrix}, \tag{2.2}$$

where $\mathrm{j} = \sqrt{-1}$. Then, the Time Domain (TD) OFDM symbol vector on the mth substream is given by

$$\mathbf{x}^{(m)} = \left[x_0^{(m)}\ x_1^{(m)} \cdots x_{N_{\mathrm{F}}-1}^{(m)}\right]^{\mathrm{T}} = \mathbf{F}\mathbf{X}^{(m)}. \tag{2.3}$$

All the negative-valued elements in $\mathbf{x}^{(m)}$ are forced to become zero by the clipping operation. As a benefit of this ACO-OFDM modulation arrangement, the useful odd-indexed subcarriers are protected from the detrimental effects of clipping. Consequently, both the real and imaginary information of the original FD data in $\mathbf{X}^{(m)}$, which are spread across all the TD OFDM symbols, are well preserved. After concatenating the N_{cp}-length Cyclic Prefix (CP) to $\mathbf{x}^{(m)}$, the resultant $(N_{\mathrm{F}} + N_{\mathrm{cp}})$-length[2] vector $\mathbf{x}_{\mathrm{o}}^{(m)}$ is converted into the optical signal by the Electronic to Optical (E/O) converter for transmission.

At the receiver end, after the Optical to Electronic (O/E) conversion and the removal of the CP, the N_{F}-length TD signal vector received by the nth receiver chain is given by

$$\mathbf{y}^{(n)} = \xi \cdot \bar{\mathbf{H}}^{(n,m)}\mathbf{x}_{\mathrm{o}}^{(m)} + \mathbf{v}^{(n,m)}, \tag{2.4}$$

where $\bar{\mathbf{H}}^{(n,m)}$ represents the $N_{\mathrm{F}} \times (N_{\mathrm{F}} + N_{\mathrm{cp}})$-element linear convolution channel matrix between the mth transmitter and the $n$the receiver, while $\mathbf{v}^{(n,m)}$ denotes the TD AWGN vector imposed on

[2]Here we assume that the length of CP is always higher than or at least equal to the number of dispersive channel taps.

the channel linking the mth TAp to the nth RAp, whose elements have zero mean and a variance of σ^2, while ξ [W/A] is the responsivity of the photodiode. Eq. (2.4) is equivalent to

$$\mathbf{y}^{(n)} = \xi \cdot \mathbf{H}^{(n,m)}\mathbf{x}^{(m)} + \mathbf{v}^{(n,m)}, \tag{2.5}$$

where $\mathbf{H}^{(n,m)}$ is the circulant convolution channel matrix of $(N_{\mathrm{F}} \times N_{\mathrm{F}})$ elements [203]

$$\mathbf{H}^{(n,m)} = \begin{bmatrix} H_0 & 0 & \cdots & 0 & \cdots & H_2 & H_1 \\ H_1 & H_0 & \cdots & \vdots & \cdots & H_3 & H_2 \\ \vdots & \vdots & \ddots & 0 & \ddots & \vdots & \vdots \\ H_{\mathrm{N_{cp}}} & H_{\mathrm{N_{cp}}-1} & \cdots & H_0 & \cdots & H_{\mathrm{N_{cp}}-2} & H_{\mathrm{N_{cp}}-1} \\ 0 & H_{\mathrm{N_{cp}}} & \cdots & \vdots & \ddots & \vdots & \vdots \\ \vdots & \vdots & \ddots & H_{\mathrm{N_{cp}}-1} & \cdots & H_0 & 0 \\ 0 & 0 & \cdots & H_{\mathrm{N_{cp}}} & \cdots & H_1 & H_0 \end{bmatrix}, \tag{2.6}$$

where each of the channel impulse responses are independent random variables obeying the Gamma-Gamma distribution. Furthermore, we have $\xi \cdot \mathbf{H}^{(n,m)} = \mathbf{F}\mathbf{\Lambda}^{(n,m)}\mathbf{F}^{\mathrm{H}}$, where $\mathbf{\Lambda}^{(n,m)}$ is the $(N_{\mathrm{F}} \times N_{\mathrm{F}})$-element diagonal matrix with eigenvalues of $\mathbf{H}^{(n,m)}$ at its diagonal entries. By applying Fast Fourier Transform (FFT)-based OFDM demodulation to $\mathbf{y}^{(n)}$, we obtain the received N_{F}-length FD symbol vector

$$\mathbf{Y}_{\mathrm{o}}^{(n)} = \mathbf{F}^{\mathrm{H}}\mathbf{y}^{(n)} = \mathbf{\Lambda}^{(n,m)}\mathbf{X}^{(m)} + \mathbf{V}^{(n,m)}, \tag{2.7}$$

where the FD channel noise vector $\mathbf{V}^{(n,m)} = \mathbf{F}^{\mathrm{H}}\mathbf{v}^{(n,m)}$ also obeys the same AWGN distribution as $\mathbf{v}^{(n,m)}$.

Upon collecting all the odd-indexed elements in the first half of $\mathbf{Y}_{\mathrm{o}}^{(n)}$ and arranging them in the $N_{\mathrm{F}}/4$-length vector $\mathbf{Y}_{\mathrm{ACO}}^{(n)}$, we have

$$\mathbf{Y}_{\mathrm{ACO}}^{(n)} = \mathbf{\Lambda}_{\mathrm{ACO}}^{(n,m)}\mathbf{X}_{\mathrm{ACO}}^{(m)} + \mathbf{V}_{\mathrm{ACO}}^{(n,m)}, \tag{2.8}$$

where $\mathbf{\Lambda}_{\mathrm{ACO}}^{(n,m)}$ is the $\left(N_{\mathrm{F}}/4\right) \times \left(N_{\mathrm{F}}/4\right)$-element diagonal matrix representing the first $N_{\mathrm{F}}/4$ odd-indexed elements extracted from the diagonal of $\mathbf{\Lambda}^{(n,m)}$, which $\mathbf{V}_{\mathrm{ACO}}^{(n,m)}$ contains the first $N_{\mathrm{F}}/4$ odd-indexed elements of $\mathbf{V}^{(n,m)}$. Clearly, $\mathbf{Y}_{\mathrm{ACO}}^{(n)}$ constitutes sufficient statistics for estimating $\mathbf{X}_{\mathrm{ACO}}^{(m)}$.

2.2.2 FSO Channel Characteristics

As we elaborated in Chapter 1, the FSO turbulent channels impose numerous detrimental effects, which can be modelled by a Gamma-Gamma distribution [17]. The Probability Density Function (PDF) of the CIR is given by [17]

$$p_{\mathrm{GG}}(x_0) = \frac{2(\alpha_{\mathrm{g}}\beta_{\mathrm{g}})^{\frac{\alpha_{\mathrm{g}}+\beta_{\mathrm{g}}}{2}}}{\Gamma(\alpha_{\mathrm{g}})\Gamma(\beta_{\mathrm{g}})} x_0^{\frac{\alpha_{\mathrm{g}}+\beta_{\mathrm{g}}}{2}-1} \cdot K_{\alpha_{\mathrm{g}}-\beta_{\mathrm{g}}}\left(2\sqrt{\alpha_{\mathrm{g}}\beta_{\mathrm{g}} \cdot x_0}\right), \tag{2.9}$$

Table 2.1: A Comparison between Rayleigh Fading Channel and FSO Turbulence Channel

	RF Rayleigh channel	FSO turbulence channel
CIR's values	complex	real and positive
main cause	fading	turbulence
pathloss	yes	yes
scattering	yes	yes
CIRs vary with f_{d} or C_n^2	yes	yes
variance varies with f_{d} or C_n^2	no	yes

where $\Gamma(\cdot)$ denotes the Gamma function, $K_\nu(\cdot)$ is the modified Bessel function of the second kind, while α_{g} and β_{g} are the pair of parameters controlling the two Gamma functions.

Specifically, α_{g} determines the large scale scattering caused by refractive effects, which results in beam direction deviation, and it is expressed by [17]

$$\alpha_{\mathrm{g}} = \left\{ \exp\left[\frac{0.49\sigma_{\mathrm{r}}^2}{\left(1+0.18d^2+0.56\sigma_{\mathrm{r}}^{12/5}\right)^{7/6}} \right] - 1 \right\}^{-1}, \tag{2.10}$$

whilst β is attributed to the diffraction that leads to beam spreading and irradiance fluctuation, which is given by [17]

$$\beta_{\mathrm{g}} = \left\{ \exp\left[\frac{0.51\sigma_{\mathrm{r}}^2\left(1+0.69\sigma_{\mathrm{r}}^{12/5}\right)^{-5/6}}{\left(1+0.9d^2+0.62\sigma_{\mathrm{r}}^{12/5}\right)^{5/6}} \right] - 1 \right\}^{-1}. \tag{2.11}$$

In Eqs. (2.10) and (2.11), $d_{\mathrm{g}} = \sqrt{k_{\mathrm{g}} D_{\mathrm{aper}}^2 / 4L_{\mathrm{dis}}}$, where $k_{\mathrm{g}} = 2\pi/\lambda$ denotes the number of optical waves with λ being the wavelength, L_{dis} indicates the physical link distance between the TAp and the RAp, while D_{aper} is the diameter of the RAp. Furthermore, σ_{r}^2 is known as the Rytov variance, which directly determines the optical variance of the FSO turbulent channel, and it is given by

$$\sigma_{\mathrm{r}}^2 = 0.5C_n^2 k_{\mathrm{g}}^{7/6} L_{\mathrm{dis}}^{11/6}. \tag{2.12}$$

It is worth emphasising that although C_n^2 plays a similar role in the Gamma-Gamma modelled channel to that of the normalised Doppler frequency f_{d} in the classic RF Rayleigh fading channel, they also have significant differences. Explicitly as shown in Table 2.1, we can see apart from the CIR's value, not only the similar roles played by f_{d} and C_n^2 in the corresponding channels, but also their differences. Specifically, unlike the RF Rayleigh fading channel, whose variance does not vary with f_{d}, the variance of the FSO turbulence channel varies with C_n^2.

2.2.3 System Architecture

Our proposed ACO-OFDM based MIMO system is depicted in Fig. 2.1, where all the component blocks on the left hand side of the vertical dashed line represent the electronic hardware, while on

the right hand side of this dashed line, after the E/O and O/E conversions, the signals are transmitted to and received from the corresponding apertures. The number of available optical chains at the transmitter and receiver are L_{T} and L_{R}, respectively. Furthermore, the system of Fig. 2.1 is capable of adopting any MIMO scheme. Without any loss of generality, here we mainly consider two MIMO schemes: STBC and STSK [204].

2.2.3.1 ACO-OFDM Based STBC Scheme

In Fig. 2.1, when the STBC$(M, N, T_{\mathrm{slot}}, Q)$ scheme is employed, $N_{\mathrm{b}} = Q\log_2(M_{\mathrm{sym}}), Q = M$ bits are mapped to each STBC block, where M_{sym} is the number of bits per complex symbol. The original information bits, denoted as $\mathbf{b}$, are firstly mapped into the $N_{\mathrm{F}}/4$-length QAM symbol vector denoted by $\mathbf{S} = \left[S_0,\ S_1, \cdots S_{N_{\mathrm{F}}/4-1}\right]^{\mathrm{T}}$, which is then mapped onto the L_{T} sub-streams of $\mathbf{S}_{\mathrm{ACO}}^{(m)}$ for $0 \leq m \leq L_{\mathrm{T}} - 1$, according to the STBC MIMO scheme:

$$\mathbf{X}_{\mathrm{ACO}} = \mathcal{F}_{\mathrm{STBC}}(\mathbf{S}), \tag{2.13}$$

relying on the STBC mapping $\mathcal{F}_{\mathrm{STBC}}(\cdot)$. Considering the G2 STBC scheme ($L_{\mathrm{T}} = 2$) as an example, the two rows of $\mathbf{X}_{\mathrm{ACO}}$ are given by

$$\mathbf{X}_{\mathrm{ACO}}^{(0)} = \frac{1}{\sqrt{L_{\mathrm{T}}}}\left[S_0,\ -S_1^*, \cdots S_{N_{\mathrm{F}}/4-2},\ -S_{N_{\mathrm{F}}/4-1}^*\right]^{\mathrm{T}} \tag{2.14}$$

$$\mathbf{X}_{\mathrm{ACO}}^{(1)} = \frac{1}{\sqrt{L_{\mathrm{T}}}}\left[S_1,\ -S_0^*, \cdots S_{N_{\mathrm{F}}/4-1},\ -S_{N_{\mathrm{F}}/4-2}^*\right]^{\mathrm{T}}. \tag{2.15}$$

Each $\mathbf{X}_{\mathrm{ACO}}^{(m)}$ is processed by an ACO-OFDM modulator to generate the TD unipolar signal vector $\mathbf{x}^{(m)}$, as detailed in Sec. 2.2.1. After optical intensity modulation, $\mathbf{x}^{(m)}$ is launched through the mth TAp associated with the mth optical chain of the transmitter.

The L_{T} signal sub-streams are transmitted over the $(L_{\mathrm{R}} \times L_{\mathrm{T}})$-element MIMO FSO turbulence channel. At the receiver, after O/E, the L_{R} received TD signal sub-streams $\mathbf{y}^{(n)}$ for $0 \leq n \leq L_{\mathrm{R}} - 1$ are passed through the ACO-OFDM demodulator to extract the useful complex-valued sequences $\mathbf{Y}_{\mathrm{ACO}}^{(n)}$ for $0 \leq n \leq L_{\mathrm{R}} - 1$. Assuming the perfect knowledge of the CSI at the receiver, the joint ML detection of $\mathbf{S}$ can be carried out, given $\mathbf{Y}_{\mathrm{ACO}}^{(n)}$ for $0 \leq n \leq L_{\mathrm{R}} - 1$, which is denoted as $\widehat{\mathbf{S}}$. Finally, the estimate of the transmitted binary bit block $\mathbf{b}$, denoted as $\widehat{\mathbf{b}}$, can be obtained by QAM demapping of the ML estimate $\widehat{\mathbf{S}}$.

More specifically, upon collecting all the received $\mathbf{Y}_{\mathrm{ACO}}^{(n)}$ for $0 \leq n \leq L_{\mathrm{R}} - 1$ in the $\left(L_{\mathrm{R}} \cdot N_{\mathrm{F}}/4\right)$-length vector we have: $\mathbf{Y}_{\mathrm{ACO}} = \left[\left(\mathbf{Y}_{\mathrm{ACO}}^{(0)}\right)^{\mathrm{T}} \left(\mathbf{Y}_{\mathrm{ACO}}^{(1)}\right)^{\mathrm{T}} \cdots \left(\mathbf{Y}_{\mathrm{ACO}}^{(L_{\mathrm{R}}-1)}\right)^{\mathrm{T}}\right]^{\mathrm{T}}$. Then, according to Eq. (2.7), $\mathbf{Y}_{\mathrm{ACO}}$ can be expressed as

$$\mathbf{Y}_{\mathrm{ACO}} = \mathbf{\Lambda}_{\mathrm{ACO}}\mathbf{X}_{\mathrm{ACO}} + \mathbf{V}_{\mathrm{ACO}}, \tag{2.16}$$

in which $\mathbf{V}_{\mathrm{ACO}} = \left[\left(\mathbf{V}_{\mathrm{ACO}}^{(0)}\right)^{\mathrm{T}} \left(\mathbf{V}_{\mathrm{ACO}}^{(1)}\right)^{\mathrm{T}} \cdots \left(\mathbf{V}_{\mathrm{ACO}}^{(L_{\mathrm{R}}-1)}\right)^{\mathrm{T}}\right]^{\mathrm{T}}$ with $\mathbf{V}_{\mathrm{ACO}}^{(n)} = \sum_{m=0}^{L_{\mathrm{R}}-1} \mathbf{V}_{\mathrm{ACO}}^{(n,m)}$, while

$\mathbf{X}_{\mathrm{ACO}} = \left[\left(\mathbf{X}_{\mathrm{ACO}}^{(0)}\right)^{\mathrm{T}} \left(\mathbf{S}_{\mathrm{ACO}}^{(1)}\right)^{\mathrm{T}} \cdots \left(\mathbf{S}_{\mathrm{ACO}}^{(L_{\mathrm{T}}-1)}\right)^{\mathrm{T}} \right]^{\mathrm{T}}$ and

$$\mathbf{\Lambda}_{\mathrm{ACO}} = \begin{bmatrix} \mathbf{\Lambda}_{\mathrm{ACO}}^{(0,0)} & \mathbf{\Lambda}_{\mathrm{ACO}}^{(0,1)} & \cdots & \mathbf{\Lambda}_{\mathrm{ACO}}^{(0,L_{\mathrm{T}}-1)} \\ \mathbf{\Lambda}_{\mathrm{ACO}}^{(1,0)} & \mathbf{\Lambda}_{\mathrm{ACO}}^{(1,1)} & \cdots & \mathbf{\Lambda}_{\mathrm{ACO}}^{(1,L_{\mathrm{T}}-1)} \\ \vdots & \vdots & \vdots & \vdots \\ \mathbf{\Lambda}_{\mathrm{ACO}}^{(L_{\mathrm{R}}-1,0)} & \mathbf{\Lambda}_{\mathrm{ACO}}^{(L_{\mathrm{R}}-1,1)} & \cdots & \mathbf{\Lambda}_{\mathrm{ACO}}^{(L_{\mathrm{R}}-1,L_{\mathrm{T}}-1)} \end{bmatrix}. \tag{2.17}$$

Therefore, given that i denote the STBC block index, the ML estimate of each STBC block $\widehat{\mathbf{S}}(i) \in \mathbb{C}^{M \times T_{\mathrm{slot}}}$ is the solution of the following optimisation problem

$$\widehat{\mathbf{S}}(i) = \arg\min_{\widetilde{\mathbf{S}} \in \boldsymbol{\mathcal{S}}} \left\| \mathbf{Y}_{\mathrm{ACO}}(i) - \mathbf{\Lambda}_{\mathrm{ACO}}(i) \mathcal{F}_{\mathrm{STBC}}\left(\widetilde{\mathbf{S}}\right) \right\|^2, \tag{2.18}$$

where $\boldsymbol{\mathcal{S}}$ denotes the feasible set of $\mathbf{S}$, i.e. $\mathbf{S}$ assumes a value from the set $\boldsymbol{\mathcal{S}}$, and the size of $\boldsymbol{\mathcal{S}}$ is $M_{\mathrm{sym}}^{N_{\mathrm{F}}/4}$ for the M_{sym}-QAM signalling.

Note that there is a total of $(N \times M)$ FSO turbulence channels and the overall MIMO channel matrix can be expressed as:

$$\mathbf{H} = \begin{bmatrix} \mathbf{H}^{(0,0)} & \mathbf{H}^{(0,1)} & \cdots & \mathbf{H}^{(0,M-1)} \\ \mathbf{H}^{(1,0)} & \mathbf{H}^{(1,1)} & \cdots & \mathbf{H}^{(1,M-1)} \\ \vdots & \vdots & \vdots & \vdots \\ \mathbf{H}^{(N-1,0)} & \mathbf{H}^{(N-1,1)} & \cdots & \mathbf{H}^{(N-1,M-1)} \end{bmatrix}. \tag{2.19}$$

According to Eq. (2.5), the corresponding overall MIMO channel model is then given by

$$\mathbf{y} = \xi \cdot \mathbf{H}\mathbf{x} + \mathbf{v}, \tag{2.20}$$

where we have $\mathbf{y} = \left[\left(\mathbf{y}^{(0)}\right)^{\mathrm{T}} \left(\mathbf{y}^{(1)}\right)^{\mathrm{T}} \cdots \left(\mathbf{y}^{(N-1)}\right)^{\mathrm{T}} \right]^{\mathrm{T}}$, and $\mathbf{x} = \left[\left(\mathbf{x}^{(0)}\right)^{\mathrm{T}} \left(\mathbf{x}^{(1)}\right)^{\mathrm{T}} \cdots \left(\mathbf{x}^{(M-1)}\right)^{\mathrm{T}} \right]^{\mathrm{T}}$, while $\mathbf{v} = \left[\left(\mathbf{v}^{(0)}\right)^{\mathrm{T}} \left(\mathbf{v}^{(1)}\right)^{\mathrm{T}} \cdots \left(\mathbf{v}^{(N-1)}\right)^{\mathrm{T}} \right]^{\mathrm{T}}$ with $\mathbf{v}^{(n)} = \sum_{m=0}^{M-1} \mathbf{v}^{(n,m)}, 0 \leq n \leq N-1$. To support such a large-scale MIMO system, we need $L_{\mathrm{T}} = M$ optical chains at the transmitter and $L_{\mathrm{R}} = N$ optical chains at the receiver, which is costly.

2.2.3.2 ACO-OFDM Based STSK Scheme

Similar to the STBC mapping, when the STSK($M, N, T_{\mathrm{slot}}, Q$) [205–208] scheme is employed, there are a total of $N_{\mathrm{b}} = \log_2 Q + \log_2 M_{\mathrm{sym}}$ bits mapped to each STSK block. The first $\log_2(Q)$ bits are used for choosing a single dispersion matrix $\mathbf{A}(i)$ from the Q pre-assigned dispersion matrices $\left\{ \boldsymbol{\mathcal{A}}^{(q)} \in \mathbb{C}^{M \times T_{\mathrm{slot}}}, 1 \leq q \leq Q \right\}$. Let i denote the STSK block index, while the remaining $\log_2(M_{\mathrm{sym}})$ bits are mapped to the complex-valued symbol $\mathbf{S}(i)$ of a QAM scheme [205]. A total of N_{b} binary bits are mapped to a single STSK signalling block $\mathbf{X}_{\mathrm{ACO}}(i) \in \mathbb{C}^{M \times T_{\mathrm{slot}}}$. Owing to the spreading effect of the dispersion matrix, the STSK symbols $\mathbf{X}$ could not be simply expressed

in the form of Eq. (2.14) and (2.15). Instead, we express the STSK symbols as

$$\begin{aligned}\mathbf{X}_{\mathrm{ACO}}(i) &= \mathcal{F}_{\mathrm{STSK}}\left[\mathbf{S}(i)\right] \\ &= \mathbf{S}(i)\mathbf{A}(i),\end{aligned} \tag{2.21}$$

and with the aid of multiple STSK signalling blocks, we construct the STSK symbols $\mathbf{X}_{\mathrm{ACO}}$. Having obtained the STSK symbols, the rest of the procedure can follow the same steps as those in Eq. (2.8) - (2.20). More specifically, when applying joint ML-based HD to each STSK block, Eq. (2.18) becomes

$$\begin{aligned}\widehat{\mathbf{S}}(i) &= \arg\min_{\widetilde{\mathbf{S}}\in\boldsymbol{\mathcal{S}}} \left\|\mathbf{Y}_{\mathrm{ACO}}(i) - \mathbf{\Lambda}_{\mathrm{ACO}}(i)\mathcal{F}_{\mathrm{STSK}}\left(\widetilde{\mathbf{S}}\right)\right\|^2, \\ &= \arg\min_{\widetilde{\mathbf{S}}\in\boldsymbol{\mathcal{S}},\widetilde{\mathbf{A}}\in\boldsymbol{\mathcal{A}}} \left\|\mathbf{Y}_{\mathrm{ACO}}(i) - \mathbf{\Lambda}_{\mathrm{ACO}}(i)\widetilde{\mathbf{A}}\widetilde{\mathbf{S}}\right\|^2,\end{aligned} \tag{2.22}$$

where we search for the optimal combination of $\widetilde{\mathbf{S}}$ and $\widetilde{\mathbf{A}}$, in order to estimate the results.

2.2.4 Uncoded Performance in Non-Dispersive Channels

Let us commence by investigating the performance of different ACO-OFDM based MIMO systems in non-dispersive turbulent FSO channel conditions based on simulations. Explicitly, we simulate the turbulent FSO channel assuming a physical distance of L_{dis} = 1000 meter with the aid of the three different refractive index values of C_n^2 = 4 $\times$ 10^{-15}, 5 $\times$ 10^{-14} and 4 $\times$ 10^{-13} [$\mathrm{m}^{-2/3}$] to represent weak, moderate and strong turbulence levels, respectively. The modulation schemes employed were 4-QAM as well as 16-QAM, and we consider both the G2 and G4 STBC configurations associated with $M = L_{\mathrm{T}}$ and $N = L_{\mathrm{R}}$. Additionally, the STSK(2,2,2,4) scheme is also considered in this section. Furthermore, to investigate the effect of the OFDM block length on the achievable performance, it was set to N_{F} = 32, 64 and 512. The SNR was defined as the ratio of the total transmit signal power over the total channel noise power. The simulation parameters can be found in Table 2.2.

2.2.4.1 Length of OFDM block

First the effect of different OFDM symbol-length N_{F} is studied. The N_{F} length of the OFDM symbols also determines the number of subcarriers in the OFDM system. In Fig. 2.2, the performance of the ACO-OFDM based STBC and STSK systems using different-length OFDM symbols for transmission over non-dispersive turbulent FSO channels is illustrated. Observe that as expected over non-dispersive channels, the system's performance is not affected by N_{F}. This is because in a non-dispersive scenario the channel is non-frequency-selective, hence the channel matrix $\mathbf{H}^{(n,m)}$ between each TAp and RAp pair is a diagonal matrix. Hence, each subcarrier experiences exactly the same Frequency Domain Channel Transfer Function (FDCTF) and the performance remains

Table 2.2: Parameters of ACO-OFDM based MIMO system in non-dispersive channel

Parameters	Values
MIMO schemes	STBC G2, G4 and STSK(2,2,2,4)
Modulation Scheme	BPSK, 4-QAM,16-QAM
Physical link distance L_{dis}	1000 [m]
Refractive index C_n^2	4×10^{-15}, 5×10^{-14} and 4×10^{-13} [$\text{m}^{-2/3}$]
Length of OFDM N_{F}	32, 64 and 512
No. of TAps M	1,2,4
No. of RAps N	1,2,3,4
No. of transmit optical chains L_{T}	M
No. of receive optical chains L_{R}	N
Receiver responsivity ξ	1 [A/W]
Throughput	2 and 4 bits/symbol
FEC	None and RSC-URC coding

unchanged. We may also observe in Fig. 2.2 that, the performance differences between the STBC scheme and the STSK scheme are identical to those of the conventional RF system. Since each STSK block conveys $\log_2(M_{\text{sym}})$ additional bits, the transmit power allocated to each bit is lower than that of STBC mapping, which finally results in a relatively poorer performance.

2.2.4.2 Performance of Uncoded ACO-OFDM Based STBC System

Let us now characterise the performance of our system in Fig. 2.3 upon increasing the number of RAps. As expected, we can see that a significant diversity gain is achieved over a SISO ACO-OFDM system operating in turbulent FSO channel. Explicitly, over 15 [dB] diversity gain is obtained at a BER level of 10^{-3}. More explicit details on the performance degradation imposed by higher-order modulation schemes can be found in Fig. 2.4.

In Fig. 2.4 we can see that there is an approximately 7 [dB] deviation between the ACO-OFDM based STBC system using 4-QAM and 16-QAM, at the BER level of 10^{-6}. Furthermore, the authors of [151] carried out a comparison between the ACO-OFDM and DCO-OFDM systems. Similarly, we also compared the ACO-OFDM based STBC system to the DCO-OFDM based STBC system. For the sake of a fair comparison, we configured the two systems to have the same throughput. Specifically, Fig. 2.4 compares the achievable BER performance of the DCO-OFDM based STBC G2 system using BPSK signalling to that of the ACO-OFDM based STBC G2 system using 4-QAM signalling. These two systems have the same throughput of 1 bit per subcarrier, but the latter requires an approximately 3 [dB] lower power than the former at the BER of 10^{-6}, as seen in Fig. 2.4. Furthermore,in Fig. 2.4, we also show the achievable BER performance of the ACO-

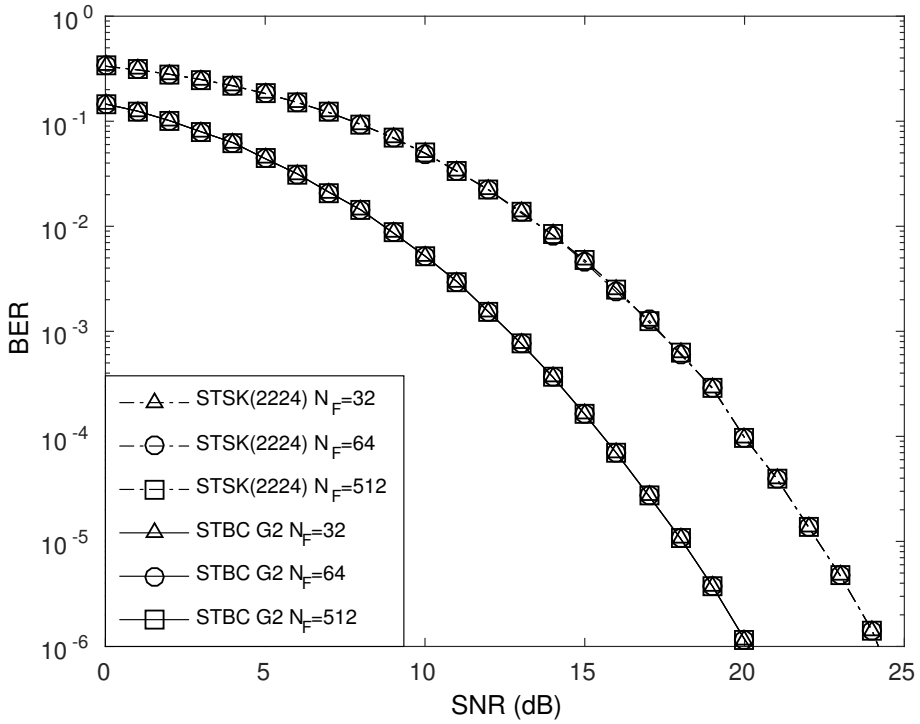

Figure 2.2: Performance of ACO-OFDM based STBC G2 with $N = 2$ represented by the solid lines and STSK(2224) system denoted by the dash-dot lines in non-dispersive moderate level turbulence channel $C_n^2 = 5 \times 10^{-14}$, where 4-QAM modulation is employed. The OFDM system uses $N_{\mathrm{F}} = 32$, 64 and 512. The schematic of Fig. 2.1 and the parameters of Table 2.2 are used. The throughput is 2 bits per symbol.

OFDM based STBC 16QAM system as well as that of the DCO-OFDM based STBC G2 4-QAM system. Again, these two systems have the same throughput of 2 bits per subcarrier. Observe from Fig. 2.4 that the ACO-OFDM based STBC 16QAM system outperforms the DCO-OFDM based STBC 4-QAM system by about 1 [dB] at the BER level of 10^{-6}, although at extremely low SNRs, the latter is slightly better than the former.

2.2.4.3 Curve Crossing Phenomenon

Based on the comparison between different optical OFDM systems and different modulation orders, let us now discuss the system's performance under different channel-turbulence conditions. We specifically consider the ACO-OFDM based STBC G2 and G4 systems, adopting 4-QAM. Their performance is shown in Fig. 2.5 As expected, the system adopting the G4 STBC scheme always outperforms the G2 STBC scheme based system, given the same channel turbulence level, since the former attains a higher diversity gain. Intuitively, we would expect that the BER curve of the system operating in a strongly turbulent channel would always be above the BER curve of the same system communicating over a weakly turbulent channel. This trend is similar to that observed for the classic STBC systems in RF communication, where the BER obtained in a high-Doppler environment is typically poorer than that of a low-Doppler environment, unless perfect channel

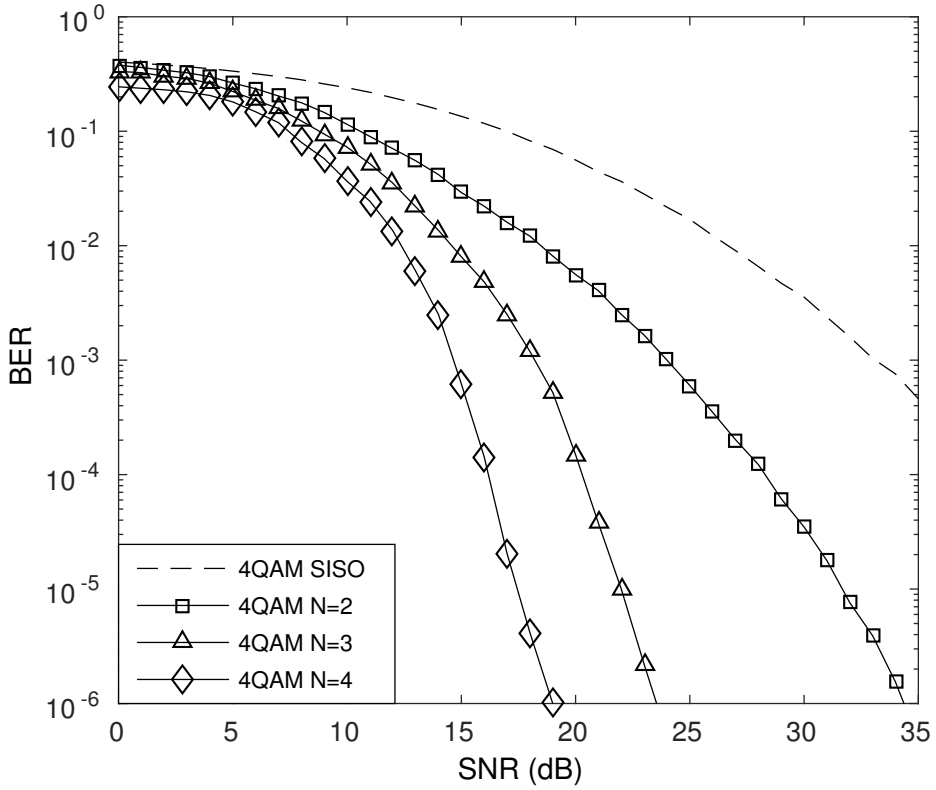

Figure 2.3: Performance of ACO-OFDM based STBC system in moderate level turbulent channel $C_n^2 = 4 \times 10^{-13}$, 4-QAM and 16-QAM modulation schemas are adopted. System's performance with different number of RAps N = 2, 3 and 4 are compared. Additionally, SISO 4-QAM and 16-QAM systems are added as benchmarks. The schematic of Fig. 2.1 and the parameters of Table 2.2 are used. The throughput is 2 bits per symbol.

estimation is assumed. However, observe the intriguing BER curve-crossing phenomenon shown in Fig. 2.5. For example, it can be seen from Fig. 2.5 that the BER curve of the G4 STBC system operating in the highly turbulent channel associated with $C_n^2 = 4 \times 10^{-13}$ is actually lower than that of the same G4 STBC system in the weakly turbulent channel of $C_n^2 = 4 \times 10^{-15}$, at SNR < 5 [dB]. At SNR $= 5$ [dB], the two BER curves cross over each other, and the performance of the G4 STBC system operating in the strongly turbulent channel becomes poorer than that communicating over the weakly turbulent channel, for SNR > 5 [dB]. For the G2 STBC scheme, the BER curve cross-over occurs at approximately SNR $= 1$ [dB], while for the higher-order G4 STBC scheme, the curve-crossing phenomenon is more pronounced and the cross-over takes place in the SNR region of 4 to 7 [dB].

The question is then, why this cross-over phenomenon takes place and why it is different from the trends observed in RF communication. The answer can be found in the comparison we made in Table 2.1 between the RF fading channel and the FSO turbulence channel. In practical RF communication, varying the Doppler shift f_{d} within reasonable limits only affects the fading rate

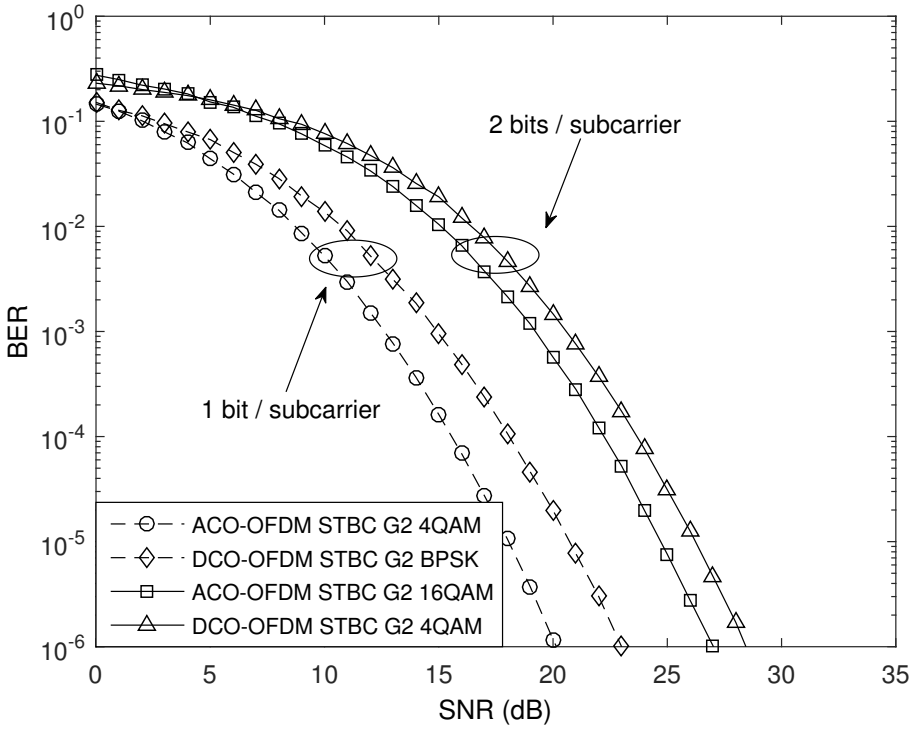

Figure 2.4: BER performance comparison between the DCO-OFDM based STBC G2 Binary Phase Shift Keying (BPSK) system and the ACO-OFDM based STBC G2 4-QAM system as well as between the DCO-OFDM based STBC G2 4-QAM system and the ACO-OFDM based STBC G2 16QAM system, in the FSO channel with moderate turbulent level of $C_n^2 = 5 \times 10^{-14}$. The OFDM length is $N_{\mathrm{F}} = 512$. The schematic of Fig. 2.1 and the parameters of Table 2.2 are used. The throughput is 1 and 2 bits per symbol.

of the channel, but the variance of the channel's fading envelop remains the same. Therefore, in the presence of a fixed pilot-spacing increasing the Doppler frequency of the fading channel typically degrades the BER performance. By contrast, the FSO turbulent channel is different from the RF fading channel in this respect. Firstly, indeed, increasing the channel turbulence's level C_n^2 has a detrimental effect on the BER performance, just as increasing the Doppler frequency will impose a detrimental effect on a RF fading channel. However, according to Eq. (2.12), the refractive index C_n^2 also affects the variance of the FSO channel. Thus, changing the turbulence level also affects the channel's PDF. Therefore, unlike in the RF fading channel, the BER curves under different turbulence levels do not start from the same point, and eventually these curves cross over at some SNR point.

2.2.5 Performance in Dispersive Channels

In FSO communication systems, operating at high data rates, the signal dispersion caused by multipath transmission results in ISI. Hence, like in RF system, OFDM may be invoked for mitigating this detrimental effect, also in optical systems. However, in contrast to RF wireless systems experiencing Rayleigh fading, optical systems encounter Gamma-Gamma fading. The properties of

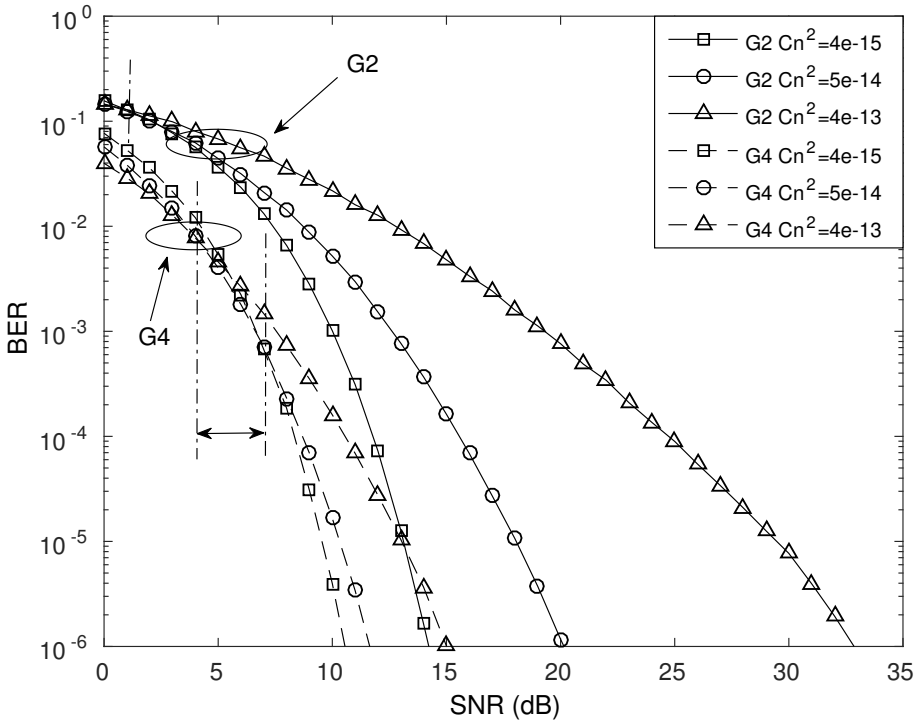

Figure 2.5: BER performance of the G2 and G4 STBC based ACO-OFDM MIMO systems employing 4-QAM scheme, communicating over the FSO turbulence channels of weak, moderate and strong turbulence levels. The 'curve crossing' phenomenon is marked by a vertical dash-dot line. The schematic of Fig. 2.1 and the parameters of Table 2.2 are used. The throughput is 2 bits per symbol.

the FSO channel depend on the effect of signal dispersion at both a microscopic and macroscopic scale [158]. To elaborate, the microscopic effect is mainly caused by light arriving through different path at the PD. By contrast, the macroscopic effect is attributed to the different longer delays caused by the reflections of the optical signal from surfaces, such as walls and ceilings. Hence, the light arrives at the receiver via different-delay paths, which is similar to a hybrid LOS and diffuse channel. This is reminiscent of IR communication, where the channel is frequency-selective. ACO-OFDM has the innate ability to eliminate the dispersion imposed by multipath reflections, because each subcarrier transmits a low-rate sequence that remains unaffected by dispersion. In contrast to the small indoor attocells, FSO systems typically communicate over much larger distances and encounter commensurately longer CIRs, which is beneficially counteracted by the anti-dispersion capability of ACO-OFDM, as argued in [209–212].

Here we assume that the length of the CP is always higher than the dispersive CIR. The other parameters involved in our simulations can be found in Table 2.2. Recall from Sec. 2.2.4.1 that the ACO-OFDM based STSK system and the STBC system exhibited similar performance trends. Hence we only investigate the effects of dispersive channels using our ACO-OFDM based STSK system.

The BER performance of dispersive channels, where the power is equally shared across the CIR

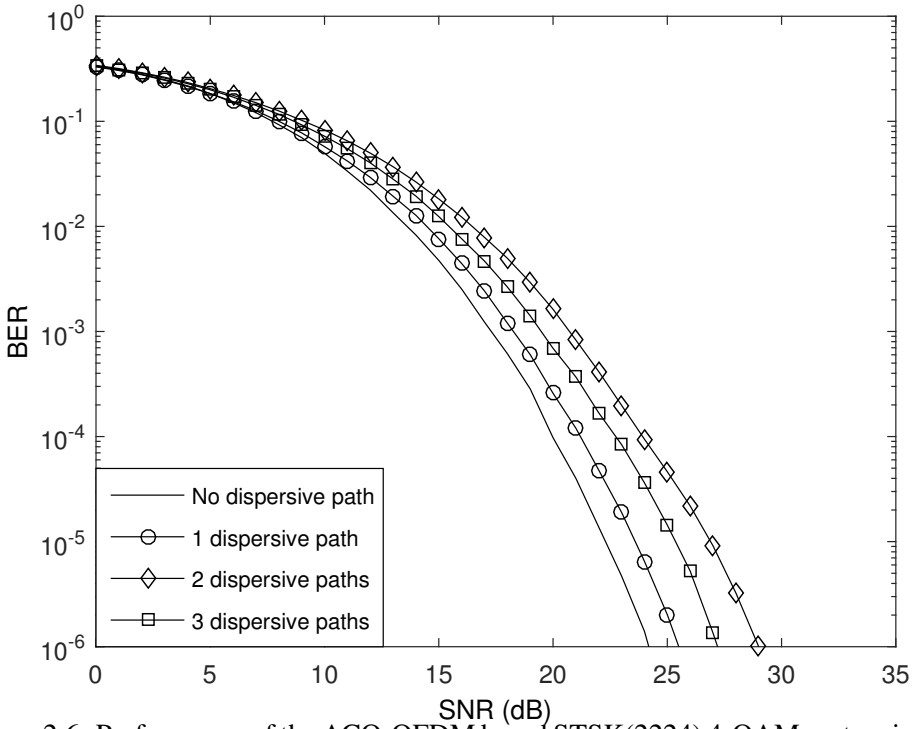

Figure 2.6: Performance of the ACO-OFDM based STSK(2224) 4-QAM system in dispersive moderate-turbulence channels having $C_n^2 = 5 \times 10^{-14}$, where the number of multipath components increases from 1 to 2, the power level of all paths is identical, the length of the OFDM symbol is 512 and the number of the cyclic prefix is 3. The schematic of Fig. 2.1 and the parameters of Table 2.2 are used. The throughput is 2 bits per symbol.

taps is shown in Fig. 2.6 regardless of the number of paths. We may observe that upon increasing the number of paths, the attainable performance is degraded. The worst-case scenario is encountered when there are two dispersive paths in addition to the main path. An increased spatial diversity gain is obtained, when the number of dispersive paths increased to 2, but this gain is insufficient to perfectly counteract the dispersion-induced performance erosion with respect to the non-dispersive scenario.

2.3 Joint Transmit Receive Aperture Selection

Since the concept of ApS has its roots in RF AS, let us commence our discourse on ApS classification. By borrowing the ideas from the classic RF systems, the ApS schemes may be classified into three categories, namely Transmit Aperture Selection (TApS), Receive Aperture Selection (RApS) and JTRApS.

2.3.1 ApS Classification

In conventional RF AS a pair of dominant AS optimisation criteria have been used: capacity based AS and NB AS. Let us assume that there are L_{T} and L_{R} optical chains at the transmit as well as

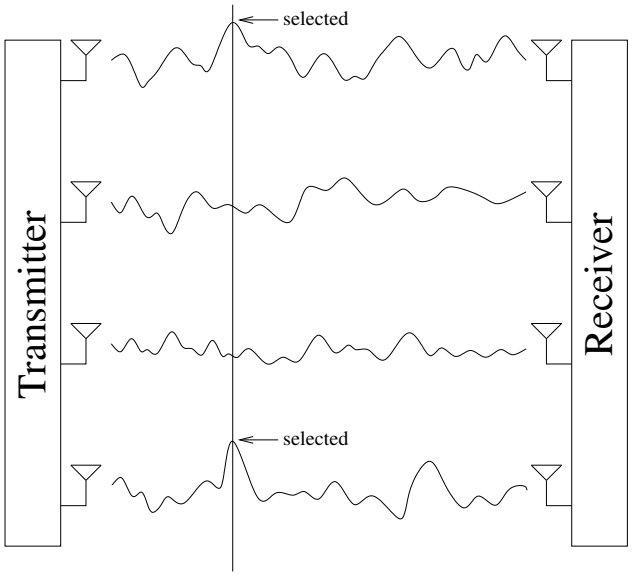

Figure 2.7: A simple example of selected channel at a specific time slot of ApS.

receive side and that we have a total of M and N transmit and receive PDs respectively, where the number of optical chain is lower than that of the transmit and receive PDs, i.e. we have $L_{\mathrm{T}} < M$ and $L_{\mathrm{R}} < N$. According to [213], a RF MIMO system associated with the channel matrix $\mathbf{H}_{\mathrm{sub}} \in \mathbb{C}^{L_{\mathrm{R}} \times L_{\mathrm{T}}}$ and the channel noise power N_0 has a channel capacity given by [214]

$$C_{\mathrm{MIMO}}\left(\mathbf{H}_{\mathrm{sub}}, L_{\mathrm{T}}, L_{\mathrm{R}}; N_0\right) = \log\left(\mathbf{I}_{\mathrm{L_R}} + \frac{N_0}{L_{\mathrm{T}}}\mathbf{H}_{\mathrm{sub}}\mathbf{H}_{\mathrm{sub}}^{\mathrm{H}}\right), \tag{2.23}$$

where we assumed that similarly to the ApS aided FSO system, there are L_{T} and L_{R} RF chains. However, in FSO systems, the channel capacity cannot be calculated from the above equation, since instead of bipolar symbols, we only have positive and zero symbols. Hence at the time of writing the FSO capacity is unknown. Nonetheless, we can improve the achievable FSO system's performance with the aid of AS relying on the following optimisation problem:

$$\begin{aligned}\mathbf{H}_{\mathrm{sub}}^{\mathrm{opt}} &= \underset{\mathbf{H}_{\mathrm{sub}} \in \mathbf{H}}{\arg\max} \|\mathbf{H}_{\mathrm{sub}}\|^2, \\ &= \underset{\mathbf{H}_{\mathrm{sub}} \in \mathbf{H}}{\arg\max} \left\{ \sum_{l_{\mathrm{t}}}^{L_{\mathrm{T}}} \sum_{l_{\mathrm{r}}}^{L_{\mathrm{R}}} \|\mathbf{H}_{\mathrm{sub}}(l_{\mathrm{t}}, l_{\mathrm{r}})\|^2 \right\},\end{aligned} \tag{2.24}$$

where $\mathbf{H} \in \mathbb{C}^{N \times M}$ is the full MIMO channel matrix and $\mathbf{H}_{\mathrm{sub}}(l_{\mathrm{T}}, l_{\mathrm{r}})$ represents the matrix element at the l_{r}th row and l_{T}th column of $\mathbf{H}_{\mathrm{sub}}$. Recall that in FSO communication the channel is modelled by the Gamma-Gamma distribution, where the CIR taps are real and positive. As a result of Eq. (2.24), the elements of the carefully selected $\mathbf{H}_{\mathrm{sub}}^{\mathrm{opt}}$ have the largest channel amplitude, which are hence used for actual transmission. A simple example is shown in Fig. 2.7, where a specific time slot is indicated by the vertical dashed line and the specific links associated with the two highest power are selected.

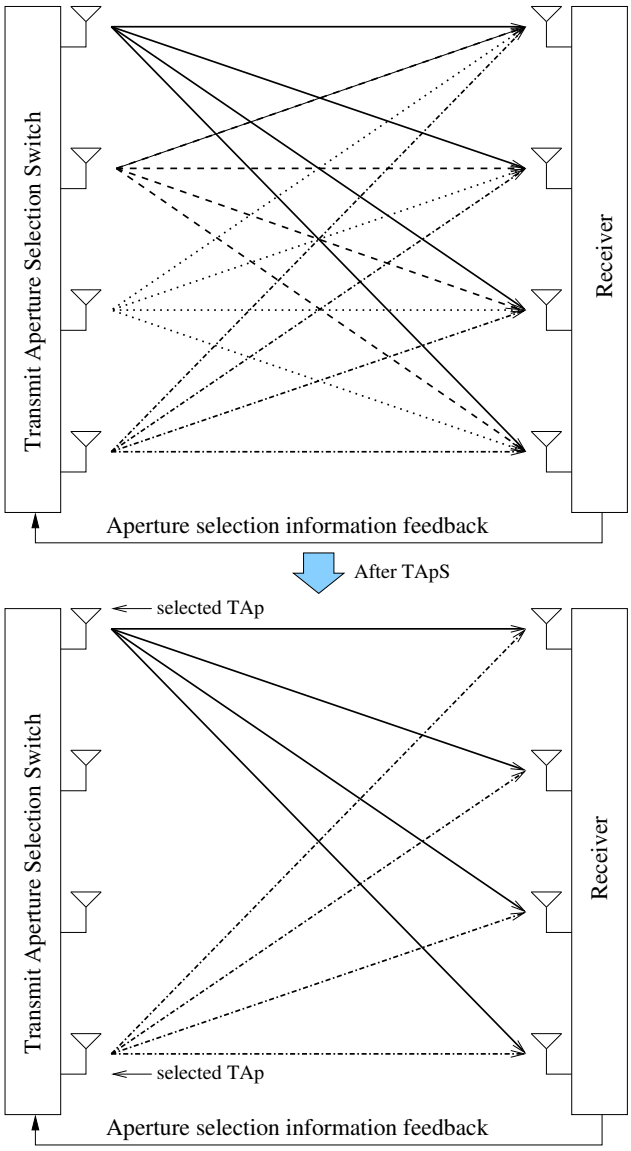

Figure 2.8: A simple example of TApS, where the selected aperture is fed back from the receiver to the transmitter.

2.3.1.1 Transmit Aperture Selection

Based on the above rationale, let us now discuss the main concept of TApS, which relies on choosing those specific transmit aperture(s), for which the channel power is the highest [183–185]. The basic schematic of TApS of a FSO MIMO system is shown in Fig 2.8, where it may be seen that ApS only takes place at the transmitter of the MIMO system. Furthermore, a feedback message containing the index of the selected aperture has to be fed back from the receiver to the transmitter. As a result, the data to be transmitted is mapped to the specifically chosen aperture, while the rest of the apertures are not transmitting.

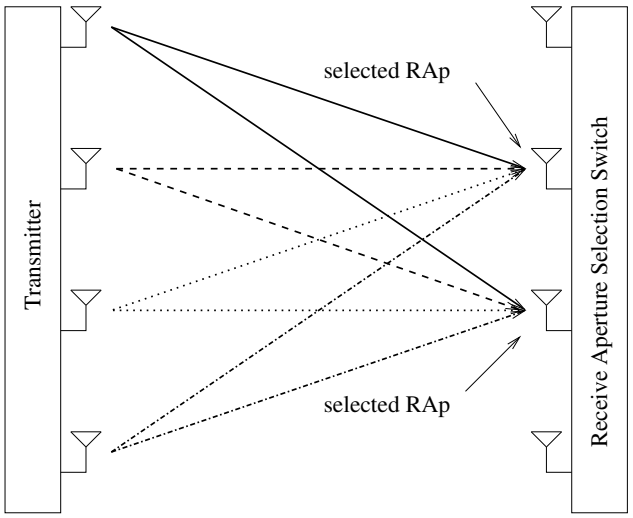

Figure 2.9: A simple example of RApS, where there is no feedback from the receiver to the transmitter.

2.3.1.2 Receive Aperture Selection

Similar to the TApS scheme, based on the criterion described in Eq. (2.24), the idea of RApS is to select the specific receive aperture(s) associated with the highest channel power [186–189]. The corresponding schematic conceived for FSO MIMO systems is shown in Fig. 2.9. It may be seen that, unlike in the TApS scheme shown in Fig. 2.8, no ApS information feedback is required in RApS aided MIMO systems, since aperture selection only takes place at the receiver side of the MIMO system.

2.3.1.3 Joint Transmit-Receive Aperture Selection

As a combined version of TApS and RApS, JTRApS schemes were proposed in [182,191,196,198], where it was shown that MIMO systems employing the JTRApS scheme are capable of improving the achievable system performance, while maintaining a low hardware complexity compared to the family of MIMO-aided FSO systems employing the same number of optical chains and operating without JTRApS. In contrast to the above TApS and RApS schemes, the JTRApS arrangement jointly selects the transmit and and receive aperture(s). The optimal JTRApS relies on a full search, which however, may impose an excessive computational complexity. Therefore, in this chapter we advocate the low-complexity yet efficient JTRApS algorithm, which was inspired by [199, 215]. The system is capable of significantly outperforming the FSO MIMO system operating without the aid of ApS in terms of both its BER performance and throughput, while utilising the same number of optical chains. Additionally, the JTRApS scheme is capable of achieving an extra diversity gains over that of the original FSO MIMO system operating without JTRApS under the condition of relying on the same number of optical chains, albeit this gain is achieved at the cost of employing

more apertures than the latter.

2.3.2 Joint Transmit-Receive Aperture Selection Algorithm

In this section, we aim for $L_{\mathrm{T}} < M$ and $L_{\mathrm{R}} < N$, where the JTRApS module of Fig. 2.10 selects L_{T} TAps from the total of M TAps plus L_{R} RAps from the total of N RAps to form an $(M \times N)$-element MIMO OW system for communication, where we assume having perfect knowledge of the CSI both at the transmit and receive sides. Additionally, we can see in Fig. 2.10 that electronic switches are used at both sides to connect the available limited number of optical chains to the apertures selected. In this ACO-OFDM based and JTRApS aided FSO MIMO system, MIMO symbol blocks are transmitted over the activated subset channel matrix $\mathbf{H}_{\mathrm{sub}}^{\mathrm{opt}} \in \mathbb{C}^{L_{\mathrm{R}} \times L_{\mathrm{T}}}$ with $\mathbf{H}_{\mathrm{sub}}^{\mathrm{opt}} \subset \mathbf{H}$.

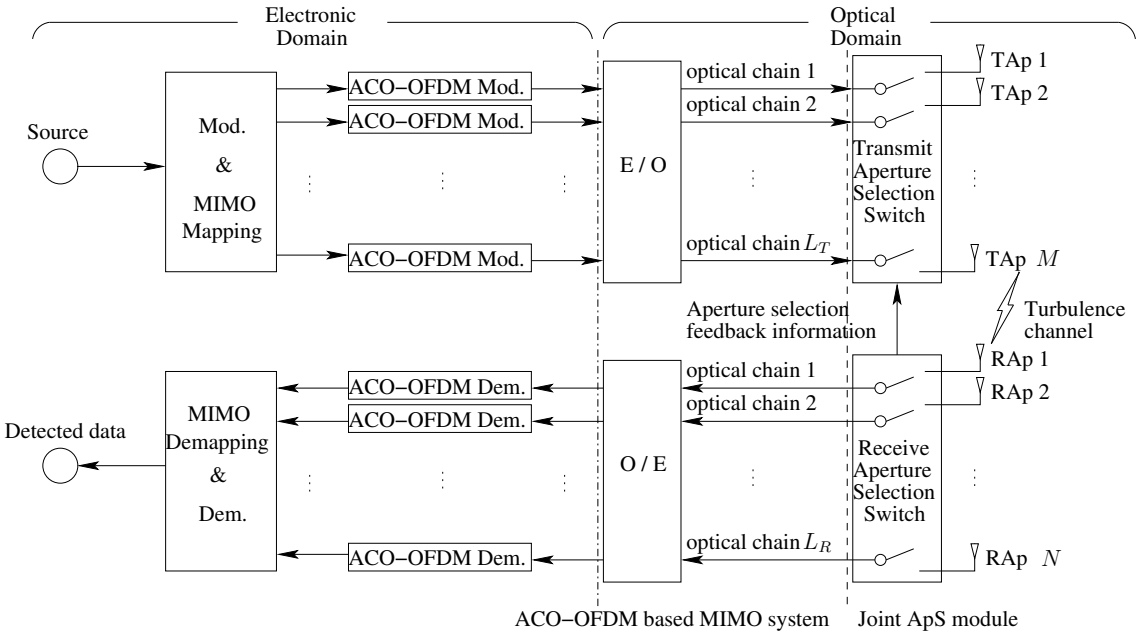

Figure 2.10: A simple example of the JTRApS aided MIMO system employed, where we have $L_{\mathrm{T}} < M$ and $L_{\mathrm{R}} < N$.

It has been widely recognised that increasing the channel gain improves the SNR, which yields an improved system performance. Hence in this chapter, we aim for solving the optimisation problem of Eq. (2.24). To be more explicit, given that $\mathsf{C}_N^{L_{\mathrm{R}}}$ and $\mathsf{C}_N^{L_{\mathrm{T}}}$ denotes the number of row and column combinations of $\mathbf{H}_{\mathrm{sub}}^{\mathrm{opt}}$, respectively, the exhaustive search based solution of our optimisation problem requires the assessment of all the $\left(\mathsf{C}_N^{L_{\mathrm{R}}} \times \mathsf{C}_M^{L_{\mathrm{T}}}\right)$ candidate subset matrices, where $\mathsf{C}_{(\cdot)}^{(\cdot)}$ denotes the combination operation. This exhaustive search operation will impose an excessively high computational complexity. Hence we propose an algorithm for large-scale aperture arrays to solve this optimisation problem at the cost of a reasonable complexity.

Given the full channel matrix $\mathbf{H} \in \mathbb{C}^{N\times M}$,

$$\mathbf{H} = \begin{bmatrix} \mathbf{H}^{(0,0)} & \mathbf{H}^{(0,1)} & \cdots & \mathbf{H}^{(0,M-1)} \\ \mathbf{H}^{(1,0)} & \mathbf{H}^{(1,1)} & \cdots & \mathbf{H}^{(1,M-1)} \\ \vdots & \vdots & \ddots & \vdots \\ \mathbf{H}^{(N-1,0)} & \mathbf{H}^{(N-1,1)} & \cdots & \mathbf{H}^{(N-1,M-1)} \end{bmatrix} \tag{2.25}$$

and for the simplicity of exposition without loss of generality, we consider a downlink scenario, where we have $\mathsf{C}_N^{L_\mathrm{R}} \leq \mathsf{C}_M^{L_\mathrm{T}}$. Furthermore, in practice, the number of available optical chains is limited, hence we typically have $L_\mathrm{T} \ll M$ and $L_\mathrm{R} \ll N$. In order to efficiently exploit the available optical chains, it is highly desirable to select the most appropriate subset of the $(L_\mathrm{R} \times L_\mathrm{T})$-FSO links from the full set of the $(N \times M)$ channels for the ACO-OFDM based MIMO system having only L_T optical chains at the transmitter and L_R optical chains at the receiver. The ApS module of Fig. 2.10 is responsible for carrying out this task. Then the optimisation of Eq. (2.24) may be accomplished in two steps.

Step 1): 'Row'-Block Dimension Operations.

Let $i_\mathrm{r} \in \left\{1, 2, \cdots, \mathsf{C}_N^{L_\mathrm{R}}\right\}$ be the 'row'-block combination index, and the 'row'-block indices corresponding to the i_rth candidate sub-matrix $\mathbf{H}_{i_\mathrm{r}}$ of the L_R row-blocks and N column blocks be given by

$$\mathbf{l}_{i_\mathrm{r}} = \left[l_{i_\mathrm{r}}^{(0)}\ l_{i_\mathrm{r}}^{(1)} \cdots l_{i_\mathrm{r}}^{(L_\mathrm{R}-1)}\right]^\mathrm{T}. \tag{2.26}$$

Then the i_rth 'row'-block based candidate sub-matrix $\mathbf{H}_{i_\mathrm{r}}$ is given by

$$\mathbf{H}_{i_\mathrm{r}} = \begin{bmatrix} \left(\mathbf{H}^{(l_{i_\mathrm{r}}^{(0)})}\right)^\mathrm{T} \\ \left(\mathbf{H}^{(l_{i_\mathrm{r}}^{(1)})}\right)^\mathrm{T} \\ \vdots \\ \left(\mathbf{H}^{(l_{i_\mathrm{r}}^{(L_\mathrm{R}-1)})}\right)^\mathrm{T} \end{bmatrix} = \begin{bmatrix} \mathbf{H}_{i_\mathrm{r}}^{(0,0)} & \mathbf{H}_{i_\mathrm{r}}^{(0,1)} & \cdots & \mathbf{H}_{i_\mathrm{r}}^{(0,M-1)} \\ \mathbf{H}_{i_\mathrm{r}}^{(1,0)} & \mathbf{H}_{i_\mathrm{r}}^{(1,1)} & \cdots & \mathbf{H}_{i_\mathrm{r}}^{(1,M-1)} \\ \vdots & \vdots & \ddots & \vdots \\ \mathbf{H}_{i_\mathrm{r}}^{(L_\mathrm{R}-1,0)} & \mathbf{H}_{i_\mathrm{r}}^{(L_\mathrm{R}-1,1)} & \cdots & \mathbf{H}_{i_\mathrm{r}}^{(L_\mathrm{R}-1,M-1)} \end{bmatrix}, \tag{2.27}$$

where $\left(\mathbf{H}^{(l_{i_\mathrm{r}}^{(0)})}\right)^\mathrm{T}$ denotes the $l_{i_\mathrm{r}}^{(0)}$th row of $\mathbf{H}$. The magnitude evaluation may be obtained by evaluating:

$$m_{i_\mathrm{r}}^{(x)} = \sum_{i=0}^{L_\mathrm{R}-1} \|\mathbf{H}_{i_\mathrm{r}}^{(i,x)}\|^2,\ 0 \leq x \leq M-1, \tag{2.28}$$

where $m_{i_\mathrm{r}}^{(x)}$ represents the norm of the xth column-block in $\mathbf{H}_{i_\mathrm{r}}$, yields the norm metric vector

$$\mathbf{m}_{i_\mathrm{r}}^\mathrm{T} = \left[m_{i_\mathrm{r}}^{(0)}\ m_{i_\mathrm{r}}^{(1)} \cdots m_{i_\mathrm{r}}^{(M-1)}\right]. \tag{2.29}$$

Applying Eq. (2.29) to all the $\mathsf{C}_N^{L_\mathrm{r}}$ possible combinations leads to the $(\mathsf{C}_N^{L_\mathrm{r}} \times M)$-element metric matrix $\mathbf{M}_{\text{metric}}$ given by

$$\mathbf{M}_{\text{metric}} = \begin{bmatrix} \mathbf{m}_1^{\mathrm{T}} \\ \mathbf{m}_2^{\mathrm{T}} \\ \vdots \\ \mathbf{m}_{\mathsf{C}_N^{L_\mathrm{r}}}^{\mathrm{T}} \end{bmatrix} = \begin{bmatrix} m_1^{(0)} & m_1^{(1)} & \cdots & m_1^{(M-1)} \\ m_2^{(0)} & m_2^{(1)} & \cdots & m_2^{(M-1)} \\ \vdots & \vdots & \cdots & \vdots \\ m_{\mathsf{C}_N^{L_\mathrm{r}}}^{(0)} & m_{\mathsf{C}_N^{L_\mathrm{r}}}^{(1)} & \cdots & m_{\mathsf{C}_N^{L_\mathrm{r}}}^{(M-1)} \end{bmatrix}. \tag{2.30}$$

Step 2): 'Column'-Block Dimension Operations.

Find the largest L_T elements in the i_rth row of $\mathbf{M}_{\text{metric}}$ and sum them up, which is denoted as $m_{i_\mathrm{r}}^{\max}$, as well as record the column-block indices of these L_T blocks in the index vector

$$\mathbf{l}_{i_\mathrm{c}}(n_r) = \left[l_{i_\mathrm{c}}^{(0)}(i_r)\ l_{i_\mathrm{c}}^{(1)}(i_r) \cdots l_{i_\mathrm{c}}^{(L_\mathrm{T})}(i_r) \right]^{\mathrm{T}}. \tag{2.31}$$

This produces the max-magnitude metric vector

$$\left(\mathbf{m}^{\max}\right)^{\mathrm{T}} = \left[m_1^{\max}\ m_2^{\max} \cdots m_{\mathsf{C}_N^{L_\mathrm{R}}}^{\max} \right]. \tag{2.32}$$

Next find

$$\hat{i}_\mathrm{r} = \arg \max_{1 \le i_\mathrm{r} \le \mathsf{C}_N^{L_\mathrm{R}}} m_{i_\mathrm{r}}^{\max}. \tag{2.33}$$

Then the selected TAp and RAp indices are specified by $\mathbf{l}_{i_\mathrm{c}}\left(\hat{i}_\mathrm{r}\right)$ and $\mathbf{l}_{\hat{i}_\mathrm{r}}$, respectively, and the corresponding subset channel matrix $\mathbf{H}_{\text{sub}}^{\text{opt}}$ is the optimal solution of Eq. (2.24). In other words, we have the solution of the optimization problem in Eq. (2.24) given by

$$\mathbf{H}_{\text{sub}}^{\text{opt}} = \begin{bmatrix} \mathbf{H}^{\left(l_{\hat{i}_\mathrm{r}}^{(0)}, l_{i_\mathrm{c}}^{(0)}(\hat{i}_\mathrm{r})\right)} & \mathbf{H}^{\left(l_{\hat{i}_\mathrm{r}}^{(0)}, l_{i_\mathrm{c}}^{(1)}(\hat{i}_\mathrm{r})\right)} & \cdots & \mathbf{H}^{\left(l_{\hat{i}_\mathrm{r}}^{(0)}, l_{i_\mathrm{c}}^{(M-1)}(\hat{i}_\mathrm{r})\right)} \\ \mathbf{H}^{\left(l_{\hat{i}_\mathrm{r}}^{(1)}, l_{i_\mathrm{c}}^{(0)}(\hat{i}_\mathrm{r})\right)} & \mathbf{H}^{\left(l_{\hat{i}_\mathrm{r}}^{(1)}, l_{i_\mathrm{c}}^{(1)}(\hat{i}_\mathrm{r})\right)} & \cdots & \mathbf{H}^{\left(l_{\hat{i}_\mathrm{r}}^{(1)}, l_{i_\mathrm{c}}^{(M-1)}(\hat{i}_\mathrm{r})\right)} \\ \vdots & \vdots & \vdots & \vdots \\ \mathbf{H}^{\left(l_{\hat{i}_\mathrm{r}}^{(N-1)}, l_{i_\mathrm{c}}^{(0)}(\hat{i}_\mathrm{r})\right)} & \mathbf{H}^{\left(l_{\hat{i}_\mathrm{r}}^{(N-1)}, l_{i_\mathrm{c}}^{(1)}(\hat{i}_\mathrm{r})\right)} & \cdots & \mathbf{H}^{\left(l_{\hat{i}_\mathrm{r}}^{(N-1)}, l_{i_\mathrm{c}}^{(M-1)}(\hat{i}_\mathrm{r})\right)} \end{bmatrix}. \tag{2.34}$$

2.3.3 Complexity Analysis

In the case of $\mathsf{C}_N^{L_\mathrm{R}} \le \mathsf{C}_M^{L_\mathrm{T}}$, the complexity of the above JTRApS algorithm is on the order of

$$J_{\text{JTRApS}} \approx \mathcal{O}\left((M \cdot L_\mathrm{R}) \cdot \mathsf{C}_N^{L_\mathrm{R}} \right). \tag{2.35}$$

Additionally, if we have $\mathsf{C}_N^{L_\mathrm{R}} > \mathsf{C}_M^{L_\mathrm{T}}$, our JTRApS algorithm starts with **Step 1)** of the column-based operations, followed by **Step 2)** of the row-based operations. Hence the complexity becomes

$$J_{\text{JTRApS}} \approx \mathcal{O}\left((N \cdot L_\mathrm{T}) \cdot \mathsf{C}_M^{L_\mathrm{T}} \right). \tag{2.36}$$

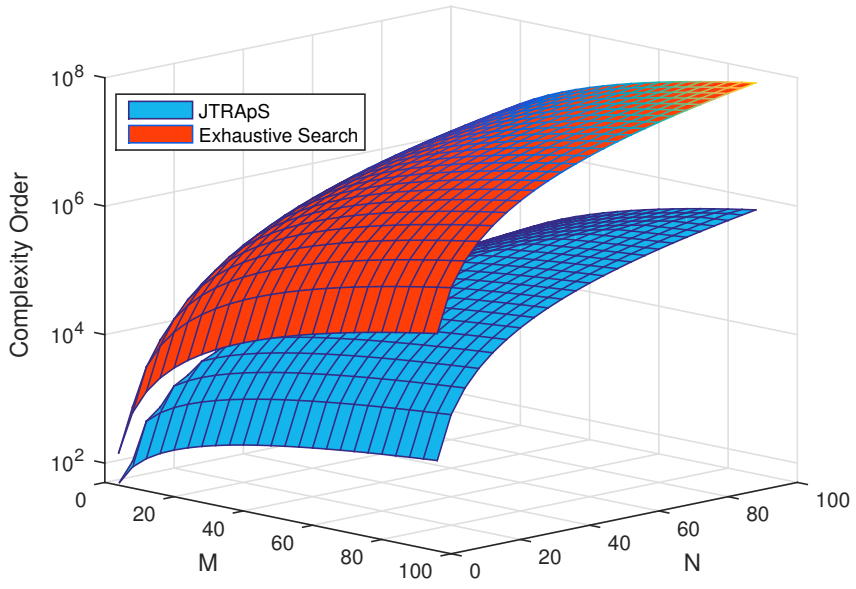

Figure 2.11: Complexity comparison of our JTRApS and the exhaustive search method, where the number of optical chains at the transmit and receive sides are $L_{\mathrm{T}} = L_{\mathrm{R}} = 2$.

By contrast, the complexity of the exhaustive search is

$$J_{\mathrm{ES}} \approx \mathcal{O}\left((L_{\mathrm{T}} \cdot L_{\mathrm{R}}) \cdot \left(\mathrm{C}_M^{L_{\mathrm{T}}} \mathrm{C}_N^{L_{\mathrm{R}}}\right)\right). \tag{2.37}$$

Clearly, J_{JTRApS} is much lower than J_{ES}, as shown in Fig. 2.11, which explicitly compares the complexity of our JTRApS to that of the exhaustive search method. We assume that there are $L_{\mathrm{T}} = L_{\mathrm{R}} = 2$ optical chains at both the transmit and receive sides. It can be clearly seen that, J_{JTRApS} is substantially lower than J_{ES}, especially when the number of transmit and receive apertures is large.

2.3.4 Achievable Diversity Order

Since L_{T} and L_{R} represent the number of optical chains available at the receiver and transmitter, respectively, and considering that the number of candidate channels is $N \times M$, where we have $N > L_{\mathrm{R}}$ and $M > L_{\mathrm{T}}$, the multiplexing gain of the FSO MIMO system may be quantified. Let us define the loading factor of ApS as

$$f_{\mathrm{ApS}}(M, N) = \frac{M + N}{L_{\mathrm{T}} + L_{\mathrm{R}}}, \tag{2.38}$$

which determines the additional diversity order attainable by JTRApS schemes over the ACO-OFDM based FSO MIMO system formed by employing L_{T} TAps and L_{R} RAps, whilst operating without ApS. Then if we revisit Table 2.1, we would discover the advantages of turbulent FSO

channel when deploying JTRApS schemes, the channel characteristics have the potential of acquiring a considerable diversity gain by exploiting ApS techniques in FSO MMIMO communication, especially under stronger turbulence. This is because ApS is capable of choosing the channels with higher gains, leading to an enhanced performance in FSO MIMO communication.

2.4 JTRApS Aided ACO-OFDM Based MIMO System

On the basis of our investigation of the ACO-OFDM based MIMO system of Sec. 2.2, and of the JTRApS scheme of Sec. 2.3, let us now characterise the performance enhancement achieved by the ACO-OFDM based MIMO system having $N > L_{\mathrm{R}}$ and $M > L_{\mathrm{T}}$. Explicitly, we invoke the JTRApS scheme in conjunction with various ApS factors and compare it to the original ACO-OFDM based MIMO system, given $N = L_{\mathrm{R}}$ and $M = L_{\mathrm{T}}$, which operated without the JTRApS arrangement.

The system structure of our JTRApS aided ACO-OFDM based MIMO system is shown in Fig. 2.10, while more details of the ACO-OFDM based MIMO system can be found in Fig. 2.1. Based on the MIMO schemes of Sec. 2.2.3, for simplicity of exposition, we will only consider ACO-OFDM based STBC system as an example to discuss the performance attained by the JTRApS scheme.

2.4.1 Bit Error Ratio Performance

Let us first consider the BER performance of the JTRApS aided ACO-OFDM based STBC system in FSO channels having different turbulent level. Since the performance enhancements achieved by the G2 and G4 STBC schemes exhibited similar trends in Fig. 2.5, here we only show the corresponding results for the G2 STBC based systems in Fig. 2.12.

It can be clearly seen from Fig. 2.12 that the performance enhancements achieved by the ACO-OFDM based STBC G2 MIMO system relying on the JTRApS over the original ACO-OFDM based STBC G2 system operating without ApS is significantly higher for strongly turbulent channels, than for the weakly turbulent channels. Specifically, as an explicitly benefit of the JTRApS regime, under the weak turbulence level of $C_n^2 = 4 \times 10^{-15}$, the SNR gains at the BER level of 10^{-4} are approximately 1.6 [dB], 2.1 [dB] and 2.5 [dB] for the ApS factors of 2, 3 and 4, respectively. By contrast, under the strong turbulence level of $C_n^2 = 4 \times 10^{-13}$, the SNR gains at the BER level of 10^{-4} increase to approximately 15 [dB], 18 dB and 22 [dB] for the ApS factors of 2, 3 and 4, respectively. This is because in a weakly turbulent channel the fluctuations of the CIRs remain low, and the envelope differences among all the candidate aperture pairs are relative small. Therefore, the achievable performance enhancement of ApS remains relatively modest. However, in a high-turbulence channel, the fluctuations of the fading envelope are more dramatic, hence the

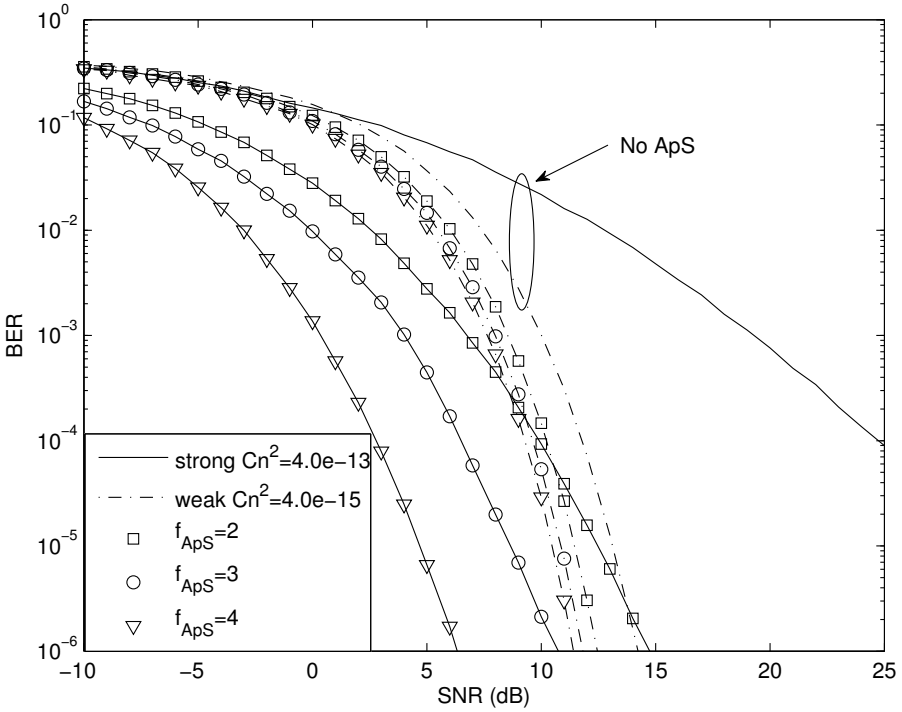

Figure 2.12: BER performance enhancement of the ACO-OFDM based STBC G2 system with the aid of the JTRApS for three different ApS factors over the original ACO-OFDM based STBC G2 system operating without ApS, communicating over the FSO channels of weak and strong turbulence levels, where 4-QAM modulation is employed. The schematic of Fig. 2.10 and parameters in Table 2.2 are used.

system becomes capable of attaining a much more significant diversity gain. Consequently, more significant performance benefits can be attained by ApS. It can also be observed from Fig. 2.12 that for ApS factors higher than 3, the system's achievable performance under the strongly turbulent channel is actually significantly better than that under weak turbulence. This trend is in stark contrast to that of the original G2 STBC based ACO-OFDM system operating without ApS. Evidently, the performance gain attained by the proposed JTRApS scheme is more significant under strongly turbulent channel conditions.

2.4.2 Equivalent SNR

Intuitively, the diversity gain attained by the JTRApS can be attributed to the carefully selected subset channel matrix of Eq. (2.33), which contains the particular subset of the specific CIRs having the highest channel gains. Given the system's transmit SNR, let us now define the equivalent ApS-based SNR as

$$\gamma_{\text{equ}} = 10\log_{10}\left(\frac{\gamma}{L_{\text{T}}L_{\text{R}}}\left\|\mathbf{H}_{\text{sub}}^{\text{opt}}\right\|^2\right). \tag{2.39}$$

Figs. 2.13 and 2.14 portray the increased equivalent ApS-based SNRs versus ApS factor f_{ApS} in the three different turbulent channels, given the actual SNRs of 0 [dB] and 3 [dB] in the absence of ApS, respectively. It can be seen from Figs. 2.13 and 2.14 that for the strongly turbulent channel,

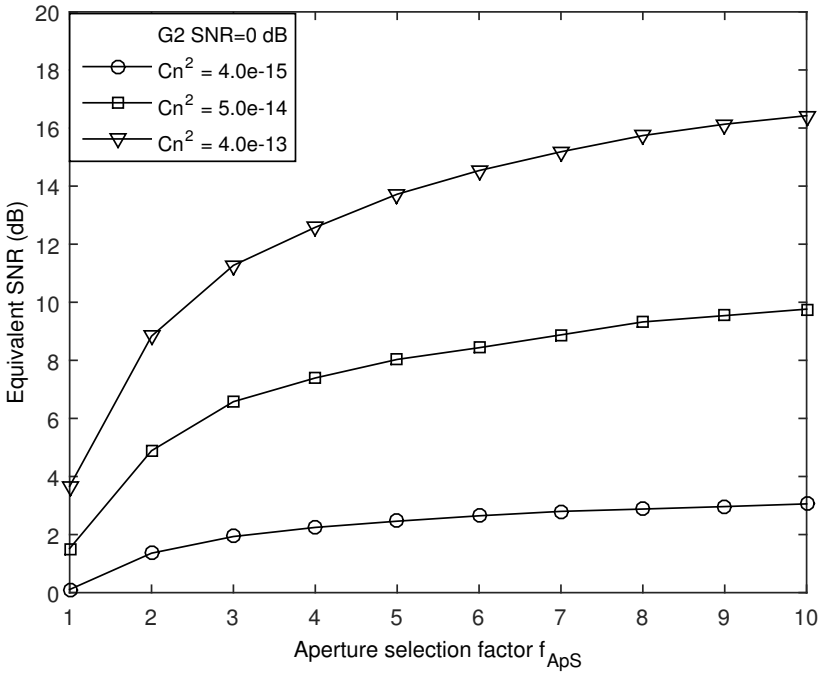

Figure 2.13: The equivalent ApS-based SNR as a function of the ApS factor for the ACO-OFDM based STBC G2 MIMO system operating with the aid of the JTRApS, under different channel turbulence conditions and given an SNR of 0 [dB] in the absence of ApS, where 4-QAM modulation is employed. The schematic of Fig. 2.10 and parameters in Table 2.2 are used.

the equivalent ApS-based SNR exhibits the most significant improvement owing to ApS, which explicitly justifies correlated by the substantial BER performance improvement shown in Fig. 2.12. Furthermore, increasing the ApS factor from 1 to 2 provides the highest increase in the equivalent ApS-based SNR. As expected, if we double the transmit power, the corresponding equivalent ApS-based SNR is also increased by about 3 [dB], as seen by comparing Fig. 2.13 and Fig. 2.14.

2.5 JTRApS Aided Three-Stage ACO-OFDM Based MIMO System

Let us now investigate the more powerful three-stage concatenated channel coded ACO-OFDM based STBC G2 MIMO system. Because of the channel coding components employed, the system structure of Fig. 2.10 is updated with the newly added RSC and URC coding blocks, along with the corresponding iterative decoding structure at the receiver. The final system structure is shown in Fig. 2.15.

2.5.1 System Description

In this section familiarity with the principles of three-stage concatenated coding is assumed, as detailed in [216]. The schematic of Fig. 2.15 and the parameters of Table 2.2 are used.

The information bit sequence $\mathbf{b}$ is first channel encoded by a half-rate RSC based outer encoder,

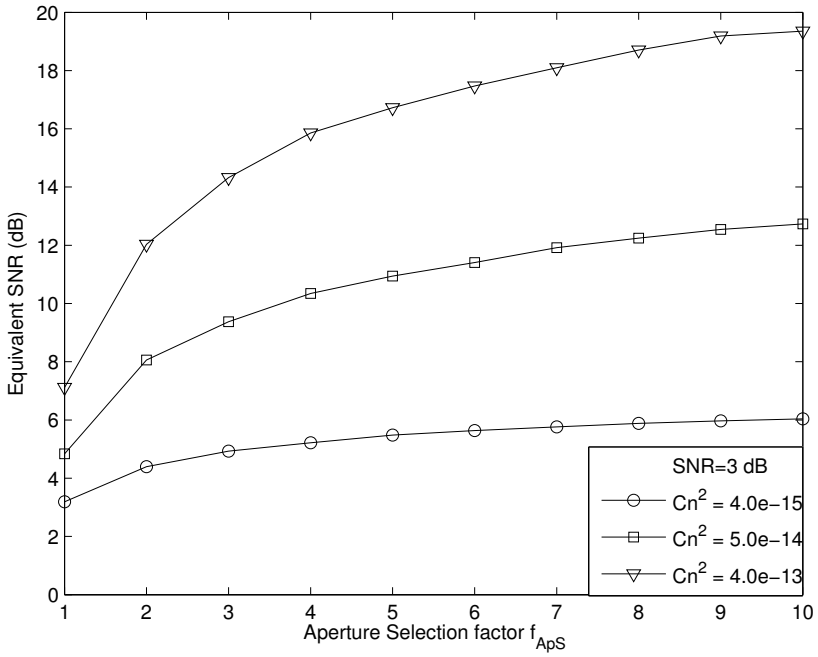

Figure 2.14: The equivalent ApS-based SNR as a function of the ApS factor for the ACO-OFDM based STBC G2 MIMO system operating with the aid of the JTRApS, under different channel turbulence conditions and given an SNR of 3 [dB] in the absence of ApS, where 4-QAM modulation is employed. The schematic of Fig. 2.10 and parameters in Table 2.2 are used.

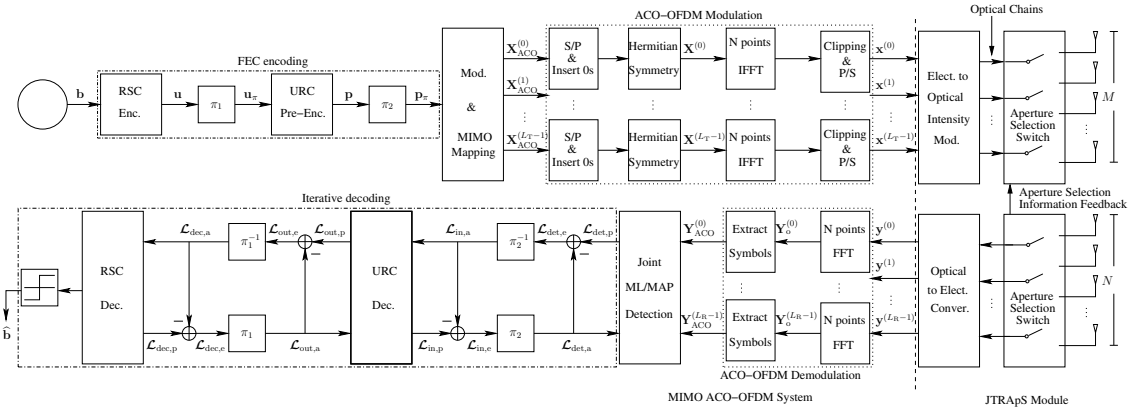

Figure 2.15: Schematic of the proposed ACO-OFDM based MIMO system with the aid of the JTRApS, where L_{T} and L_{R} are the numbers of optical chains at the transmitter and receiver, respectively, while M and N are the numbers of transmit and receive apertures, respectively. In general, we have $L_{\mathrm{T}} < M$ and $L_{\mathrm{R}} < N$.

yielding the coded bit sequence $\mathbf{u}$, which is then bit-interleaved by π_1 of Fig. 2.15. Furthermore, we invoke a URC as the inner encoder, which is associated with the bit-interleaver π_2 of Fig. 2.15. The explicit benefit of incorporating a low-complexity memory-1 URC is that it allows the system to beneficially spread the *extrinsic* information across the iterative decoder components without increasing its delay and, as a result, a vanishingly low BER is attainable [217–219]. Following the two-stage encoding process, the coded bits traverse through the same QAM modulator and STBC

mapper as described in Sec 2.2.3.1.

The corresponding three-stage turbo decoder of the receiver is also depicted in Fig. 2.15, which consists of a joint MAP-based SD, a URC decoder and a RSC decoder. More explicitly, the composite inner decoder is formed by the combined joint MAP-based SD and the URC decoder, where the associated *a priori* information and *extrinsic* information are firstly interleaved and exchanged I_{inner} times. The outer decoder is constituted by the RSC decoder, where the information gleaned from the inner decoder is iteratively exchanged I_{outer} times. The final HD is then carried out by the RSC decoder to produce the estimate $\widehat{\mathbf{b}}$ of the transmitted information bit block $\mathbf{b}$.

For ease of explanation, the information exchanged between the decoder components, in terms of Log-Likelihood Ratios (LLRs) [219] as depicted in Fig. 2.15, are first defined.

- $\boldsymbol{\mathcal{L}}_{\text{det,p}}$, $\boldsymbol{\mathcal{L}}_{\text{det,a}}$, $\boldsymbol{\mathcal{L}}_{\text{det,e}}$: the *a posteriori*, *a priori* and *extrinsic* LLRs, respectively, associated with the joint MAP-based SD block of Fig. 2.15, which are detailed in [217, 220].
- $\boldsymbol{\mathcal{L}}_{\text{in,p}}$, $\boldsymbol{\mathcal{L}}_{\text{in,a}}$, $\boldsymbol{\mathcal{L}}_{\text{in,e}}$: the *a posteriori*, *a priori* and *extrinsic* LLRs, respectively, associated with the URC decoder block of Fig. 2.15.
- $\boldsymbol{\mathcal{L}}_{\text{out,p}}$, $\boldsymbol{\mathcal{L}}_{\text{out,a}}$, $\boldsymbol{\mathcal{L}}_{\text{out,e}}$: the *a posteriori*, *a priori* and *extrinsic* LLRs, respectively, associated with the composite inner decoder block of Fig. 2.15.
- $\boldsymbol{\mathcal{L}}_{\text{dec,p}}$, $\boldsymbol{\mathcal{L}}_{\text{dec,a}}$, $\boldsymbol{\mathcal{L}}_{\text{dec,e}}$: the *a posteriori*, *a priori* and *extrinsic* LLRs, respectively, associated with the outer RSC decoder block of Fig. 2.15.

Since the M_{sym}-QAM scheme maps a set of $N_{\text{b}} = \log_2 M_{\text{sym}}$ consecutive incoming bits onto a symbol value, we consider a set of $\mathbf{p}_{(1:N_{\text{b}})} = \{p_1, p_2, \cdots, p_{M_{\text{sym}}}\}$ consecutive bits without loss of generality. For the vth bit of $\mathbf{p}_{(1:N_{\text{b}})}$, its bit-wise *a posteriori* LLR can be derived by the classic Max-Log approximation [217] as

$$\begin{aligned}\boldsymbol{\mathcal{L}}_{\text{det,p}}(p_v) = \boldsymbol{\mathcal{L}}_{\text{det,a}}(p_v) &+ \max_{\widetilde{\mathbf{S}} \in \boldsymbol{\mathcal{S}}_1^{p_v}} \left\{ - \left\| \mathbf{Y}_{\text{ACO}} - \boldsymbol{\Lambda}_{\text{ACO}} \mathcal{F}_{\text{STBC}}\left(\widetilde{\mathbf{S}}\right) \right\|^2 / 2\sigma^2 + A_{\text{sub}} \right\} \\ &- \max_{\widetilde{\mathbf{S}} \in \boldsymbol{\mathcal{S}}_0^{p_v}} \left\{ \left\| \mathbf{Y}_{\text{ACO}} - \boldsymbol{\Lambda}_{\text{ACO}} \mathcal{F}_{\text{STBC}}\left(\widetilde{\mathbf{S}}\right) \right\|^2 / 2\sigma^2 + A_{\text{sub}} \right\}, \end{aligned} \tag{2.40}$$

where we have $A_{\text{sub}} = \sum_{\tau=1,\tau\neq v}^{M_{\text{sym}}} p_v \boldsymbol{\mathcal{L}}_{\text{det,a}}(p_\tau)$, while we define two subsets of $\boldsymbol{\mathcal{S}}$ as $\boldsymbol{\mathcal{S}}_0^{p_v} = \left\{ \widetilde{\mathbf{S}} \in \boldsymbol{\mathcal{S}}|_{p_v=0} \right\}$ and $\boldsymbol{\mathcal{S}}_1^{p_v} = \left\{ \widetilde{\mathbf{S}} \in \boldsymbol{\mathcal{S}}|_{p_v=1} \right\}$. The *extrinsic* LLRs $\boldsymbol{\mathcal{L}}_{\text{det,e}}$ gleaned from the joint MAP-based SD block are deinterleaved and then they are fed as the *a priori* LLRs $\boldsymbol{\mathcal{L}}_{\text{in,a}}$ into the URC pre-decoder of Fig. 2.15, which in turn calculates its *a posteriori* LLRs $\boldsymbol{\mathcal{L}}_{\text{in,p}}$. Then the updated *extrinsic* LLRs $\boldsymbol{\mathcal{L}}_{\text{in,e}}$ are fed back and re-interleaved, before being processed as the *a priori* LLRs $\boldsymbol{\mathcal{L}}_{\text{det,a}}$ by the SD block in the next inner iteration [217–219]. Following the convergence of the inner iteration process after I_{in} iterations, the outer iteration follows a similar procedure, which involves exchanging the corresponding *extrinsic* LLRs between the URC decoder and the RSC

decoder, until the predefined stopping criterion, specified by the number of outer iterations I_{out}, is met.

2.5.2 EXIT Chart-Based Analysis

In this section, familiarity with the EXIT-chart concept is assumed [216]. We then considered the performance of FEC coded ACO-OFDM based STBC G2 MIMO system employing the three-stage iterative joint MAP-based SD and decoding scheme of Fig. 2.15 presented in Sec. 2.5.1. In particular, we investigated the beneficial effects of applying the proposed JTRApS scheme to this coded system. In our simulation study, the generator polynomials of the half-rate RSC encoder were expressed in binary format as $G_{\text{RSC}} = [1, 0, 1]_2$ and $G^r_{\text{RSC}} = [1, 1, 1]_2$, while those of the URC encoder were $G_{\text{URC}} = [1, 0]_2$ and $G^r_{\text{URC}} = [1, 1]_2$, where G^r_{RSC} and G^r_{URC} denoted the feedback polynomials of the RSC and URC encoders, respectively. The number of inner iterations and outer iterations were set to $I_{\text{inner}} = 2$ and $I_{\text{outer}} = 5$. An interleaver length of 10^6 bits was used by both of the system interleavers.

Having obtain the soft LLRs of the composite inner decoder, let us now invoke EXIT charts for conveniently analysing the associated convergence behaviour by examining the exchange of the input/output mutual information $I_{\text{out,a}}$ and $I_{\text{out,e}}$. According to [220], the *extrinsic* mutual information $I_{\text{out,e}}$ can be expressed as a function of the *a priori* information $I_{\text{out,a}}$ and of the SNR as

$$I_{\text{out,e}} = \mathbb{T}\left(I_{\text{out,a}}, \gamma\right). \tag{2.41}$$

Furthermore, it has been shown in [220] that the area under the EXIT curve of the composite inner decoder's EXIT chart approximately equals to the system's normalised throughput $\mathcal{A}_{\text{det}}$, which is directly related to the SNR by [220]:

$$\mathcal{A}_{\text{det}}\left(\gamma\right) = \int_0^1 I_{\text{out,e}}\, d\, I_{\text{out,a}} = \int_0^1 \mathbb{T}\left(I_{\text{out,a}}, \gamma\right)\, d\, I_{\text{out,a}}. \tag{2.42}$$

Thus the overall achievable throughput $r_{\mathcal{T}}$ can be written as:

$$r_{\mathcal{T}}\left(\gamma\right) = \mathcal{A}_{\text{det}}\left(\gamma\right) \cdot L_{\text{T}} \cdot \log_2 M_{\text{sym}}. \tag{2.43}$$

The *a priori* and *extrinsic* mutual information associated with the outer RSC decoder, denoted by $I_{\text{dec,a}}$ and $I_{\text{dec,e}}$, can also be similarly calculated.

The EXIT curves of the three-stage coded ACO-OFDM based STBC G2 MIMO system employing the three-stage iterative joint MAP-based SD and decoding scheme communicating over the strongly turbulent channel are depicted in Fig. 2.16. The BER performance of this system under 1 to 5 iterations is also displayed, where the BER performance under different iterations are linked to it corresponding trajectory. It can be seen from Fig. 2.16 that with the aid of the proposed JTRApS scheme and having an ApS factor of 2, an open EXIT-tunnel exists between the

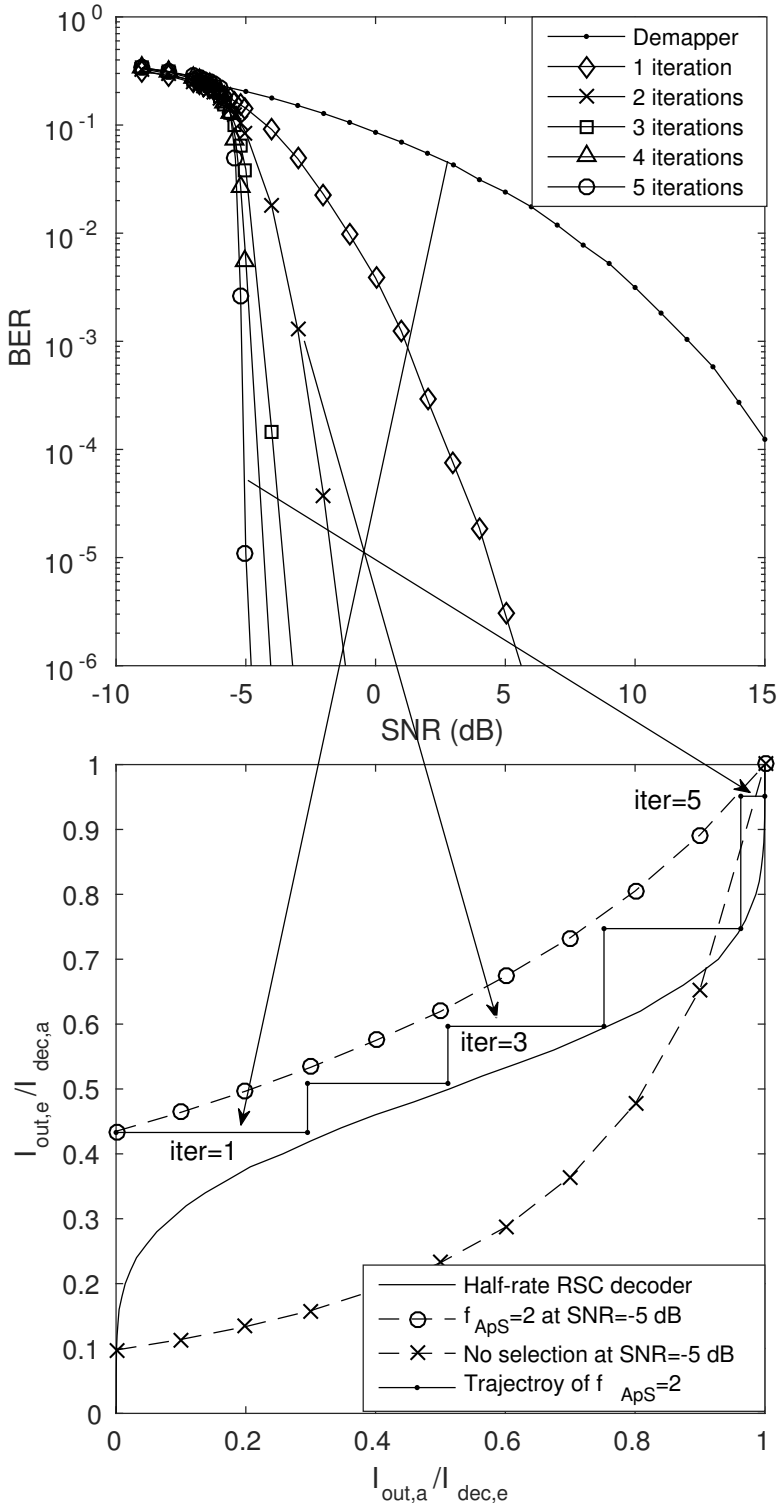

Figure 2.16: The BER performance and EXIT characteristics of the three-stage iteratively decoded ACO-OFDM based STBC G2 MIMO system, where ApS factor f_{ApS} = 2.0 is used. The BER curves of iterations 1 to 5 are linked to its corresponding EXIT trajectory. The system communicate over the strongly turbulent channel of $C_n^2 = 4 \times 10^{-13}$ and given the SNR of -5 [dB], where 4-QAM modulation is employed. The schematic of Fig. 2.15 and parameters in Table 2.2 are used.

EXIT chart curves of the inner SD-URC decoder and the outer RSC decoder at SNR $= -5$ [dB]. The actual stair-case shaped decoding trajectory is also depicted at SNR $= -5$ [dB] for this ApS assisted system, which shows that the point of perfect convergence at $(1.0, 1.0)$ can be reached after $I_{\text{outer}} = 5$ iterations. This indicates that this ApS assisted system is capable of achieving a vanishingly low BER at SNR $= -5$ [dB], which is confirmed by the system's BER performance shown in Fig. 2.19 in the following discussion. By contrast, the system operating without ApS fails to achieve an open tunnel between the EXIT chart curves of the inner SD-URC decoder and the outer RSC decoder at SNR $= -5$ [dB]. This implies that the system operating without ApS cannot achieve perfect decoding at SNR $= -5$ [dB], which is further confirmed by its BER performance employing different ApS factor of f_{ApS} shown in Fig. 2.19 as follows.

2.5.3 Achievable Throughput

According to Eq. (2.43), Fig. 2.17 portrays the achievable throughputs of our employed JTRApS assisted systems having ApS factors of 2, 3 and 4 and communicating over three different turbulence-level channels. For this system, the maximum achievable throughput is $0.5 \cdot L_{\text{T}} \cdot \log_2 M_{\text{sym}} = 2$ [bits/symbol/block]. It can be observed from Fig. 2.17 that for higher ApS factors and for stronger turbulence, a higher throughput is attained for a given SNR value or equivalently a lower SNR is required for reaching a given throughput. The results of Fig. 2.17 clearly indicate that the performance improvement attained by the proposed JTRApS scheme is much more significant under the strongly turbulent channel of $C_n^2 = 4 \times 10^{-13}$, particularly for a large ApS factor of 4.

2.5.4 Error Performance

Fig. 2.18 compares the BER performance of the three-stage iteratively decoded ACO-OFDM based STBC G2 MIMO system relying on the proposed JTRApS scheme having the ApS factors of 2, 3 and 4, respectively, to that of its counterpart operating without ApS, when communicating over the weakly turbulent channel of $C_n^2 = 4 \times 10^{-15}$. For the system operating without ApS, the BER convergence of the three-stage iterative decoder is portrayed in Fig. 2.18, where it can be seen that the system is capable of converging to a vanishing low BER, with the 'turbo-cliff' of the BER curve occurring approximately at SNR $= 2.1$ [dB] after $I_{\text{outer}} = 5$ iterations. By contrast, for the proposed system assisted by our joint ApS scheme having the ApS factors of 2, 3 and 4, the turbo-cliff of the BER curve occurs at the SNR values of 0.9 [dB], 0.3 [dB] and 0.0 [dB], respectively.

Similarly, Fig. 2.19 compares the BER performance of the two systems, namely assisted assisted by the JTRApS scheme as well as that operating without ApS, when communicating over the strongly turbulent channel associated with $C_n^2 = 4 \times 10^{-13}$. It can be seen from Fig. 2.19 that for the ApS assisted system having an ApS factor of 2, a vanishing low BER is achieved at SNR $= -5$ [dB], which matches the performance prediction of the EXIT chart analysis presented

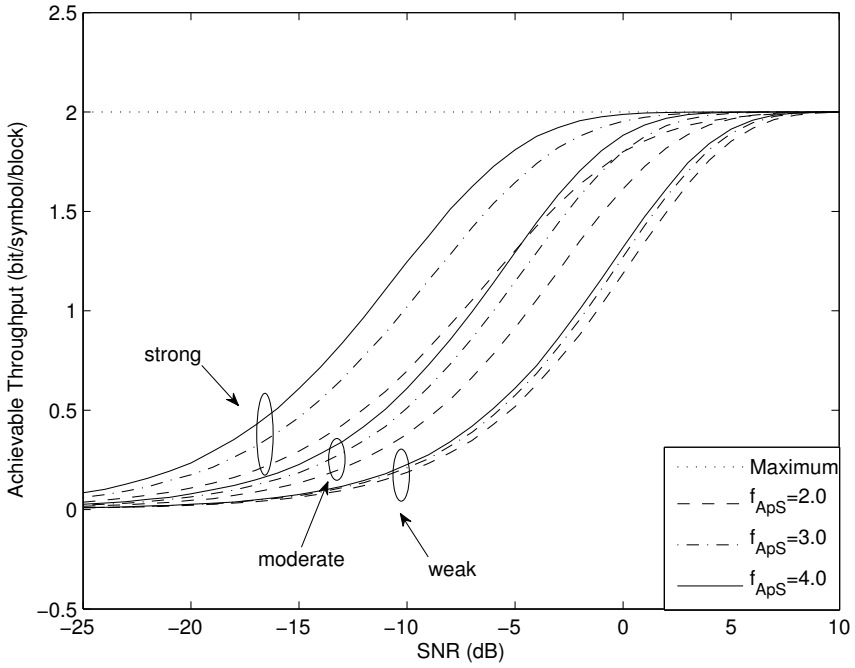

Figure 2.17: The achievable throughputs of the three-stage iteratively decoded ACO-OFDM based STBC G2 MIMO system of Fig. 2.15 with the aid of the JTRApS scheme having ApS factors of 2, 3 and 4, communicating over different turbulent channels, where 4-QAM modulation is employed and the parameters in Table 2.2 are used.

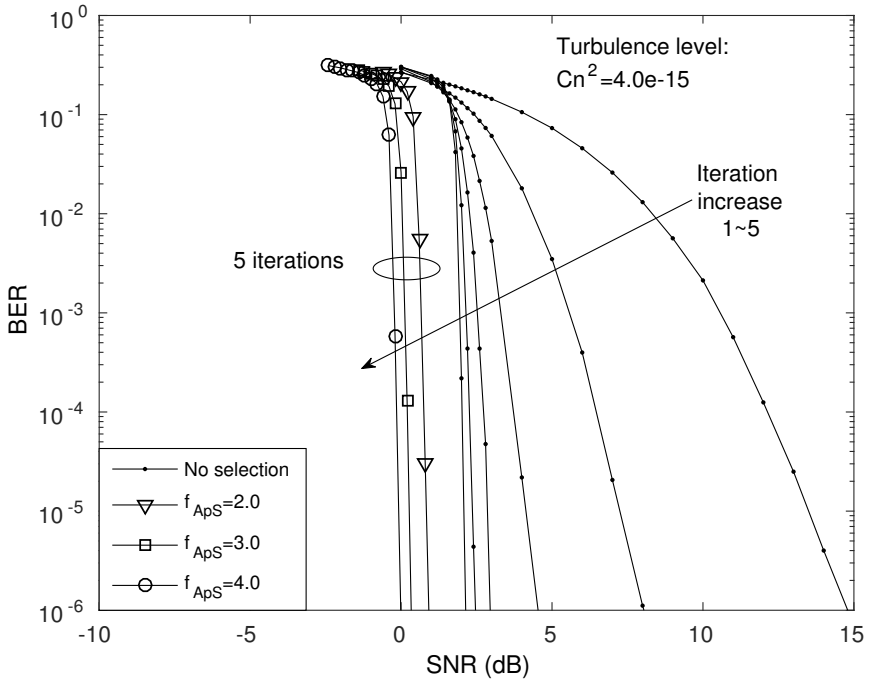

Figure 2.18: BER performance comparison of the three-stage iteratively decoded ACO-OFDM based STBC G2 MIMO systems of Fig. 2.15 employing the JTRApS scheme having ApS factors of 2, 3 and 4, respectively, as well as operating without ApS, communicating over the weakly turbulent channel, associated with $C_n^2 = 4.0 \times 10^{-15}$, where 4-QAM modulation is employed and the parameters in Table 2.2 are used.

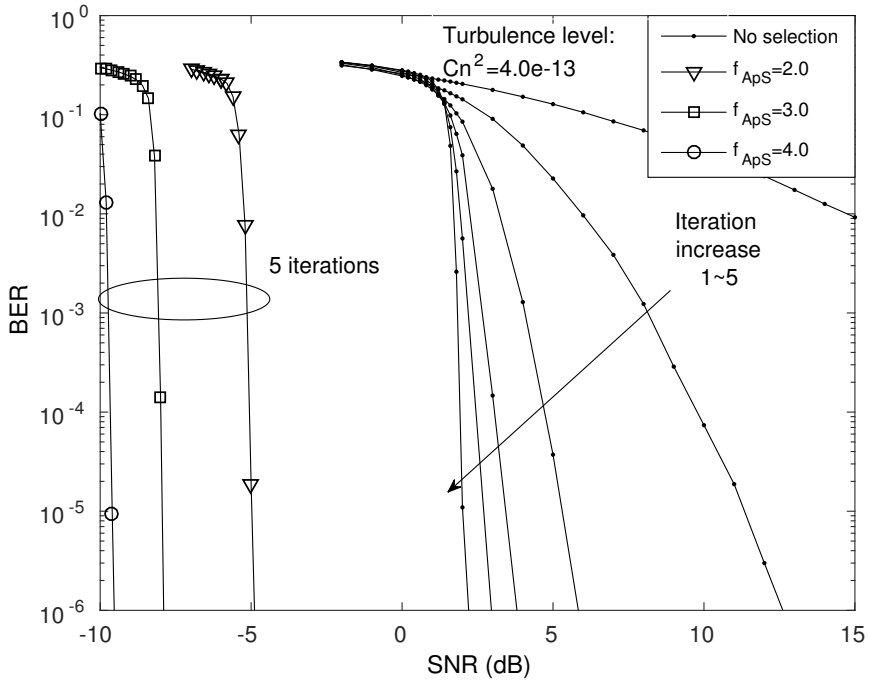

Figure 2.19: BER performance comparison of the three-stage iteratively decoded ACO-OFDM based STBC G2 MIMO systems of Fig. 2.15 employing the JTRApS scheme having ApS factors of 2, 3 and 4, respectively, as well as operating without ApS, communicating over the strongly turbulent channel, associated with $C_n^2 = 4.0 \times 10^{-13}$, where 4-QAM modulation is employed and the parameters in Table 2.2 are used.

in Fig. 2.16. When the ApS factor is increased to 3 and 4, a further performance enhancement is attained and the turbo-cliff of the system's BER curve occurs at the SNR values of -8 [dB] and -9.7 [dB], respectively. By contrast, the system operating without ApS can only attain a vanishing low BER at approximately SNR $= 2$ [dB]. By comparing Fig. 2.19 and Fig. 2.18, it can be confirmed again that the performance enhancement achievable by ApS is much more significant under strongly turbulent channel conditions. Specifically, given the ApS factor of 4, the turbo-cliff of the BER curve occurs at approximately SNR $= -9.7$ [dB] under the strong turbulence level of $C_n^2 = 4 \times 10^{-13}$, while it requires SNR $= 0$ [dB] to attain a vanishingly low BER under the weakly turbulent channel associated with $C_n^2 = 4 \times 10^{-15}$.

2.6 Conclusions

In this chapter, we have conceived a ACO-OFDM based MIMO system for FSO turbulence channels. Based on our investigation of the system's BER performance under different channel conditions and various types of MIMO schemes using joint ML-based HD, a substantially further enhancement was attained by a three-stage concatenated coding scheme, relying on iterative decoding. Our main contribution has been the conception of the novel joint transmit-receive aperture selection scheme for the sake of assisting the proposed three-stage iteratively decoded ACO-OFDM

based MIMO system in order to substantially improve the system's achievable diversity gain, BER performance as well as its throughput, while imposing a moderate hardware complexity. Moreover, our results have demonstrated that the performance gain obtained by the novel JTRApS assisted MIMO-aided optical wireless system is more significant under strongly-turbulent channel conditions.

Chapter 3

PHY II: Video Streaming in the Multiuser Indoor Visible Light Downlink

3.1 Introduction

3.1.1 Video Streaming Optimisation in the Multiuser Indoor VLC Downlink

The Fifth Generation (5G) wireless system represents the next phase of mobile communication, which is the subject of intensive research around the world. Whilst the Long Term Evolution (LTE) system has been rolled out in the large parts of the globe, the 5G system is expected to provide ubiquitous access to information anywhere and anytime for anyone and anything [221–223]. The recent concept of Heterogeneous Networks (HetNet) constitutes a beneficial structural evolution towards the 5G system concept, while the exploration of both Millimeter-Wave (MMW) and OW networks [1,146,224] opens up further emerging venues. In the OW regime, apart from the already well-documented IR region of the optical spectrum [5], high data rate VLC along with advanced illumination has become a reality in indoor environments [224]. The family of VLC systems exhibits several beneficial characteristics such as inherent security, vast available bandwidth, unlicensed spectrum, low-cost electronics (LEDs and PDs), etc. Hence, VLC is especially suitable for high-quality multimedia video transmission, as one of its killer application.

More specifically, exploiting content-aware video streaming becomes extremely promising, which has been widely studied in conventional RF systems from various perspectives [225–231]. In [225], the problem of choosing the best streaming policy under both bandwidth and playback delay constraints is addressed, whilst resource allocation and packet scheduling is studied in [226]. In [227], the rate based fairness of video flows is studied, while the problem of scheduling delay-sensitive media-sources, such as lip-synchronised video is considered in [228]. The content-

aware optimisation of a Wideband Code Division Multiple Access (WCDMA) system in proposed in [229], where the authors use the Peak Signal-to-Noise Ratio (PSNR) for characterising the video distortion. Furthermore, a novel distortion estimation parameter referred to as the 'distortion impact' was proposed in [231]. Finally, the subject of content-aware video transmission is investigated in the context of HetNets in [230].

Designing content-aware video streaming in VLC systems is non-trivial, since the VLC system transmission are highly directional. This results into confined coverage of VLC attocells, which are also referred to as "attocells". In this context, the initial study of [124] analysed the fundamental factors affecting the performance of the VLC system, assuming that all the LEDs in the system illuminate a single attocell. This appealing simple philosophy provides a reliable coverage without imposing interference, but the price to pay is that, the system is only capable of serving a single Mobile Terminal (MT) in a transmission slot. A simple and straightforward way of circumventing this disadvantage is to arrange for every single LED light to create and illuminate its own attocell and to simultaneously serve a multiplicity different MTs requesting different traffic. However, the ubiquitous inter-cell interference between the neighbouring attocells formulated by the neighbouring LED lights imposes detrimental effects on the MTs at the attocell edge. In order to solve this problem, more sophisticated transmission regimes have to be conceived. At the time of writing, there is paucity of studies on the transmission schemes conceived for VLC cells. The authors of [232] discussed the so-called Fractional Frequency Reuse (FFR) scheme, which strikes a compromise between the cell-edge MT performance and the system throughput, whilst maintaining a low system complexity. Subsequently, a joint multi-user transmission regime was discussed in [233, 234], which relies on concurrent data transmission from multiple cooperated LED points to a MT in the Down Link (DL).

3.1.2 Novel Contribution of This Chapter

Against this background, in this chapter, we investigate video streaming optimisation in an indoor VLC system relying on both classic UFR and HFRFT, as well as on a VT scheme. Furthermore, we conduct content-aware optimisation for minimising the total distortion of video streaming, whilst satisfying both the minimum rate constraints as well as the optical constraints. Finally, the video distortion, achieved video rate and consumed energy are investigated in the context of our optimisation.

3.2 Transmission Schemes

The indoor VLC system relies on multiple LED lights mounted on the ceiling as the transmitters, where the receivers are randomly distributed on the receiver plane. Depending on the specific

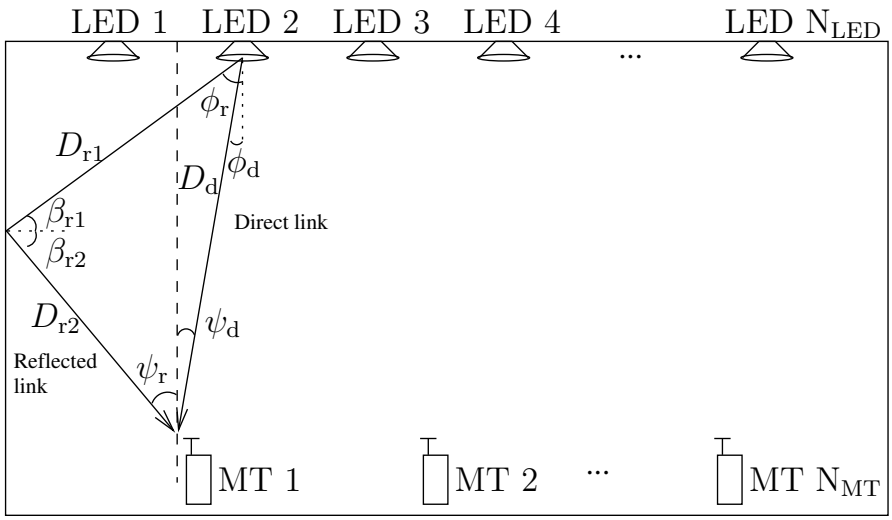

Figure 3.1: The 2-D vertical axis-section of the room model in the VLC system.

system configurations, which include the room size, the receivers' locations and the particular LED layout, etc. the indoor channel conditions widely differ. For the simplicity of exposition but without any loss of generality, in this section we will introduce a 2-Dimensional (2D) plane model, which includes all the essential features of indoor VLC system.

3.2.1 2D Multiple LED Model

Let us consider a 2D room having the length of 30 [m] and N_{LED} LED lights equi-distantly installed on the ceiling for serving N_{MT} MTs, as shown in Fig. 3.1, which are randomly distributed. In the following, we will introduce the channel model of this 2D room and further elaborate on a range of different transmission schemes in the context of this 2D model, as detailed in Table 3.1.

3.2.1.1 Indoor Channel Model

As demonstrated in Fig. 3.1, if we assume that ϕ_{d} is the angle of irradiation of the LED lights, ψ_{d} represents the angle of incidence, and D_{d} is the distance between a transmitter and a receiver. In an optical link, the channel's DC gain on directed path is characterised as [124]

$$H_{\mathrm{d}}(0) = \begin{cases} \dfrac{(l_{\mathrm{lam}}+1)\cos^{l_{\mathrm{lam}}}(\phi_{\mathrm{d}})A_{\mathrm{r}}}{2\pi D_{\mathrm{d}}^2}\mathcal{G}_{\mathrm{d}}, & \text{if } \psi_{\mathrm{d}} \leq \Psi_{\mathrm{c}}\,, \\ 0, & \text{if } \psi_{\mathrm{d}} > \Psi_{\mathrm{c}}\,, \end{cases} \tag{3.1}$$

where l_{lam} is the Lambertian emission order, which is given by semi-angle $\Phi_{1/2}$ at half illumination of an LED as $l_{\mathrm{lam}} = -\log_2\cos(\Phi_{1/2})$ [5]. Furthermore, A_{r} is the physical area of the PD and Ψ_{c} denotes the FOV at the receiver. Eq. (3.1) indicates that once the angle of irradiation of a receiver is higher than the FOV, the receiver's LOS would be blocked. We assume $\mathcal{G}_{\mathrm{d}} = T_{\mathrm{s}}g_{\mathrm{c}}(\psi_{\mathrm{d}})\cos(\psi_{\mathrm{d}})$,

Table 3.1: System Parameters of the Indoor VLC System

Room size and MTs' configuration	
Length of room	30 [m]
Height of room	3 [m]
Number of MTs N_{MT}	6
Height of MTs	0.85 [m]
Configuration of the VLC system	
Number of LEDs N_{LED}	8
Height of LEDs	2.5 [m]
Optical transmit power of LEDs $P_{\mathrm{t,o}}$	5.0, 7.0, 20.0 [W]
Semi-angle at half power $\Phi_{1/2}$	70°
Field-of-View Ψ_{c}	60°
Physical area of Detector on a PD A_{r}	1.0 [cm^2]
Gain of optical filter T_{s}	1.0
Refractive index of a lens at a PD n_{re}	1.5
Responsivity of a PD ξ	0.53 [A/W]
System modulation bandwidth B	1, 20 [MHz]
Reflectance factor ρ_{f}	0.8
Electronic charge q	1.6×10^{-19} [C]
Boltzmann's constant κ	1.3806488×10^{-19}
Background current I_{bg}	5.1×10^{-3} [A]
Open-loop voltage gain G	10
Fixed capacitance of the PD per unit area η	1.12×10^{-6} [F]
FET channel noise factor Γ	1.5
FET transconductance g_m	3.0×10^{-2}
Noise bandwidth factor 1 I_{nb1}	0.562
Noise bandwidth factor 2 I_{nb2}	0.0868

where T_{s} is the gain of optical filter, $g_{\mathrm{c}}(\psi_{\mathrm{d}})$ is the gain of an optical concentrator. If we let n_{re} represents the refractive index, the gain of the optical concentrator can be characterised as [124]:

$$g_{\mathrm{c}}(\psi_{\mathrm{d}}) = \begin{cases} \dfrac{l_{\mathrm{lam}}^2}{\sin^2(\Psi_{\mathrm{c}})}, & \text{if } \psi_{\mathrm{d}} \leq \Psi_{\mathrm{c}}\,, \\ 0, & \text{if } \psi_{\mathrm{d}} > \Psi_{\mathrm{c}}\,. \end{cases} \tag{3.2}$$

Apart from the VLC LOS reception, the MTs may also receive the VLC reflected path owing to the wall. The received optical power is given by the channel's DC gain on the direct LOS path $H_{\mathrm{d}}(0)$ and reflected path $H_{\mathrm{r}}(0)$, which may be written as:

$$P_{\mathrm{r,o}} = P_{\mathrm{t,o}} H_{\mathrm{d}}(0) + \int_{\mathrm{walls}} P_{\mathrm{t,o}} dH_{\mathrm{r}}(0), \tag{3.3}$$

where $P_{\mathrm{t,o}}$ and $P_{\mathrm{r,o}}$ denote the transmitted and received optical power, respectively. The channel

DC gain on the first reflection dH_{r} is given by [124]:

$$dH_{\mathrm{r}} = \begin{cases} \dfrac{(l_{\mathrm{lam}}+1)\cos^{l_{\mathrm{lam}}}(\phi_{\mathrm{r}})A_{\mathrm{r}}\rho_{\mathrm{f}}}{2\pi^2 D_{\mathrm{r1}}^2 D_{\mathrm{r2}}^2}\mathcal{J}\mathcal{G}_{\mathrm{r}}dA_{\mathrm{wall}}, & \text{if } \psi_{\mathrm{r}} \leq \Psi_{\mathrm{c}}\,, \\ 0, & \text{if } \psi_{\mathrm{r}} > \Psi_{\mathrm{c}}\,, \end{cases} \tag{3.4}$$

where D_{r1} is the distance between an LED light and a reflecting surface, D_{r2} denotes the distance between a reflective point and a MT receiver, ρ_{f} is the reflectance factor, whilst dA_{wall} is a small reflective area. Similarly, we let $\mathcal{G}_{\mathrm{r}} = T_{\mathrm{s}}g(\psi_{\mathrm{r}})\cos(\psi_{\mathrm{r}})$, where $g(\psi_{\mathrm{r}})$ could be calculated in the same way of Eq. (3.2). Furthermore, we assume that $\mathcal{J} = \cos(\beta_{\mathrm{r1}})\cos(\beta_{\mathrm{r2}})$, where β_{r1} and β_{r2} represent the angle of irradiance to a reflective point and the angle of irradiance to a MT's receiver, respectively.

The dominant noise contribution is assumed to be the shot noise due to ambient light from windows. We also take thermal noise into account. Hence, the Gaussian noise of the receiver filter's output having a total variance of σ^2 may be expressed as [124]:

$$\sigma^2 = \sigma_{\mathrm{shot}}^2 + \sigma_{\mathrm{thermal}}^2. \tag{3.5}$$

According to [124], the variance of shot noise σ_{shot}^2 may be formulated as:

$$\sigma_{\mathrm{shot}}^2 = 2q\xi P_{\mathrm{r,o}}B + 2qI_{\mathrm{bg}}I_{\mathrm{nb1}}B, \tag{3.6}$$

where q is the electronic charge, ξ is the detector's responsivity. B is the equivalent noise bandwidth and I_{bg} denotes the background current caused by the background light. Additionally, the thermal noise variance is given by [124]:

$$\sigma_{\mathrm{thermal}}^2 = \frac{8\pi\kappa T_{\mathrm{K}}}{G}\eta A_{\mathrm{r}} I_{\mathrm{nb1}}B^2 + \frac{16\pi^2\kappa T_{\mathrm{k}}\Gamma_{\mathrm{FET}}}{g_{\mathrm{FET}}}\eta^2 A_{\mathrm{r}}^2 I_{\mathrm{nb2}}B^3, \tag{3.7}$$

where κ is the Boltzmann's constant, T_{K} represents the absolute temperature, G is the open-loop voltage gain, η denotes the fixed capacitance of the PD per unit area, Γ is the FET transconductance. The noise bandwidth factors I_{nb1} and I_{nb2} are constant experimental values. Here, according to [5, 124], we opt for their typical values, as shown in Table 3.1.

3.2.1.2 VLC Achievable Throughput

Because the system is constituted by multiple independent attocells serving multiple MTs, the interference emanating from the adjacent attocells is inevitable and has to be taken into account. We define the Signal-to-Interference-plus-Noise-Ratio (SINR) γ as the total electronic power received from the desired signal source normalised by the scale of the electronic noise power in a bandwidth of B plus the total electronic power received from the destructive interference sources according to different schemes $\mathcal{I}_{\mathrm{sch}}$.

Furthermore, we assume that the system employs ACO-OFDM [148]. As detailed in [150], when an ACO-OFDM scheme is introduced into our VLC system, the relationship between the electronic transmit power and optical transmit power is defined as

$$P_{\mathrm{t,e}} = \pi P_{\mathrm{t,o}}^2, \tag{3.8}$$

where $\pi \approx 3.1415926$ is the circumference ratio. Hence, we define the received electronic SINR γ as:

$$\gamma = \frac{P_{\mathrm{r,e}}}{\sigma^2 + \mathcal{I}_{\mathrm{sch}}} = \frac{\pi \left[\xi P_{\mathrm{t,o}} \left(H_{\mathrm{d}}(0) + \int_{\mathrm{wall}} dH_{\mathrm{r}}(0)\right)\right]^2}{\sigma^2 + \mathcal{I}_{\mathrm{sch}}}. \tag{3.9}$$

According to [152], the maximum achievable rate of the ACO-OFDM system may be characterised by its channel capacity of [150]

$$C_{\mathrm{ACO}} = \frac{B}{4} \log_2 (1 + \gamma). \tag{3.10}$$

This simple formulation is based on the assumption that the signal is Gaussian distributed and that ACO-OFDM only has a normalised effective throughput of 1/4, because it exploits the so-called Hermitian symmetry property for the sake of generating real and positive symbols. Below we will investigate three different transmission schemes: UFR, HFRFT and VT.

3.2.2 Unity Frequency Reuse

Let us commence our discourse from the most straightforward technique of constructing a VLC attocell, which is simply based on considering each individual LED light as an independent attocell, resulting into UFR. Then the total number of attocells N_{cell} equals the total number of LED lights N_{LED} in this UFR transmission scheme. In this case, the ith MT suffers form the interference contributed by the power $P_{\mathrm{t,o}}^{(c',i)}$ emanating from the other attocells, which is represented by $\mathcal{I}_{\mathrm{UFR}} = \pi\xi^2 \sum_{c' \neq c, c \in [1, N_{\mathrm{cell}}]} \left(P_{\mathrm{t,o}}^{(c',i)} H^{(c',i)}\right)^2$, where c and c' denote the indices of the serving attocell and interfering attocell, respectively. As a result, the received SINR $\gamma_{\mathrm{UFR}}^{(c,i)}$ of the ith MT served by the cth attocell using UFR transmission may be written as

$$\gamma_{\mathrm{UFR}}^{(c,i)} = \frac{\pi \left(\xi P_{\mathrm{t,o}}^{(c,i)} H^{(c,i)}\right)^2}{\sigma^2 + \mathcal{I}_{\mathrm{UFR}}}, \tag{3.11}$$

where σ^2 is the total noise variance at the receiver obtained from Eq. (3.5), while $P_{\mathrm{t,o}}^{(c,i)}$ represents the DL transmit power assigned to the ith MT from the cth attocell. In this scheme, each attocell may serve multiple MTs within its coverage using the time-division based round-robin scheme of [235].

Let $P_{\mathrm{r,e}}^{(c,i)} = \pi \left(\xi P_{\mathrm{t,o}}^{(c,i)} H^{(c,i)}\right)^2$ represent the received electronic power of the ith MT, based on Eq. (3.10). Then the instantaneous achievable rate of the ith MT can be formulated as

$$r_{\mathrm{UFR}}^{(c,i)} = \frac{B}{4} \log_2 \left[1 + \frac{P_{\mathrm{r,e}}^{(c,i)}}{\sigma^2 + \mathcal{I}_{\mathrm{UFR}}}\right]. \tag{3.12}$$

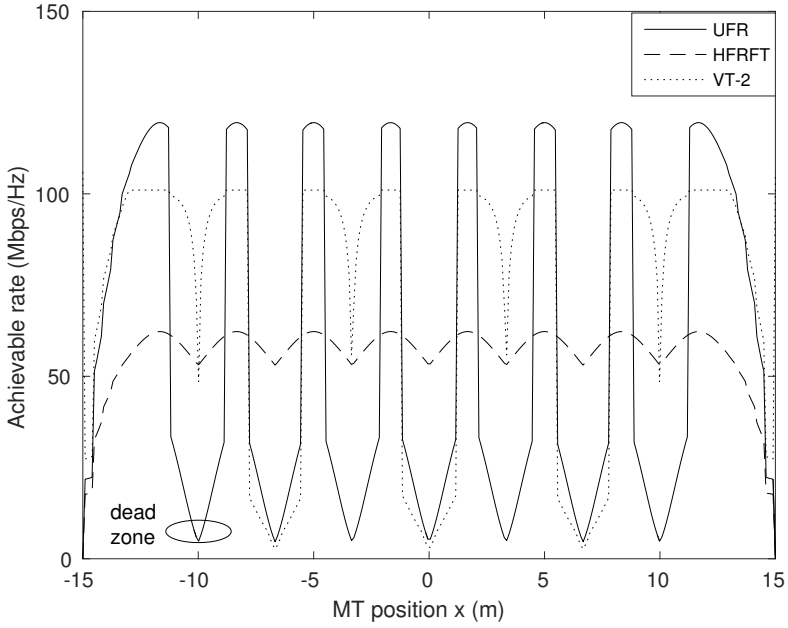

Figure 3.2: The achievable rate distribution of a VLC system using different transmission schemes: UFR, HFRFT and VT relying on a pair of attocells (VT-2), with fixed optical transmission power of $P_{\text{t,o}}$ = 20 [W] of each LED light source and FOV = 60° at the receiver. Reflection is considered, while the specific system parameters can be found in Table 3.1.

Additionally, consider the optical transmit power limitation of $P_{\text{t,o}}^{\min} \leq P_{\text{t,o}}^{(c,i)} \leq P_{\text{t,o}}^{\max}$, where $P_{\text{t,o}}^{\min}$ is a small value higher than 0. If we let $P_{\text{r,e}}^{\max} = \pi \left(\xi P_{\text{t,o}}^{\max} H^{(c,i)}\right)^2$ at receiver side, the dynamic range of received electronic power as determined by the transmit power constraint in the UFR scheme is given by

$$0 \leq P_{\text{r,e}}^{(c,i)} \leq P_{\text{r,e}}^{\max}. \tag{3.13}$$

Given the system parameters listed in Table 3.1, the distribution of the MTs' achievable rate based on Eq. (3.12) in this 2D VLC model under the UFR transmission scheme is shown in Fig. 3.2. For the time being, let us focus our attention on the UFR transmission scheme denoted by the solid line. All the other techniques will be discussed in the forthcoming Sec. 3.2.3 and Sec. 3.2.4. As seen in Fig. 3.2, certain areas are inadequately, covered in the overlapping areas between two attocells, hence creating a dead-zone. This is because of the severe interference emanating from the neighbouring attocells. Therefore, to eliminate the inter-cell interference, more sophisticated transmission schemes should be considered for alleviating the interference.

3.2.3 Higer Frequency Reuse Factor Based Transmission

Given the shortcomings of the UFR, the HFRFT scheme is capable of eliminating the interference by simply assigning a pair of orthogonal frequencies to the neighbouring two LED lights. This

is possible, because only a limited frequency-range of 20 [MHz] of the white LEDs is exploited for communications[1]. Explicitly, in this transmission scheme, each LED light still illuminates an individual attocell, hence, the total number of attocells remains the same as in the UFR case. However, in each attocell, only half of the frequency band can be used, which results into a frequency reuse factor of 2, hence the adjacent-cell interference can be mitigated and the SINR can be improved at the cell-edge. For odd indexed attocells, the interference of the ith MT imposed by the HFRFT scheme is characterised as $\mathcal{I}_{\text{HFRFT}} = \pi\xi^2 \sum_{c' \neq c, c' \in [1,3,\cdots]} \left(P_{\text{t,o}}^{(c',i)} H^{(c',i)}\right)^2$, where c and c' denote the indices of the serving attocell and the interfering attocells from the other odd numbered attocells. The corresponding instantaneous SINR $\gamma_{\text{HFRFT}}^{(c,i)}$ may be defined as

$$\gamma_{\text{HFRFT}}^{(c,i)} = \frac{\pi \left(\xi P_{\text{t,o}}^{(c,i)} H^{(c,i)}\right)^2}{\sigma^2/2 + \mathcal{I}_{\text{HFRFT}}}. \tag{3.14}$$

If we let $P_{\text{r,e}}^{(c,i)} = \pi \left(\xi P_{\text{t,o}}^{(c,i)} H^{(c,i)}\right)^2$, the instantaneous achievable rate of the ith a MT of the cth attocell may be written as

$$r_{\text{HFRFT}}^{(c,i)} = \frac{B}{8} \log_2 \left[1 + \frac{P_{\text{r,e}}^{(c,i)}}{\sigma^2/2 + \mathcal{I}_{\text{HFRFT}}}\right]. \tag{3.15}$$

Similarly, the dynamic range of the received electronic power as determined by the transmit power constraint in the HFRFT scheme can also be described by Eq. (3.13).

The achievable rate of the HFRFT scheme is indicated by the dashed line in Fig. 3.2. Observe that compared to the UFR transmission scheme, the dead-zone is mitigated, which indicates that the HFRFT is an appealing low-complexity solution of mitigating the detrimental cell-edge interference, albeit this is achieved at the cost of halving both the bandwidth as well as the achievable rate.

3.2.4 Vectored Transmission

For the sake of reducing the size of the dead-zone in the UFR regime of Fig. 3.2 without sacrificing the bandwidth efficiency, we may opt for merging several neighbouring LED attocells into a virtual cell. In each virtual cell, we could employ more advanced transmission schemes. More specifically, we introduce the Zero-Forcing (ZF) based VT[2] regime into our VLC system for mitigating the mutual interference amongst the attocells within a virtual cell. Explicitly, we propose the VT-2 scheme[3], where two neighbouring LED lights form a virtual cell and exploit ZF transmission in order to simultaneously serve two MTs as a pair. For the n_{p}th MT pair, we have $\mathcal{P}_{n_{\text{p}}}$. Then the

[1]The Fractional Frequency Reuse (FFR) concept is not considered in this treatise, since it would require prompt frequency switching for every MT during their movement, which would gravely degrade the users' experience [232].

[2]VT may be viewed as a specific example of the classic Transmission Precoding (TPC) based on the CSI of RF systems, with the slight difference that the VLC channel is typically non-dispersive.

[3]For the simplicity of demonstration without any loss of generality, we only consider the coordination of the neighbouring pair of LED lights. More involved VT schemes increase the complexity of the VT scheme.

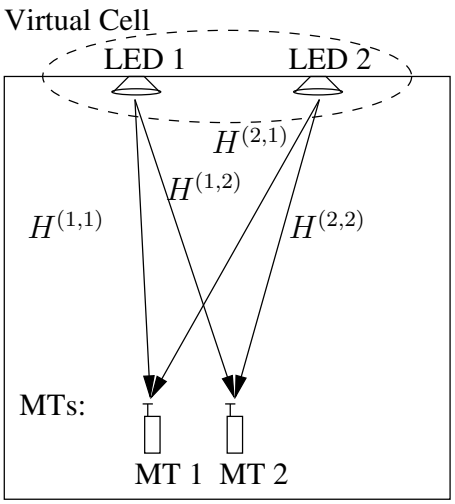

Figure 3.3: A simple illustration of VT-2 transmission in a virtual cell with multiple MTs.

definition of an attocell set is given by $\mathcal{C} = \left\{\mathbf{c}_{\mathrm{v}}^{(1)}, \cdots, \mathbf{c}_{\mathrm{v}}^{(c)}, \cdots, \mathbf{c}_{\mathrm{v}}^{(N_{\mathrm{cell}}/2)}\right\}$, where we assume having an even number of LED. More explicitly, as shown in Fig. 3.1, LED 1 and LED 2 form $\mathbf{c}_{\mathrm{v}}^{(1)}$, LED 3 and LED 4 constitute $\mathbf{c}_{\mathrm{v}}^{(2)}$, etc. Therefore, for the $i_{\mathrm{s}i}$th MT served by the cth virtual cell $\mathbf{c}_{\mathrm{v}}^{(c)}$, the interference in our VT-2 scheme is mainly contributed by the power $P_{\mathrm{t,o}}^{(c',i_{\mathrm{s}i})}$ leaking from the other neighbouring virtual cells, namely $\mathcal{I}_{\mathrm{VT2}}^{(c',i_{\mathrm{s}i})} = \pi\xi^2 \sum_{c'\neq c, c'\in[1,N_{\mathrm{cell}}/2]} \left(P_{\mathrm{t,o}}^{(c',i_{\mathrm{s}i})} H^{(c',i_{\mathrm{s}i})}\right)^2$, where c and c' represent the indices of the serving virtual cell and the interfering virtual cells, respectively.

As mentioned above, the proposed VT-2 scheme is capable of supporting the pair of MTs $\mathcal{P}_{n_{\mathrm{p}}}$ in a certain frequency band. These two MTs of this virtual cell constitute a (2×2)-element MIMO system, as shown in Fig. 3.3, where for the cth virtual cell $\mathbf{c}_{\mathrm{v}}^{(c)}$, the MIMO channel matrix $\mathbf{H}^{(c,\mathcal{P}_{n_{\mathrm{p}}})}$ can be written as the individual channels' DC gain between the two LEDs and the two MTs. Then, within this virtual cell, a precoding matrix $\mathbf{G}^{(c,\mathcal{P}_{n_{\mathrm{p}}})}$ is constructed for the sake of eliminating the interference between the MTs in $\mathcal{P}_{n_{\mathrm{p}}}$, where we have $\mathbf{H}^{(c,\mathcal{P}_{n_{\mathrm{p}}})}\mathbf{G}^{(c,\mathcal{P}_{n_{\mathrm{p}}})} = \mathbf{I}$ and $\mathbf{I}$ is an identity matrix. To satisfy this requirement, $\mathbf{G}^{(c,\mathcal{P}_{n_{\mathrm{p}}})}$ may readily be obtained by the pseudo-inverse of the channel matrix $\mathbf{H}^{(c,\mathcal{P}_{n_{\mathrm{p}}})}$, which may be written as

$$\begin{aligned}\mathbf{G}^{(c,\mathcal{P}_{n_{\mathrm{p}}})} &= \left(\mathbf{H}^{(c,\mathcal{P}_{n_{\mathrm{p}}})}\right)^{\mathrm{T}} \left[\mathbf{H}^{(c,\mathcal{P}_{n_{\mathrm{p}}})} \left(\mathbf{H}^{(c,\mathcal{P}_{n_{\mathrm{p}}})}\right)^{\mathrm{T}}\right]^{-1} \\ &= \begin{bmatrix} g_{1,1} & g_{1,2} \\ g_{1,2} & g_{2,2} \end{bmatrix},\end{aligned} \tag{3.16}$$

with $(\cdot)^{\mathrm{T}}$ denoting the transpose operation and $g_{c,i_{\mathrm{s}i}}$ representing the elements of the matrix. Then, if we let the signals transmitted from the LEDs within a virtual cell be represented by $\mathbf{x} = [x_1, x_2]^{\mathrm{T}}$, the received signals may be written as

$$\mathbf{y} = \mathbf{H}^{(c,\mathcal{P}_{n_{\mathrm{p}}})}\mathbf{G}^{(c,\mathcal{P}_{n_{\mathrm{p}}})}\mathbf{x} + \mathbf{v}, \tag{3.17}$$

where we have $\mathbf{v} = [v_{i_{\mathrm{s}1}}, v_{i_{\mathrm{s}2}}]^{\mathrm{T}}$, with each element denoting the noise imposed on the received

signals, which have a variance given by Eq. (3.5). Thus, unlike in the UFR and HFRFT regimes, according to this scheme, the instantaneous SINR definition of MT $i_{\mathrm{s}i}$ in the VT-2 scheme is given by

$$\gamma_{\mathrm{VT2}}^{(c,i_{\mathrm{s}i})} = \frac{\xi^2 P_{\mathrm{r_e,e}}^{(c,i_{\mathrm{s}i})}}{\sigma^2 + \mathcal{I}_{\mathrm{VT2}}^{(c,i_{\mathrm{s}i})}}, \tag{3.18}$$

where for each MT $i_{\mathrm{s}i}$, the received electronic power $P_{\mathrm{r,e}}^{(c,i_{\mathrm{s}i})} = \xi^2 P_{\mathrm{r_e,e}}^{(c,i_{\mathrm{s}i})}$ is contributed by the equivalent received electronic power $P_{\mathrm{r_e,e}}^{(c,i_{\mathrm{s}i})}$ multiplied by the square of the responsivity ξ in a pair of LED lights within a virtual cell, and each LED light allocates only a commensurate fraction of optical power within its capability to serve a MT, while the rest of the power serves the other MT.

Since VT-2 does not partition its frequency resource, the instantaneous achievable rate is no longer halved, for MT $i_{\mathrm{s}i}$ in virtual cell, its achievable rate can be expressed as

$$r_{\mathrm{VT2}}^{(c,i_{\mathrm{s}i})} = \frac{B}{4}\log_2\left[1 + \frac{P_{\mathrm{r,e}}^{(c,i_{\mathrm{s}i})}}{\sigma^2 + \mathcal{I}_{\mathrm{VT2}}^{(c,i_{\mathrm{s}i})}}\right]. \tag{3.19}$$

The achievable rate of the VT-2 scheme of our indoor VLC system is shown by dotted line in Fig. 3.2. While drawing its achievable rate distribution in each virtual cell, we assume that one of the MTs in $\mathcal{P}_{n_{\mathrm{p}}}$ has a fixed location and we calculate the achievable rate of the other MT in $\mathcal{P}_{n_{\mathrm{p}}}$ at different locations in this 2D system model. We can see in Fig. 3.2 that the achievable rate of VT-2 is higher than that of the HFRFT scheme. Furthermore, the dead-zone in the virtual cell is mitigated, but the dead-zone still persists between each virtual cells, since the interference emerging from other virtual cells still affects the MTs.

MT Scheduling: In this 2D VLC model, if the number of MTs is higher than the number of LED arrays in a virtual cell, then the order in which each MT is served has to be carefully determined, since the MT pairing process is of prime importance. Hence, we propose a two-stage MT pairing algorithm for finding beneficial pairing combinations of MTs, where the serving order of each pair is based on their channel conditions. Here, we have to point out that the MT pairing algorithm we proposed does not involve any specific power allocation based on Eq. (3.18). Instead, the power assigned to each light in the virtual cell remains the same. More explicitly, the two-stage MT pairing algorithm can be summarised as follows:

- **Cell association stage**: In this stage, each MT estimates the distance with respect to all LED lights, for example with the aid of an indoor positioning system and builds up the link to the nearest LED light, which results in the MT becoming associated with the virtual cell.

- **Search stage**: In this stage, the MTs within the virtual cell are divided into different pairs for the sake of exploiting the VT-2 regime. After exhaustively searching all possible pairing combinations with the goal of maximising the sum of the achievable rate, we then obtain the best pairs and their serving orders in a virtual cell.

To be more specific, in the search stage, we assume that there is always an even number of MTs in a virtual cell. The search stage is formally detailed in Table 3.2.

Table 3.2: Searching Algorithm for MT Pairing

Searching :
For $\mathbf{c}_{\mathrm{v}}^{(c)} \in \mathcal{C}$
Find the MTs in its coverage
Determine the number of serving MTs: (assume the number of serving MT is even)
List all possible sorting combination
For each sorting combination
For for each MT pair
Sum the achievable rate of each serving pair using Eq. (3.19)
end
Recoded the sum rate for this sorting combination
end
Find the best sorting pattern, which achieves the highest sum rate
end
Output : The sorted best MTs pairs in orders for all virtual cell

3.3 Video Streaming Optimisation

Let us now discuss the content-aware optimisation of our VLC system employing the above-mentioned transmission schemes.

3.3.1 Video Traffic Model

Let us first discuss the basic traffic model and the principle of our video optimisation. We construct a system supporting a total of N_{MT} MTs, where each MT aims for downloading a pre-encoded video stream over an independent link. For simplicity, all MTs request the same video streams. In a video stream, the video frames are encoded on a Group-of-Pictures (GOPs) basis, by the video codecs, e.g. the H.264 [236] and H.265 [237] schemes. Within each GOP structure, the video frames are encoded using motion estimation inter-dependently. Each video frame within a GOP can be of Intra-frame (I) Type, Bidirectional (B) Type or Predicted (P) type, as detailed in [238]. The dependency of the intra-GOP video frames is shown in Fig. 3.4. In this example, the GOP structure is IBBPBBP, where the I type video frame is independent of any other video frames, which is hence the most important one in a GOP. By contrast, the P type video frame depends on the preceding I and P video frames. Finally, the B type video frame is dependent on both the preceding and succeeding I or P video frames. Hence the following B and P type video frames will

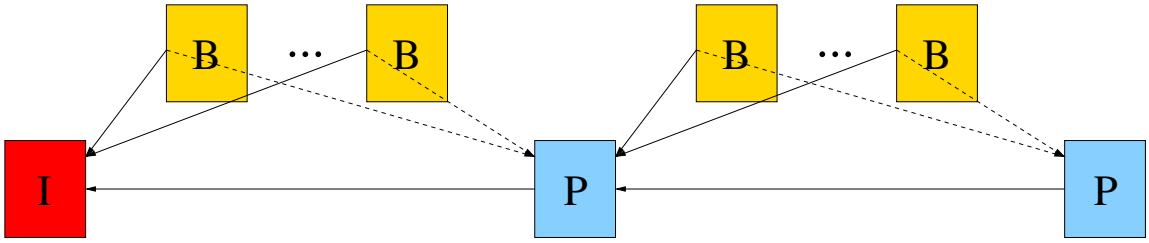

Figure 3.4: Structure of video frames in a GOP, where we use the IBBPBBP video frame structure. The dependency among the intra-GOP video frames is represented by arrows.

Figure 3.5: Four video frames of the Foreman video test stream, with the 1st video frame contaminated. The upper four video frames are the original video frames, and the middle four video frames are distorted version of the video frames. The differences between the original video frame and distorted video frames are shown in the lower four pictures, which had to be multiplied by a factor of 6 to make them visible.

be affected, if the I video frame is corrupted.

For the simplicity of exposition and without any loss of generality, in this treatise, we assume an N_{F}-video frame video stream relying on the same GOP structure for each MT. Let the set of video frames in a GOP downloaded by the ith MT be denoted by $\mathcal{F}_{\mathrm{GOP}}^{(i)} = \left\{ f^{(i,1)}, \cdots, f^{(i,j)}, \cdots, f^{(i,N_{\mathrm{F}})} \right\}$, where $f^{(i,j)}$ represents the jth video frame in the ith MT's GOP. Furthermore, due to the different content of each video frame in the video stream, we assume that the rate required for transmitting this video frame $f^{(i,j)}$ is $r_{\mathrm{req}}^{(i,j)}$, where we define the video frames' required rate as the number of bits in the video frame over the time interval between consecutive video frames. Let $\gamma_{\mathrm{P}}^{(i,j)}$ denote

the PSNR of the video frame $f^{(i,j)}$. To be more explicit, before its transmission the video stream is compressed by the video codec. The PSNR of each video frame represents the logarithmic Mean Square Error (MSE) between the original video frame and the compressed video frame in [dB].

We assume that in our model, we let an estimation window include n_{f} video frames $\mathcal{F}^{(i)} = \left\{f^{(i,1)}, \cdots f^{(i,n_{\mathrm{f}})}\right\}$ stored in a buffer before the transmission. Based on the knowledge of CSI among different MTs, the video frames are first scheduled and then assigned the appropriate transmit power. Consequently the achievable VLC rate of each MT is calculated, which is higher than the required rate of transmitting all the video frames in this window. As a result, before each MT is served, each transmitter will choose the best set of video frames to be transmitted and to be discarded. By employing 'frame copy' scheme, every discarded video frame will be directly replaced by the previous video frame.

We then denote the reconstructed window of the ith MT by $\mathcal{F}'^{(i)} = \left\{f'^{(i,1)}, \cdots f'^{(i,j)}, \cdots f'^{(i,n_{\mathrm{f}})}\right\}$ at the receiver. Since the video frames in a GOP are closely related to the other video frames, discarding an important video frame might affect the quality of other video frames. A simple example is shown in Fig. 3.5. Using the 'Foreman' sequence, where the upper row shows the four original compressed video frames $\mathcal{F}^{(i)}$, the middle four video frames are the recovered ones and the lower four video frames display the differences between the original and recovered video frames. We can observe that due to the loss of the 1st video frame, the quality of the following four video frames is also affected. Considering the sophisticated bit allocation of a video clip, we hence invoke a relatively simple model for our simulations in this chapter, namely that a frame dropping event only affects the dropped video frame itself without any inter-frame error propagation. Naturally, due to the differences between the above-mentioned pair of models having a difference is inevitable. However, we will demonstrate the rationale of invoking our simplified model in the following discussions.

For the ith MT, we let $\boldsymbol{\theta}^{(i)} = \left\{\theta^{(i,1)}, \cdots, \theta^{(i,j)}, \cdots, \theta^{(\mathrm{i},\mathrm{n_f})}\right\}$, which indicates the video frames' transmission status. Explicitly, $\theta^{(i,j)}$ characterises the status of each video frame, where $\theta^{(i,j)} = 0$ represents transmitting and $\theta^{(\mathrm{i,j})} = 1$ represents discarding a video frame. Then the total distortion experienced by the ith MT is simply the sum of the single-video-frame distortion's expressed in terms of PSNR, which is written as

$$\mathcal{D}^{(i)}\left(\boldsymbol{\theta}^{(i)}\right) = \sum_{j=1}^{n_{\mathrm{f}}} \Delta^{(i,j)}\theta^{(i,j)}, \tag{3.20}$$

where $\Delta^{(i,j)} = \gamma_{\mathrm{P}}^{(i,j)} - \gamma_{\mathrm{P}}^{\prime(i,j)}$, is a weighting factor that represents the PSNR difference between the original video frame $f^{(i,j)}$ and the recovered video frame $f'^{(i,j)}$. We also denote the video frame-status vector of the ith MT $\boldsymbol{\theta}^{(i)}$ as the ith row of the matrix $\boldsymbol{\theta}$, which includes the video frame status of all MTs. Additionally, owing to the specific GOP structure, we should consider the dependence relationship among the different types of video frames. Based on the features of the I

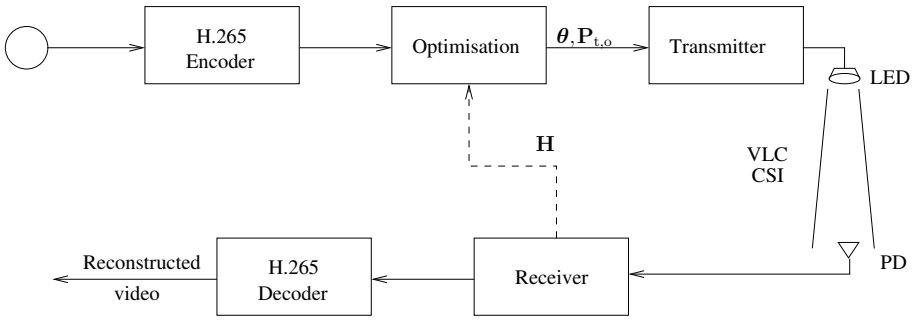

Figure 3.6: The structure of our video stream optimisation system, where the content-aware distortion-fair algorithm is invoked.

and P video frames, when an I video frame is not scheduled for transmission, due to encountering an interference-contaminated links, the rest of the video frames in the GOP should will also be affected. As a consequence, the whole GOP is replaced by the most recently received one. Thus we define binary scheduling-decision flag a decisive set $\mathcal{Z}_{\text{dec}}$, which contains the scheduling-decision information of all the I video frames for each GOP. In the best situation, the set $\mathcal{Z}_{\text{dec}}$ represents a copy of the binary valued $\theta^{(i,j)}$ in a GOP, since none of the I video frames are discarded. Otherwise, apart from the I video frame, any other video frames in the GOP will be affected as well owing to the associated video frame dependence.

Given the scheduling-decision status of each video frame, the bit rate[4] required for transmitting the selected video frames of the ith MT is the total rate of the ith original video frames $\sum_{j=1}^{n_{\text{f}}} r_{\text{req}}^{(i,j)}$ minus the total rate of discarded video frames, which is the actually achieved video rate expressed as

$$\mathcal{R}^{(i)}\left(\boldsymbol{\theta}^{(i)}\right) = \sum_{j=1}^{n_{\text{f}}} r_{\text{req}}^{(i,j)}\left(1-\theta^{(i,j)}\right). \tag{3.21}$$

The system structure is shown in Fig. 3.6, the video stream is first stored in a long enough buffer. In the optimisation block, the content-aware distortion-fair algorithm determine transmit or discard the video frames based on the known CSI. At receive side, the received date is then recovered to video stream.

3.3.2 Optimisation Problem Formulation

In a GOP, the video frames scheduling and power control is carried out individually for each MT based on the channel conditions and interference levels encountered on a frame-by-frame basis, where again only the selected video frames in a GOP are transmitted. The process of deciding about the most appropriate transmitted video frames can be solved as a content-aware distortion-fair optimisation problem, which is described below.

[4]Here we define the required bit rate of each frame as the length (in bytes) of video frame divided by each video frame's decoder time stamp.

The objective of the optimisation problem is to minimise the total distortion of all video frames for all MT's video stream. For each MT, the optimisation problem is subject to the constraint that the total achievable VLC rate of a MT's transmission scheme could provide should be at least equal to the total required video rate $\mathcal{R}^{(i)}\left(\boldsymbol{\theta}^{(i)}\right)$. The total achievable VLC rate available for the video frames in the entire video stream is dominated by the instantaneous SINR γ, as we defined in Eq. (3.11), (3.14) and (3.18). Given the upper bound $P_{\mathrm{t,o}}^{\max}$ of the maximum transmit power and Eq. (3.8), the instantaneous SINR γ is a function of the received electronic power of each video frame $P_{\mathrm{r,e}}^{(c,i,j)}$. Furthermore, considering that the constraints imposed on the optical transmit power in different schemes are also different, we specifically elaborate on the content-aware distortion-fair problem in the UFR and HFRFT schemes, which can be deemed to be identical. On the other hand, the content-aware distortion-fair problem of the VT-2 scheme has to be described by a different problem.

3.3.2.1 Problem Formulation for UFR and HFRFT

Based on Eq. (3.20) and (3.21), we aim for minimising the total distortion of all video frames for each MT's video stream, as detailed in Eq. (3.22). Furthermore, for each MT, the achievable VLC rate defined in Eq. (3.21) should be higher than its total required video rate by a GOP, which is described by Eq. (3.23), based on the channel capacity detailed in Eq. (3.10). Additionally, the optical transmit power assigned to each video frame should also not exceed the maximum optical power constraint.

Based on these, the optimisation problem of the UFR and HFRFT schemes may be formulated as:

$$\text{Problem 1}: \quad \min_{\boldsymbol{\theta}^{(i)}} \sum_{i=1}^{N_{\mathrm{MT}}} \mathcal{D}^{(i)}\left(\boldsymbol{\theta}^{(i)}\right) \tag{3.22}$$

$$\text{subject to}: \quad \mathcal{R}^{(i)}\left(\boldsymbol{\theta}^{(i)}\right) \leq \sum_{j=1}^{n_{\mathrm{f}}} B_{\mathrm{avb}} \log_2\left[1+\frac{P_{\mathrm{r,e}}^{(c,i,j)}(1-\theta^{(i,j)})}{\sigma_{\mathrm{sch}}^2+\mathcal{I}_{\mathrm{sch}}}\right], \ \forall i \tag{3.23}$$

$$\text{variables}: \quad 0 \leq P_{\mathrm{r,e}}^{(c,i,j)} \leq \pi\left(\xi H^{(c,i,j)} P_{\mathrm{t,o}}^{\max}\right)^2, \ \forall i,j \tag{3.24}$$

$$\theta^{(i,j)} = \begin{cases} 0, & f^{(i,j)} \text{ transmitted}, \\ 1, & f^{(i,j)} \text{ discarded}, \end{cases} \tag{3.25}$$

where B_{avb} and σ_{sch}^2 represent the available system bandwidth and the noise variance of the different schemes, as detailed in Eq. (3.12) and (3.15). Explicitly, for a video clip associated with a scanning-rate of 30 Frame per Second (FPS), we have UFR: $B_{\mathrm{avb}} = \frac{B}{4\mathrm{FPS}}$, $\sigma_{\mathrm{sch}}^2 = \sigma^2$ and HFRFT: $B_{\mathrm{avb}} = \frac{B}{8\mathrm{FPS}}$, $\sigma_{\mathrm{sch}}^2 = \sigma^2/2$. Furthermore, we let $P_{\mathrm{r,e}}^{(c,i,j)}$ represent the received electronic power of the ith MT's jth video frame under the cth attocell, which is dominated by its corresponding optical transmit power $P_{\mathrm{t,o}}^{(c,i,j)}$. Furthermore, we let $H^{(c,i,j)}$ denote the channel DC gain of the jth video frame between the ith MT and the cth attocell. Finally, $\mathcal{I}_{\mathrm{sch}}$ is the total

interference, where we consider the worst-case scheme that the interference received from the interfering cells is maximum, hence we have $\mathcal{I}_{\text{sch}} = \pi\xi^2 \sum_{c'\neq c, c'\in[1,\cdots,N_{\text{cell}}]} \left(P_{\text{t,o}}^{\max} H^{(c',i,j)}\right)^2$ and $\mathcal{I}_{\text{sch}} = \pi\xi^2 \sum_{c'\neq c, c'\in[1,3,\cdots]} \left(P_{\text{t,o}}^{\max} H^{(c',i,j)}\right)^2$ for the UFR and HFRFT scheme, respectively, if we consider an odd-indexed attocell as an example.

3.3.2.2 Problem Formulation for VT-2

Since the VT-2 scheme serves a pair of MTs simultaneously instead of a single one, the problem formulation is different from the above.

Explicitly, we will formulate the optimisation problem for the VT-2 scheme as:

$$\text{Problem 2}: \min_{\boldsymbol{\theta}^{(n_{\text{p}},i_{\text{s}i})}} \sum_{n_{\text{p}}=1}^{N_{\text{MT}}/2} \sum_{i_{\text{s}i}=1}^{2} \mathcal{D}^{(n_{\text{p}},i_{\text{s}i})} \left(\boldsymbol{\theta}^{(n_{\text{p}},i_{\text{s}i})}\right) \tag{3.26}$$

$$\text{subject to}: \mathcal{R}^{(n_{\text{p}},i_{\text{s}i})}\left(\boldsymbol{\theta}^{(n_{\text{p}},i_{\text{s}i})}\right) \leq \sum_{j=1}^{n_{\text{f}}} \frac{B}{4\text{FPS}} \log_2\left[1+\frac{\xi^2\left(1-\theta^{(n_{\text{p}},i_{\text{s}i},j)}\right)P_{\text{re,e}}^{(c,n_{\text{p}},i_{\text{s}i},j)}}{\sigma^2+\mathcal{I}_{\text{VT2}}^{(c,n_{\text{p}},i_{\text{s}i})}}\right], \forall n_{\text{p}} \tag{3.27}$$

$$\begin{cases} \frac{1}{\sqrt{\pi}}\sqrt{\left(g_{1,1}^{(n_{\text{p}},j)}\right)^2 P_{\text{re,e}}^{(c,n_{\text{p}},i_{\text{s}1},j)} + \left(g_{1,2}^{(n_{\text{p}},j)}\right)^2 P_{\text{re,e}}^{(c,n_{\text{p}},i_{\text{s}2},j)}} \leq P_{\text{t,o}}^{\max}, \forall n_{\text{p}}, j \\ \frac{1}{\sqrt{\pi}}\sqrt{\left(g_{2,1}^{(n_{\text{p}},j)}\right)^2 P_{\text{re,e}}^{(c,n_{\text{p}},i_{\text{s}1},j)} + \left(g_{2,2}^{(n_{\text{p}},j)}\right)^2 P_{\text{re,e}}^{(c,n_{\text{p}},i_{\text{s}2},j)}} \leq P_{\text{t,o}}^{\max}, \forall n_{\text{p}}, j \end{cases} \tag{3.28}$$

$$\theta^{(n_{\text{p}},i_{\text{s}i},j)} = \begin{cases} 0, & f^{(n_{\text{p}},i_{\text{s}i},j)} \text{ transmitted}, \\ 1, & f^{(n_{\text{p}},i_{\text{s}i},j)} \text{ discarded}. \end{cases} \tag{3.29}$$

In Problem 2, we let n_{p} represent the index of the MT pairs, hence $\boldsymbol{\theta}^{(n_{\text{p}},i_{\text{s}i})}$ denotes the scheduling-decision based video frame status of the $i_{\text{s}i}$th MT in the n_{p}th MT pair. Furthermore, $P_{\text{re,e}}^{(c,n_{\text{p}},i_{\text{s}i},j)}$ is the $i_{\text{s}i}$th MT's equivalent received electronic power of the jth video frame in the n_{p}th MT pair within the virtual cell $\mathbf{c}_{\text{v}}^{(c)}$. Finally, $g_{c,i_{\text{s}i}}^{(n_{\text{p}},j)}$ denotes the specific element of the jth video frame's precoding matrix in the n_{p}th MT pair. We may notice that, since ZF TPC is used in the VT-2 scheme, the equivalent received electronic power of each MT is constrained by the elements of the precoding matrix $\mathbf{G}$ described in Eq. (3.16), which indicates that the power transmitted to each MT in a pair should not exceed the power limit of a LED light in an attocell.

3.4 Numerical Results and Discussions

In this section, we present our numerical results for characterising the proposed problem using the Nonlinear Optimization by Mesh Adaptive Direct Search (NOMAD) algorithm of [239] in the context of our indoor VLC video transmission system. More specifically, we mainly consider the following pair of transmission scenarios:

- **Fixed position based scenario**: we fix the position of a MT and investigate its PSNR degradation for characterising the performance attained at this specific location.
- **Random-walk based scenario**: we allow the MTs to randomly move in the 2D room model. Then the CIR experienced during each video frame of each MT becomes different, which are averaged in order to characterise the average performance across the room. These experiments are repeated 30 times for the sake of generating statistically relevant results.

Furthermore, in the different transmission schemes, the MTs are served in different order, depending whether the transmission scheme we considered involves a MT transmission scheduling scheme. Additionally, we assume that the channel conditions experienced by each user are identical during each of the different transmission schemes for the sake of fair performance comparisons among the three different transmission schemes, namely the UFR, the HFRFT and the VT-2. We transmit the widely-used 'Football' video test sequence scanned at 30 FPS constituted by a total of 8 GOPs, where the length of a GOP is 8 video frames. We used the H.265 video codec, while all other parameters used are listed in Table 3.3.

Table 3.3: Parameters Used in our Video Streaming Optimisation

Parameters	Values
Estimation window length n_f	2,4,8,16
Transmission schemes	UFR, HFRFT, VT-2
Video clip	Football
GOP per MT	8
GOP length	8 video frames
Video frames' structure in a GOP	IPPPPPPP
FOV	60°
Video-frame-size	CIF 352 × 288
FPS	30
Video codec	H.265
Packet length	1000
ACO-OFDM length	512

3.4.1 Packet Loss Ratio

Let us commence by briefly discussing the relationship between the PSNR degradation vs. Packet Loss Ratio (PLR)[5], which is shown in Fig. 3.7. We may observe that the video distortion quantified in terms of the average PSNR increases substantially as a function of the PLR. Explicitly, when the PLR reaches 30%, the average PSNR degradation reaches 16 [dB].

[5]Here we define the packet as a unit including 1000 bits (given in Table 3.3).

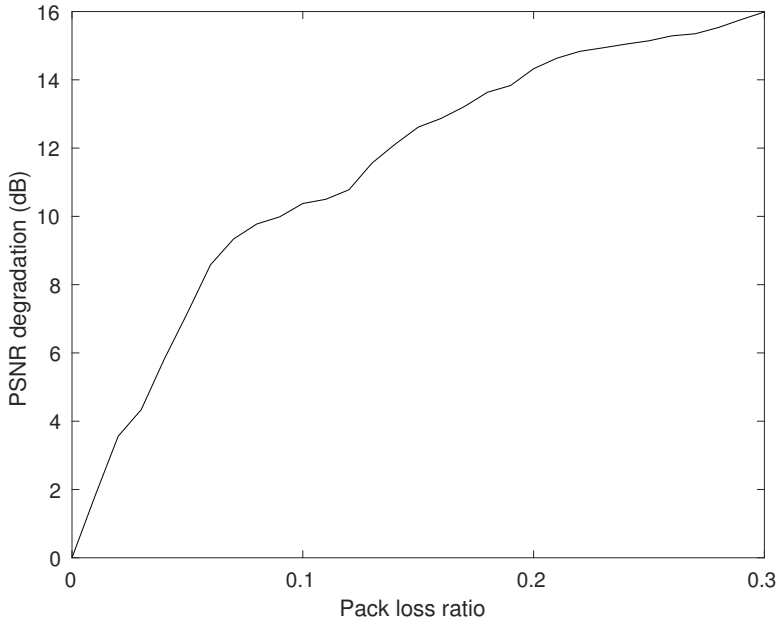

Figure 3.7: The PSNR degradation vs. PLR for the video clip 'Foreman'encoded by the H.264 codec, where the video frame size is CIF 352 $\times$ 288 and the transmission packet length is 1000 bits. The schematic of Fig. 3.6 and the parameters of Table 3.3 are used.

3.4.2 Video Distortion

3.4.2.1 PSNR Degradation Distribution

Let us first consider the video PSNR degradation of a particular MT moving in the room. Fig. 3.8 shows the average PSNR degradation of a MT being served a 64-frame video clip at each different position in the room. Explicitly, Fig. 3.8b demonstrates the exact PSNR degradation, while Fig. 3.8a displays the potential positions of this particular MT between a pair of points A and B. Here we have to mention that since the VT-2 scheme simultaneously serves a pair of MTs, we set the other MT at the fixed location marked by the black dot in Fig. 3.8a to pair with our moving MT for calculating the PSNR degradation. At each position, the MT will download the whole video clip constituted by 64 video frames under three different transmission schemes.

Let us first consider the PSNR degradation when we have $P_{\text{t,o}}^{\max} = 7.0$ [W]. We observe that as expected, the PSNR degradation varies with the MT's position. More specifically, when the MT is right under the LED lights (-11.6 [m]), all three schemes provide a good PSNR performance, hence the PSNR degradation remains low. However, when the MT moves away from the LED lights, the performance degrades, especially when it is in the interference-contaminated area at Position 4 of Fig. 3.8b under the UFR scheme, when the video frames are discarded. This is because when the MT is exactly halfway between two LED lights, the MT suffers from the maximum amount of interference imposed by the adjacent attocell. In contrast to the UFR scheme, the PSNR degra-

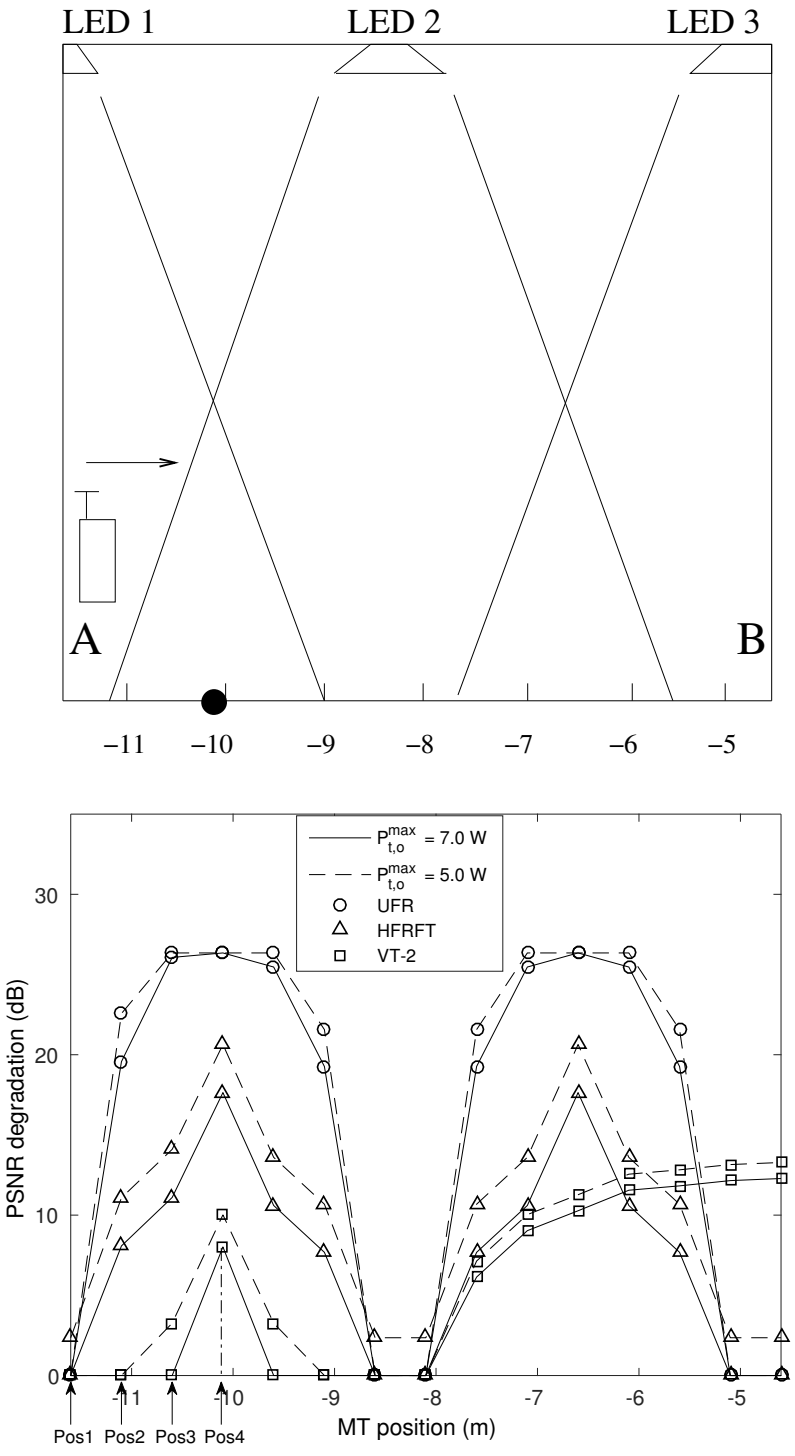

(b)

Figure 3.8: PSNR degradation vs. a single MT's position under the UFR, HFRFT and VT-2 in the indoor VLC system of Fig. 3.1. The maximum optical transmit power is $P_{t,o}^{max}$ = 5.0 and 7.0 [W], FOV = 60°, while the estimation window length is n_f = 4 video frame duration. The 'Football' video clip encoded by the H.265 codec associated with the length of 8 GOPs × 8 = 64 video frames is transmitted to this MT at each position. The performance of frame-by-frame degradation and achieved video rate of UFR, HFRFT and VT-2 at Position 1 (-11.6 [m]), Position 2 (-11.1 [m]), Position 3 (-10.6 [m]) and Position 4 (-10.1 [m]) will be discussed in Fig. 3.9 - 3.12 and Fig. 3.15 - 3.18, respectively. The schematic of Fig. 3.6 and parameters in Table 3.3 are used.

dation under the HFRFT scheme is much lower, because the adjacent attocells use non-interfering frequencies for the adjacent LED lights. Instead of being affected by the interfering power arriving from the neighbouring attocell, the PSNR degradation is now caused by the reduced interference as a benefit of having an increased distance from the interfering light source. Importantly, we observe that the VT-2 scheme outperforms the other two schemes. The system only suffers from an approximately 8 [dB] PSNR degradation, when the MT is halfway between the two LED lights in a virtual cell. The reduced PSNR degradation is an explicit benefit of the VT-2 scheme jointly serving two MTs. However, when one of the paired MTs moves to -10.1 [m], its position almost overlaps with the paired MT denoted by the black dot in Fig. 3.8a. Hence, their CIR becomes very similar and therefore their separation by the VT-2 scheme becomes imperfect. Furthermore, we have to mention that the PSNR degradation under the VT-2 scheme starts to increase more dramatically from the point onwards, when MT is at -8.1 [m]. This is because, the MT starts to suffer from the interfering power of LED 3. The PSNR degradation continues to increase, when the MT passed the -6.6 [m] position, because this MT is handed over to the virtual cell constructed by LED 3 and LED 4. If we still pair this MT with the MT at the fixed position of -10.6 [m], the system will no longer perform well. This is why the PSNR degradation keeps on increasing.

Additionally, if we reduce the maximum optical transmit power to $P_{\mathrm{t,o}}^{\max} = 5.0$ [W], as expected the system's performance degrades correspondingly, because only a lower power could be allocated to each video frame. Therefore, the PSNR degradation becomes more severe. Hence, in our following discussions, all the results are obtained for the system having the maximum transmit power of $P_{\mathrm{t,o}}^{\max} = 7.0$ [W].

3.4.2.2 Fixed Position based Scenario

Let us now explore the performance of VLC system under the UFR, HFRFT and VT-2 schemes. More explicitly, when the MT is at the four positions of -11.6, -11.1, -10.6 and -10.1 [m] in Fig. 3.8a. We investigate the performance of these three schemes in Fig. 3.9 - 3.12, where the curves represent the achievable VLC rate of the system under our three schemes, while the markers exhibit the resultant video frame dropping events frame-by-frame. We may observe that the relative frequency of frame dropping events increases from Position 1 to 4, as shown in Fig. 3.9 to Fig. 3.12. This is mainly due to the degraded channel conditions explicitly portrayed in Fig. 3.8. More concretely, we may observe from Fig. 3.9 that both the UFR and VT-2 schemes are capable of providing a sufficiently high achievable VLC rate for satisfying the required video rate, when the MT is at Position 1. By contrast, the achievable HFRFT VLC rate is lower, but even then, no video-frames are dropped. This is because, we have to emphasise that according to the constraints of the optimisation detailed in Eq. (3.23) and Eq. (3.27), we evaluate the sum of the achievable VLC rate for all $n_{\mathrm{f}} = 4$ video frames, rather than that of every single video frame. Hence, even

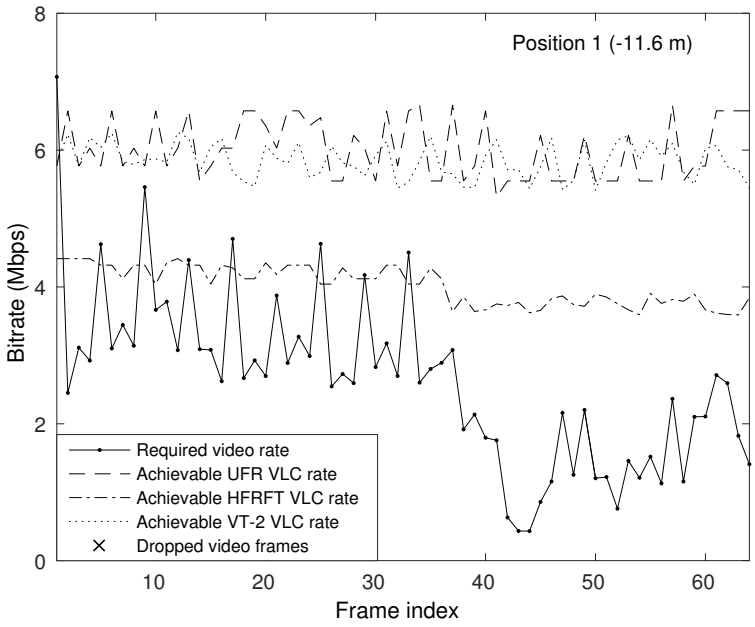

Figure 3.9: The required video rate before frame dropping (dotted solid line) and the achievable VLC rate under the three different transmission schemes of UFR, HFRFT and VT-2 in the indoor VLC system, when the MT is at Position 1 (-11.6 [m]) of Fig. 3.8b. The maximum optical transmit power is $P_{\mathrm{t,o}}^{\max}$ = 7.0 [W] and FOV = 60°, while the estimation window length is n_{f} = 4 video frame duration. The 'Football' video clip is encoded by the H.265 codec associated with the length of 8 GOPs = 64 video frames is transmitted to this MT, where the GOP is set to 8 video frames. The curves displays the achievable VLC rate that system could provide, and the the dropped-frames' indices are denoted by the markers. The schematic of Fig. 3.6 and the parameters of Table 3.3 are used.

if the achievable VLC rate of the HFRFT scheme at a specific frame index is slightly lower than the required video rate, this is compensated by the lower required rate of the other video frames. As a result, the overall achievable VLC rate of all three scheme is sufficiently high. Therefore at Position 1, no video frames are dropped.

When the MT moves to Position 2, the performance of the three schemes is shown in Fig. 3.10. We may observe that compared to the performance at Position 1 of Fig. 3.10, the achievable VLC rate of the VT-2 scheme remains almost unchanged. By contrast, the achievable VLC rate of the HFRFT scheme is slightly degraded, but its overall achievable VLC rate still remains higher than the sum of the required video rate. This indicates that the HFRFT scheme is still capable of transmitting the whole video clip without dropping any video frames. By contrast, the achievable UFR VLC rate is dramatically reduced. Therefore, the sum of the achievable VLC rate is insufficient for transmitting all video frames. Hence, the optimisation algorithm tends to drop the specific video frames, which the system is unable to transmit. Explicitly, when the achievable VLC rate of the UFR scheme in an estimation window is lower than the required video rate of a specific

video frame, but higher than the average required video rate, then the system may still be capable of transmitting the video frame, provided that some video-frames have a lower rate-requirement within this window. However, when the average video rate becomes higher than the achievable

Table 3.4: Video Frame Dropping Algorithm

Initialising:
$r_{\text{req}}^{(j)}$: required video rate of the jth video frame $r_{\text{vlc}}^{(j)}$: achievable VLC rate of the jth video frame
$R_{\text{sur}} = 0$: throughput surplus of video frames $\Delta_{\text{length}} = 0$: No. of pending frames
Δ_{index}: index of pending video frames
$\Delta_{\text{short}}^{(j)}$: throughput deficit of the jth pending video frame

If $\sum_{j=1}^{n_{\text{f}}} r_{\text{req}}^{(j)} \leq \sum_{j=1}^{n_{\text{f}}} r_{\text{vlc}}^{(j)}$
  For $j = 1 : n_{\text{f}}$
    If $r_{\text{vlc}}^{(j)} \to 0$
      $\theta^{(j)} = 1$ // dropped
    Otherwise
      $\theta^{(j)} = 0$ // transmitted
    End If
  End For
Otherwise If $\sum_{j=1}^{n_{\text{f}}} r_{\text{req}}^{(j)} > \sum_{j=1}^{n_{\text{f}}} r_{\text{vlc}}^{(j)}$
  For $j = 1 : n_{\text{f}}$
    If $r_{\text{req}}^{(j)} \leq r_{\text{vlc}}^{(j)}$
      $\theta^{(j)} = 0$ // transmitted
      $R_{\text{sur}} = R_{\text{sur}} + r_{\text{vlc}}^{(j)} - r_{\text{req}}^{(j)}$ // accumulate the throughput surplus
    Otherwise
    $\theta^{(j)} = 1$ // hold and buffered
      $\Delta_{\text{length}} = \Delta_{\text{length}} + 1$ // update the No. of pending video frames
      $\mathbf{\Delta}_{\text{index}}(\Delta_{\text{length}}) = j$ // update the index of pending video frames
      $\mathbf{\Delta}_{\text{short}}(\Delta_{\text{length}}) = r_{\text{req}}^{(j)} - r_{\text{vlc}}^{(j)}$ // update the throughput deficit
    End If
  End For
  $[\bar{\mathbf{\Delta}}_{\text{short}} \ \bar{\mathbf{\Delta}}_{\text{index}}] = \text{sort}(\mathbf{\Delta}_{\text{short}})$ // sort the throughput deficit ascendingly and record indices
  For $j = 1 : \Delta_{\text{length}}$ // check all hold and buffered video frames
    If $R_{\text{sur}} \geq \bar{\mathbf{\Delta}}_{\text{short}}^{(j)}$ // associated deficit of the jth video frame could be compensated
      $\theta^{(j)} = 0$ // transmit the video frame
      $R_{\text{sur}} = R_{\text{sur}} - \bar{\mathbf{\Delta}}_{\text{short}}^{(j)}$ // update the deficit
    Otherwise
      Terminate For Loop // drop the rest of video frames
    End If
  End For
End If

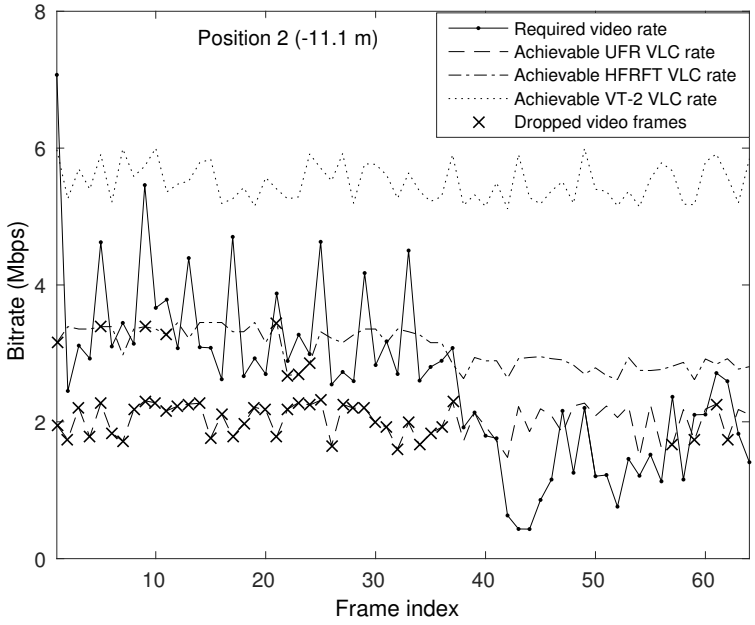

Figure 3.10: The required video rate before frame dropping (dotted solid line) and the achievable VLC rate under the three different transmission schemes of UFR, HFRFT and VT-2 in the indoor VLC system, when the MT is at Position 2 (-11.1 [m]) of Fig. 3.8b. The maximum optical transmit power is $P_{\mathrm{t,o}}^{\max}$ = 7.0 [W] and FOV = 60°, while the estimation window length is n_{f} = 4 video frame duration. The 'Football' video clip is encoded by the H.265 codec associated with the length of 8 GOPs = 64 video frames is transmitted to this MT, where the GOP is set to 8 video frames. The curves displays the achievable VLC rate that system could provide, and the the dropped-frames' indices are denoted by the markers. The schematic of Fig. 3.6 and the parameters of Table 3.3 are used.

VLC rate, then some of the video frames have to be dropped. The indices of the dropped video frames are selected from the algorithm Table 3.4, which is constructed based on Eq. (3.23) and (3.27). When the achievable VLC rate experienced during a specific video frame is lower than the required video rate, but 'throughput deficit' is sufficiently low to be compensated during frame 38, this specific video frame is transmitted. By contrast, when the 'throughput deficit' is within the current optimisation window, as exemplified too high to be compensated by the rest of the frames in this optimisation window by the low rate of the future frames, as exemplified by frame 37, including the video frame will result in an overall achievable rate, which is lower than the sum of required video rates. Hence this video frame has to be dropped. As a result, observe in Fig. 3.10 that as many as 41 video frames of the UFR scheme are discarded.

To elaborate a little furhter, the performance of the three schemes at Position 3 is characterised in Fig. 3.11, where we may observe that the achievable VLC rate of the VT-2 scheme remains almost unchanged. By contrast, the achievable VLC rate of the UFR and HFRFT schemes is further degraded compared to their performance at Position 2 of Fig. 3.10, which is due to the

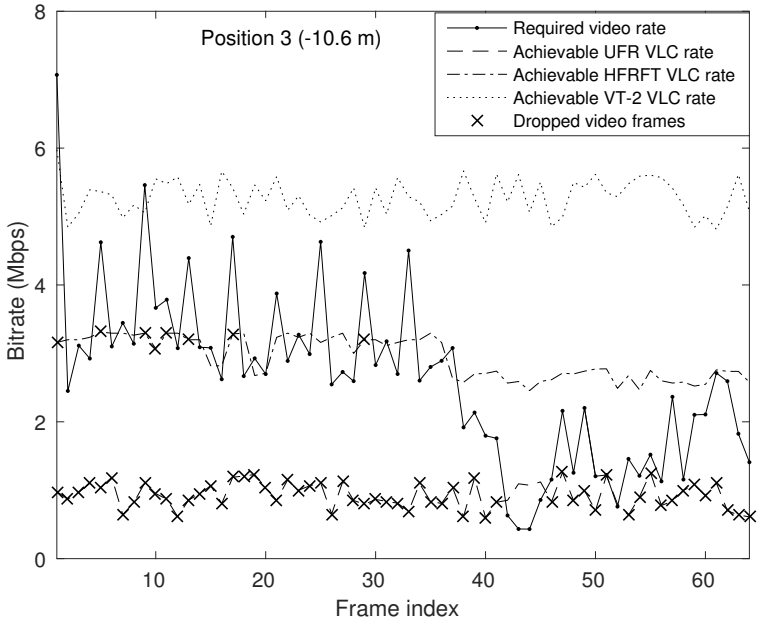

Figure 3.11: The required video rate before frame dropping (dotted solid line) and the achievable VLC rate under the three different transmission schemes of UFR, HFRFT and VT-2 in the indoor VLC system, when the MT is at Position 3 (-10.6 [m]) of Fig. 3.8b. The maximum optical transmit power is $P_{\mathrm{t,o}}^{\max}$ = 7.0 [W] and FOV = 60°, while the estimation window length is n_{f} = 4 video frame duration. The 'Football' video clip is encoded by the H.265 codec associated with the length of 8 GOPs = 64 video frames is transmitted to this MT, where the GOP is set to 8 video frames. The curves displays the achievable VLC rate that system could provide, and the the dropped-frames' indices are denoted by the markers. The schematic of Fig. 3.6 and the parameters of Table 3.3 are used.

further degraded channel condition, seen in Fig. 3.8b. Then the achievable VLC rate of the UFR and HFRFT schemes is no longer capable of transmitting all the video frames at the Position 3 of Fig. 3.8b. As a result, 8 video frames of the HFRFT scheme are discarded at this position. The most serious video degradation occurs in the UFR scheme, since almost all of the 64-video frames are dropped. The performance of the three schemes is further degraded, when the MT moves to Position 4 of Fig. 3.8b, even that of the VT-2 scheme. Hence, even the VT-2 scheme starts to discard video frames. As we can see in Fig. 3.12, 5 video frames are dropped. In the UFR scheme the interference imposed by the adjacent attocell becomes as high as the derived signal itself. Hence, the achievable UFR VLC rate has been decreased to almost zero, therefore the system has to discard all the video frames. As a result, the PSNR degradation reaches a maximum of 26.35 [dB].

3.4.2.3 Random-Walk Scenario

Based on characterising the performance of the four featured positions of Fig. 3.8b in the room, let us now continue by considering the PSNR degradation of a particular MT in a set of 6 MTs moving

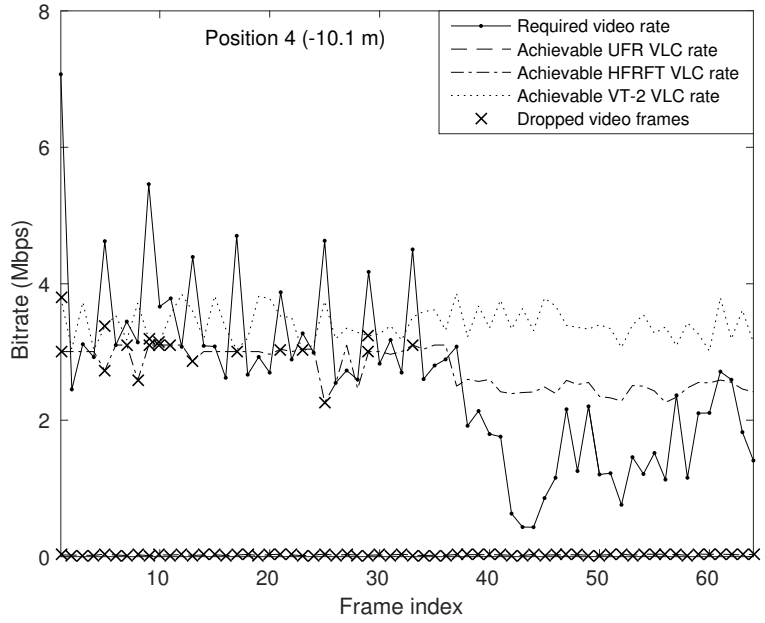

Figure 3.12: The required video rate before frame dropping (dotted solid line) and the achievable VLC rate under the three different transmission schemes of UFR, HFRFT and VT-2 in the indoor VLC system, when the MT is at Position 4 (-10.1 [m]) of Fig. 3.8b. The maximum optical transmit power is $P_{\mathrm{t,o}}^{\max}$ = 7.0 [W] and FOV = 60°, while the estimation window length is n_{f} = 4 video frame duration. The 'Football' video clip is encoded by the H.265 codec associated with the length of 8 GOPs = 64 video frames is transmitted to this MT, where the GOP is set to 8 video frames. The curves displays the achievable VLC rate that system could provide, and the the dropped-frames' indices are denoted by the markers. The schematic of Fig. 3.6 and the parameters of Table 3.3 are used.

around in the room randomly. Fig. 3.13 shows the frame-by-frame video PSNR degradation of a MT, where the movement trajectories of the MT in the UFR, HFRFT and the VT-2 schemes are identical. At this stage, we have to clarify the differences between the two different video distortion models, as we mentioned in the Sec. 3.3.1, which is:

- **The simulated distortion model**: The video distortion quantified in terms of the PSNR degradation is obtained from our simulation results using the simplified video model mentioned in Sec. 3.3.1.
- **The practical distortion model**: Given the frame dropping indices extracted from the above simulation results, we can readily calculate the PSNR degradation caused by the dropped frames.

More explicitly, the dashed line marked by the dots represents the video distortion in terms of the PSNR for each frame of the video stream using the simulation-based distortion model over the time duration of a 8-GOP = 8 × 8 = 64 video frame clip for our UFR, HFRFT and VT-2 transmis-

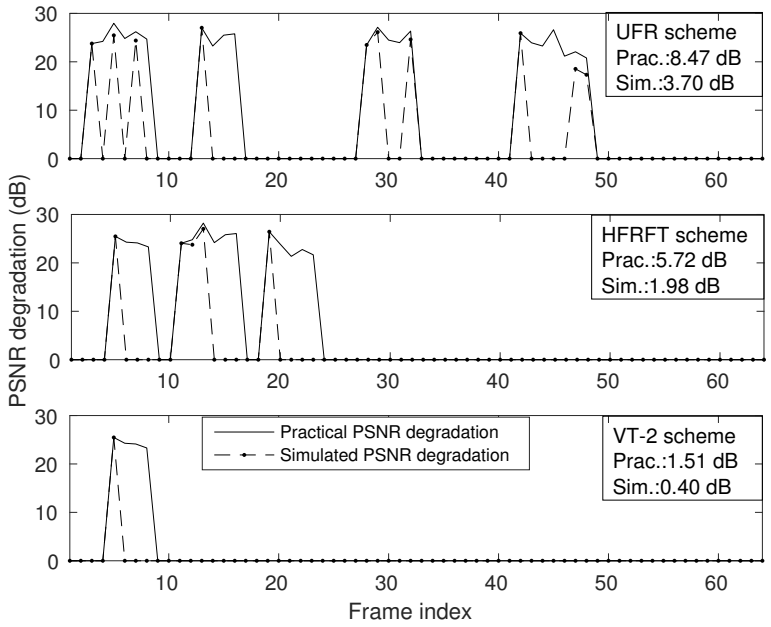

Figure 3.13: The PSNR degradation vs. video frame index for a single MT served under three different transmission schemes: UFR (top), HFRFT (middle) and VT-2 (bottom) in the indoor VLC system of Fig. 3.1. The maximum optical transmit power is $P_{\mathrm{t,o}}^{\max} = 7.0$ [W] and FOV = 60°, while the estimation window length is $n_{\mathrm{f}} = 4$ video frame duration. The 'Football' video clip is encoded by the H.265 codec associated with the length of 8 GOPs = 64 video frames is transmitted to this MT, where the GOP is set to 8 video frames. The curves displays the achievable VLC rate that system could provide, and the the dropped-frames' indices are denoted by the markers. The schematic of Fig. 3.6 and the parameters of Table 3.3 are used. In contrast to Fig. 3.9 - 3.12, where the MTs are stationary at Points 1 - 4, in this scenario the MTs move around randomly.

sion schemes. As seen in Fig. 3.13, the optimisation algorithm of Eq. (3.22) - (3.25) and Eq. (3.26) - (3.29) uses the parameters detailed in Table 3.3 for beneficially selecting the specific video frames, which may be discarded based on the constraints of Sec. 3.3.2. By contrast, in practice, the dropped frames also affect the following video frames in a GOP. Hence, the solid line seen in Fig. 3.13 without markers portrays the resultant PSNR degradation of the video clip using the practical distortion model of Sec. 3.4.2.3. A video frame dropped in the previous GOP does not affect the video quality in the current GOP. Observe in Fig. 3.13 that the more video frames are dropped, the higher the PSNR distortion of the video clip becomes. Explicitly, the PSNR degradation extracted from the simulations is seen to be lower than the practical video distortion. However, both methods we used for estimating the PSNR degradation are reasonable, demonstrating similar trends for the UFR, HFRFT and VT-2 transmission schemes. In conclusion, the PSNR degradations characterised in this chapter are adequately reflect the practical video distortion.

Figure 3.14: Five video frames of the 'Football' video test stream after video frame dropping, where the 4th, 8th, 12th, 16th and 20th video frames have been extracted from the original video stream (first row), UFR (second row), HFRFT (third row) and VT-2 (forth row) schemes, respectively. Observe with reference to the Fig. 3.13 that the UFR scheme imposes a PSNR degradation of 25 [dB] for the 4th video frame, which is similar to the HFRFT scheme, but a degradation of 0 [dB] is experienced to the VT-2 regime. Similar observation can be made at the remaining frame indices.

We may observe in Fig. 3.13 that some video frames discarded in the VT-2 scheme such as the 5th video frame, are also discarded in the UFR and HFRFT scheme, because the inferior channel conditions experienced by the MT in the VT-2 scheme are also experienced in the UFR and HFRFT schemes. In this situation, the resultant achievable VLC rate is too low for the transmission of the frame in the estimation optimisation window as seen for Position 4 in Fig. 3.12. Furthermore, we may notice that some of the video frames that are dropped in the UFR scheme are retailed in the HFRFT and VT-2 scheme, as exemplified by video frames 28, 29 and 32. This is because these video frames were scheduled for transmission in low-SINR zone of Fig. 3.13 in the UFR scheme, whilst at the same position in the HFRFT and VT-2 schemes, the SINR still remains sufficiently high for transmitting this video frame. Similar trends are also observed for Positions 2 and 3 as shown in Fig. 3.10 and 3.11. By contrast, some video frames, such as the 11th and 12th video frames are dropped in the HFRFT scheme, while the corresponding video frames are transmitted in the UFR and VT-2 schemes. This is because the channel conditions at these positions guarantee a sufficiently high achievable VLC rate in the UFR and the VT-2 schemes. By contrast, although

the achievable VLC rate of the HFRFT scheme at these positions is still relatively high, it remains insufficient for transmitting all the video frames of a specific estimation window, as exemplified by Position 1 in Fig. 3.9. More specifically, this situation occurs in the first half of the video clip, where the required video rate is consistently higher than in the second half. Moreover, we may observe that only a single video frame is discarded in the VT-2 scheme. Hence, the VT-2 scheme suffers from the lowest PSNR degradation and the discarded video frames have different indices compared to the other two schemes. This is because the VT-2 scheme jointly serves two MTs. Hence the video distortion is jointly affected by the channels of both MTs. Thus we may tentatively conclude that the VT-2 scheme has the best performance of the three in terms of mitigating the detrimental channel conditions. Based on Fig. 3.13, a simple example of the test video streaming after video frame dropping has been displayed in Fig. 3.14 for the UFR, HFRFT and VT-2 schemes, respectively. Observe with reference to the Fig. 3.13 that the UFR scheme imposes a PSNR degradation of 25 [dB] for the 4th video frame, which is similar to the HFRFT scheme, but a degradation of 0 [dB] is experienced to the VT-2 regime. Similar observation can be made at the remaining frame indices.

3.4.3 The Video Rate Achieved

3.4.3.1 The Video Rate Achieved of Fixed Position Scenario

Having discussed the PSNR degradation of a single MT, let us now investigate the attainable performance by investigating the achieved video rate of the three schemes at the four fixed positions seen in Fig. 3.8b, which are portrayed in Fig. 3.15 - Fig. 3.18.

We may observe from Fig. 3.15 - 3.18 that the actual achieved video rate is gradually reduced, as the MT moves from Position 1 to Position 4, which corresponds to the results we have shown in Fig. 3.9 - 3.12. More specifically, the final achieved video rate of the three transmission schemes at Position 1 is displayed in Fig. 3.15. We can see that since all the 64-video frames are transmitted, the achieved video rate of the three schemes remains identical to the original required video rate. When the MT moves to Position 2, we may observe that due to the dropped video frames of the UFR scheme, its achieved video rate at the corresponding frame indices of Fig. 3.10 becomes zero. By contrast, the achieved video rate of both the HFRFT as well as of the VT-2 schemes still remains identical to the required video rate. When the MT moves to Position 3 and Position 4, we observe that the achieved video rates are reduced. For example, for the UFR scheme at Position 4, the achieved video rate becomes zero, since the video could not be recovered at the receiver.

3.4.3.2 The Video Rate Achieved of Randomly Move Scenario

Having discussed the PSNR degradation and the achieved video rate of a single MT, let us now investigate the attainable performance from a multi-MT perspective by investigating the average

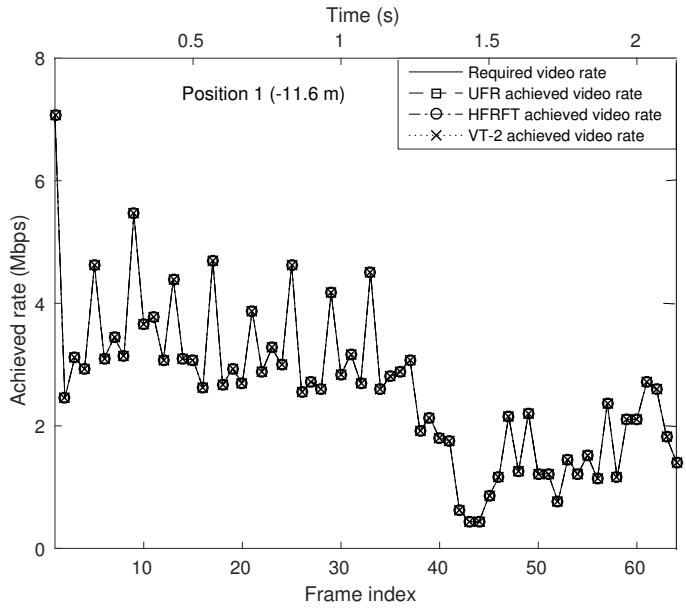

Figure 3.15: Achieved video rate vs. the video frame index under the three different transmission schemes of UFR, HFRFT and VT-2, when the MT is located at Position 1 (-11.6 [m]) of Fig. 3.8. The maximum optical transmit power is $P_{\mathrm{t,o}}^{\max} = 7.0$ [W] and FOV = 60°, while the estimation window length is $n_{\mathrm{f}} = 4$ video frame duration. The 'Football' video clip is encoded by the H.265 codec associated with 8 GOPs $\times$ 8 = 64 video frames transmitted to this MT. The schematic of Fig. 3.6 and the parameters of Table 3.3 are used.

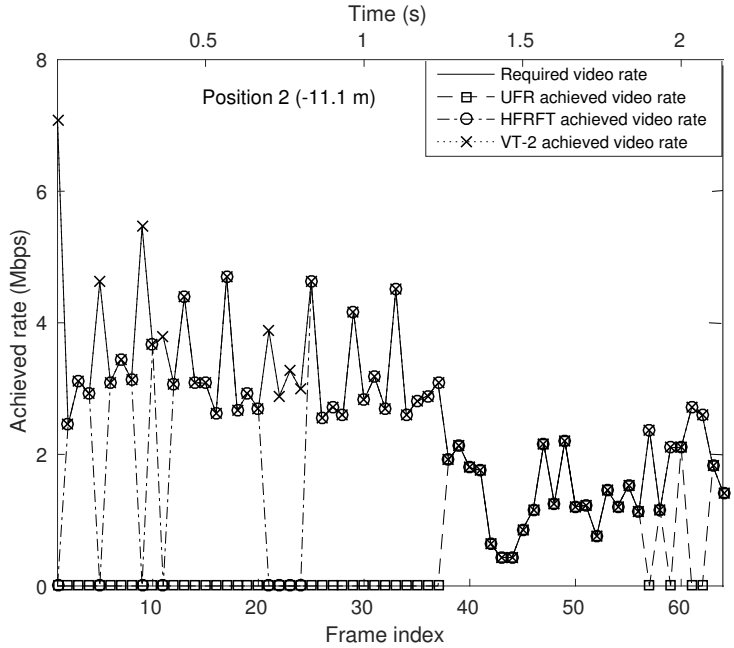

Figure 3.16: Achieved video rate vs. the video frame index under the three different transmission schemes of UFR, HFRFT and VT-2, when the MT is located at Position 2 (-11.1 [m]) of Fig. 3.8. The maximum optical transmit power is $P_{\mathrm{t,o}}^{\max} = 7.0$ [W] and FOV = 60°, while the estimation window length is $n_{\mathrm{f}} = 4$ video frame duration. The 'Football' video clip is encoded by the H.265 codec associated with 8 GOPs $\times$ 8 = 64 video frames transmitted to this MT. The schematic of Fig. 3.6 and the parameters of Table 3.3 are used.

performance of multiple MTs randomly moving in the room of Fig. 3.1. Fig. 3.19 portrays the average achieved rate of the reconstructed video for all the six MTs considered, where we calculate

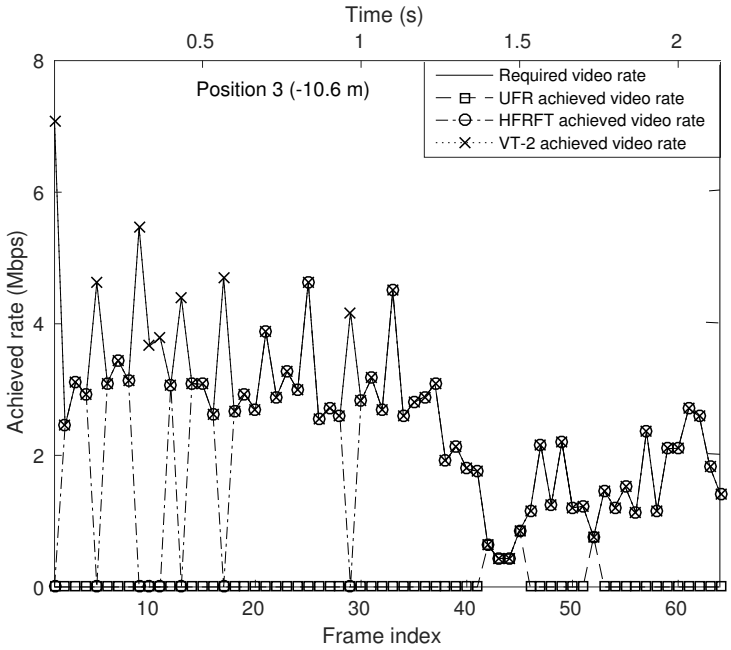

Figure 3.17: Achieved video rate vs. the video frame index under the three different transmission schemes of UFR, HFRFT and VT-2, when the MT is located at Position 3 (-10.6 [m]) of Fig. 3.8. The maximum optical transmit power is $P_{\mathrm{t,o}}^{\max} = 7.0$ [W] and FOV = 60°, while the estimation window length is $n_{\mathrm{f}} = 4$ video frame duration. The 'Football' video clip is encoded by the H.265 codec associated with 8 GOPs $\times$ 8 = 64 video frames transmitted to this MT. The schematic of Fig. 3.6 and the parameters of Table 3.3 are used.

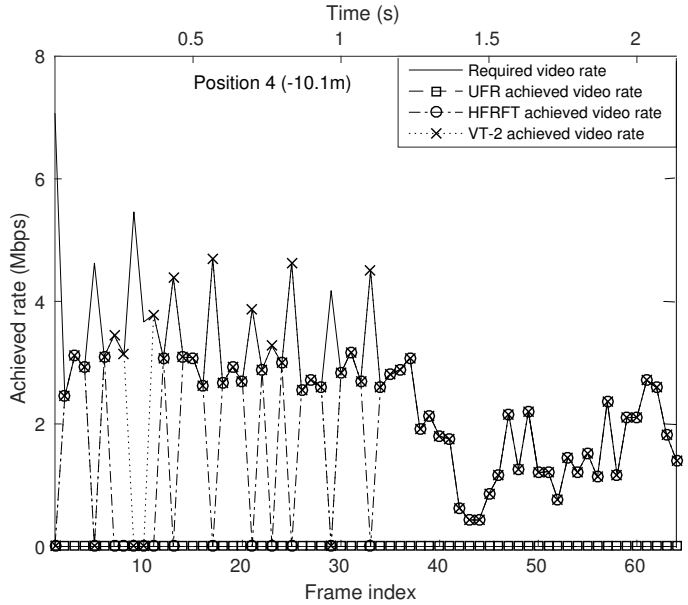

Figure 3.18: Achieved video rate vs. the video frame index under the three different transmission schemes of UFR, HFRFT and VT-2, when the MT is located at Position 4 (-10.1 [m]) of Fig. 3.8. The maximum optical transmit power is $P_{\mathrm{t,o}}^{\max} = 7.0$ [W] and FOV = 60°, while the estimation window length is $n_{\mathrm{f}} = 4$ video frame duration. The 'Football' video clip is encoded by the H.265 codec associated with 8 GOPs $\times$ 8 = 64 video frames transmitted to this MT. The schematic of Fig. 3.6 and the parameters of Table 3.3 are used.

the average achieved rate of each video frame deducting the bit rate requirements of the dropped video frames after video frame discarding in all three schemes. The original bit rate of the video

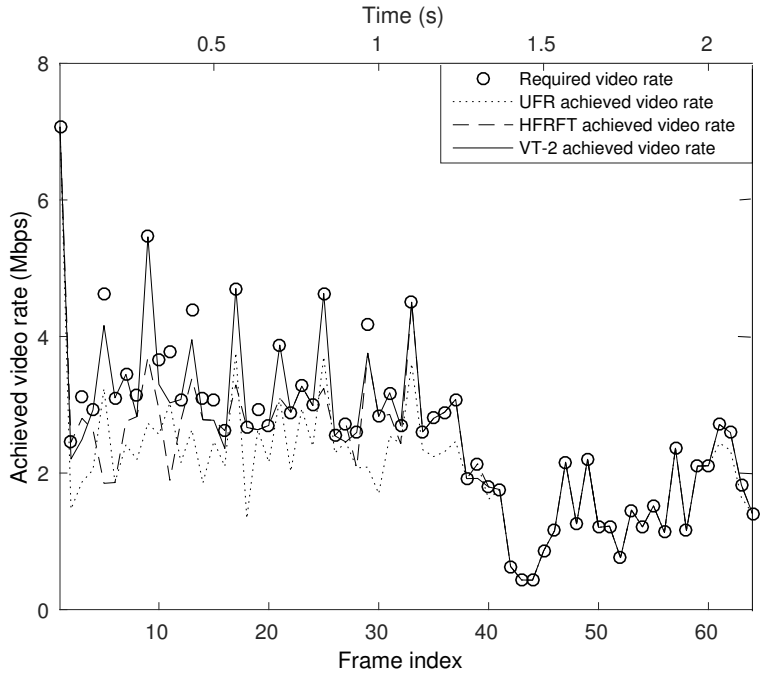

Figure 3.19: Average achieved rate of the system vs. the video frame index for all 6 MTs served under three different transmission schemes: UFR, HFRFT and VT-2 in the indoor VLC system of Fig. 3.1. The maximum optical transmit power is $P_{\mathrm{t,o}}^{\max}$ = 7.0 [W] and FOV = 60°, while the estimation window length is n_{f} = 4 video frames. The 'Football' video clip is encoded by the H.265 codec associated with the length of 8 GOPs $\times$ 8 = 64 video frames is transmitted to this MT. The schematic of Fig. 3.6 and the parameters of Table 3.3 are used.

stream before frame-discarding is also represented by the circle markers. Observe that the VT-2 scheme achieves the highest rate in all three transmission schemes, especially the achieved video rate at all the I frames. By contrast, observe in Fig. 3.19 that the SINR of the I frames in the UFR and the HFRFT schemes is relatively low, while the VT-2 scheme is capable of preserving the I frames to avoid excessively video quality degradations. Hence, the VT-2 system is capable of providing high quality video coverage in the indoor environment considered.

3.4.4 PSNR Distortion versus Delay

Let us now characterise the effects of the estimation window length n_{f}, which indicates the number of video frames we store in the streaming buffer before their transmission. Hence, the window length directly determines the system delay. In other words, the longer the estimation window, the higher the system delay becomes. Given the video scanning-rate of FPS = 30, in a delay sensitive system, we may opt for an estimation window length of n_{f} = 4, when the delay is 4/30 $\approx$ 0.13 seconds. However, if the system is capable of tolerating a longer streaming delay, we could employ a longer estimation window, such n_{f} = 8 and 16. Fig. 3.20 demonstrates the average PSNR

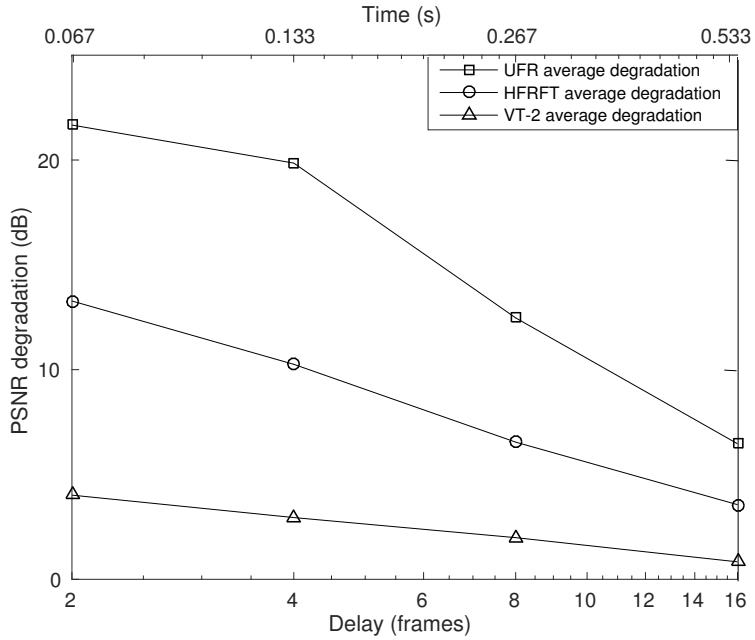

Figure 3.20: The average PSNR degradation vs. the delay in terms of the estimation window length of n_f = 2, 4, 8 and 16 averaged for all 6 MTs randomly moving in the room, served under our three different transmission schemes: UFR, HFRFT and VT-2 in the indoor VLC system of Fig. 3.1. The maximum optical transmit power is $P_{t,o}^{max}$ = 7.0 [W] and FOV = 60°. The 'Football' video clip is encoded by the H.265 codec associated with the length of 8 GOPs $\times$ 8 = 64 video frames is transmitted to this MT. The schematic of Fig. 3.6 and the parameters of Table 3.3 are used.

degradation vs. the delay quantified in terms of the estimation window length for all three different transmission schemes in our indoor VLC system. As expected, the average PSNR degradation is reduced for a longer estimation window. This is because a longer estimation window allows the system to buffer and hence average the required rate of more video frames at specific channel conditions. Hence, if the achievable VLC rate associated with a specific video frame is lower than the required video rate, this may still be compensated as a benefit of having a longer estimation window and vice versa. Furthermore, for longer estimation window lengths, the PSNR degradation difference among the schemes is also reduced. More specifically, when the estimation window length equals n_f = 2, the PSNR degradation difference among the UFR, HFRFT and VT-2 regimes is approximately 8 [dB]. However, when the window length is increased to n_f = 16, the difference becomes as low as 3 [dB]. This implies that for longer estimation windows the performance of the UFR and the HFRFT schemes might be able to approach the performance of the VT-2 scheme more closely at the cost of a longer system delay, which is suitable for non-real-time broadcasting, but not for lip-synchronised multimedia tele-conferencing.

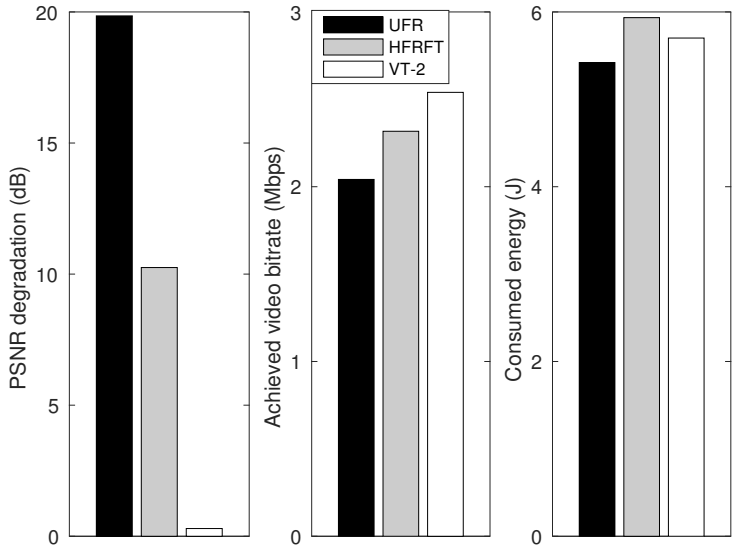

Figure 3.21: The average PSNR degradation (left), the achieved rate of the reconstructed video (middle) and the consumed energy (right) averaged for all 6 MTs served under three different transmission schemes: UFR (black), HFRFT (gray) and VT-2 (white) in the indoor VLC system of Fig. 3.1. The maximum optical transmit power is $P_{\mathrm{t,o}}^{\max} = 7.0$ [W] and FOV = 60°, while the estimation window length is $n_{\mathrm{f}} = 4$ video frames. The 'Football' video clip encoded by the H.265 codec associated with 8 GOPs $\times$ 8 = 64 video frames is transmitted to this MT. The schematic of Fig. 3.6 and the parameters of Table 3.3 are used.

3.4.5 Overall Statistics

Based on the results we have shown in Fig. 3.8 to Fig. 3.19, let us conclude with the evaluation of the average PSNR degradation, of the achievable rate and of the consumed energy in Fig. 3.21 using randomly move scheme. Based on the discussions on a specific MT, overall, the UFR scheme suffers from the highest PSNR degradation, the HFRFT scheme is slightly lower than that of the UFR scheme. However, both of these schemes are outperformed by the VT-2 scheme. In terms of the average achievable rate, we observe the same trends. Explicitly, the VT-2 scheme has the highest performance of the three. Recall from Fig. 3.19, the average achieved rate is almost 95% of that regime by the original video clip. By contrast, the achieved video rate of the UFR and of the HFRFT schemes is lower, but the latter performs better. In all of these results, we may observe that the VT-2 scheme has the best performance at the similar energy level to that of the HFRFT scheme. This implies that the VT-2 scheme intellectually allocates the transmit power and hence achieves an excellent PSNR performance.

3.5 Conclusions and Design Guideline

3.5.1 Conclusions

A novel video streaming optimisation framework was conceived for efficient video delivery in our VLC system. The performance of the UFR, HFRFT and VT-2 schemes was compared in terms of their PSNR degradation, consumed energy, system delay and achievable rate. We characterised the attainable performance of the MT at fixed positions and then quantified the average performance of the randomly moving MTs. Based on these studies we conclude that the proposed indoor VLC system is capable of supporting high-quality multimedia transmissions, and that the VT-2 scheme provides a significantly better performance than the UFR and HFRFT schemes.

3.5.2 Design Guideline

We improved the overall quality of video streaming systems in terms of striving a better compromise amongst the conflicting design constrains as the basic motivation of our designs. These effects leads to the design guideline listed below:

- Based on the characteristics of our indoor room model, we introduced three different transmission schemes, namely: UFR, HFRFT and VT-2.
- Dropping a video frame would result in the distortion of the video clip, we then extract a simple model and formulate two optimisation problems for these three transmission schemes, aiming at minimising the video distortion in terms of PSNR degradation.
- We commenced our study from evaluating the performance of the MT at specific positions and portrayed the PSNR degradation distribution of the room model. We then further exploit the random-walk based scenario for characterising the performance when the MT randomly move in the room.
- To study the achieved video rate, we firstly observed the achieved video rate in the fixed position based scenario and then extended it to the average performance relying on the random-walk based scenario.
- Due to the different video transmission requirements on delay, i.e. delay sensitive multimedia tele-conferencing and non-real-time broadcasting, we investigate the effect of delay on PSNR degradation in terms of the estimation window length.
- To demonstrate the average performance of the three transmission schemes in our indoor VLC system, we comprehensively investigate the PSNR degradation, achieved video rate and consumed energy by invoking the random-walk based scenario.

Chapter 4

PHY III: Analysis and Design of Colour-Shift Keying

4.1 Introduction

VLC relies on the abundant unlicensed bandwidth resources of the visible light frequency band. To minimise the risk of the impending capacity crunch imposed by the exponentially increased mobile data explosion, HetNet composed of multiple Radio Access Technologies (RAT), relying on diverse cellular architectures and adaptive transmission modes have been recognised as one of the most promising solutions. Hence the 5G wireless system is expected to rely on the HetNet philosophy [1, 240]. Amongst others, Millimetre Wave Communications (MWC) [241] and VLC [124,126,158,242–244] constitute two important complementary access technologies in addition to the development of traditional RATs along the LTE 'avenue' [245]. This is why VLC has attracted substantial research attention across both the academic and industrial community, whilst supporting the dual benefits of both communications and illumination [124, 126, 244].

In contrast to the more mature employment of LDs for outdoor communications [8], in indoor environments, LED may be used for conveying information by modulating the driver current at a sufficient high frequency [119, 132, 133, 243, 246], which is far beyond the fusion frequency of the human eye. In PHYsical layer III (PHY III) of the IEEE standard, the so-called CSK is introduced, when employing colour LEDs. To elaborate a little further, Drost and Sadler proposed a CSK constellation design using the so-called Billiards Algorithm of [247] and expanded their research to an arbitrary number of LEDs in [145], as a further development, Monterio and Hranilovic proposed another design by invoking the interior point method of [248,249], where optimised colour constellations were proposed. Furthermore, Singh *et al.* [250] conceived a novel QuadCSK arrangement by invoking four source lights. A multiuser CSK scheme was presented by Luna-Rivera *et al.* in [251], and finally, a system combined with CSK and PPM are proposed in [252]. Nonetheless,

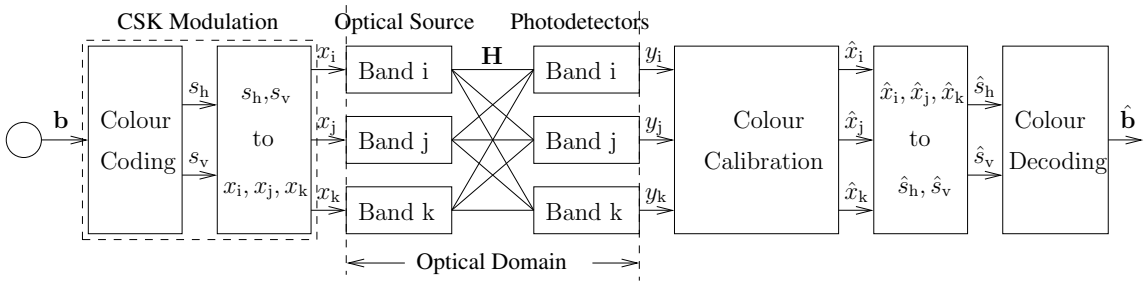

Figure 4.1: Transceiver architecture of M_{sym}-CSK using joint ML-based HD.

at the time of writing, there is a paucity of research on iterative CSK transceiver design, hence in this chapter we analyse the performance of the CSK system's colour constellation and design its bit-to-symbol mapping [146]. Our contributions are thus two-fold:

- We conceive the MAP-based SD of CSK and characterise its *extrinsic* mutual information improvement achieved by our iterative receiver with the aid of EXIT charts [217, 220, 253], of which the EXIT curve demonstrate modest slope.
- We characterise the performance-limitations of the IEEE standard's constellation labelling and we circumvent them by designing improved signal labelling strategies with the aid of EXIT charts [254]. As a result, we demonstrate that the power gain attained by this signal labelling improves the achievable transmission distance, and/or enhances the link's reliability in VLC applications.

4.2 CSK Modulation

The transceiver architecture of the uncoded M_{sym}-CSK modulation and detection scheme, which includes the colour calibration block invoked for mitigating the colour attenuation and interference during propagation as well as a number of other components to be detailed later are shown in Fig. 4.1. Let us first discuss how we map the bits b_1 and b_2 of the input vector $\mathbf{b}$ onto the 4-CSK colour constellation points of Fig. 4.2 representing the Commission Internationale de L'éclairage (CIE) 1931 colour plane as the information-carrying colours. The specific assignment of the pair of 4-CSK bits b_1 and b_2 to a particular wavelength is summarised in Table 4.1. In line with the CIE 1931 specifications [255], we have three information-carrying colours having a specific frequency, which are indicated by three circles in Fig. 4.2. Hence we can construct a triangle as the constellation plane for the CSK modulation. However, since we need four points for conveying a 2-bit symbol, the standard [4] recommends the point c_4 as the fourth one in Fig. 4.2.

To generalise our discussions, according to [4], the M_{sym}-ary colour coding scheme groups the $N_{\text{b}} = \log_2 M_{\text{sym}}$ consecutive incoming bits $\mathbf{b}$ into M_{sym}-ary CSK symbols mapped onto M_{sym}

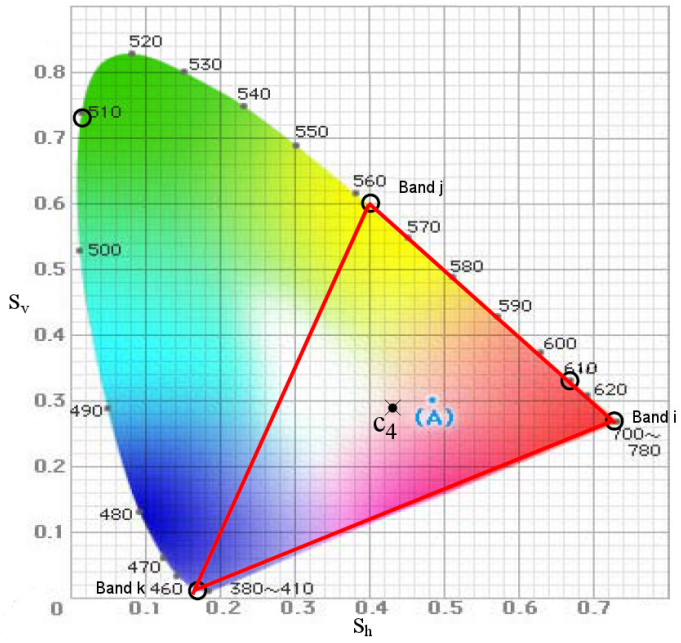

Figure 4.2: The CIE1931 colour plane for CSK modulation [256] © IEEE, where point (A) in the centroid of the triangle. The point c_4 and the three corner points represent four wavelength conveying 2 bits/symbol in 4-ary CSK.

Table 4.1: The information-carrying colours of 4-CSK modulation specified by the IEEE standard [4], where the constellation point c_4 is constituted by a weighted mixture of the red, yellow and blue colours.

Wavelength Band [nm]	Band	Centre [nm]	(s_h, s_v)	$b_1 b_2$	$[x_i, x_j, x_k]$
380 - 478	Band k	429	(0.169,0.007)	1 0	[0 0 1]
540 - 588	Band j	564	(0.402,0.597)	0 0	[0 1 0]
726 - 780	Band i	753	(0.734,0.265)	1 1	[1 0 0]
See caption	c_4	-	(0.435,0.290)	0 1	[0.333 0.333 0.333]

points of Fig. 4.2 in a two-dimensional colour plane. Having discussed the bit to colour-plane mapping, let us now return to the overall transceiver schematic of Fig. 4.1, which relies on the three colour bands, i.e wavelength of Fig. 4.2 and of Table 4.1, because the optical LED transmitters and PDs are readily available at these wavelengths. Explicitly, this $[b_1, b_2] \rightarrow (s_h, s_v)$ mapping takes place in the left-most block of Fig. 4.1. Then the resultant (s_h, s_v) components are mapped to the Red, Yellow and Blue (RYB) LED transmitters according to the mapping scheme of Table 4.1. Explicitly, for the corner points of the triangle seen in Fig. 4.2, only one of the RYB LEDs is activated, as also seen in Table 4.1, but for the point c_4, all of the RYB LEDs are activated according to the weights seen at the bottom right corner of Table 4.1. As expected, these weights add up to unity. In analogy to classic Frequency Shift Keying (FSK), which detects the energy at the output of the detection filters, here the PDs detect the different visible-light colours falling into the 400 -

800 [THz] band. This justifies the terminology of CSK. Observe in Fig. 4.1 that the optical channel is represented by the matrix $\mathbf{H}$. The optical signal received by the PDs is then input to the colour compensation block of Fig. 4.1, which again mitigates the colour-attenuation and interference.

4.2.1 Light Intensity Conversion

The two-dimensional colour coordinates $\mathbf{s}^{(n)} = (s_\mathrm{h}, s_\mathrm{v})$ of the symbols are generated by the intensity of the three light sources $\mathbf{x}^{(n)} = \left[x_\mathrm{i}, x_\mathrm{j}, x_\mathrm{k}\right]^\mathrm{T}$, which represents the power of the light source. We let $\boldsymbol{\mathcal{X}}$ denote the alphabet of the transmitted intensity vector $\mathbf{x}^{(n)}$ as shown in Table 4.1.

Example 1: For the 4-CSK modulation, given Band i, j and k of the CIE1931 colour plane of Fig. 4.2, the basic coordinates of the source colours RYB are $\mathbf{s}_{\mathrm{h,c}}$ = [R_h, Y_h, B_h] = [0.734, 0.402, 0.169], $\mathbf{s}_{\mathrm{v,c}}$ = [R_v, Y_v, B_v] = [0.265, 0.597, 0.007]. Then to generate the colour at the point c_4 $(s_\mathrm{h}, s_\mathrm{v}) = (0.435, 0.290)$ in Fig. 4.2, the intensity vector $\mathbf{x}^{(n)} = \left[x_\mathrm{i}, x_\mathrm{j}, x_\mathrm{k}\right]^\mathrm{T}$ is obtained by solving the following equation:

$$\begin{cases} 0.435 = 0.734x_\mathrm{i} + 0.402x_\mathrm{j} + 0.169x_\mathrm{k} \\ 0.290 = 0.265x_\mathrm{i} + 0.597x_\mathrm{j} + 0.007x_\mathrm{k} \\ x_\mathrm{i} + x_\mathrm{j} + x_\mathrm{k} = 1, \end{cases} \tag{4.1}$$

where the resultant intensity vector becomes $\mathbf{x}^{(n)} = \left[x_\mathrm{i}, x_\mathrm{j}, x_\mathrm{k}\right]^\mathrm{T}$ = [0.333049 0.334023 0.332928]. The intensity vector of other colour constellation points may be obtained in the same way, which has also been listed in Table 4.1.

Example 2: For the 16-CSK modulation, the basic coordinates of the source colours RYB for Band i, j and k are still $\mathbf{s}_{\mathrm{h,c}}$ = [R_h, Y_h, B_h] = [0.734, 0.402, 0.169], $\mathbf{s}_{\mathrm{v,c}}$ = [R_v, Y_v, B_v] = [0.265, 0.597, 0.007]. The constellation points of 16-CSK modulation on the CIE 1931 colour plane are shown in Fig. 4.3, which are represented by the two-component colour coordinates and three-component intensity vectorss, as listed in Table 4.2. For example, the two-component coordinates of point c_{11} are represented by $(s_\mathrm{h}, s_\mathrm{v}) = (0.446, 0.187)$ in Fig. 4.3, which the intensity vector $\mathbf{x}^{(n)} = \left[x_\mathrm{i}, x_\mathrm{j}, x_\mathrm{k}\right]^\mathrm{T}$ is obtained by

$$\begin{cases} 0.446 = 0.734x_\mathrm{i} + 0.402x_\mathrm{j} + 0.169x_\mathrm{k} \\ 0.187 = 0.265x_\mathrm{i} + 0.597x_\mathrm{j} + 0.007x_\mathrm{k} \\ x_\mathrm{i} + x_\mathrm{j} + x_\mathrm{k} = 1. \end{cases} \tag{4.2}$$

Hence, the resultant intensity vector becomes $\mathbf{x}^{(n)} = \left[x_\mathrm{i}, x_\mathrm{j}, x_\mathrm{k}\right]^\mathrm{T}$ = [0.445, 0.444, 0.111], as shown in Table 4.2.

Hence to summarise, the conversion of two-dimensional colour coordinates $(s_\mathrm{h}, s_\mathrm{v})$ of the symbol to the three-dimensional optical signal intensity $\left[x_\mathrm{i}, x_\mathrm{j}, x_\mathrm{k}\right]^\mathrm{T}$ is achieved by simultaneously

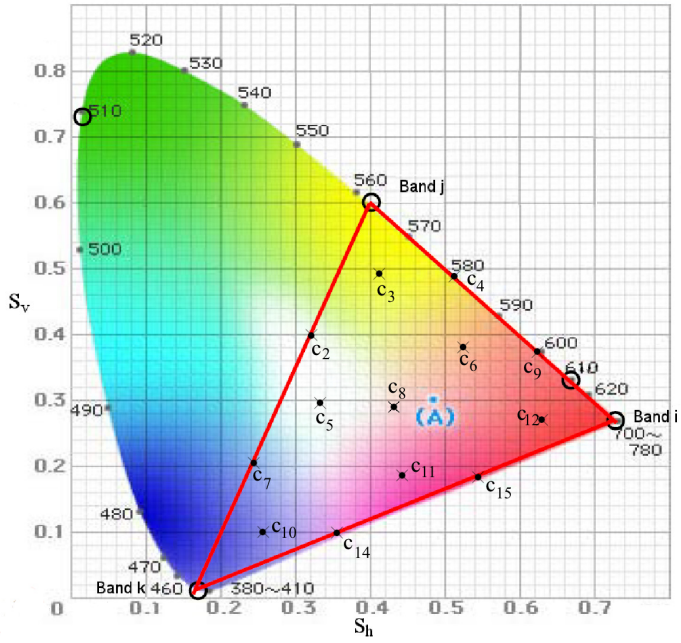

Figure 4.3: The CIE1931 colour plane for CSK modulation [256] © IEEE, where point (A) in the centroid of the triangle. The point c_2 - c_{15} and the three corner points represent sixteen wavelength conveying 4 bits/symbol in 16-ary CSK.

solving a simple system of three equations, which is given by

$$\begin{cases} s_{\mathrm{h}} = \mathbf{s}_{\mathrm{h,c}}^{\mathrm{T}}\mathbf{x} \\ s_{\mathrm{v}} = \mathbf{s}_{\mathrm{v,c}}^{\mathrm{T}}\mathbf{x} \\ \sum \mathbf{x} = I_{\mathrm{mat}} \end{cases}. \tag{4.3}$$

Here we define the coordinate-vector of the three light sources as $\mathbf{s}_{\mathrm{h,c}} = \left[s_{\mathrm{h,i}}, s_{\mathrm{h,j}}, s_{\mathrm{h,k}}\right]^{\mathrm{T}}$ and $\mathbf{s}_{\mathrm{v,c}} = \left[s_{\mathrm{v,i}}, s_{\mathrm{v,j}}, s_{\mathrm{v,k}}\right]^{\mathrm{T}}$ [4]. Thus the entire CSK modulation process may be interpreted as a one-to-one mapping function.

4.2.2 Colour Constellation Points

With the given triangle for colour constellation plane, let us characterise the colour constellation points on this plane. The colour constellations[1] of 4-CSK, 8-CSK and 16-CSK proposed in IEEE standard [4] are displayed in Fig. 4.4, where the above-mentioned colour coordinates represent the specific locations of the CSK symbols (marked by $c_{\tau,\tau=1,\cdots M_{\mathrm{sym}}}$). The operating light-intensity is normalised to unity. Since CSK operates at a fixed intensity, a constraint is imposed on the maximum output light intensity [247]. Furthermore, for the sake of fixing the perceived colour, we

[1]The constellation is a collection of colour coordinates, defined by the international commission on illumination in CIE 1931 colour space of [255], where each location corresponds to a colour with a specific wavelength, as perceived by the human eye. The location of constellation points may be on the edge, the vertices or within a triangle where the vertices represent the optical light sources, as detailed in [256].

Table 4.2: The information-carrying colours of 16-CSK modulation specified by the IEEE standard [4], where the constellation points c_2 - c_{15} are constituted by the weighted mixture of the red, yellow and blue colours.

Wavelength Band [nm]	Band	Centre [nm]	(s_h, s_v)	$b_1 b_2$	$[x_i, x_j, x_k]$
380 - 478	Band k	429	(0.169,0.007)	1 0 0 1	[0 0 1]
540 - 588	Band j	564	(0.402,0.597)	0 0 0 0	[0 1 0]
726 - 780	Band i	753	(0.734,0.265)	1 0 0 0	[1 0 0]
-	c_2	-	(0.324,0.400)	0 1 1 0	[0.333 0.334 0.332]
-	c_3	-	(0.413,0.495)	0 0 0 1	[0.111 0.779 0.115]
-	c_4	-	(0.513,0.486)	0 1 0 1	[0.334 0.666 0]
-	c_5	-	(0.335,0.298)	0 0 1 0	[0.110 0.445 0.445]
-	c_6	-	(0.524,0.384)	0 1 1 1	[0.445 0.444 0.111]
-	c_7	-	(0.247,0.204)	1 0 1 0	[0.0004 0.334 0.6656]
-	c_8	-	(0.435,0.290)	0 1 1 0	[0.333 0.334 0.333]
-	c_9	-	(0.623,0.376)	0 1 0 0	[0.666 0.334 0]
-	c_{10}	-	(0.258,0.101)	1 0 1 1	[0.112 0.110 0.777]
-	c_{11}	-	(0.446,0.187)	1 1 1 0	[0.445 0.111 0.445]
-	c_{12}	-	(0.634,0.273)	1 1 0 1	[0.777 0.111 0.112]
-	c_{14}	-	(0.357,0.093)	1 1 1 1	[0.3327 0.0003 0.667]
-	c_{15}	-	(0.546,0.179)	1 1 0 0	[0.667 0 0.333]

impose an average colour constraint on the CSK symbols for the colour as follows [248],

$$\sum_n \omega_{\text{avg}}^{(n)} \mathbf{x}^{(n)} = \mathcal{C}_{\text{avg}} \,, \tag{4.4}$$

where $\omega_{\text{avg}}^{(n)}$ is the probability of $\mathbf{x}^{(n)}$, and $\mathcal{C}_{\text{avg}}$ is a vector representing the average perceived colour of the transmitted light, which is known as *colour balance*. To elaborate a little further, there are a pair of two-dimensional colour constellations are discussed in this Chapter. Specifically, in *Type I* the colour constellation obeys the IEEE standard of [4], while in *Type II* we rely on a colour-balanced constellation [249] displayed in Fig. 4.5, where $\mathcal{C}_{\text{avg}}$ represents a specific perceived colour. In this chapter, we employed a White Balanced (WB) colour constellation.

The 8-CSK and 16-CSK *Type I* colour constellations are portrayed in Fig. 4.4 (b) and (c). By contrast, in Fig. 4.5(a) and (b), the 8-CSK and 16-CSK *Type II* colour constellations maintaining WB [247, 248] are presented. Owing to the constellation simplicity of 4-CSK the standard colour constellation automatically retains the WB property. Having considered these two types of constellations, the bits $\mathbf{b}$ are mapped to the corresponding colour coordinates according to the signal labelling strategy of $\mu^l(\mathbf{b}) \rightarrow (s_h, s_v)$, where l denotes the l^{th} possible signal labelling strategy of all possible candidates, μ represents the mapping criterion and our specific signal labelling design will be detailed in Sec. 4.5.1.

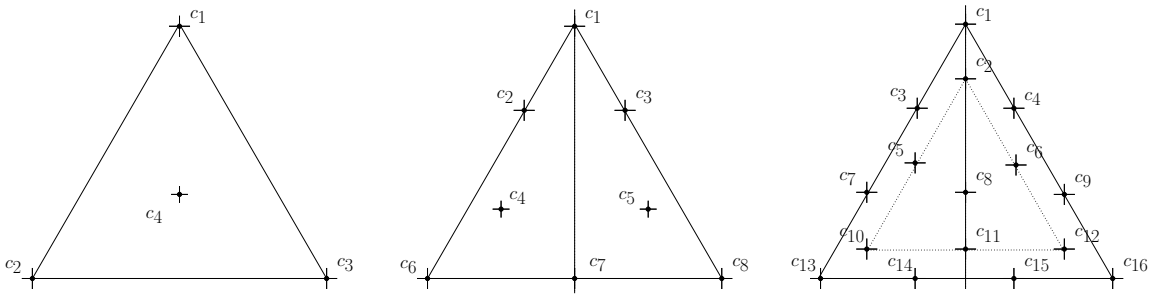

(a). 4 - CSK *Type I* (b). 8 - CSK *Type I* (c). 16 - CSK *Type I*

Figure 4.4: Colour constellation of 4-CSK 8-CSK and 16-CSK specified by the IEEE standard [4], and used in the schematic of Fig. 4.1, where the operating intensity is normalised to 1.

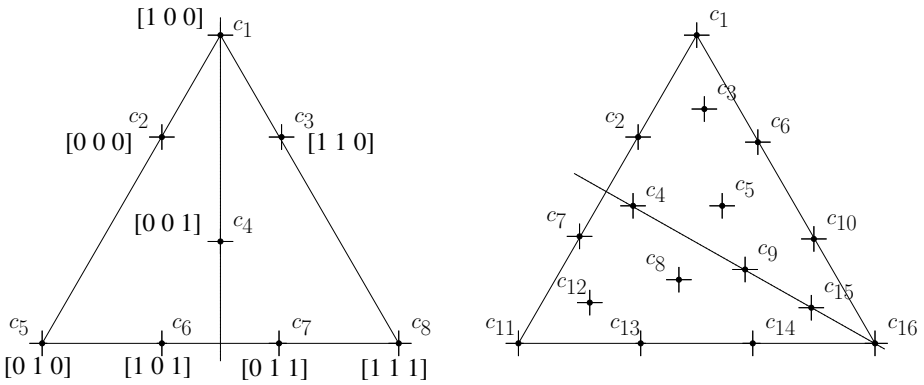

(a). 8 - CSK *Type II*, *White balance* (b). 16 - CSK *Type II*, *White balance*

Figure 4.5: Colour constellation of 8-CSK and 16-CSK with WB constraints proposed in [249], the details of Fig. 4.5(a) will be further explained. These constellations are used in the schematic of Fig. 4.1.

4.2.3 Optical Domain Propagation

In this chapter, we consider a point-to-point transmission system, where the optical signal intensities $\{x_{\mathrm{i}}, x_{\mathrm{j}}, x_{\mathrm{k}}\}$ of the three light bands $\{\mathrm{i}, \mathrm{j}, \mathrm{k}\}$ emitted from the M_{sym}-CSK modulator block of Fig. 4.1 propagate through an optical channel. At the receiver, a dedicated PD corresponding to each of the three light bands is used for converting the received colour component into their electronic representations. Explicitly, the output $\mathbf{y}$ is a distorted and noise-contaminated intensity vector of the colour light bands formulated as:

$$\mathbf{y} = \mathbf{H}\mathbf{x} + \mathbf{v}. \tag{4.5}$$

The optical channel is subjected to potential colour-band interference, hence $\mathbf{H}$ is a (3×3)-element matrix,

$$\boldsymbol{H} = \begin{bmatrix} H_{\mathrm{ii}} & H_{\mathrm{ij}} & H_{\mathrm{ik}} \\ H_{\mathrm{ji}} & H_{\mathrm{jj}} & H_{\mathrm{jk}} \\ H_{\mathrm{ki}} & H_{\mathrm{kj}} & H_{\mathrm{kk}} \end{bmatrix}, \tag{4.6}$$

with each element of the matrix represents the channel gain from one colour band to another, where the diagonal entries of $\mathbf{H}$ represent the channel gain of the corresponding band, while the other entries host the interference imposed by the other bands. As pointed out in [251], other propagation factors such as diffuse multipath, dispersion and the none-LOS components, should also be considered in the future, but again, 90% of the received power is concentrated in the LOS component, whilst the contribution of the power received from reflections is small enough to be neglected. Therefore, in this chapter, we would only consider Inter-Band Interference (IBI), which is the main source of interference contributed by the light leaking from the adjacent colour bands. Based on these discussions, the channel model may be formulated as

$$\mathbf{H} = \begin{bmatrix} 1-\varepsilon_0 & \varepsilon_0 & 0 \\ \varepsilon_0 & 1-2\varepsilon_0 & \varepsilon_0 \\ 0 & \varepsilon_0 & 1-\varepsilon_0 \end{bmatrix}, \tag{4.7}$$

where we assume that the channel matrix is normalised, and let ε_0 represent the IBI quantified in terms of percentage. In ideal conditions, when there is no IBI, the channel matrix may be assumed to be an identity matrix, and the entire system experiences an ideal AWGN channel.

Furthermore, $\mathbf{v}$ represents the noise imposed in the electronic domain at the receiver, given the total electronic domain noise power at the receiver is σ^2, and assume the noise is uniformly added on each colour band, then at each entry of $\mathbf{v}$, we have the added noise with a zero mean and a variance of $\sigma_0^2 = \sigma^2/3$, where we define the received electronic SNR $\gamma_{\mathrm{e}} = 1/\sigma^2$. Thus we have $E_{\mathrm{b_{elec.}}}/N_0 = 1/(N_{\mathrm{b}}\sigma_0^2)$, and we may also conveniently define the optical SNR as $\gamma_{\mathrm{o}} = \rho_{\mathrm{c}}\gamma_{\mathrm{e}}$, where $\rho_{\mathrm{c}} = \sigma\mathbb{E}\left\{\|\mathbf{x}\|\right\}/\mathbb{E}\left\{\|\mathbf{x}\|^2\right\}$.

4.3 Detection Schemes

According to different system requirement, different detection scheme will be elaborated in this section. Generally, two detection schemes are involved, joint ML-based HD and joint MAP-based SD with iterative receiver.

4.3.1 Joint ML-Based CSK HD

In practice, all the above-mentioned detrimental channel effects can be mitigated by the RGB compensation block of Fig. 4.1 for the sake of retrieving the transmitted optical intensities[2]. When we assume perfect CSI at the receiver, the estimated intensity vector $\tilde{\mathbf{x}}$ is obtained by the joint ML-based HD of the three colours. When an order value of M_{sym} = 4, 8, 16 are considered, the full-search-based joint ML detection complexity remains moderate and the estimated intensity vector may then be expressed as

$$\hat{\mathbf{x}} = \arg\min_{\tilde{\mathbf{x}} \in \boldsymbol{\mathcal{X}}} \|\mathbf{y} - \mathbf{H}\tilde{\mathbf{x}}\|^2, \tag{4.8}$$

which implies that the estimated intensity vector $\hat{\mathbf{x}}$ is given by that specific legitimate intensity vector $\tilde{\mathbf{x}} \in \boldsymbol{\mathcal{X}}$, which exhibits the lowest distance between $\mathbf{y}$ and $\mathbf{H}\tilde{\mathbf{x}}$. The estimated intensity vector $\hat{\mathbf{x}}$ is then finally converted back to the resultant bits. Considering colour band combination [110, 010, 000] as an example, the alphabet of intensity vectors $\boldsymbol{\mathcal{X}}$ of 4, 8 and 16-CSK in the standard [4] are listed in Table 4.1, 4.3 and 4.4

Table 4.3: Alphabet of intensity vectors $\boldsymbol{\mathcal{X}}$ of the 8-CSK system, using the colour combination band [110,010,000] [4]

	$(s_{\text{h}}, s_{\text{v}})$	x_{i}	x_{j}	x_{k}
0 0 0	(0.324 0.597)	0	0.6663	0.3337
0 0 1	(0.297 0.200)	0.111817	0.278225	0.609969
0 1 0	(0.597 0.329)	0.610732	0.278697	0.110571
0 1 1	(0.452 0.136)	0.501	0.499	0
1 0 0	(0.402 0.597)	0	1	0
1 0 1	(0.169 0.007)	0	0	1
1 1 0	(0.513 0.486)	0.334337	0.665663	0
1 1 1	(0.734 0.265)	1	0	0

4.3.2 Performance Analysis of CSK

With the joint ML-based HD results, let us now characterise the analytical performance of CSK. Here we compare two analysis methods, decoupled method and union-bound based approach described as below.

[2]Note that, we implicitly assumed here lossless conversion from the electronic domain to the optical domain at the transmitter and from the optical domain to the electronic domain at the receiver. Hence we may use the optical signal intensity and electronic signal amplitude interchangeable.

Table 4.4: Alphabet of intensity vectors $\boldsymbol{\mathcal{X}}$ of the 16-CSK system, using the colour combination band [110,010,000] [4]

	$(s_{\mathrm{h}}, s_{\mathrm{v}})$	x_{i}	x_{j}	x_{k}
0 0 0 0	(0.402 0.597)	0	1	0
0 0 0 1	(0.413 0.495)	0.110732	0.778697	0.115071
0 0 1 0	(0.335 0.298)	0.110297	0.444989	0.444714
0 0 1 1	(0.324 0.400)	0	0.6663	0.3337
0 1 0 0	(0.623 0.376)	0.665663	0.334337	0
0 1 0 1	(0.513 0.486)	0.334337	0.665663	0
0 1 1 0	(0.435 0.290)	0.333094	0.334023	0.332928
0 1 1 1	(0.524 0.384)	0.445069	0.444346	0.110571
1 0 0 0	(0.734 0.265)	1	0	0
1 0 0 1	(0.169 0.007)	0	0	1
1 0 1 0	(0.247 0.204)	0.000436	0.333708	0.665857
1 0 1 1	(0.258 0.101)	0.112020	0.110337	0.777643
1 1 0 0	(0.546 0.179)	0.667300	0	0.332700
1 1 0 1	(0.634 0.273)	0.777248	0.110996	0.111786
1 1 1 0	(0.446 0.187)	0.444634	0.110652	0.444714
1 1 1 1	(0.357 0.093)	0.332616	0.000315	0.667072

4.3.2.1 Decoupled Analysis

In [257], the analytical performance of CSK was characterised based on an implicitly assumed separate treatment of the i, j, k light bands. More explicitly, let us denote the optical light intensity of the fth light band by x_f, where $f = \mathrm{i}, \mathrm{j}, \mathrm{k}$. We also let $\boldsymbol{\mathcal{X}}_f = [x_f^{(1)}, \ldots, x_f^{(\iota)}, \ldots, x_f^{(|\boldsymbol{\mathcal{X}}_f|)}]$ represent the corresponding alphabet of the fth optical light intensity, where we have the relationship of $\boldsymbol{\mathcal{X}} << \prod_f \mathcal{X}_f$. For example, as seen in Table 4.1, we have $\mathcal{X}_i = [0, 0.333049, 1]$. Let $x_f^{(\iota)}$ denote the ιth intensity level transmitted through the fth light band, while assuming that the alphabet of $\mathcal{X}_f$ is an equi-probable PAM constellation. Then assume in AWGN channel, the probability of error P_{e} of $x_f^{(\iota)}$ is given by [257]

$$P_{\mathrm{e}}(x_f^{(\iota)}) = Pr\left[v_f > \frac{x_f^{(\iota+1)} - x_f^{(\iota)}}{2}\right] + Pr\left[v_f < \frac{x_f^{(\iota)} - x_f^{(\iota-1)}}{2}\right], \tag{4.9}$$

where Pr denotes the probability and v_f is the AWGN imposed on the fth light band. Eq. (4.9) may thus be reformulated as

$$P_{\mathrm{e}}(x_f^{(\iota)}) = \mathcal{Q}\left[\frac{x_f^{(\iota+1)} - x_f^{(\iota)}}{2}\sqrt{\gamma_o}\right] + \mathcal{Q}\left[\frac{x_f^{(\iota-1)} - x_f^{(\iota)}}{2}\sqrt{\gamma_o}\right]. \tag{4.10}$$

Note however that for $x_f^{(1)}$ and $x_f^{(|\boldsymbol{\mathcal{X}}_f|)}$ at the two extreme values of the alphabet $\boldsymbol{\mathcal{X}}_f$, we have $P_{\mathrm{e}}(x_f^{(1)})$ and $P_{\mathrm{e}}(x_f^{(|\boldsymbol{\mathcal{X}}_f|)})$ values, which are equal to the first half and the second half of Eq. (4.10) respectively, since decision errors can only occur in one direction. Hence, the average probability of error for the fth light band is given by [257]

$$P_{\mathrm{e}}(x_f) = \frac{1}{M_{\mathrm{sym}}}\sum_{\iota=1}^{|\boldsymbol{\mathcal{X}}_f|} P_{\mathrm{e}}(x_f^{(\iota)}), \tag{4.11}$$

where we assume an equal probability of occurrence for $x_f^{(m)}, \iota = 1, \ldots, |\mathcal{X}_f|$ of the fth light intensity. Assuming furthermore the independence of the three light bands, the overall probability of bit error may be written as

$$P_{\mathrm{e,decoupled}} = [1 - (1 - P_{\mathrm{e}}(x_{\mathrm{i}}))(1 - P_{\mathrm{e}}(x_{\mathrm{j}}))(1 - P_{\mathrm{e}}(x_{\mathrm{k}}))]/N_{\mathrm{b}}. \tag{4.12}$$

4.3.2.2 Union Bound Approach

Let us now characterise the analytical performance of our joint ML-based HD by the union-bound based approach for deriving an upper bound, which may be deemed tight at high SNRs, where the average bit error probability may be written as [258]

$$P_{\mathrm{e,union}} \leq \frac{1}{M_{\mathrm{sym}}N_{\mathrm{b}}}\sum_{\zeta=1}^{M_{\mathrm{sym}}}\sum_{\iota=1,\iota\neq\zeta}^{M_{\mathrm{sym}}} d_{\mathrm{Ham}}(\tilde{\mathbf{x}}^{(\zeta)}, \tilde{\mathbf{x}}^{(\iota)}) Pr(\tilde{\mathbf{x}}^{(\zeta)} \mapsto \tilde{\mathbf{x}}^{(\iota)}), \tag{4.13}$$

with $d_{\mathrm{Ham}}(\tilde{\mathbf{x}}^{(\zeta)}, \tilde{\mathbf{x}}^{(\iota)})$ representing the Hamming distance of the legitimate intensity vectors $\tilde{\mathbf{x}}^{(\zeta)}$ and $\tilde{\mathbf{x}}^{(\iota)}$. Furthermore, $Pr(\tilde{\mathbf{s}}^{(\zeta)} \mapsto \tilde{\mathbf{s}}^{(\iota)})$ denotes the Pairwise Error Probability (PEP) of these legitimate intensity vectors, which is given by [258]

$$\begin{aligned} Pr(\tilde{\mathbf{x}}^{(\zeta)} \mapsto \tilde{\mathbf{x}}^{(\iota)}) &= Pr\left[||\mathbf{y} - \mathbf{H}\tilde{\mathbf{x}}^{(\zeta)}||^2 > ||\mathbf{y} - \mathbf{H}\tilde{\mathbf{x}}^{(\iota)}||^2\right] \\ &= Pr\left[||\mathbf{H}\tilde{\mathbf{x}}^{(\zeta)}||^2/2 - \mathbf{y}^{\mathrm{T}}\mathbf{H}\tilde{\mathbf{x}}^{(\zeta)} > ||\mathbf{H}\tilde{\mathbf{x}}^{(\iota)}||^2/2 - \mathbf{y}^{\mathrm{T}}\mathbf{H}\tilde{\mathbf{x}}^{(\iota)}\right] \\ &= Pr\left[(\mathbf{H}\tilde{\mathbf{x}}^{(\zeta)} + \mathbf{v})^{\mathrm{T}}\mathbf{H}(\tilde{\mathbf{x}}^{(\iota)} - \tilde{\mathbf{x}}^{(\zeta)}) > \frac{||\mathbf{H}\tilde{\mathbf{x}}^{(\iota)}||^2 - ||\mathbf{H}\tilde{\mathbf{x}}^{(\zeta)}||^2}{2}\right] \\ &= Pr\left[\mathbf{v}^{\mathrm{T}}\mathbf{H}(\tilde{\mathbf{x}}^{(\iota)} - \tilde{\mathbf{x}}^{(\zeta)}) > \Psi_{\mathrm{s}}\right], \end{aligned} \tag{4.14}$$

where we have:

$$\Psi_{\mathrm{s}} = (||\mathbf{H}\tilde{\mathbf{x}}^{(\iota)}||^2 - ||\mathbf{H}\tilde{\mathbf{x}}^{(\zeta)}||^2)/2 - (\mathbf{H}\tilde{\mathbf{x}}^{(\zeta)})^{\mathrm{T}}\mathbf{H}(\tilde{\mathbf{x}}^{(\iota)} - \tilde{\mathbf{x}}^{(\zeta)}). \tag{4.15}$$

Since $\mathbf{H}(\tilde{\mathbf{x}}^{(\iota)} - \tilde{\mathbf{x}}^{(\zeta)})$ is a matrix that containing constant numbers, the term $\mathbf{v}^T\mathbf{H}(\tilde{\mathbf{x}}^{(\iota)} - \tilde{\mathbf{x}}^{(\zeta)})$ obeys the Gaussian distribution with $\mathcal{N}_{\mathrm{Gau}}(0, ||\mathbf{H}\tilde{\mathbf{x}}^{(\iota)} - \mathbf{H}\tilde{\mathbf{x}}^{(\zeta)}||^2\sigma_0^2)$. As a result, the PEP between $\tilde{\mathbf{x}}^{(\zeta)}$ and $\tilde{\mathbf{x}}^{(\iota)}$ can be written as

$$P_{\mathrm{e}}(\tilde{\mathbf{x}}^{(\zeta)} \mapsto \tilde{\mathbf{x}}^{(\iota)}) = \mathcal{Q}(\Psi_{\mathrm{s}}/||\mathbf{H}\tilde{\mathbf{x}}^{(\iota)} - \mathbf{H}\tilde{\mathbf{x}}^{(\zeta)}||\sigma_0). \tag{4.16}$$

Remark: In decoupled analysis, correct detection occurs when all three light bands are *simultaneously* correct, as suggested by Eq. (4.12). By contrast, this event in joint ML-based HD happens, when all three light bands are *jointly* correct, which implies that even if the intensity of a particular band is incorrectly detected, the resultant overall joint intensity vector of the three bands may still be correct. Hence, the probability of error in joint ML based HD is lower than the bound derived in the decoupled analysis. As we will demonstrate in Sec. 4.3.2.3, the discrepancy between the bound based on the decoupled analysis and on the Monte-Carlo simulated joint ML-based HD is relatively wide, when 8-CSK and 16-CSK are employed. Hence, the decoupled analysis proposed in [257] can only serve as a loose bound of 4-CSK, when using joint ML-based HD. By contrast, the union bound we proposed remains tight for all the M_{sym}-CSK scheme at high electronic SNR considered.

4.3.2.3 Numerical Results of Joint ML-based HD

The empirical results of above performance analysis is carried out below, where the simulation parameters we used are detailed in Table 4.5

Table 4.5: Parameters of CSK modulation in indoor VLC channel

Parameters	Values
CSK modulation order M_{sym}	4, 8 and 16
Interference level ε_0	0 - 0.35
Colour band combination	[110,010,000]
FEC	None, RSC, RSC-URC and IrCC URC
Interleaver length	1.0×10^6
Inner iterations	2
Outer iterations	5

Having completed the above empirical analysis, let us now discuss on the numerical results deceived for our uncoded CSK system using joint ML-based HD. Fig. 4.6 and Fig. 4.7 characterise

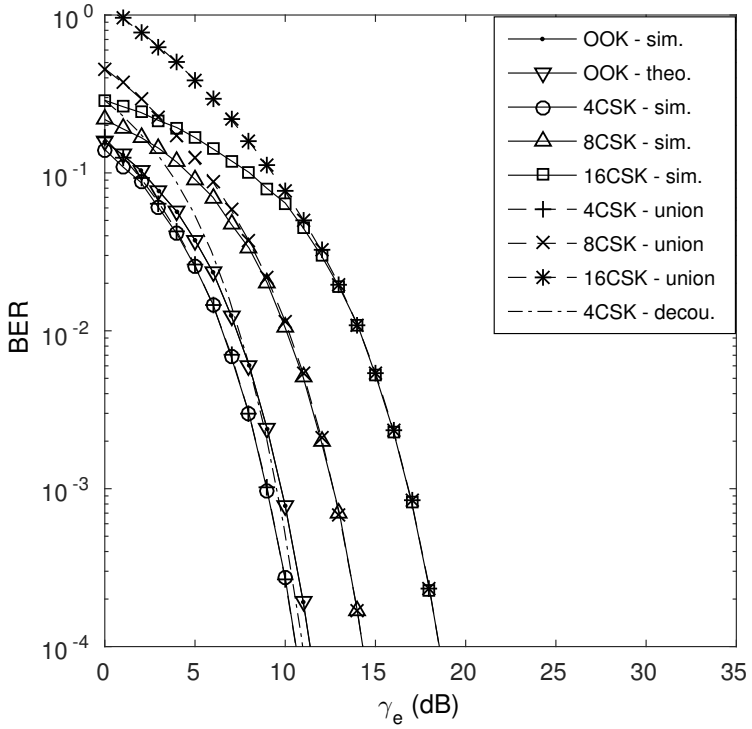

Figure 4.6: Analytical and empirical BER performance of hard-detection CSK schemes and conventional OOK scheme as benchmarker in $\varepsilon_0 = 0$ channel. The schematic of Fig. 4.1 and system parameters detailed in Table 4.5 are used.

the performance of the joint ML-based HD aided CSK system for different values of ε_0 in Eq. (4.7). In detail, Fig. 4.6 shows that all our simulation results recoded for $M_{\text{sym}} = 4$, 8, 16-CSK and associated with $\varepsilon_0 = 0$ are well matched to their corresponding union-bound based analytical results represented by the dashed line. Furthermore, the union-bound based approach is more accurate than the upper bound derived based on the decoupled analysis, as indicated by the dashed-dot line, which is inappropriate for $M_{\text{sym}} = 8$, 16. As a benchmarker, the BER performance of the conventional OOK scheme is also depicted, which is outperformed by the basic 4-CSK scheme by about 0.8 [dB] at the BER of 10^{-4}. Furthermore, Fig. 4.7 shows the performance of our 4-CSK scheme subject to different interference and attenuation levels. As expected, the system performance degrades upon increasing the interference level characterised by ε_0 of Eq. (4.7), and the analytical union-bound matches the associated simulation results for different ε_0 values.

4.3.3 Soft Detection of CSK

Let us now discuss the more powerful joint MAP-based SD of M_{sym}-CSK and its iterative receiver.

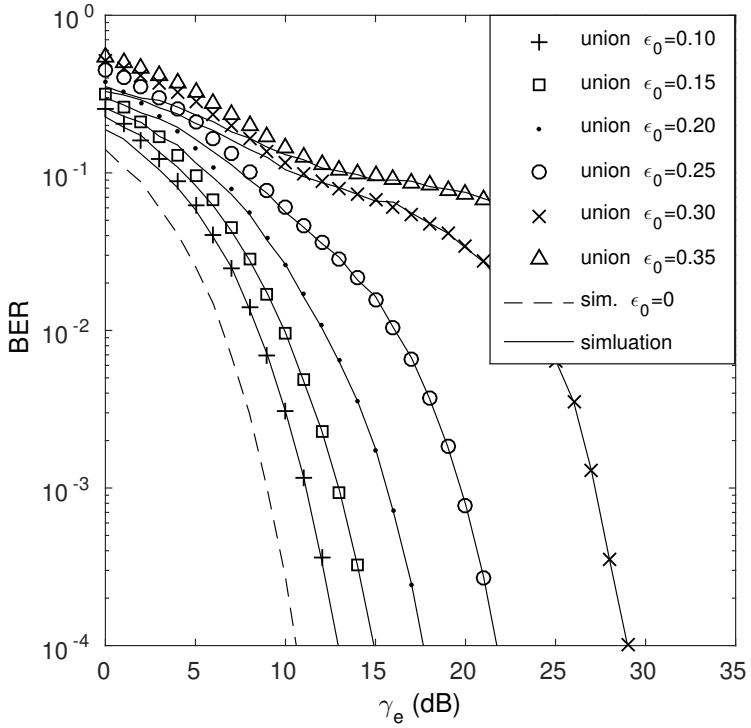

Figure 4.7: Simulated BER performance of 4-CSK hard-detection system in different interference level channels (refer to Eq. (4.7)) compare to BER of no interference ideal ε_0 = 0 channel. The schematic of Fig. 4.1 and system parameters detailed in Table 4.5 are used.

4.3.3.1 Two-Stage Iterative Receiver

In this section, familiarity with the turbo detection principles of [216] is assumed. The two-stage iterative receiver in Fig. 4.8 is employed, when a sophisticated channel-coded system is considered. The information bit sequence $\mathbf{b}$ is first channel encoded, yielding the coded bit sequence $\mathbf{u}$ and

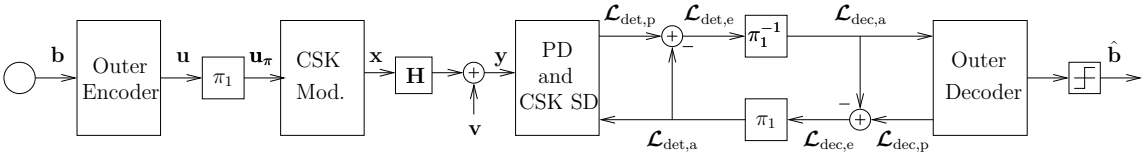

Figure 4.8: Transceiver architecture of the two-stage M_{sym}-CSK iterative receiver using joint MAP-based SD.

then bit-interleaved by π_1, before entering into the M_{sym}-CSK block. The subsequent one-to-one mapping of Fig. 4.8 from the incoming bits to the resultant optical light intensities follows the procedure detailed in Sec. 4.2. Following the PDs employed at the receiver's front-end in Fig. 4.8, a joint MAP-based SD block is used for directly converting the received optical signal intensities back to channel-coded soft-values, rather than going through the consecutive stages of

RGB compensation, demapping and colour decoding, which was required when joint ML-based HD was employed.

The joint MAP-based SD block of Fig. 4.8 exchanges *extrinsic* information with the channel decoder and the final HD is carried out by the channel decoder, once a predefined stopping criterion, such as the maximum affordable number of iterations has been met. For ease of explanation, the following terms are defined:

- $\mathcal{L}_{\text{det,p}}$, $\mathcal{L}_{\text{det,a}}$, $\mathcal{L}_{\text{det,e}}$: the *a posteriori*, *a priori* and *extrinsic* LLR of the detection block, which are detailed in [217, 220].
- $\mathcal{L}_{\text{dec,p}}$, $\mathcal{L}_{\text{dec,a}}$, $\mathcal{L}_{\text{dec,e}}$: the *a posteriori*, *a priori* and *extrinsic* LLR of the channel decoder block.

Recall that the M_{sym}-CSK scheme groups a set of $N_{\text{b}} = \log_2 M_{\text{sym}}$ consecutive incoming bits, when we consider $\mathbf{u}_{(1:N_{\text{b}})}$ to be a binary sequence constituted by N_{b} consecutive bits. Then, for the fth bit of $\mathbf{u}_{(1:N_{\text{b}})}$, its bit-wise *a posteriori* information $\mathcal{L}_{\text{det,p}}(u_f)$ can be derived by the Max-Log approximation [213],

$$\begin{aligned}\mathcal{L}_{\text{det,p}}(u_f) = \mathcal{L}_{\text{det,a}}(u_f) &+ \max_{\tilde{\mathbf{x}} \in \boldsymbol{\mathcal{X}}^1_{u_f}} \left[-\left\|\mathbf{y} - \mathbf{H}\tilde{\mathbf{x}}\right\|^2 / 2\sigma^2 + A_{\text{sub}} \right] \\ &- \max_{\tilde{\mathbf{x}} \in \boldsymbol{\mathcal{X}}^0_{u_f}} \left[-\left\|\mathbf{y} - \mathbf{H}\tilde{\mathbf{x}}\right\|^2 / 2\sigma^2 + A_{\text{sub}} \right],\end{aligned} \tag{4.17}$$

where we introduce the shorthand of $A_{\text{sub}} = \sum_{\tau=1,\tau\neq f}^{N_{\text{b}}} u_f \mathcal{L}_{\text{det,a}}(u_\tau)$ for compactness. Additionally, we define $\boldsymbol{\mathcal{X}}^0_{u_f}$ and $\boldsymbol{\mathcal{X}}^1_{u_f}$ as two subsets of $\boldsymbol{\mathcal{X}}$, namely as $\boldsymbol{\mathcal{X}}^0_{u_f} = \left\{\tilde{\mathbf{x}} \in \boldsymbol{\mathcal{X}} | u_f = 0\right\}$ and $\boldsymbol{\mathcal{X}}^1_{u_f} = \left\{\tilde{\mathbf{x}} \in \boldsymbol{\mathcal{X}} | u_f = 1\right\}$.

As a result, the *extrinsic* LLRs $\mathcal{L}_{\text{det,e}}$ gleaned from the detection block of Fig. 4.8 are deinterleaved and then they are fed as the *a priori* LLRs $\mathcal{L}_{\text{dec,a}}$ into the outer decoder of Fig. 4.8. Similarly, as seen in Fig. 4.8, the updated *extrinsic* LLRs $\mathcal{L}_{\text{dec,e}}$ are fed back and reinterleaved, before being processed as the *a priori* LLRs $\mathcal{L}_{\text{det,a}}$ by the detection block [259].

4.3.3.2 Three-Stage Iterative Receiver

If we further improve the system structure of our two-stage CSK iterative receiver with the aid of unity-rate pre-coding, the overall system is constituted by three stages, as seen in Fig. 4.9, where a pre-coder and its inner decoder pair along with the associated interleaver π_2 and deinterleaver π_2^{-1} are inserted at transmitter and receiver, respectively. Again, the design of three-stage concatenated systems was detailed in [216].

There are several potential activation orders for the iterations amongst the three components and in this section, we treat the inner component as the amalgam of the pre-coder's decoder counter-

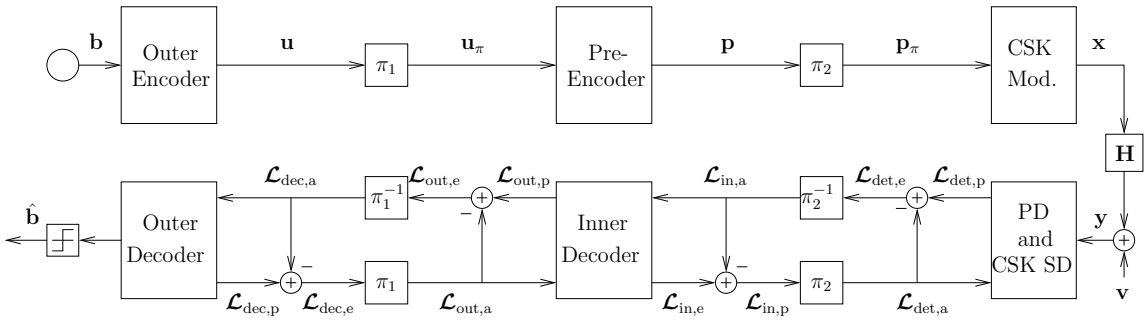

Figure 4.9: Transceiver architecture of the three-stage concatenated M_{sym}-CSK iterative receiver using joint MAP-based SD. The unity-rate precoder has an Infinite Impulse Response (IIR) and hence efficiently spreads *extrinsic* information without increasing the system's delay. This improves the performance of the two-stage transceiver of Fig. 4.8.

parts[3] and the CSK SD block of Fig. 4.9. Explicitly, this implies that first these two blocks exchange their extrinsic information a sufficiently high number of times, beyond which only marginal mutual information improvement can be achieved. Hence they can be treated as a single block, which exchanges information with the outer decoder. Again, for ease of explanation, the following terms are defined:

- $\mathcal{L}_{\text{in,p}}$, $\mathcal{L}_{\text{in,a}}$, $\mathcal{L}_{\text{in,e}}$: the *a posteriori*, *a priori* and *extrinsic* LLR of the inner-decoder which exchanges LLRs with the CSK SD block during join the inner iteration.
- $\mathcal{L}_{\text{out,p}}$, $\mathcal{L}_{\text{out,a}}$, $\mathcal{L}_{\text{out,e}}$: the *a posteriori*, *a priori* and *extrinsic* LLR of the inner-decoder, which take part in the outer iterations, exchanging LLRs with the outer decoder.

Thus, at the receiver we first perform a sufficiently high number of inner iterations within this composite inner component and its output is then forwarded to the outer outer decoder for further processing. Naturally, invoking the pre-decoding imposes a modest extra complexity by requiring iterations between the pre-decoder and the CSK detection block of Fig. 4.9. The output $\mathcal{L}_{\text{out,p}}$ of this combined block is then forwarded to the outer decoder for exchanging the LLRs. The outer decoder then provides *extrinsic* information in form of the *a priori* information $\mathcal{L}_{\text{out,a}}$ fed to the inner decoder. These iterations continue, until the maximum affordable number of outer iterations has been reached.

4.4 Standard Signal Labelling Analysis

Let us first investigate the standard bit-to-symbol mapping with the aid of EXIT charts. EXIT charts [216, 217, 253] may be conveniently applied for analysing the convergence behaviour of our

[3] In this treatise, we define the precoder as one component of the FEC code at the transmitter using URC. Correspondingly, we define the decoder of the precoder as the inner decoder of the three-stage iterative detection.

coded M_{sym}-CSK system. Specifically, they are constituted by the EXIT curves of the input *a priori* and the output *extrinsic* mutual information of the two concatenated components, namely $I_{\text{det,a}}$ and $I_{\text{det,e}}$ of the detection block and $I_{\text{dec,a}}$ and $I_{\text{dec,e}}$ of the channel decoder block, respectively. Since the *extrinsic* mutual information of one component is used as the *a priori* mutual information of the other, the resultant two EXIT curves rely on swapped coordinates, when plotted in the EXIT charts. As detailed in [217, 253], iterative detection aided systems are capable of achieving an infinitesimally low BER, when there is an open tunnel between these two EXIT curves all the way to the top-right corner at the (1.0, 1.0) point, where convergence to perfect mutual information was achieved. By contrast, a residual BER floor emerges, if there is an intersection between the EXIT curve. before reaching the (1.0, 1.0) point. In this section, we assume $\varepsilon_0 = 0$, when we conduct our EXIT charts investigations, which implies having a perfectly diagonal channel matrix in Eq. (4.7).

4.4.1 EXIT Chart Analysis of Standard Mapping

In this section, familiarity with the EXIT chart concept is assumed, as detailed in [216]. We continue by investigating the characteristics of the RSC-aided two-stage system, as well as of the RSC-URC-aided three-stage system and of the more advanced but more complex Irregular Convolutional Code (IrCC)-URC-adied three-stage system. For a detailed introduction to irregular codes, please refer to [216].

4.4.1.1 RSC-Aided Two-Stage System

Fig. 4.10 illustrates the EXIT charts of our RSC coded system employing M_{sym}-CSK and of our OOK-based benchmarker. In all four sub-figures, the straight-line shaped EXIT curves represent the mutual information the CSK or OOK demonstrators of Fig. 4.10, while the rotated S-shaped EXIT curves represent the mutual information of the RSC decoder. A common observation related to the EXIT curves of the inner component is that, as expected, the higher the electronic SNR, the higher the *extrinsic* mutual information becomes.

However, the most important observation related to M_{sym}-CSK is that its EXIT curves exhibit a modest but visible slope, which are flat for OOK. Having a sloping EXIT curve implies that the employment of an iterative receiver is beneficial for fully exploiting the so-called iteration gain inherent in M_{sym}-CSK, where the iteration gain may be interpreted as imposed *extrinsic* mutual information of the CSK SD upon increasing the *a priori* mutual input information. This iteration gain also translates into an SNR gain. Naturally, the flat EXIT curve observed for the OOK benchmarker exhibits no such increments. A close observation of Fig. 4.10 also suggests that the steepness of the EXIT curves is slightly lower for higher-order CSK, albeit no dramatic difference is visible.

A plausible explanation of the sloped EXIT curve of M_{sym}-CSK is that the mapping from

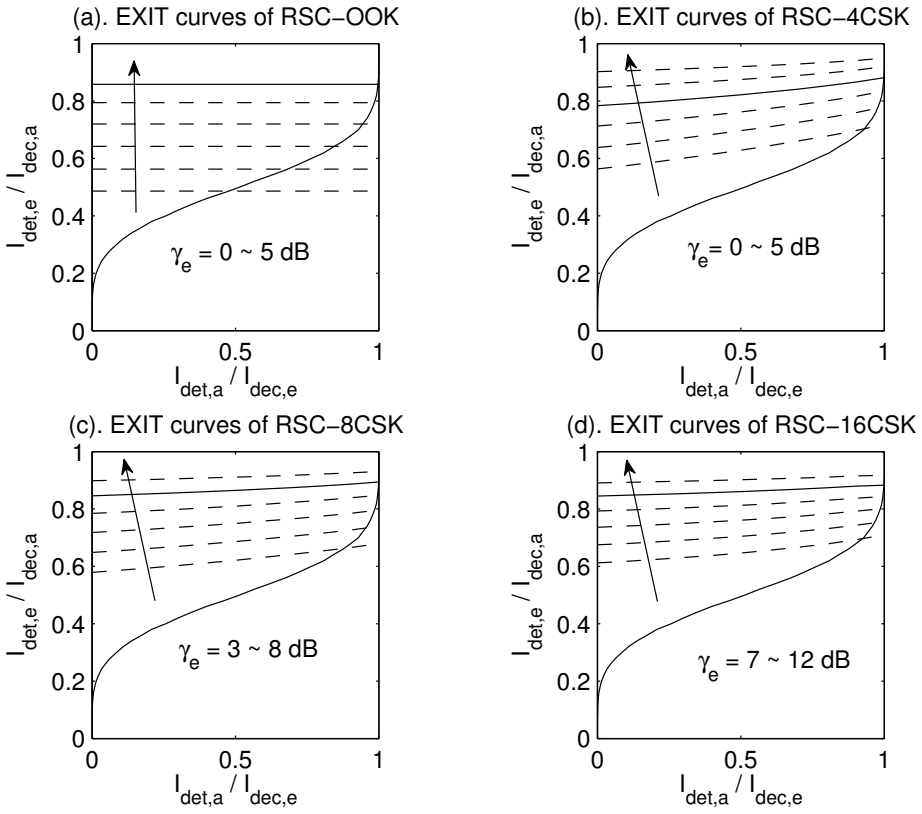

Figure 4.10: EXIT characteristics of CSK soft demodulator in $\varepsilon_0 = 0$ channel (dash line) and half-rate RSC outer decoder, OOK as benchmarker, ascending electrical SNR of CSK EXIT curves along the arrow direction; open tunnels of 4-CSK, 8-CSK and 16-CSK systems consist at γ_e = 3, 7 and 11 [dB] respectively (solid line). The schematic of Fig. 4.8 and system parameters detailed in Table 4.5 are used.

bits to M_{sym}-CSK symbols and then to the two-dimensional colour constellation does not follow the Gray-mapping rule, as seen in Fig. 4.10 and this is true for all values of M_{sym}. Furthermore, observe from Eq. (4.17) that the *extrinsic* LLR of a particular bit output from the detection block of Fig. 4.8 is a function of both the channels output as well as of the *a priori* LLRs of other bits belonging to the same CSK symbol. Hence, the reliability of the *extrinsic* LLRs improves upon iterating, since more reliable *a priori* LLRs are gleaned.

4.4.1.2 RSC-URC Aided Three-Stage System

Despite the modest iteration gain facilitated by the sloped EXIT curve of CSK observed in Fig. 4.10, we also see that the straight-line shaped EXIT curve fails to reach the (1.0, 1.0) point at the top-right corner of the EXIT charts. This implies a potential intersection with the S-shaped EXIT curve of the RSC decoder, before the (1.0, 1.0) point, thus near-capacity operation cannot be achieved. A beneficial technique of circumventing this problem is to employ a pre-coder between

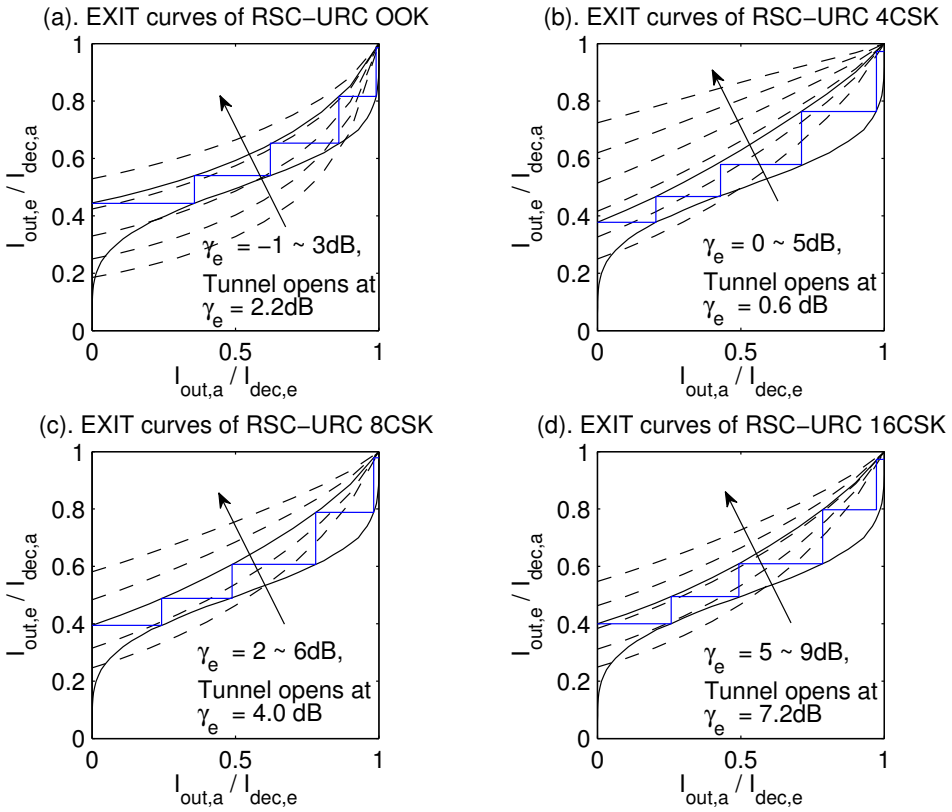

Figure 4.11: EXIT characteristics of CSK soft demodulator aid URC pre-decoder with 2 inner iterations in $\varepsilon_0 = 0$ channel (dash line), OOK as benchmarker, ascending electrical SNR of EXIT curves along the arrow; trajectory opens at γ_e = 0.6, 4.0 and 7.2 [dB] respectively for M_{sym}-CSK (solid line). The schematic of Fig. 4.9 and system parameters detailed in Table 4.5 are used.

the channel encoder and the M_{sym}-CSK block for the sake of shaping the EXIT curve of CSK. Hence, we invoke a URC, which does not reduce the code-rate of the system [260].

Fortunately, using as few as two inner iterations is sufficient for approaching convergence, as we will demonstrate in Fig. 4.11. The URC introduced in Fig. 4.9 has an Infinite Impulse Response (IIR) due to its recursive encoder structure. Hence, as seen in Fig. 4.11, the EXIT curve of the composite inner component decoder becomes capable of approaching the top right corner at the (1.0, 1.0) point with the aid of the URC precoder. Again, the second interleaver π_2 within the inner component of Fig. 4.10 decorrelates the soft information and its action is thus beneficial for enhancing the performance of the iterative receiver.

By introducing the URC as a pre-coder, the Monte-Carlo-simulation based stair-case-shaped iterative decoding trajectory perfectly matches the EXIT chart's prediction and reaches the (1.0, 1.0) point, as seen in Fig. 4.11. We also observe that the EXIT tunnel of the three-stage arrangement opens at electronic SNR values of 0.6, 4.0 and 7.2 [dB] for 4-CSK, 8-CSK and 16-CSK, respec-

Table 4.6: The IrCC Encoding Algorithm

Initialising:	$\gamma_e \leftarrow$ *small value*
Step 1:	produce EXIT curve of $\mathcal{L}_{out,e}$ at γ_e
Step 2:	**if** (inner area < 0.5)
	γ_e++ and **return to** *Step 1*
	else
	go to *Step 3*
Step 3:	**if** ($\sum_{j=1}^{N_P} \eta_{sub}^{(j)} = 1$ & $R = \sum_{j=1}^{P} \eta_{sub}^{(j)} r_{sub}^{(j)} \in [0,1]$)
	finish and output $\boldsymbol{\alpha}$
	else
	γ_e++ and **return to** *Step 1*

tively. Note that the tunnel is only declared to be open, when the Monte-Carlo-simulation based iterative trajectory does become capable of passing through it, which requires a slightly higher electronic SNR than the channel-opening's SNR of the ideal EXIT chart based prediction. For example, in Fig. 4.11(d), the tunnel opens at an electronic SNR of 7 [dB], while the Monte-Carlo-simulation based true iterative trajectory can only pass through at about SNR = 7.2 [dB]. Since the URC does not reduce the system's coding rate, the benefit of introducing a pre-coder is that of achieving the same system throughput at a reduced electronic SNR at a modest complexity price. The corresponding BER performance will be discussed in Sec. 4.4.2.

4.4.1.3 IrCC-URC Aided Three-Stage System

The introduction of a URC has just been shown to be of significant benefits. Let us now further improve the sophistication of our code design by appropriately shaping the EXIT curve of the channel decoder. This becomes possible by exploiting the fact that the area within the open tunnel is proportional to the distance from the system's capacity. Hence, near-capacity operation becomes possible by minimising the area of the open EXIT tunnel. More explicitly, our design philosophy is that we appropriately shape the EXIT curve of the channel decoder so that it matches the EXIT curve shape of the composite inner decoder at the lowest possible electronic SNR.

As proposed by Tüchler and Hagenauer in [261, 262], an IrCC is constituted by a set of RSC codes associated with N_P different component code rates $r_{sub}^{(j)}$, $\forall j$, where every member of this family constitutes a component code. When considering an IrCC code, each component code contributes to shaping the final IrCC EXIT curve by weighting the component EXIT curves with the aid of different coefficients $\eta_{sub}^{(j)} \in [0,1]$, $\forall j$ subject to $\sum_{j=1}^{N_P} \eta_{sub}^{(j)} = 1$, while ensuring that the overall target average code rate $R_{FEC} = \sum_{j=1}^{N_P} \eta_{sub}^{(j)} r_{sub}^{(j)} \in [0,1]$ remains the same. Further details on the design of irregular codes may be found in [216, 217]. As a result, the EXIT charts aided

curve matching is carried out and shown in Table 4.6. The ultimate γ_e values of the EXIT curves of the inner component is found when there is no decease is allowed in Step 3 and the corresponding parameters of IrCC are the resultant EXIT charts aided curve matching.

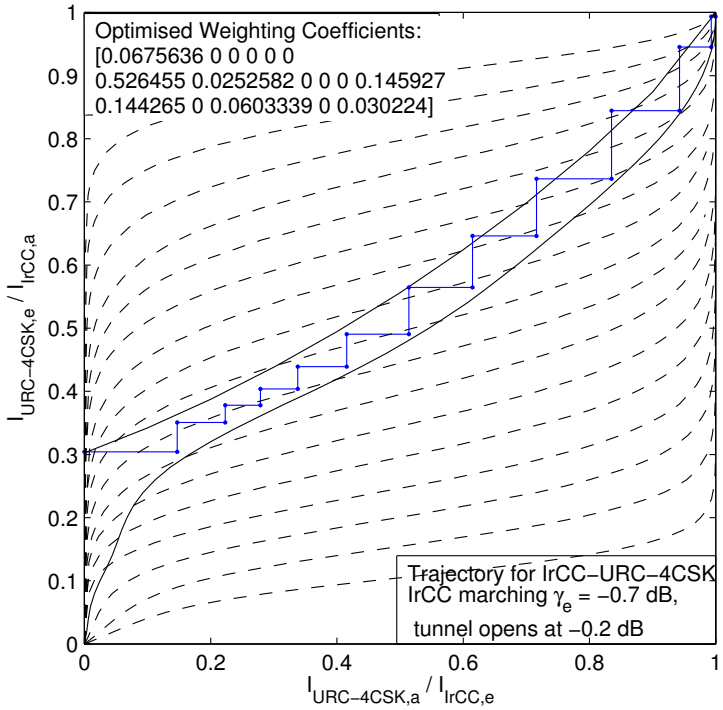

Figure 4.12: EXIT characteristics of URC aided 4-CSK demodulator at γ_e = -0.2 [dB] in ε_0 = 0 channel and half-rate IrCC outer decoder matching with URC-CSK curves at γ_e = -0.7 [dB], where open tunnel consists (solid line); dash lines denote the characteristics of 17 subcodes.The schematic of Fig. 4.9 and system parameters detailed in Table 4.5 are used.

Fig. 4.12 shows the EXIT chart of our URC precoded 4-CSK system having a code rate of 1/2. The IrCC parameters of $[\eta_{\text{sub}}^{(j)}, r_{\text{sub}}^{(j)}], \forall j$ having $N_P = 17$ component codes are shown in Fig. 4.12. It can be seen that when an IrCC is employed, the EXIT curve of the channel decoder matches very well that of the composite inner decoder. Furthermore, the Monte-Carlo-simulation based empirical iterative decoding trajectory exhibits a stair-case shape, closely following our EXIT curves. Again, although the IrCC matches the EXIT curve of the composite inner decoder at an electronic SNR of -0.2 [dB], the stair-case-shaped iterative decoding trajectory can only pass through the tunnel at a higher electronic SNR in excess of γ_e = -0.7 [dB], which demonstrates that practical convergence is typically achieved at a slightly higher electronic SNR than the idealised tunnel-opening threshold. Recall from Fig. 4.10(b) that convergence is achieved at γ_e = 3.2 [dB], when the classic RSC code is employed, indicating that an extra 3.9 [dB] electronic power reduction is attained when using IrCCs. Due to the similarity trends of different M_{sym}-CSK system on EXIT chart using IrCC-URC

scheme, the EXIT characteristics of 16-CSK is shown in Fig. 4.13.

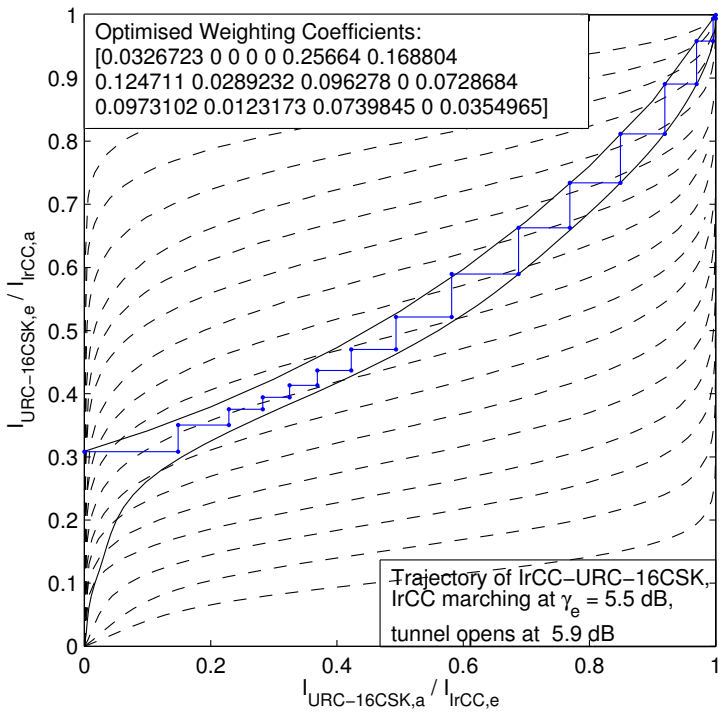

Figure 4.13: EXIT characteristics of URC aided 16-CSK demodulator at γ_e = 5.9 [dB] in ε_0 = 0 channel and half-rate IrCC outer decoder matching with URC-CSK curves at γ_e = 5.5 [dB], where open tunnel consists (solid line); dash lines denote the characteristics of 17 subcodes. The schematic of Fig. 4.9 and system parameters detailed in Table 4.5 are used.

4.4.2 Numerical Results of CSK Using Standard Mapping

Fig. 4.14 characterises the performance of our half-rate RSC coded M_{sym}-CSK system for ε_0 = 0. Similarly to our EXIT-chart based predictions shown in Fig. 4.10, all the M_{sym}-CSK schemes benefit from different iteration gains, where the highest BER improvements are attained after the first two iterations. Furthermore, the higher the CSK order, the lower the iteration gain attained. Additionally, in our EXIT charts analysis of Fig. 4.10, the tunnels are predicted to become open at γ_e = 3, 7 and 11 [dB] for 4-CSK, 8-CSK and 16-CSK, as indicated by the solid straight line respectively. This trend is also reflected in the BER simulation results of Fig. 4.14, where BER = 10^{-4} is achieved at γ_e = 2.7, 6.8 and 11.4 [dB], respectively. By contrast, no iterative gain is observed for OOK due to its flat EXIT curve seen in Fig. 4.10(a). However, after two iterations the iterative gain become limited for M_{sym}-CSK. This suggests that the iteration gain potential of the two-stage system is not fully exploited, which motivates our investigations of the three-stage system.

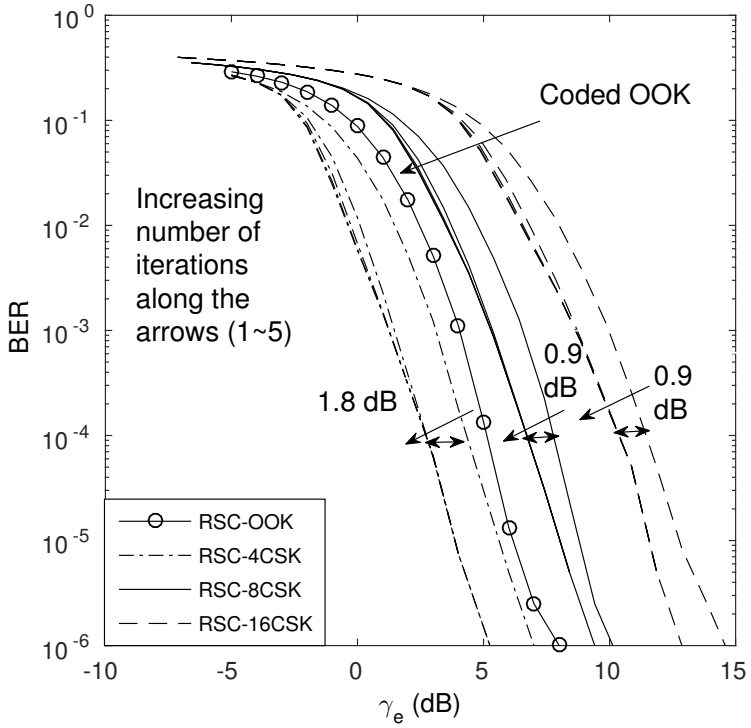

Figure 4.14: BER performance of two-stage half-rate coded 4-CSK, 8-CSK and 16-CSK with different times of iterative detection in $\varepsilon_0 = 0$ channel, ascending number of iterations along the arrow direction, coded OOK with 5 iterations is added as benchmarker (link to Fig. 4.10).The schematic of Fig. 4.8 and system parameters detailed in Table 4.5 are used.

Fig. 4.15 characterises the BER performance of our three-stage half-rate RSC-URC coded CSK system for $\varepsilon_0 = 0$, where we employ two inner iterations between the CSK detector as well as the URC decoder. By adopting this three stage system, the improvement between each outer iteration becomes more substantial compared to the two-stage RSC coded system, as seen in Fig. 4.14. As displayed in Fig. 4.11, the Monte-Carlo-simulation based decoding trajectory reaches the top right corner at the (1.0, 1.0) point with the aid of the URC precoder, and a 'BER cliff' is observed in Fig. 4.15. After five iterations, a BER of 10^{-4} is achieved at γ_e = 0.6, 4.0 and 7.2 [dB] for 4-CSK, 8-CSK and 16-CSK respectively. Again, this trend is perfectly matched to the EXIT-chart predictions detailed in Sec. 4.3.3.2. This corresponds to a 2.1, 2.8 and 4.2 [dB] electronic power reduction compared to a two-stage system.

Fig. 4.16 shows the performance of 16-CSK using our half-rate IrCC-URC aided three-stage M_{sym}-CSK system, when we have $\varepsilon_0 = 0$ and $\varepsilon_0 = 0.2$. Again, we employ two inner iterations between the CSK detector and the URC decoder and five outer iterations for the RSC-URC aided system, as well as 14 or 16 outer iterations for our IrCC-URC aided system. Compared to the RSC-URC aided three-stage system, our IrCC-URC assisted system provides a better BER performance and attains an approximately 1 [dB] electronic SNR gain for both channel scenarios. Importantly,

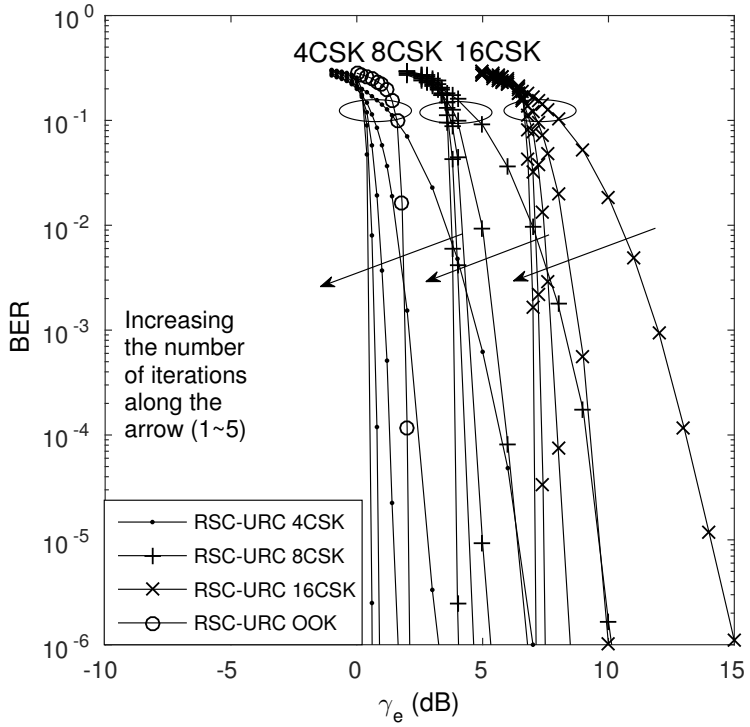

Figure 4.15: BER performance of three-stage half-rate RSC encoding, URC precoded 4-CSK, 8-CSK and 16-CSK with 2 times inner iteration and different times outer iterative detection in $\varepsilon_0 = 0$ channel, ascending number of iterations along the arrow direction, RSC-URC coded OOK with 5 iterations is added as benchmarker (link to Fig. 4.11). The schematic of Fig. 4.9 and system parameters detailed in Table 4.5 are used.

in our RSC-URC aided system, an SNR degradation of about 5 [dB] is observed for $\varepsilon_0 = 0.2$ in Eq. (4.7). However, when our IrCC-URC arrangement is employed, less than 5 [dB] degradation is imposed by the above-mentioned detrimental effects. Furthermore, the BER performance curve of the IrCC-URC scheme is about 1.5 [dB] and 1 [dB] away from the ultimate capacity-related SNR-threshold at which a vanishingly low BER may be ensured. As detailed in [216, 217], this SNR maybe determined with the aid of EXIT charts.

4.5 Signal Labelling Analysis

Based on the analysis of standard bit-to-symbol mapping, we find out in the two-stage iterative detecting system, the obtained iteration gain using the standard signal labelling is relatively limited, as the standard signal labelling is designed for HD. Inspired by [220, 254], let us now investigate various signal labelling for CSK. To be more explicit, by investigating the EXIT characteristics and the area of the open EXIT tunnel between the EXIT curves of the inner and outer decoders, we were able to find the most beneficial signal labelling for diverse design objectives.

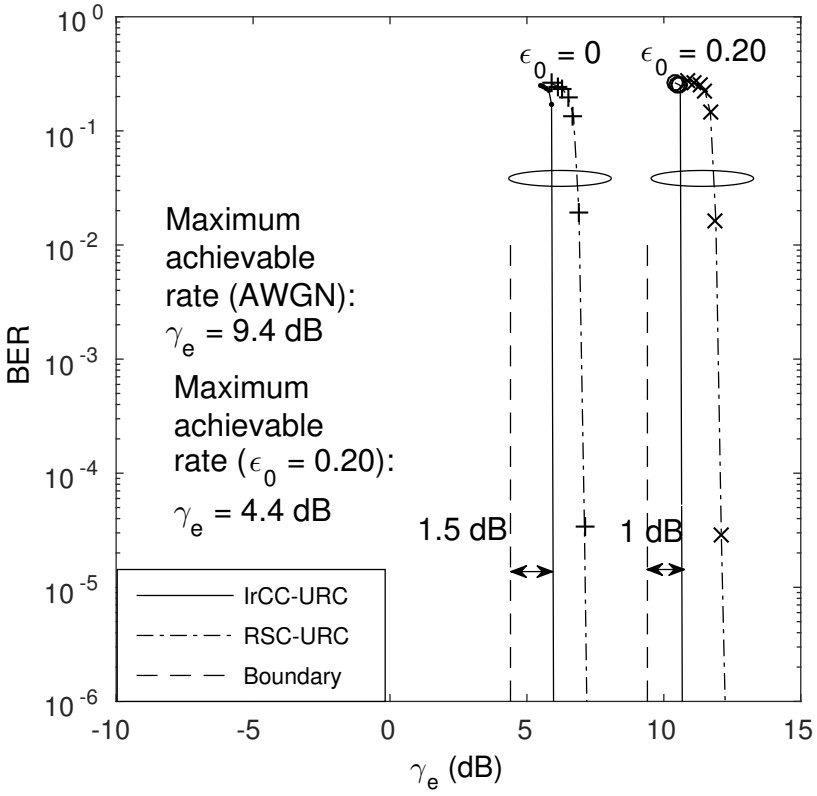

Figure 4.16: BER performance of three-stage 16-CSK system introducing half-rate IrCC and RSC as outer encoder and URC as precoding in ε_0 = 0 and 20% interference ε_0 = 0.20 channel, adopts 2 inner iteration, 5 times outer iterations for RSC-URC scenario, 14 and 16 times outer iterations for IrCC-URC scenario in ideal and interference channel respectively (interference level refer to Eq. (4.7), BER link to Fig. 4.13). The schematic of Fig. 4.9 and system parameters detailed in Table 4.5 are used.

4.5.1 Design Criterion I

Fig. 4.17 portrays the EXIT characteristics of 8-CSK and 16-CSK employing both types of colour constellations of Fig. 4.4 and Fig. 4.5 for transmission over a LOS AWGN channel, where the S-shaped solid lines represent the EXIT characteristics of a half-rate RSC outer decoder, while the dashed or dash-dot lines represent the specific $E_{b_{elec.}}/N_0$ values, where an open EXIT-chart tunnel emerges.

For the time being, let us focus our attention on the dashed lines in Fig. 4.17. Like in Fig. 4.10, the EXIT characteristic exhibits a perceivable slope. But again, the gradient of the joint MAP-based SD's curve is low. This is because the signal labelling design of [4] minimises the sum of Hamming distances between the pair of closest adjacent colour constellation points of 8-CSK and 16-CSK. To elaborate a little further, the bit-to-symbol mapping rule, which is also referred to as the constellation labelling μ of the 8-CSK and 16-CSK schemes obeying **Criterion I** is formulated

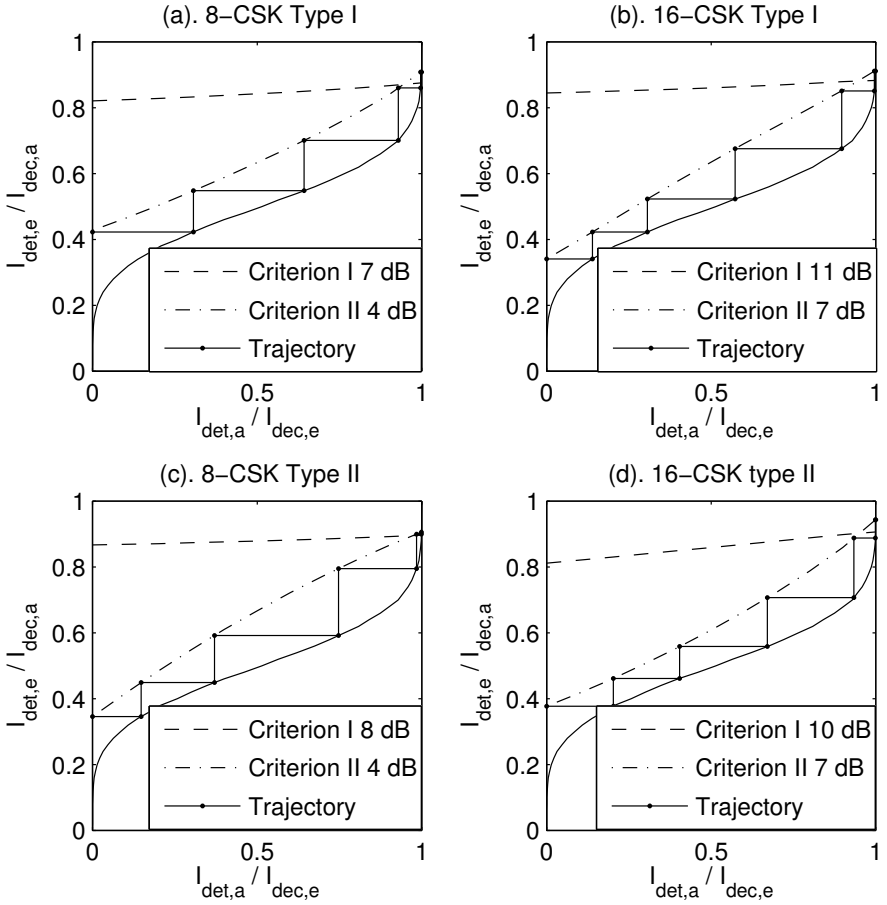

Figure 4.17: EXIT characteristics of CSK joint MAP-based SD using different colour constellations in an AWGN channel and a half-rate RSC outer decoder (solid line). In all figures, the dashed line and dash-dot line represent the approximately required minimum electronic $E_{\mathrm{b}_{\mathrm{elec.}}}/N_0$ (detailed in legend) to provide an open tunnel for **Criterion I** and **II**, OOK is added as benchmarker.The schematic of Fig. 4.8 and system parameters detailed in Table 4.5 are used.

as:

$$\textbf{Criterion I: } \widetilde{\mu}_{\mathrm{I}}^{l} = \underset{\mu^{l} \in \mathbb{M}_{\mathrm{sym}}}{\arg\min} \sum_{1}^{M_{\mathrm{sym}}} d_{\mathrm{adj}}\left(\mu^{l}\right), \tag{4.18}$$

where $\mathbb{M}_{\mathrm{sym}}$ denotes a $(M_{\mathrm{sym}}! \times M_{\mathrm{sym}})$-element matrix, and each row of the matrix contains a set of legitimate signal labelling s(signal labelling examples can be found in Table II), d_{adj} represents the Hamming distance between the adjacent colour constellation points and μ^{l} is the specific signal labelling. We launch a full search within the set $\mathbb{M}_{\mathrm{sym}}$, and choose the specific signal labelling that meets the requirement of Eq. (4.18). We invoke this criterion for designing a Gray-coded bit-to-symbol mapping for *Type II* colour constellations, noting that owing to the specific arrangement of the colour constellation points seen in Fig. 4.5, it is impossible to realise a perfect and consistent Gray bit-to-symbol mapping. Explicitly, our proposed signal labelling designed for the

Type II colour constellation using **Criterion I** is listed in Table 4.7, where the decimal numbers represent the corresponding bit-combinations, which are assigned to their corresponding locations $(c_1, c_2 \cdots c_8)$ in Fig. 4.5(a). Additionally, when using this criterion, we obtained the same signal labelling scheme as the IEEE standard constellation labelling of [4].

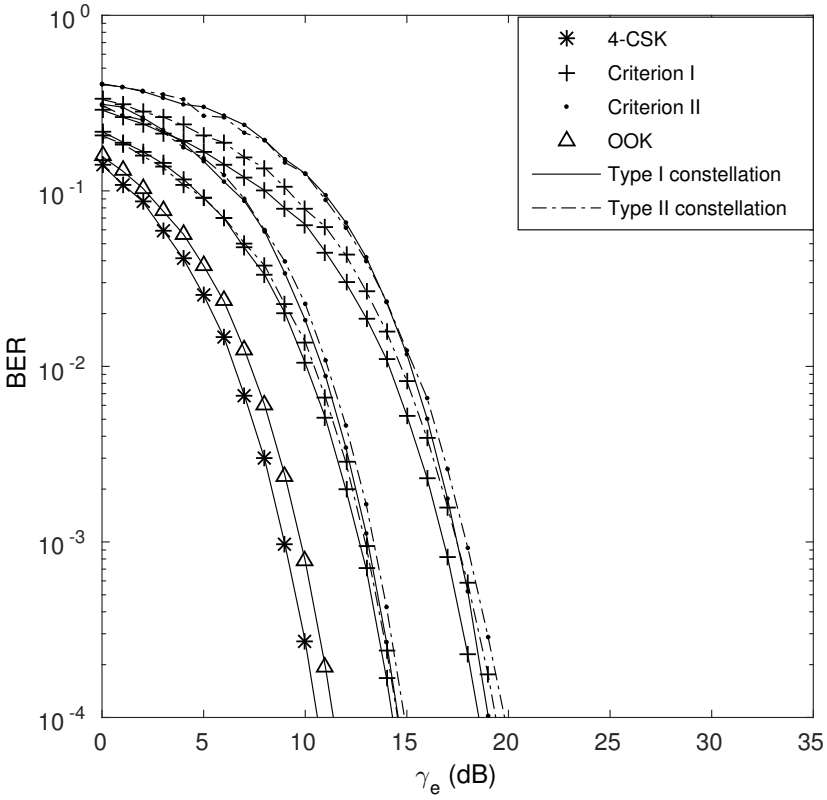

Figure 4.18: Analytical and empirical BER performance of the joint ML-based HD CSK schemes using both types of colour constellations and different signal labelling strategies in an AWGN channel. The corresponding 3 and 4 bits/symbol constellation layouts are described in Fig. 4.4 and Fig. 4.5, additionally the various signal labelling schemes are detailed in Table 4.7. The schematic of Fig. 4.1 and system parameters detailed in Table 4.5 are used.

Fig. 4.18 portrays the BER performance of the joint ML-based HD aided CSK system of Fig. 4.1 using different colour constellations and signal labelling strategies in an AWGN channel. Observe in Fig. 4.18 that all our simulation using *Type I* colour constellations is slightly better than that *Type II* colour constellations.

4.5.2 Design Criterion II

Having considered the signal labelling designed for HD, let us now discover the signal labelling conceived for joint MAP-based SD.

4.5.2.1 Design Criterion

When we design the signal labelling for our iterative joint MAP-based SD aided receiver, the bit-to-symbol mapping is different from the Gray-like mapping of **Criterion I**. In general, when an iterative receiver is invoked, the Free squared Euclidean Distance Conditioned (FEDC) on having ideal feedback usually dominates the performance of iterative detection system [263, 264], hence a signal labelling having a large FEDC provides a good performance.

Additionally, the authors of [263] also proposed an alternative objective function for the constellation labelling search procedure relying on the *harmonic mean* of the minimum squared Euclidean distance after the feedback, which is formulated as [264]:

$$d_{\mathrm{h}}^2(\mu) = \left(\frac{1}{N_{\mathrm{b}} 2^{N_{\mathrm{b}}}} \sum_{n=1}^{N_{\mathrm{b}}} \sum_{b=0}^{1} \sum_{\mathbf{x} \in \boldsymbol{\mathcal{X}}_b^n} \frac{1}{\|\mathbf{x} - \mathbf{z}\|^2} \right)^{-1}, \tag{4.19}$$

where $\boldsymbol{\mathcal{X}}_b^n$ is the specific subset of $\boldsymbol{\mathcal{X}}$, whose label has the binary value b at the nth bit position, while $\mathbf{z}$ is the same as $\mathbf{x}$, except that its nth bit is inverted. As pointed out in [263, 264], a specific signal labelling associated with a large d_{h}^2 usually also has a large FEDC, hence we rely on the d_{h}^2 opjective function value for characterising a signal labelling, rather than on the computationally more complex evaluation of the FEDC.

However, purely relying on evaluating the FEDC value alone is insufficient, because it does not guarantee finding near-capacity signal labellings, as also pointed out in [265]. Namely, our goal is to find that specific signal labelling which leads to the smallest open tunnel area in the EXIT chart [264, 265]. Hence, in this contribution, we first evaluate all legitimate the signal labelling schemes based on Eq. (4.19) and then verify the result with the aid of EXIT chart analysis.

Example: Given the 8-CSK *Type II* colour constellation of Fig. 4.5(a), based on studying the Hamming distance between the closest-neighbour adjacent constellation points, we carried out a full search in the space of all possible $M_{\mathrm{sym}}!$ signal labelling possibilities and used the one associated with the largest d_{h}^2 opjective function value, while relying on the design criterion of

$$\textbf{Criterion II: } \widetilde{\mu}_{\mathrm{II}}^l = \underset{\mu^l \in \mathbb{M}_{\mathrm{sym}}}{\arg\max}\, d_{\mathrm{h}}^2\left(\mu^l\right). \tag{4.20}$$

The resultant signal labelling designed for the for 8-CSK *Type II* colour constellation relying on our iterative joint MAP-based SD-aided receiver is also shown in Table 4.7. For other CSK colour constellations using joint MAP-based SD, the signal labelling design follows the same procedure, which has also been detailed in Table 4.7. Inspired by the method of [254], we use EXIT charts for comparing the performance of the signal labelling schemes employed.

Table 4.7: labelling maps presented for different constellation and detection schemes.

name	labels ($c_1 \cdots c_{M_{\text{sym}}}$) in Fig. 4.4 and 4.5
8-CSK *Type I*, **Crit. I**	(4,0,6,1,2,5,3,7)
8-CSK *Type I*, **Crit. II**	(2,5,1,0,4,3,7,6)
8-CSK *Type II*, **Crit. I**	(3,2,1,0,6,4,5,7)
8-CSK *Type II*, **Crit. II**	(2,1,7,4,5,6,3,0)
16-CSK *Type I*, **Crit. I**	(0,1,3,5,2,7,10,6,4,11,14,13,9,15,12,8)
16-CSK *Type I*, **Crit. II**	(7,1,5,8,9,15,0,3,14,11,10,4,12,2,6,13)
16-CSK *Type II*, **Crit. I**	(1,0,3,5,4,2,7,13,12,6,15,9,10,14,11,8)
16-CSK *Type II*, **Crit. II**	(8,14,13,4,1,3,10,7,11,6,9,12,0,15,5,2)

4.5.2.2 EXIT Chart Based Verification of the d_{h}^2 aided labelling Optimisation

It has been shown in [254] that the area under the EXIT curve of a joint MAP-based SD's EXIT chart approximately equals to the system's achievable throughput, which is directly related to its electronic SNR, but remains unaffected by its signal labelling [220]

$$\mathcal{A}_{\text{det}}\left(\gamma_{\text{e}}\right) = \int_0^1 I_{\text{det,e}} dI_{\text{det,a}} \tag{4.21}$$

$$= \int_0^1 \mathbb{T}_{\text{det}}\left(I_{\text{det,a}}, \mu^l, \gamma_{\text{e}}\right) dI_{\text{det,a}}. \tag{4.22}$$

Furthermore, the area under the outer decoder's EXIT curve equals to its coding rate R_{FEC}. Again, if we expect the system to achieve a vanishingly low BER, it has to exhibit an open tunnel all the way, leading to the (1.0, 1.0) point. Then the open tunnel area $\mathcal{A}_{\text{diff}}$ between these two curves characterises the system's binary data-rate loss in comparison to its true capacity and the size of this area depends on the specific the signal labelling [254]

$$\mathcal{A}_{\text{diff}}\left(\mu^l, \gamma_{\text{e}}\right) = \mathcal{A}_{\text{det}}\left(\gamma_{\text{e}}\right) - R_{\text{FEC}}. \tag{4.23}$$

If we aim for attaining a near-capacity performance, the area $\mathcal{A}_{\text{diff}}$ should be small. Based on Eq. (4.23), we proceed by: finding the specific signal labelling strategy that results in which has a 'just' open EXIT-tunnel at the lowest possible electronic SNR, which leads to a vanishingly low BER at the lowest SNR, provided that the interleaver is sufficiently long to ensure that the soft-information is near-Gaussian. For practical finite-length interleavers, this is not the case and hence usually a slightly higher SNR is required for the stair-case-shaped decoding-trajectory to pass through the EXIT-chart's constriction. To demonstrate the associated $\mathcal{A}_{\text{diff}}$ differences, we consider the 8-CSK *Type II* colour constellation as an example and randomly opt for the signal labelling schemes of Table 4.8. When we invoke a half-rate RSC code, the corresponding results are shown in Fig. 4.19, while some specific numerical results are listed in Table 4.8.

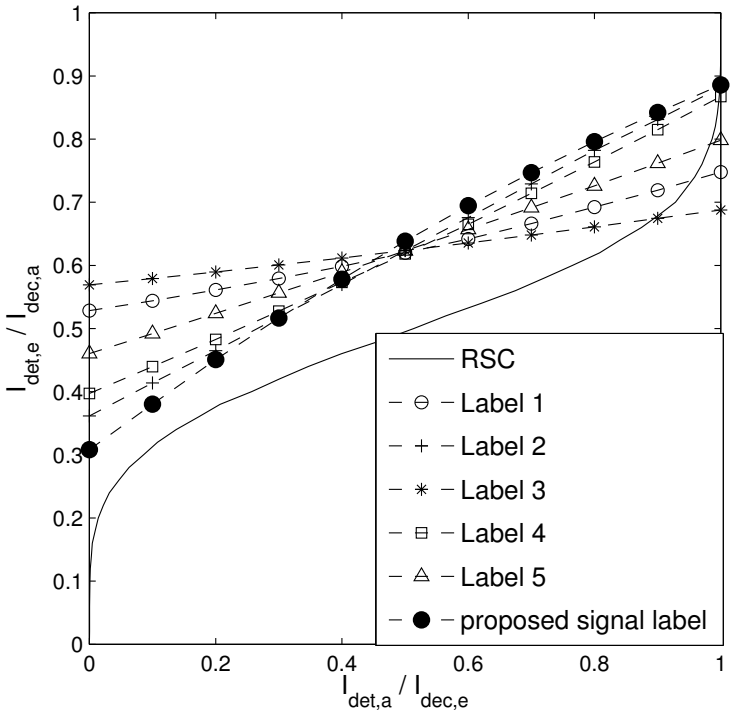

Figure 4.19: EXIT characteristics of our proposed signal labelling candidates for 8-CSK *Type II* at $E_{b_{elec.}}/N_0$ =3.5 [dB] (dashed lines) for joint MAP-based SD for our iterative receiver of Fig. 4.8 in an AWGN channel, where the solid S-shaped line represents the half-rate RSC decoder, while the index of the different signal labelling strategies has been detailed in Table 4.8. The schematic of Fig. 4.8 and system parameters detailed in Table 4.5 are used.

Observe in Fig. 4.19 that the EXIT characteristics of the randomly selected Labels 1-5 exhibit different gradients and that our proposed signal labelling has the smallest open tunnel as well as a cross-over point closest to the (1.0, 1.0) point, which implies having the lowest residual BER, as detailed in [217, 220, 253]. The tunnel opens at $E_{b_{elec.}}/N_0$ = 3.5 [dB], while for the other signal labelling schemes, the EXIT characteristics intersect with that of the outer decoder. This suggests that our proposed signal labelling is capable of achieving a significant iteration gain. Following this approach, our other proposed signal labelling schemes are listed in Table 4.7.

4.5.2.3 Performance Comparison of Criterion I and II

Let us now return to Fig. 4.17 and observe the dash-dot lines in each sub-figure, which represent the EXIT characteristics of the labelling schemes obeying **Criterion II**. For all colour constellations, the dash-dot style curves are associated with a steeper gradient and a lower open-tunnel area than for **Criterion I**. This implies that the reliability of the *extrinsic* LLRs improves more substantially upon iterating, since more reliable *a priori* LLRs are gleaned from the outer decoder. Furthermore, the

Table 4.8: An example of optimising signal labelling candidates follow **Criterion II** for 8-CSK *Type II* colour constellation.

name	labels ($c_1 \cdots c_{M_{\text{sym}}}$)	d_{h}^2	open tunnel	$\mathcal{A}_{\text{diff}}$
Label 1	(7,3,6,0,2,1,5,4)	0.0653	6.5 [dB]	0.3166
Label 2	(4,1,2,6,7,0,3,5)	0.1217	4.0 [dB]	0.1625
Label 3	(4,1,5,0,3,2,6,7)	0.0519	7.5 [dB]	0.3694
Label 4	(7,4,2,0,3,5,6,1)	0.0934	4.5 [dB]	0.1951
Label 5	(4,5,7,0,3,6,2,1)	0.0763	5.5 [dB]	0.2582
Proposed	(2,1,7,4,5,6,3,0)	0.1280	3.5 [dB]	0.1333

dash-dot lines cross the S-shaped RSC-decoder curves closer to the (1.0, 1.0) point, hence a lower residual BER-floor is expected. Having said this, we also note that these benefits are achieved at the cost of an increased number of iterations, i.e. at a higher complexity.

Furthermore, as for the performance of **Criterion II** using HD seen in Fig. 4.18, we can observe that although the differences between the designs relying on **Criterion I** and **II** are relatively small, the performance of the signal labelling obeying **Criterion I** is consistently better than that of **Criterion II**. This is because having the lowest Hamming distance between the points of closest-neighbour adjacent constellation points ensures having the least number of bit-errors between the adjacent constellation points, when decision errors occur in an AWGN channel. Moreover, regardless of the specific signal labelling criterion used, the *Type II* colour constellation is outperformed by the colour constellation *Type I*. Hence, in line with [248, 249], the colour constellation *Type I* is confirmed to be a better solution for an uncoded CSK system.

Additionally, the corresponding BER characteristics of Fig. 4.17 are shown in Fig. 4.20 [4], where both the *Type I* and *Type II* colour constellations of Fig. 4.4 and Fig. 4.5 are characterised in an AWGN channel, and both **Criterion I** and **Criterion II** are considered. Similarly to our EXIT-chart based predictions shown in Fig. 4.17, the different M-CSK schemes exhibit rather different iteration gains in Fig. 4.20. The maximum attainable iteration gain of the systems relying on **Criterion I** is essentially achieved during the first two rounds, which is due to the limited slope of the related EXIT curves shown by the dashed-lines in Fig. 4.17. By contrast, the systems relying on **Criterion II** benefit from a more substantial iteration gain. Consequently, the shape of the BER curves exhibits a 'turbo-cliff' effect. After five iterations, the electronic SNR difference between the two different signal labelling schemes is around 5-7 [dB] in all sub-figures.

Another important observation in Fig. 4.20 is that there is a gradient-change in the BER curves

[4] Although introducing a redundant FEC code reduce the effective data rate of the system, it result in considerable performance gains. Furthermore, in [4] half-rate or even lower-rate Reed Solomon codes were considered, which is outperformed by the FEC scheme employed in this paper.

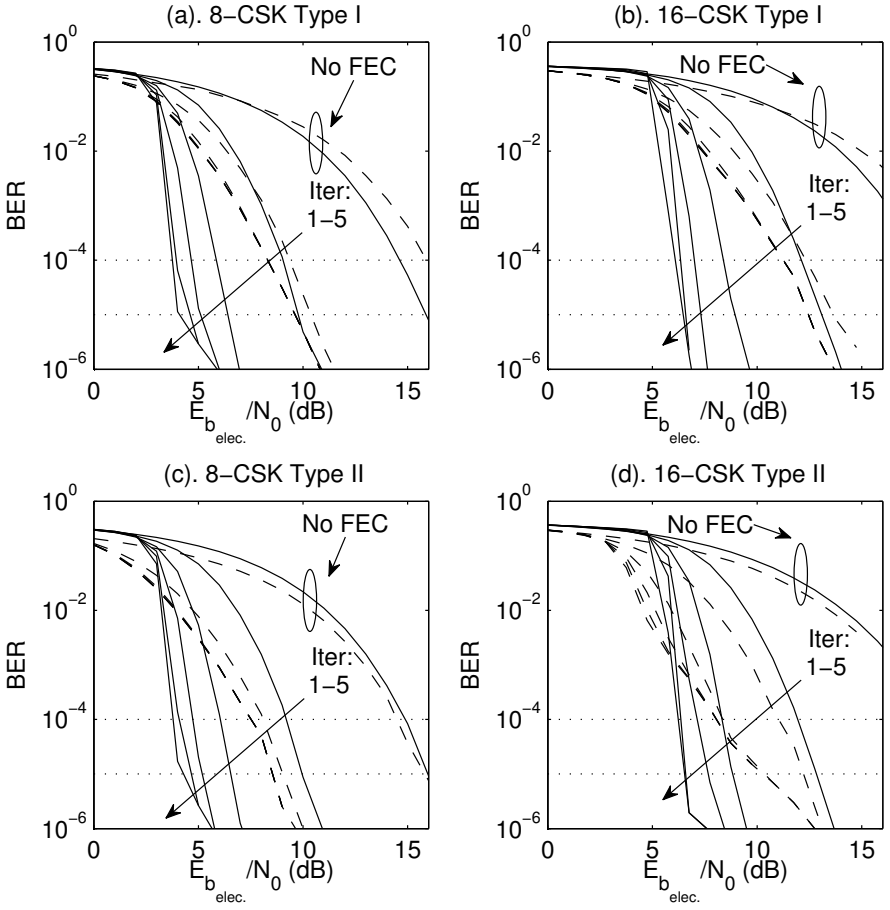

Figure 4.20: BER performance of the two-stage half-rate RSC coded CSK system of Fig. 4.17 using our joint MAP-based SD aided iterative receiver, where different colour constellations are considered. **Criterion I** is represented by the dashed line and **Criterion II** by the solid line. From right to left the multiple solid and dashed lines represent the BER curves associated with an increasing number of iterations from 1 to 5 (link to Fig. 4.17). The schematic of Fig. 4.8 and system parameters detailed in Table 4.5 are used.

around 10^{-5}, as mentioned in Sec. 4.5.3. This point is associated with the intercept point observed in the EXIT-chart of Fig. 4.17. Hence the EXIT characteristic of the joint MAP-based SD scheme fails to reach the (1.0, 1.0) point. More specifically, to interpret the emergence of this 'error floor', we would introduce the concept of a codeword's free distance to aid our explanation. The free distance of a codeword is the characteristic of the error correction capability of a FEC code, which is the minimum distance in terms of number of bits between any pair of codewords. For an FEC code having a free distance of d_{free}, every possible pair of codewords exhibits at least d_{free} number of different bits [266]. However, if the free distance of an FEC code is only $d_{\text{free}} = 1$, then we have a single bit difference between the correct codeword and another legitamate codeword. In this situation, the correct codeword cannot be identified without ambiguity. Consequently, the FEC decoder would result in an error-floor. In contrast to the situation of $d_{\text{free}} = 1$, for an FEC code

having a free distance of $d_{\text{free}} \geq 2$, the difference between the correct FEC codeword and any other legitimate one will be higher. In this case, the correct FEC codeword can indeed be identified and the decoder is capable of determining all bits with almost 100% certainty. Hence, a free distance of $d_{\text{free}} \geq 2$ is a sufficient and necessary condition for a FEC code to avoid an error floor in iterative detection [267]. Therefore, if we employ a URC, which has an IIR and construct a three-stage system, then the free distance of this FEC code combination becomes at least to $d_{\text{free}} = 2$, so that a vanishingly low BER may be achieved. We will demonstrate in Sec. 4.5.3 that this performance limitation is eliminated by our three-stage concatenated system.

4.5.3 Three-Stage Concatenated Error Correction Coding

In this section, familiarity with the Turbo detection priciples of [216] is assumed. Again, despite the above-mentioned benefits, all the EXIT characteristics of the iterative joint MAP-based SD schemes fail to reach the (1.0, 1.0) point at the top-right conner of the EXIT chart, which implies the potential emergence of an 'error-floor' in the low BER range. Suffice to say here that it was demonstrated in [217, 220, 253] that an open EXIT-tunnel leading to the (1.0, 1.0) point of the EXIT-chart is a sufficient condition for achieving iterative decoding convergence to a vanishingly low BER. Invoking an additional URC is capable of eliminating this problem.

In Fig. 4.21, we use the solid line marked by the square and circle markers for representing the different signal labelling strategies and operating with the aid of the URC precoder. We also portray the corresponding results achieved by our two-stage concatenated system operating without the URC, which is represented by the dashed and dash-dot lines for comparison. Upon introducing the URC precoder of Fig. 4.9, all the EXIT curves become capable of reaching the (1.0, 1.0) point in Fig. 4.21, Although, we note that consequently we have a starting point in the EXIT curve which is at a lower value than that of the two-stage system. However, the introduction of this unity-rate code does not reduce the overall code-rate. Hence it does not change the area under the EXIT curve of its corresponding three-stage system either. Its ultimate benefit is that it allows the curve to reach the (1.0, 1.0) point. To elaborate a little further, this URC will beneficially affect the shape of the original EXIT curve, making the curve steeper, which may result in a smaller open tunnel area in the EXIT chart, hence requiring a reduced SNR. We note however that it might also increase the risk of intersecting with the outer decoder's curve before it reaches the (1.0, 1.0) point of decoding convergence to an infinitesimally low BER. Hence, it necessitates an increased number of iterations for approaching the (1.0, 1.0) point associated with an infinitesimally low BER. For example, observe furthermore in Fig. 4.21 that having an open tunnel for **Criterion II** requires an electronic SNR of 6 [dB], while **Criterion I** has an open tunnel at 4 [dB] for our three-stage system. The same trends are valid for the other three colour constellations, which will not be specified here.

Correspondingly, the BER performance of Fig. 4.21 recorded in an AWGN channel is displayed

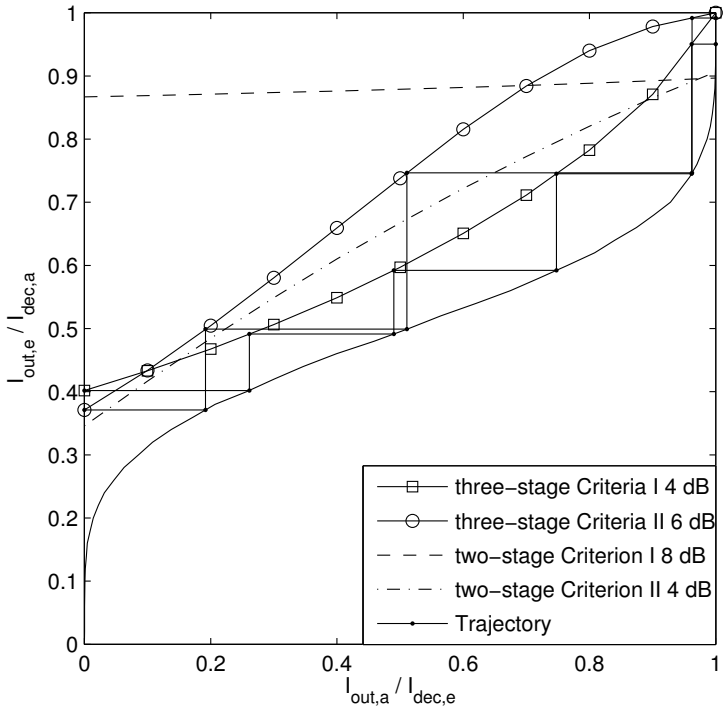

Figure 4.21: EXIT characteristics of our joint MAP-based SD assisted 8-CSK *Type II* colour constellation with the aid of the URC predecoder after two inner iterations using different colour constellations in AWGN channel and half-rate RSC outer decoder (solid line), where the solid lines with square and circle markers represent the approximately required minimum electronic $E_{b_{elec.}}/N_0$ (detailed in legend) to achieve an open tunnel for **Criterion I** and **II**, respectively. The dashed and dash-dot lines denote the EXIT characteristics of the signal labelling adopting **Criterion I** and **Criterion II** without URC from Fig. 4.17(c) as our benchmarker. The schematic of Fig. 4.9 and system parameters detailed in Table 4.5 are used.

in Fig. 4.22, where the performance of adopting **Criterion I** is represented by the dashed line, while the solid lines represent **Criterion II**. The most important result is that the URC precoder eliminates the performance limitations of the two-stage system. Furthermore, the BER results closely match the EXIT-chart based performance predictions seen in Fig. 4.21. However, compared to the results seen in Fig. 4.20(c), the BER performance was not improved but actually degraded for all the systems relying on **Criterion II**. On the other hand, with the aid of the URC precoder, **Criterion I** attained a substantial iteration gain in the low SNR range, which is an explicit benefit of its capability of efficiently spreading the *extrinsic* information. Again, for the other colour constellation schemes of Fig. 4.4 and 4.5, the BER performance would exhibit the same trend, which we will not detailed here.

Upon comparing Fig. 4.20(c) and Fig. 4.22, we observe that the BER performance of the two-stage system relying on **Criterion II** is similar to that of the three-stage system using **Criterion I** in

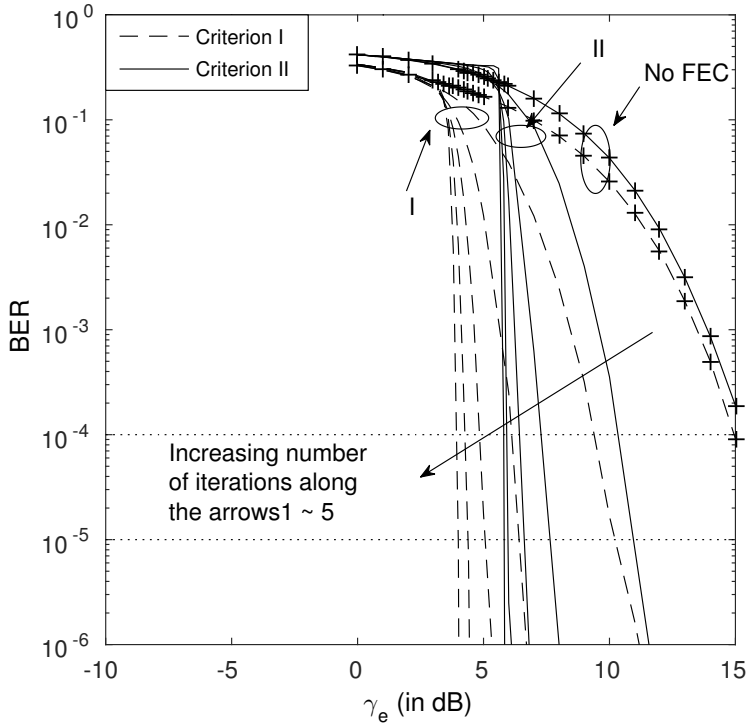

Figure 4.22: BER performance of the three-stage half-rate RSC-URC coded CSK system of Fig. 4.21 using the joint MAP-based SD aided iterative receiver (two inner iterations), where different colour constellations are considered. **Criterion I** is represented by the dashed line and **Criterion II** by the solid line. The performance of the system operating without RSC coding is highlighted by an ellipse circle (link to Fig. 4.21). The schematic of Fig. 4.9 and system parameters detailed in Table 4.5 are used.

the BER range of 10^{-4} to 10^{-5}. The overall coding gain summary of our coded M_{sym}-CSK system has been listed in Table 4.9, where we define the overall coding gain as the SNR improvement at the BER level of 10^{-6} after each iteration. Hence, we can opt for the most appropriate system according to the specific BER versus complexity requirements.

Similarly, when we introduce the IrCC code as the outer encoder, it will allow the system to operate closer to the ultimate performance boundary, facilitating operation 1.5 [dB] away from the maximum achievable rate at $E_{b_{\text{elec.}}}/N_0 = 3.15$ [dB]. The difference between the different signal labelling strategies becomes less pronounced, but the near-capacity substantially increases the system complexity.

4.5.4 Transmission Distance Improvement

Based on the BER results of Fig. 4.20(c), let us now investigate how the different signal labelling designs would effect the attainable transmission distance. To demonstrate this, let us assume a simple point-to-point transmission. Hence the channel matrix $\mathbf{H}$ still remains a diagonal matrix,

Table 4.9: Coding Gain (dB) of M_{sym}-CSK at BER Level of 10^{-6}

Constellation labelling	2-stage iterations: 1-5 in [dB]					3-stage iterations: 1-5 in [dB]				
4-CSK	6.4	7.6	7.6	7.6	7.6	5.2	9.6	11.1	11.9	12.2
8-CSK *Type-I* **Criterion I**	6.5	7.2	7.2	7.2	7.2	6.3	10.1	11.7	12.4	13.0
8-CSK *Type-I* **Criterion II**	5.7	10.6	10.7	10.7	10.7	4.6	9.0	10.0	10.7	10.9
8-CSK *Type-II* **Criterion I**	6.8	7.2	7.2	7.2	7.2	5.6	10.0	11.0	11.7	11.9
8-CSK *Type-II* **Criterion II**	5.9	9.7	11.0	11.2	11.2	4.8	8.4	9.6	10.3	10.6
16-CSK *Type-I* **Criterion I**	6.5	8.0	8.0	8.0	8.0	5.0	9.0	10.5	11.1	11.5
16-CSK *Type-I* **Criterion II**	5.7	10.1	13.0	13.0	13.0	4.6	8.9	10.8	11.5	11.8
16-CSK *Type-II* **Criterion I**	9.6	10.0	10.0	10.0	10.0	6.2	10.8	12.7	13.4	13.7
16-CSK *Type-II* **Criterion II**	8.3	12.5	13.5	14.4	14.4	7.3	11.6	12.8	13.5	13.6

with each of its entry given by the channel gain, as seen in Eq. (3.1). When we use the parameters provided in Table 3.1, including a FOV $\psi_{\text{c}} = 60^{\circ}$, irradiance angle $\phi_{\text{d}} = 0^{\circ}$ and incidence angle $\psi_{\text{d}} = 0^{\circ}$, as well as additionally set the the optical transmit power without conversion loss be $P_{\text{t,o}} = 10$ [mW] and aim for BER = 10^{-6}, by adopting the Eq. (3.9), the achievable transmit distance D_{d} can be expressed as:

$$D_{\text{d}} = \sqrt{\frac{A_{\text{r}} P_{\text{t,o}} g(\psi_d)}{\pi \sqrt{\gamma_{\text{e}} \sigma^2}}}. \tag{4.24}$$

Hence, based on Eq. (4.24), we investigate the beneficial effect of different signal labelling design criteria on the attainable transmit distance D, which is characterised in Fig. 4.24. Observe that our proposed signal labelling using **Criterion II** has the best performance, which is capable of increasing the transmit distance, while maintain a BER of 10^{-6}. In practical vehicle-to-vehicle communication and vehicle-to-infrastructure communication, the transmission power is larger than the experimental power that we used here. This implies, by carefully designing signal labelling according to proper FEC coding and detection scheme, we could realise higher transmission quality in limited range, or longer but reliable data transmission. However, as predicted in Fig. 4.17, due to the limited iteration gain of all other signal labelling strategies, except for the proposed one using **Criterion II**, the distance improvement attained after two iterations tends to be small, especially for **Criterion I**. By contrast, observe in Fig. 4.24 that for our proposed signal labelling using **Criterion II**, the improvement between each iteration is a more considerable. This distance-improvement is indeed expected for the two-stage system **Criterion II**, because we demonstrated in Fig. 4.22 that it needs 4 [dB] lower electronic SNR than its **Criterion I** counterpart based on the BER vs. SNR curves of Fig. 4.20(c).

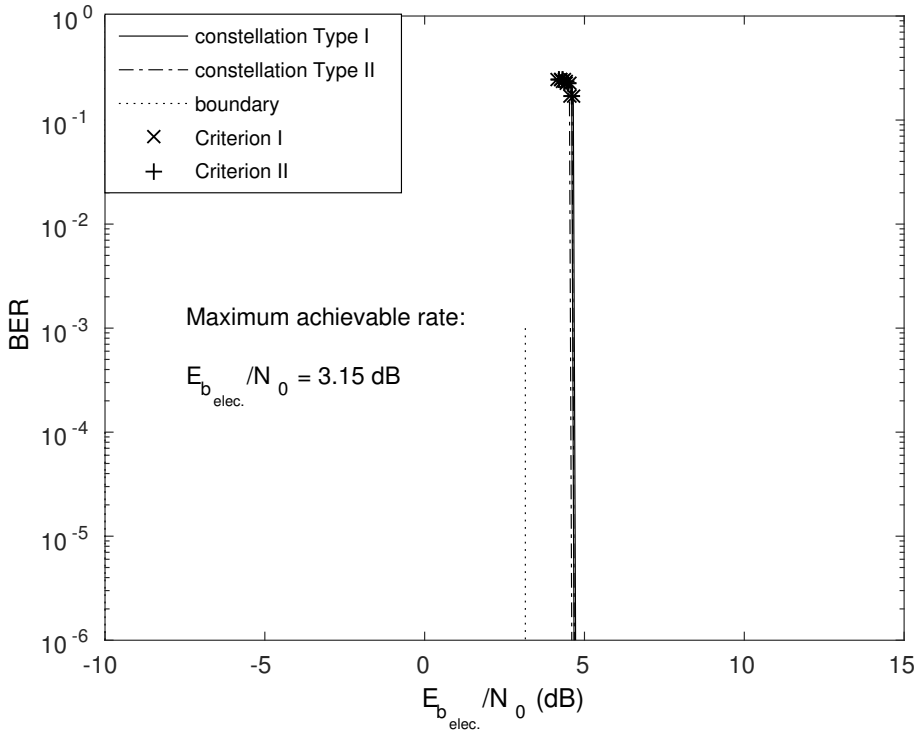

Figure 4.23: BER performance of the three-stage half-rate IrCC-URC coded 16-CSK system using the joint MAP-based SD aided iterative receiver (two inner iterations), where different colour constellations are considered. **Criterion I** is represented by the $+$ marker and **Criterion II** by the $\times$ marker. The schematic of Fig. 4.9 and system parameters detailed in Table 4.5 are used.

4.6 Conclusions

In this chapter, we presented the EXIT chart analysis of the iterative detection aided CSK systems. Commencing from ML HD scheme of Fig. 4.1 in Fig. 4.6 and 4.7, we characterised both the empirical and analytical BER performance of different CSK schemes. We demonstrated that the union-bound provides more accurate analytical results than the decoupled analysis of Sec. 4.3.2, which relies on the separate detection of the RGB compensation. We then conceived the SD-aided CSK system of Fig. 4.8 and 4.9 in Fig 4.10 to 4.13. We demonstrated with the aid of EXIT charts that all CSK schemes have the inherent advantage of benefiting from a modest, but non-negligible iteration gain over conventional OOK modulation. However, since the EXIT-curves of the decoder components failed to reach the (1.0, 1.0) point of perfect decoding convergence to a vanishingly low BER, the system exhibited a modest BER performance in Fig. 4.10. Hence the URC-pre-coder of Fig. 4.9 was introduced, which facilitated reaching the (1.0, 1.0) point of the EXIT-chart of Fig. 4.11, therefore yielding a substantially improved BER in Fig. 4.15. Nonetheless, the open EXIT-tunnel area of this RSC-URC-coded system was relatively high, which indicated that the system failed to approach its maximum attainable capacity. As a final improvement, we designed

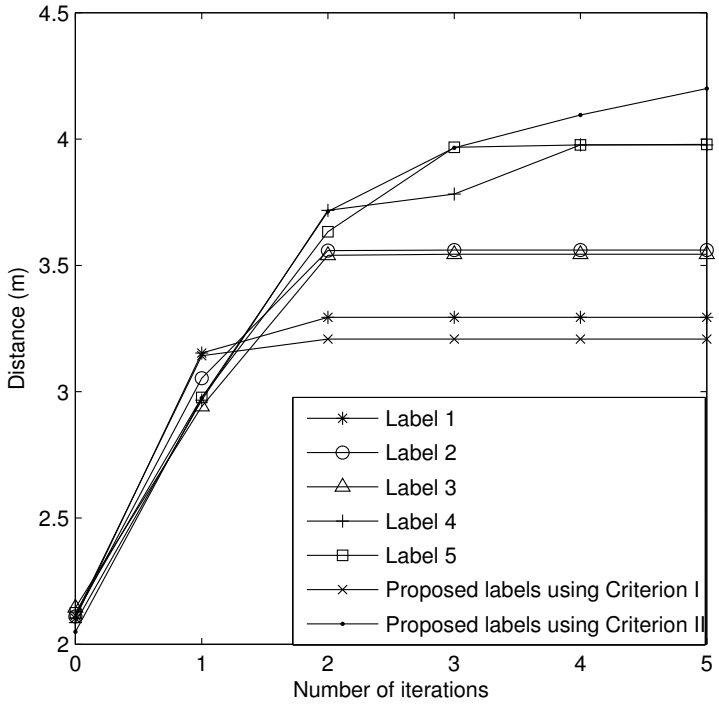

Figure 4.24: The achievable transmit distance of a coloured LED relying on the two-stage half-rate RSC coded 8-CSK *Type II* system of Fig. 4.8 using the different labelling strategies detailed in Fig. 4.19, where the LED's transmit optical power is 10 mW, and error tolerance level is BER = 10^{-6}. Additionally, the signal labelling using **Criterion I** is used as a benchmarker. The schematic of Fig. 4.8 and system parameters detailed in Table 4.5 are used.

an IrCC code for matching the EXIT-curve-shape of the amalgamated URC-CSK inner decoder component, which reduced the area of the open EXIT-tunnel in Fig. 4.12 and 4.13 and the resultant system achieved a vanishingly low BER in Fig. 4.16 at near-capacity SNRs.

Based on the investigation of CSK, efficient signal labelling techniques were designed for both types of CSK color constellations of Fig. 4.4 and 4.5, which were proposed in [4, 145, 247–249]. Hence, more beneficial signal labeling schemes were proposed based on the design criterion of Eq. (4.19). The associated numerical BER performances were presented in Fig. 4.14. We discussed the potential distance and BER improvements of coded CSK and concluded that **Criterion II** of Sec. 4.5.2 is more beneficial in the two-stage system of Fig. 4.20, while **Criterion I** has the edge in the three-stage system of Fig. 4.22.

Chapter 5

Conclusions and Future Work

In this concluding chapter, we will provide the overall summary and conclusions of this treatise in Sec. 5.1. Finally, several promising topics will be briefly discussed as future research directions in Sec. 5.2.

5.1 Summary and Conclusions

Chapter 2: In Chapter 2, we proposed a three-stage RSC-URC coded ACO-OFDM based MIMO system assisted by our JTRApS scheme transmitting data over outdoor FSO turbulence channels. Explicitly, we firstly proposed an uncoded ACO-OFDM based MIMO system operating without the aid of JTRApS, as shown in Fig. 2.1 and then improved the system by the JTRApS scheme of Fig. 2.10. The attainable performance was then further enhanced by three-stage RSC-URC coding in Fig. 2.15. In Sec. 2.1, we briefly introduced the background of ACO-OFDM based MIMO systems and ApS schemes. Our MIMO-aided ACO-OFDM MIMO system was presented in Sec. 2.2, where we specifically discussed the system adopting different MIMO schemes, such as STBC and STSK arrangements. The attainable BER performance was characterised in Fig. 2.2, Fig. 2.3, Fig. 2.4, Fig. 2.5 and Fig. 2.6.

In Sec. 2.3, we introduced the JTRApS scheme of Fig. 2.10. Its design philosophy is based on the investigations of the TAps selection and RAps selection schemes of in Fig. 2.7, Fig. 2.8 and Fig. 2.9. The ApS algorithm is formulated in Eq. (2.25) - Eq. (2.34). Furthermore, we analysed the complexity of both the JTRApS algorithm and of the exhaustive search method, demonstrating that our JTRApS scheme imposed a significantly lower complexity, as specified in Eq. (2.35) or Eq. (2.36).

The performance of the JTRApS aided ACO-OFDM based MIMO system was then investigated in Sec. 2.4, where the JTRApS scheme demonstrates significant performance benefits, as observed from the BER performance seen in Fig. 2.12 and from the equivalent SNR improvements quantified

Table 5.1: Summary of contributions in Chapter 2

Sections	Contributions
Section 2.2	Proposed an ACO-OFDM based MIMO system adopting various MIMO schemes and further investigated the BER performance of this system under both non-dispersive and dispersive FSO channels.
Section 2.3	Detailed the principles of TAps selection and RAps selection, proposed the JTRApS scheme and analysed its complexity compared to exhaustive search method.
Section 2.4	Applied the JTRApS scheme to the proposed ACO-OFDM based MIMO system and investigated its BER performance improvement and enhanced equivalent SNR.
Section 2.5	Further improved the above system with the aid of three-stage RSC-URC coding and analysed its performance enhancement using EXIT characteristics. We also quantified the achievable throughput and BER performance, where the most significant improvement was obtained in strong turbulence channel conditions.

in Fig. 2.13 and Fig. 2.14. In Sec. 2.5, we further improved the system of Fig. 2.1 with the aid of the sophisticated RSC-URC coding scheme shown in Fig. 2.15. The corresponding iterative decoding performance was detailed in Sec. 2.5.1. Explicitly, its EXIT characteristics were shown in Fig. 2.16, its achievable throughput was quantified in Fig. 2.17 and its BER performance was recorded in Fig. 2.18 and Fig. 2.19. Quantitatively, the three-stage coding scheme relying on iterative detection was capable of improving the BER performance in strong turbulence by as much as 12 [dB] at the BER of 10^{-6} with $f_{\mathrm{ApS}} = 4.0$. We have summarised the major contributions of Chapter 3 in Table 5.1.

Chapter 3: In Chapter 3, we designed a VLC-aided video transmission system. More specifically, we briefly introduced the background of video transmission optimisation and VLC transmissions in Sec. 3.1. In Sec. 3.2, we highlighted three different transmission schemes, namely the UFR, HFRFT and VT arrangements having the SINRs defined by Eq. (3.11), Eq. (3.14) and Eq. (3.18), while their achievable data rates were defined by Eq. (3.12), Eq. (3.15) and Eq. (3.19).Their throughput distribution was shown in Fig. 3.2. Explicitly, the UFR transmission scheme suffers from a reception dead-zone imposed by the interference arriving from the adjacent cells, which is successfully eliminated by the HFRFT and VT schemes.

In Fig. 3.4 and Fig. 3.5 we briefly highlighted the different types of video frames in a GOP and demonstrated the effect of dropped video frames. We then formulated an optimisation problem for the UFR and HFRFT regimes in Problem 1, while the optimisation problem of the VT-2 scheme was formulated in Problem 2.

The performance of the resultant system was characterised in Fig. 3.8 - 3.21. As the results indicate, the HFRFT scenario's performance was slightly better than that of the UFR scenario, while the VT-2 scenario always has the best video PSNR performance. We have summarised the major contributions of Chapter 4 in Table 5.2.

Table 5.2: Summary of contributions in Chapter 3

Sections	Contributions
Section 3.2	Highlighted three different transmission schemes, namely the UFR, HFRFT as well as VT schemes and characterised their achievable rates. The UFR suffers from a reception dead-zone, which is eliminated by the HFRFT and VT schemes.
Section 3.3	Briefly highlighted the different types of video frames in a GOP. The optimisation problems of the UFR, HFRFT and VT-2 schemes were formulated.
Section 3.4	Characterised the performance of the system demonstrating that the HFRFT was slightly better than the UFR, while the VT-2 always had the best video PSNR performance.

Chapter 4: In Chapter 4, we studied the CSK system and proposed a pair of criteria for signal labelling conceived for the different detection structures. More specifically, in Sec. 4.1, we briefly introduced the evolution of the CSK modulation scheme based on the literature. The achievable structure of the CSK HD system was shown in Fig. 4.1, while their colour constellation design was shown in Fig. 4.4 and Fig. 4.5, as discussed in Sec. 4.2.

In Sec. 4.3, we described the CSK HD regime and derived its analytical BER performance in two different ways, as seen in Eq. (4.12) and Eq. (4.16). The performance results of the CSK HD system are shown in Fig. 4.6 and Fig. 4.7, where the analytical results matched the simulated ones quite closely. We then extended our ML-based HD system to the more powerful two-stage and three-stage iterative detection regimes depicted in Fig. 4.8 and Fig. 4.9.

We then investigated the performance of CSK proposed in [4] using iterative joint MAP-based SD in Sec. 4.4. More specifically, the EXIT characteristics of the related two-stage and three-stage systems adopting RSC, RSC-URC and IrCC-URC coding schemes are displayed in Fig. 4.10, Fig. 4.11, Fig. 4.12 and Fig. 4.13, while the corresponding BER performances are characterised in Fig. 4.14, Fig. 4.15 and Fig. 4.16. Upon increasing the complexity of the system, the performance gradually approached the capacity. For example, the three-stage system adopting the RSC-URC and IrCC-URC coding schemes approaches the maximum achievable rate within a margin of just 3.5 and 1.5 [dB].

In Sec. 4.5, we proposed two different criteria for finding the best bit-to-symbol mapping strat-

egy. Explicitly, as seen in Eq. (4.18) and Eq. (4.20), the two criteria are invoked for ML-based HD aiming for the minimum sum of the Hamming distance amongst the colour constellation points and for the MAP-based SD designed for achieving the maximum iteration gain, respectively. Given these two criteria, the EXIT characteristic and BER performance of the optimal signal labellings are compared in Fig. 4.17 and Fig. 4.18 under the ML-based HD regime, where the signal labelling obtained from Criterion I outperformed its counterpart. As expected, the corresponding signal labellings are identical to the standard CSK signal labellings. By contrast, the performance of the selected signal labelling using Criterion II was displayed in Fig. 4.20, Fig. 4.21, Fig. 4.22 and Fig. 4.23, where our proposed signal labellings achieved a substantial iteration gain both for the two-stage and for the three-stage systems. Furthermore, our proposed signal labelling using Criterion II for the two-stage system and the signal labelling using Criterion I proposed for the three-stage system have a similar BER performance, but the former suffers from an error floor. Finally, we compared the maximum transmission distance of our schemes at a BER of 10^{-6} in Fig. 4.24, where our proposed labels using Criterion II provided the best performance. We have summarised the major contributions of Chapter 5 in Table 5.3.

Table 5.3: Summary of contributions in Chapter 4

Sections	Contributions
Section 4.2	Outlined the architecture of the CSK HD system and the colour constellation design was discussed.
Section 4.3	Derived the analytical BER performance of the CSK HD regime and extended it to more powerful two-stage and three-stage iterative detection.
Section 4.4	Investigated the performance of the proposed iterative detection system, where the performance of the three-stage system adopting the RSC-URC and IrCC-URC coding schemes approached the maximum achievable rate.
Section 4.5	Proposed two different criteria for finding the best bit-to-symbol mapping strategies, where both the EXIT characteristics and BER performance of the optimal signal labellings were investigated. The maximum transmission distance of our schemes was also compared.

5.2 Potential Further Research Topics

In this section, we will briefly discuss a number of future research ideas. This treatise was mainly dedicated to the design of novel physical-layer solutions for both VLC and FSO OW systems. However, there are numerous open problems in this area, some of which are listed below for employment in both VLC and FSO system:

1. Given the transmission of positive real-valued signals, new irregular FEC codes may be designed, as detailed in [216].

2. Joint modulation and coding schemes may be conceived, where the FEC-parity is absorbed by expanding the modulation constellation, as in Trellis Coded Modulation (TCM) and Turbo Trellis Coded Modulation (TTCM) [216].

3. Channel quality-controlled adaptive modulation and coding can be designed for VLC systems [268].

4. VLC- and FSO-specific large-scale MIMOs may be designed [269, 270], including vector-perturbation based transmit precoders [271].

5. Powerful multiple-symbol differential sphere-decoders can be designed for non-coherent detection by dispensing with any channel information.

6. Iterative photon-counting non-coherent receivers may be designed [272], which can also be extended to quantum-domain signal processing [273].

Additionally, in the video system of Chapter 4, the power lower limit has been defined by the constraint, however, there is no upper limit. A better solution would be to add an extra constraint to limit the total consumed power in an estimation window $\sum_{j=1}^{n_f} P_{t,o}^{(j)} \leq P_{t,o}^{limit}$. Let us consider Problem 1 in Sec. 3.3.2.1 as an example, the updated problem may be formulated as:

$$\text{Problem}: \quad \min_{\boldsymbol{\theta}^{(i)}} \sum_{i=1}^{N_{MT}} \mathcal{D}^{(i)}\left(\boldsymbol{\theta}^{(i)}\right) = \sum_{i=1}^{N_{MT}} \sum_{j=1}^{n_f} \Delta^{(i,j)} \theta^{(i,j)} \tag{5.1}$$

$$\text{subject to}: \quad \mathcal{R}^{(i)}\left(\boldsymbol{\theta}^{(i)}\right) \leq \sum_{j=1}^{n_f} B_{avb} \log_2 \left[1 + \frac{\pi \left(\xi H^{(c,i,j)} P_{t,o}^{(c,i,j)}\right)^2 \left(1 - \theta^{(i,j)}\right)}{\sigma^2 + \mathcal{I}_{sce}}\right], \forall i \tag{5.2}$$

$$\sum_{j=1}^{n_f} P_{t,o}^{(j)} \leq P_{t,o}^{limit} \tag{5.3}$$

$$0 \leq P_{t,o}^{(c,i,j)} \leq P_{t,o}^{max}, \ \forall i, j \tag{5.4}$$

$$\theta^{(i,j)} = \begin{cases} 0, & f^{(i,j)} \text{ transmitted}, \\ 1, & f^{(i,j)} \text{ discarded}. \end{cases} \tag{5.5}$$

As for the VT-2 scenario, the problem may also be modified correspondingly.

Bibliography

[1] L. Hanzo, H. Haas, S. Imre, D. O'Brien, M. Rupp, and L. Gyongyosi, "Wireless myths, realities, and futures: From 3G/4G to optical and quantum wireless," *Proceedings of the IEEE*, vol. 100, pp. 1853–1888, May 2012.

[2] M. R. Feldman, S. C. Esener, C. C. Guest, and S. G. Lee, "Comparison between electrical and optical interconnect based on power and speed consideration," *Applied Optics*, vol. 27, pp. 1742–1751, May 1988.

[3] M. A. Taubenblatt, "Optical interconnects for high-performance computing," *IEEE Journal of Lightwave Technology*, vol. 30, pp. 448–457, February 2012.

[4] IEEE Computer Society, *IEEE Standard for Local and Metropolitan Area Networks - Part 15.7: Short-Range Wireless Optical Communication Using Visible Light*, September 2011.

[5] J. M. Kahn and J. R. Barry, "Wireless infrared communications," *Proceedings of the IEEE*, vol. 85, pp. 265–298, February 1997.

[6] R. M. H. Elgala and H. Haas, "Indoor visible light communication: Potential and state-of-the-art," *IEEE Communications Magazine*, vol. 29, pp. 56–62, September 2011.

[7] M. K. Sichitiu and M. Kihl, "Inter-vehicle communication systems: A survey," *IEEE Communications Surveys and Tutorials*, vol. 10, pp. 88–105, July 2008.

[8] V. W. S. Chen, "Free-space optical communications," *IEEE Journal of Lightwave Technology*, vol. 24, pp. 4750–4762, December 2006.

[9] V. W. S. Chan, "Optical satellite networks," *IEEE Journal of Lightwave Technology*, vol. 21, pp. 2811–2827, November 2003.

[10] D. Rodewald, "MRV introduces industry's first 10G ethernet wireless point-to-point system," in *MRV Communications, Inc.*, (Chatsworth, CA), 2008.

[11] M. A. Khalighi and M. Uysal, "Survey on free space optical communication: A communication theory perspective," *IEEE Communication Surveys and Tutorials*, vol. 16, pp. 2231–2258, November Fourth quarter 2014.

[12] D. Kedar and S. Arnon, "Urban optical wireless communication networks: the main challenges and possible solutions," *IEEE Communications Magazine*, vol. 42, pp. 2–7, May 2004.

[13] S. Bloom, J. Schuster, and H. Willebrand, "Understanding the performance of free-space optics [invited]," *Journal of Optical Networking*, vol. 2, pp. 178–200, June 2003.

[14] A. K. M. andJ. C. Ricklin, *Free-Space Laser Communications: Principles and Advances*. Springer-Verlag, 2010.

[15] L. C. Andrews and E. L. Philips, *Laser Beam Propagation Through Random Media, 2nd Ed.* Bellingham, SPIE, 2005.

[16] T. Kamalakis, I. Neokosmidis, A. Tsipouras, S. Pantazis, and I. Andrikopoulos, "Hybrid free space optical/millimetre wave outdoor links for broadband wireless access networks," in *IEEE 18th International Symposium on Personal, Indoor and Mobile Radio Communications*, (Athens, Greece), pp. 1–5, September 2007.

[17] M. A. Al-Habash, L. C. Andrews, and R. L. Phillips, "Mathematical model for the irradiance probability density function of a laser beam propagation through turbulence media," *Optical Engineering*, vol. 40, pp. 1554–1562, August 2001.

[18] H. Yuksel, S. Milner, and C. C. Davis, "Aperture averaging for optimizing receiver design and system performance on free-space optics," *Journal of Optical Networking*, vol. 4, pp. 462–475, August 2005.

[19] S. Arnon, "Effects of atmospheric turbulence and building sway on optical wireless communications," *Optics Letters*, vol. 28, pp. 129–131, January 2003.

[20] J. C. Ricklin and F. M. Davidson, "Atmospheric optical communication with a Gaussian shell beam," *Journal of the Optical Society of America A*, vol. 20, pp. 856–866, May 2003.

[21] S. Arnon, "Effects of atmospheric turbulence and building sway on optical wireless communication systems," *Optics Letters*, vol. 28, pp. 129–131, January 2003.

[22] X. Liu, "Free-space optics optimization models for building sway and atmospheric interference using variable wavelength," *IEEE Transactions on Communications*, vol. 57, pp. 492–498, February 2009.

[23] A. A. Farid and S. Hranilovic, "Outage capacity optimization for free-space optical links with pointing error," *IEEE Journal of Lightwave Technology*, vol. 25, pp. 1702–1710, July 2007.

[24] D. K. Borah and D. G. Voelz, "Pointing error effects on free-space optical communication links in the presence of atmospheric turbulence," *IEEE Journal of Lightwave Technology*, vol. 27, pp. 3965–3973, September 2009.

[25] M. R. Bhatnagar and S. Anees, "On the performance of Alamouti scheme in Gamma-Gamma fading FSO links with pointing errors," *IEEE Wireless Communications Letters*, vol. 4, pp. 94–97, February 2015.

[26] H. G. Sandalidis, T. A. Tsiftsis, and G. K. Karagiannidis, "BER performance of FSO links over strong atmospheric turbulence channels with pointing errors," *IEEE Communications Letters*, vol. 12, pp. 44–46, January 2008.

[27] H. G. Sandalidis, "Coded free-space optical links over strong turbulence and misalignment fading channels," *IEEE Transactions of Communications*, vol. 59, pp. 780–789, March 2011.

[28] S. S. Muhammad, B. Flecker, E. Leitgeb, and M. Gebhart, "Characterization of fog attenuation in terrestrial free space optical links," *Optical Engineering*, vol. 46, pp. 066001–1–066001–10, June 2007.

[29] I. I. Kim, B. McArthur, and E. Korevaar, "Comparison of laser beam propagation at 785 nm and 1550 nm in fog and haze for optical wireless communications," in *Optical Wireless Communications III Proceeding of SPIE*, (Boston, MA), pp. 26–37, February 2001.

[30] M. Achour, "Simulating atmospheric free-space optical propagation: Part I, rainfall attenuations," *Free-Space Laser Communications Technology XIV*, vol. 4635, pp. 192–503, 26 April 2002.

[31] M. Achour, "Simulating atmospheric free-space optical propagation: Part II, haze, fog and low clouds attenuations," *Optical Wireless Communications V*, vol. 4873, pp. 1–12, 6 December 2002.

[32] S. S. Muhammad, P. Kohldorfer, and E. leitgeb, "Channel modeling for terrestrial free space optical links," in *Proceedings of 7th International Conference Transparent Optical Networks*, pp. 407–410, July 2005.

[33] I. E. Lee, Z. Ghassemlooy, W. P. Ng, and S. Rajbhandari, "Fundamental analysis of hybrid free space optical and radio frequency communication systems," June 2011.

[34] A. M. Obukhov, "Effect of weak inhomogeneities in the atmosphere on sound and light propagation," in *Izv. Akad. SSSR*, (Russia), pp. 155–156, 1953.

[35] S. G. Wilson, M. Brandt-Pearce, Q. L. Gao, and M. Baedke, "Optical repetition MIMO transmission with multipulse PPM," *IEEE Journal on Selected Areas in Communications*, vol. 23, pp. 1901–1910, September 2005.

[36] M. L. B. Riediger, R. Schober, and L. Lampe, "Fast multiple-symbol detection for free-space optical communications," *IEEE Transactions on Communications*, vol. 57, pp. 1119–1128, April 2009.

[37] B. Epple, "Simplified channel model for simulation of free-space optical communications," *IEEE/OSA Journal of Optical Communications and Networking*, vol. 2, pp. 293–304, May 2010.

[38] L. C. Andrews, R. L. Philips, and C. Y. Hopen, *Laser Beam Scintillation with Application*. SPIE Press, 2001.

[39] A. Garcia-Zambrana, "Error rate performance for STBC in free-space optical communications through strong atmospheric turbulence," *IEEE Communications Letters*, vol. 11, pp. 390–392, May 2007.

[40] E. Jakeman and P. Pusey, "Significance of K distributions in scattering experiments," *Physical Review Letters*, vol. 40, pp. 546–550, February 1978.

[41] L. C. Andrews and R. L. .Phillips, "Mathematical genesis of the I-K distribution for random optical fields," *Journal of the Optical Society of America A*, vol. 3, pp. 1912–1919, November 1986.

[42] K. P. Peppas, "A simple, accurate approximation to the sum of gamma-gamma variates and applications in MIMO free-space optical systems," *IEEE Photonics Technology Letters*, vol. 23, pp. 839 – 841, July 2011.

[43] Z. Xu and B. M. Sadler, "Ultraviolet communications: Potential and state-of-the-art," *IEEE Communications Magazine*, vol. 46, pp. 67–73, May 2008.

[44] P. S. Inc., "Free space optics, point-to-point wireless connectivity," in *Available:http://freespaceoptics.ca/about.html*, (Anprior, CAN [online]).

[45] Z. Wang, W. Zhong, S. Zhang, C. Yu, and Y. Ding, "Performance evaluation of OOK free-space optical transmission system with dynamic decision threshold and coherent detection," in *Photonics Global conference (PGC) 2010*, pp. 1–5, 14-16 December 2010.

[46] M. A. Khalighi, F. Xu, Y. Jaafar, and S. Bourennane, "Double laser differential signaling for reducing the effect of background radiation in free-space optical systems," *IEEE/OSA Journal of Optical Communications and Networking*, vol. 3, pp. 145–154, February 2011.

[47] F. M. Davidson and X. Sun, "Gaussian approximation versus nearly exact performance analysis of optical communication systems with PPM signaling and APD receiver," *IEEE Transactions on Communications*, vol. 36, pp. 1185–1192, November 1988.

[48] Z. Ghassemlooy and W. O. Popoola, "Terrestrial free-space optical communications," in *Mobile and Wireless Communications Network Layer and Circuit Level Design*, (Rijeka, Croatia: InTech), pp. 354–392, January 2010.

[49] F. Xu, M. A. Khalighi, Caussé, and S. Bourennane, "Channel coding and time-diversity for optical wireless links," *Optics Express*, vol. 17, pp. 872–887, January 2009.

[50] X. Zhu and J. Khan, "Free-space optical communication through atmospheric turbulence channels," *IEEE Transactions on Communications*, vol. 50, pp. 1293–1300, August 2002.

[51] X. Zhu and J. M. Kahn, "Markov chain model in maximum-likelihood sequence detection for free-space optical turbulence channels," *IEEE Transactions on Communications*, vol. 51, pp. 509–516, March 2003.

[52] J. G. Proakis and M. Salehi, *Digital Communications, 5th Edition*. McGraw-Hill, 2007.

[53] T. H. Chan and S. Hranilovic, "Capacity-achieving probability measure for conditional Gaussian channels with bounded inputs," *IEEE Transactions on Information Theory*, vol. 51, pp. 2073–2088, June 2005.

[54] M. H. A. Davis, "Capacity and error exponent for the direct detection photon channel - part II," *IEEE Transactions on Information Theory*, vol. 40, pp. 1462–1471, November 1988.

[55] R. M. Gagliardi and S. Karp, *Optical Communication, 2nd Ed.* Wiley, 1995.

[56] S. G. Wilson, M. Brandt-Pearce, Q. Cao, and J. H. Leveque, "Free-space optical MIMO transmission with Q-ary PPM," *IEEE Transactions on Communications*, vol. 53, pp. 1402–1412, August 2005.

[57] F. Xu, M. Khalighi, and S. Bourennane, "Coded PPM and multipulse PPM and iterative detection for free-space optical links," *IEEE/OSA Journal of Optical Communications and Networking*, vol. 1, pp. 404–415, October 2009.

[58] W. Gappmair and M. Flohberger, "Error performance of coded FSO links in turbulence atmospheric modeled by gamma-gamma distributions," *IEEE Transactions on Wireless Communications*, vol. 8, pp. 2209–2213, May 2009.

[59] H. Sugiyama and K. Nosu, "MPPM: A method for improving the band-utilization efficiency in optical PPM," *IEEE Journal of Lightwave Technology*, vol. 7, pp. 1969–1979, March 1989.

[60] J. Hamkins and B. Moision, "Multipulse pulse-position modulation on discrete memoryless channels," *IPN Progress Report*, vol. 42, pp. 1–13, May 2005.

[61] M. K. Simon and V. A. Vilnrotter, "Performance analysis and trade-offs for dual-pulse ppm on optical communications," *IEEE Transactions on Communications*, vol. 52, pp. 1969–1979, November 2004.

[62] H. M. H. Shalaby, "Performance of uncoded overlapping PPM under communication constraints," in *IEEE International Communication Conference Proceeding*, (Geneva, Switzerland), pp. 512–516, May 1993.

[63] D. Shiu and J. M. Kahn, "Differential pulse-position modulation for power-efficient optical communication," *IEEE Transactions of Communications*, vol. 47, pp. 1201–1210, August 1999.

[64] D. Shiu and J. M. Kahn, "Shaping and nonequiprobable signalling for intensity-modulated signals," *IEEE Transactions of Information Theory*, vol. 45, pp. 2661–2668, November 1999.

[65] Y. Fan and R. H. Green, "Comparison of pulse position modulation and pulse width modulation for application in optical communications," *Optics Engineering*, vol. 46, p. 065001, June 2007.

[66] Z. Ghassemlooy, A. R. Hayes, N. L. Seed, and E. D. Kaluarachchi, "Digital pulse interval modulation for optical communications," *IEEE Communications Magazine*, vol. 36, pp. 95–99, December 1998.

[67] T. Ohtsuki, "Multiple-subcarrier modulation in optical wireless communications," *IEEE Communications Magazine*, vol. 41, pp. 74–79, March 2003.

[68] X. Zhao, Y. Yao, Y. Sun, and C. Liu, "Circle polarization shift keying with direct detection for free-space optical communication," *IEEE/OSA Journal of Optical Communications and Networking*, vol. 1, pp. 307–312, September 2009.

[69] M. Biagi, A. M. Vegni, S. Pergoloni, P. M. Butala, and T. D. C. Little, "Trace-orthogonal PPM-space time block coding under rate constraints for visible light communication," *IEEE Lightwave Technology*, vol. 33, pp. 481–494, January 2015.

[70] D. A. Bell, *Information Theory and its Engineering Applications*. New York: Pitman, 3rd edition, 1962.

[71] J. R. Pierce, "Optical channel: Practical limits with photon counting," *IEEE Transactions on Communications*, vol. COM-6, pp. 1819–1821, December 1978.

[72] R. J. McEliece, "Practical codes for photon counting," *IEEE Transactions on Information Theory*, vol. IT-27, pp. 393–398, July 1981.

[73] E. M. Biglieri, J. Proakis, and S. Shamai, "Fading channels: Information-theoretic and communications aspects," *IEEE Transactions on Information Theory*, vol. 44, pp. 2619–2692, October 1998.

[74] M. A. Khalighi, N. Schwartz, N. Aitamer, and S. Bourennane, "Fading reduction by aperture averaging and spatial diversity in optical wireless systems," *IEEE/OSA Journal on Optical Communications and Networking*, vol. 1, pp. 580–593, November 2009.

[75] M. A. Khalighi, K. .Raoof, and G. Jourdain, "Capacity of wireless communication systems employing," *Wireless Personal Communications*, vol. 23, pp. 321–352, December 2002.

[76] N. Letzepis and A. G. Fabregas, "Outage probability of the Gaussian MIMO free-space optical channel with PPM," *IEEE Transactions on Wireless Communications*, vol. 57, pp. 3682–3690, December 2009.

[77] H. E. Nistazakis, G. S. Tombras, A. D. Tsigopoulos, E. A. Karagianni, and M. E. Fafalios, "Average capacity of wireless optical communications systems over gamma gamma atmospheric turbulence channels," in *IEEE MTT-S International Microwave Symposium Digest, 2008*, 15-20 June 2009.

[78] H. E. Nistazakis, E. A. Karagianni, A. D. Tsigopoulos, M. E. Fafalios, and G. S. Tombras, "Average capacity of optical wireless communication systems over atmospheric turbulence channels," *IEEE Journal of Lightwave Technology*, vol. 27, pp. 974–979, April 2009.

[79] H. E. Nistazakis, A. D. Teigopoulos, M. P. Hanias, C. D. Psychogios, D. Marinos, C. Aidinis, and G. S. Tombras, "Estimation of outage capacity for free space optical links over I-K and K turbulent channels," *Radio Engineering*, vol. 20, pp. 493–498, June 2011.

[80] N. Letzepis and A. G. i Fabregas, "Outage probability of the free-space optical channel with doubly stochastic scintillation," *IEEE Transactions on Communications*, vol. 57, pp. 2899–2902, October 2009.

[81] S. M. Haas and J. H. Shapiro, "Capacity of wireless optical communications," *IEEE Journal on Selected Areas in Communications*, vol. 21, pp. 1346–1357, October 2003.

[82] I. S. Ansari, M. S. Alouini, and J. Cheng, "Ergodic capacity analysis of free-space optical links with nonzero boresight pointing errors," *IEEE Transactions on Wireless Communications*, vol. (early access), 2015.

[83] V. W. S. Chan, "Coding for the turbulence atmospheric optical channel," *IEEE Transactions on Communications*, vol. COM-30, pp. 269–275, January 1982.

[84] P. Polynkin, A. Peleg, L. Klein, T. Rhoadarmer, and J. Moloney, "Optimized multi-emitter beams for free-space optical communications through turbulence channel," *Optics Letters*, vol. 32, pp. 885–887, April 2007.

[85] B. Castillo-Váquez, A. García-Zambrana, and C. Castillo-Váquez, "Closed-form BER expression for FSO links with transmit laser selection over exponential atmospheric turbulence channels," *Electronic Letters*, vol. 45, pp. 1185–1187, November 2009.

[86] F. M. Davidson and Y. T. Koh, "Interleaved convolutional coding for the turbulent atmospheric optical communication channel," *IEEE Transactions on Communications*, vol. 36, pp. 993–1003, September 1988.

[87] J. A. Anguita, I. B. Djordjevic, M. A. Neifeld, and B. V. Vasic, "Shannon capacities and error-correction codes for optical atmospheric turbulent channels," *Journal of Optical Networking*, vol. 4, pp. 586–601, September 2005.

[88] N. Cvijetic, S. G. Wilson, and R. Zarubica, "Performance evaluation of a novel converged architecture for digital-video transmission over optical wireless channels," *IEEE Journal of Lightwave Technology*, vol. 25, pp. 3366–3373, November 2007.

[89] I. B. Djordjevic, S. Denic, J. Anguita, B. Vasic, and M. A. Neifeld, "LDPC-coded MIMO optical communication over the atmospheric turbulence channel," *IEEE Journal of Lightwave Technology*, vol. 26, pp. 478–487, March 2008.

[90] I. B. Djordjevic, B. Vasic, and M. A. Neifeld, "LDPC coded OFDM over atmospheric turbulence channel," *Optics Express*, vol. 15, pp. 6336–6350, May 2007.

[91] X. M. Zhu and J. M. Kahn, "Performance bounds for coded free-space optical communications through atmospheric turbulence channels," *IEEE Transactions on Communications*, vol. 51, pp. 1233–1239, August 2003.

[92] M. Uysal, S. M. Navidpour, and L. Jing, "Error rate performance of coded free-space optical links over strong turbulence channels," *IEEE Communications Letters*, vol. 8, pp. 635–637, October 2004.

[93] M. Uysal, J. Li, and M. Yu, "Error rate performance analysis of coded free-space optical links over gamma-gamma atmospheric turbulence channels," *IEEE Transactions on Wireless Communications*, vol. 5, pp. 1226–1233, June 2006.

[94] J. H. Shapiro and A. L. Puryear, "Reciprocity-enhanced optical communication through atmospheric turbulence, Part I: Reciprocity proofs and far-field power transfer optimization," *IEEE/OSA Journal of Optical Communications and Networking*, vol. 4, pp. 947–954, December 2012.

[95] A. L. Puryear, J. H. Shapiro, and R. R. Parenti, "Reciprocity-enhanced optical communication through atmospheric turbulence, Part II: Communication architectures and performance," *IEEE/OSA Journal of Optical Communications and Networking*, vol. 5, pp. 888–900, August 2013.

[96] J. A. Anguita, M. A. Neifeld, B. Hildner, and B. Vasic, "Rateless coding on experimental temporally correlated FSO channels," *IEEE Journal of Lightwave Technology*, vol. 28, pp. 990–1002, April 2010.

[97] C. H. Lai and K. Kiasaleh, "Modified viterbi decoders for joint data detection and timing recovery of convolutionally encoded PPM and OPPM optical signals," *IEEE Transactions on Communications*, vol. 45, pp. 90–94, January 1997.

[98] G. E. Atkin and K.-S. L. Fung, "Coded multipulse modulation in optical communication systems," *IEEE Transactions on Communications*, vol. 42, pp. 574–582, February-April 1994.

[99] A. Gupta, P. K. Sharma, P. Garg, and G. Sharma, "Outage analysis of free space optical coded cooperation in weak atmospheric turbulence," in *2nd International Conference on Signal Processing and Integrated Networks*, (Delhi-NCR, India), pp. 207–210, February 2015.

[100] M. Safari and M. Uysal, "Do we really need OSTBCs for free-space optical communication with direct detection?," *IEEE Transactions on Wireless Communications*, vol. 7, pp. 4445–4448, 17 - 22 July 2008.

[101] M. Razavi and J. H. Shapiro, "Wireless optical communications via diversity reception and optical preamplification," *IEEE Transactions on Wireless Communications*, vol. 4, pp. 975–983, May 2005.

[102] F. S. Vetelino, C. Young, and L. C. Andrews, "Aperture averaging effects on the probability density of irradiance fluctuations in moderate-to-strong turbulence," *Applied Optics*, vol. 46, pp. 2099–2108, September 2007.

[103] A. G. Zambrana, C. C. Vázquez, B. C. Vázquez, and A. H. Gómez, "Selection transmit diversity for FSO links over strong atmospheric turbulence channels," *IEEE Journal of Lightwave Technology*, vol. 21, pp. 1017–1019, May 2009.

[104] M. K. Simon and V. A. Vilnrotter, "Alamouti-type space-time coding for free-space optical communication with direct detection," *IEEE Transactions on Wireless Communications*, vol. 4, pp. 35–39, January 2005.

[105] E. Bayaki and R. Schober, "On space-time coding for free-space optical systems," *IEEE Transactions on Communications*, vol. 58, pp. 58–62, January 2010.

[106] C. Abou-Rjeily, "On the optimality of the selection transmit diversity for MIMO-FSO links with feedback," *IEEE Communications Letters*, vol. 15, pp. 641–643, June 2011.

[107] A. García-Zambrana, C. Castillo-Váquez, and B. Castillo-Váquez, "Space-time trellis coding with transmit laser selection for FSO links over strong atmospheric turbulence channels," *Optics Express*, vol. 18, pp. 5356–5366, March 2010.

[108] E. J. Lee and V. W. S. Chen, "Part 1: Optical communication over the clear turbulent atmospheric channel using diversity," *IEEE Journal on Selected Areas in Communications*, vol. 22, pp. 1896–1906, November 2004.

[109] J. H. Churnside, "Aperture averaging of optical scintillations in the turbulent atmosphere," *Applied Optics*, vol. 30, pp. 1982–1994, May 1991.

[110] H. Yuksel, S. Milner, and C. C. Davis, "Aperture averaging for optimizing receiver design and system performance on free-space optical communication links," *Journal of Optical Networking*, vol. 4, pp. 462–475, August 2005.

[111] S. M. Navidpour, M. Uysal, and M. Kavehrad, "BER performance of free-space optical transmission with spatial diversity," *IEEE Transactions on Wireless Communications*, vol. 6, pp. 2813–2819, August 2007.

[112] N. Cvijetic, S. G. Wilson, and Brandt-Pearce, "Performance bounds for free-space optical MIMO systems with APD receivers in atmospheric turbulence," *IEEE Journal on Selected Areas in Communications*, vol. 26, pp. 3–12, April 2008.

[113] D. Bushuev and S. Arnon, "Analysis of the performance of a wireless optical multi-input to multi-output system," *Journal of Optical Society of America A*, vol. 23, pp. 1722–1730, July 2006.

[114] E. Bayaki, R. Schober, and R. K. Mallik, "Performance analysis of MIMO free-space optical systems in gamma-gamma fading," *IEEE Transactions on Communications*, vol. 57, pp. 3415–3424, November 2009.

[115] T. A. Tsiftis, H. G. Sandalidis, G. K. Karagiannidis, and M. Uysal, "Optical wireless links with spatial diversity over strong atmospheric turbulence channels," *IEEE Transactions on Wireless Communications*, vol. 8, pp. 951–957, February 2009.

[116] N. Letzepis, I. Holland, and W. Cowley, "The Gaussian free space optical MIMO channel with Q-ary pulse position modulation," *IEEE Transactions on Wireless Communications*, vol. 7, pp. 1744–1753, May 2008.

[117] C. Abou-Rjeily and W. Fawaz, "Space-time codes for MIMO ultra-wideband communications and MIMO free-space optical communications with PPM," *IEEE Journal on Selected Areas in Communications*, vol. 26, pp. 938–947, June 2008.

[118] M. L. B. Riediger, R. Schober, and L. Lampe, "Multiple-symbol detection for photon-counting MIMO free-space optical communications," *IEEE Transactions on Wireless Communications*, vol. 7, pp. 5369–5379, December 2008.

[119] R. Mesleh, H. Elgala, and H. Haas, "Optical spatial modulation," *IEEE Journal of Optical Communications*, vol. 3, pp. 234–244, March 2011.

[120] S. M. Aghajanzadeh and M. Uysal, "Diversity-multiplexing trade-off in coherent free-space optical systems with multiple receivers," *IEEE/OSA Journal of Optical Communications and Networking*, vol. 2, pp. 1087–1094, December 2010.

[121] C. Abou-Rjeily and A. Abdo, "Serial relaying over gamma-gamma MIMO FSO links: Diversity order and aperture allocation," *IEEE Communications Letters*, vol. 19, pp. 553–556, April 2015.

[122] D. Jackson, T. Buffaloe, and S. Leeb, "Fiat lux: A fluorescent lamp digital transceiver," *IEEE Transactions on Industry Applications*, vol. 34, pp. 625–630, May 1998.

[123] Y. Tanaka, T. Komine, S. Haruyama, and M. Nakagawa, "Wireless optical transmissions with white coloured LED for wireless home links," in *IEEE International Symposium on Personal, Indoor and Mobile Radio Communications*, pp. 1325–1329, 2000.

[124] T. Komine and M. Nakagawa, "Fundamental analysis for visible-light communication system using LED lights," *IEEE Transactions on Consumer Electronics*, vol. 50, pp. 100–107, February 2004.

[125] VLCC, "Visible light communications consortium," in *[Online]. Available: http://www.vlcc.net/modules/xpage1/*, 2007.

[126] J. Grubor, S. Randel, K.-D. Langer, and J. W. Walewski, "Broadband information broadcasting using LED-based interior light," *IEEE Journal of Lightwave Technology*, vol. 26, pp. 3883–3892, February 2009.

[127] "Home gigabit access project," in *[Online]. Available: http://www.ict-omega.eu/*, 2012.

[128] Bourns College of Engineering, "Center for ubiquitous communication by light," in *[Online]. Available: http://www.uclight.ucr.edu/*, 2012.

[129] The Pennsylvania State University, "Center on optical wireless applications," in *[Online]. Available: http://cowa.psu.edu/*, 2012.

[130] Smart Lighting Engineering Research Center, "Synthesizing light for the benefit of humanity," in *[Online]. Available: http://www.bu.edu/smartlighting*, 2008.

[131] M. H. Crawford, "LEDs for solid-state lighting: Performance challenges and recent advances," *IEEE Journal of Selected Topics in Quantum Electronics*, vol. 15, pp. 1028–1040, July-August 2009.

[132] H. Elgala, R. Mesleh, and H. Haas, "Indoor broadcasting via white LEDs and OFDM," *IEEE Transactions on Consumer Electronics*, pp. 1127–1134, August 2009.

[133] R. Mesleh, H. Elgala, and H. Haas, "LED nonlinearity mitigation techniques in optical wireless OFDM communications systems," *IEEE/OSA Journal of Optical Communications and Networking*, vol. 4, pp. 865–875, November 2012.

[134] C. W. Chow, C. H. Yeh, Y. F. Liu, and Y. Liu, "Improved modulation speed of LED visible light communication system integrated to main electricity network," *Electronic Letters*, vol. 47, pp. 867–868, July 2011.

[135] H. Hecht, "Changing the lights: Are LEDs ready to become the market standard?," *Optics and Photonics News*, vol. 23, no. 3, pp. 44–50, 2012.

[136] Cree Inc., "Cree sets new R & D performance record with 254 lumen-per-watt power LED," in *[Online]. Available: http://www.cree.com/news-and-events/cree-news/press-releases/2012/april/120412-254-lumen-per-watt*, 2012.

[137] N. Kumar and N. Lourenco, "LED based visible light communication: A brief survey and investigation," *Journal of Engineering and Applied Sciences*, vol. 5, pp. 269–307, 2010.

[138] D. Steigerwald, J. Bhat, D. Collins, R. Fletcher, M. Holcomb, M. Ludowise, P. Martin, and S. Rudaz, "Illumination with solid state lighting technology," *IEEE Journal of Selected Topics in Quantum Electronics*, vol. 8, pp. 310–320, August 2002.

[139] Multi-Chip LED, "OSRAM opto semiconductors," in *[Online]. Available: http://www.osram-os.com/osram-os/en/product-catalog/led-light-emitting-diodes/multi-chipled/index.jsp*, 2013.

[140] Konica Minolta, "OLED lighting," in *[Online]. Available: http://www.konicaminolta.com/oled/products/index.htm*, 2014.

[141] A. Kelly, J. McKendry, S. Zhang, D. Massoubre, B. Rae, R. Green, R. Henderson, and M. Dawson, "High-speed GaN micro-LED arrays for data communication," in *14th International Conference on Transparent Optical Networks (ICTON)*, (Coventry, UK), pp. 1–5, July 2012.

[142] R. Zhang and H. S.-H. Chung, "A TRIAC-dimmable LED lamp driver with wide dimming range," *IEEE Transactions on Power Electronics*, vol. 29, pp. 1434–1446, September 2014.

[143] T.-J. Liang, W.-J. Tseng, J.-F. Chen, and J.-P. Wu, "A novel line frequency multistage conduction LED driver with high power factor," *IEEE Transactions on Power Electronics*, vol. 30, pp. 5103–5115, April 2015.

[144] R. Mesleh, H. Haas, S. Sinanovic, C. W. Ahn, and S. Yun, "Spatial modulation," *IEEE Transactions on Vehicular Technology*, vol. 57, pp. 2228–2241, July 2008.

[145] R. J. Drost and B. M. Sadler, "Constellation design for color-shift keying using Billiards algorithms," in *IEEE Globecom Workshop on Optical Wireless Communications*, (Miami, FL), pp. 980–984, December 2010.

[146] J. Jiang, R. Zhang, and L. Hanzo, "Analysis and design of three-stage concatenated colour shift keying," *IEEE Transactions on Vehicular Technology*, vol. 64, pp. 5126–5136, November 2015.

[147] J. Armstrong and B. J. C. Schmidt, "Comparison of asymmetrically clipped optical OFDM and DC-biased optical OFDM in AWGN," *IEEE Communications Letters*, vol. 12, pp. 343–345, May 2008.

[148] J. Armstrong and A. J. Lowery, "Power efficient optical OFDM," *Electronics Letters*, vol. 42, pp. 370–372, March 2006.

[149] J. B. Carruthers and J. M. Kahn, "Multiple-subcarrier modulation for nondirected wireless infrared communication," *IEEE Journal on Selected Areas in Communications*, vol. 14, pp. 538–546, April 1996.

[150] S. Dimitrov, S. Sinanovic, and H. Haas, "Clipping noise in OFDM-based optical wireless communication system," *IEEE Transactions on Communications*, vol. 60, pp. 1072–1081, April 2012.

[151] J. Armstrong, B. J. C. Schmidt, D. Kalra, H. A. Suraweera, and A. J. Lowery, "SPC07-4: Performance of asymmetrically clipped optical OFDM in AWGN for an intensity modulated direct detection system," in *IEEE Global Telecommunications Conference (GLOBECOM)*, pp. 1–5, 2006 November.

[152] X. Li, R. Mardling, and J. Armstrong, "Channel capacity of IM/DD optical communication systems and of ACO-OFDM," in *IEEE International Conference on Communications, 2007. ICC*, pp. 2128–2133, June 2007.

[153] S. Tian, K. Panta, H. A. Suraweera, B. Schmidt, S. Mclaughlin, and J. Armstrong, "A novel timing synchronization method for ACO-OFDM-based optical wireless communications," *IEEE Transactions on Wireless Communications*, vol. 7, pp. 4958–4967, December 2008.

[154] J. Armstrong, "OFDM for optical communications," *IEEE Journal of Lightwave Technology*, vol. 27, pp. 189–204, February 2009.

[155] S. K. Wilson and J. Armstrong, "Transmitter and receiver methods for improving asymmetrically-clipped optical OFDM," *IEEE Transactions on Wireless Communications*, vol. 8, pp. 4561–4567, September 2009.

[156] D. J. F. Barros and J. M. Kahn, "Comparison of orthogonal frequency-division multiplexing and ON OFF keying in direct-detection multimode fiber links," *IEEE Journal of Lightwave Technology*, vol. 29, pp. 2299–2309, June 2011.

[157] S. D. Dissanayake and J. Armstrong, "Novel technique for combating DC offset in diversity combined ACO-OFDM," *IEEE Communications Letters*, vol. 15, pp. 1237–1239, September 2011.

[158] X. Li, J. Cucic, V. Jungnickel, and J. Armstrong, "On the capacity of intensity-modulated direct-detection systems and the information rate of ACO-OFDM for indoor optical wireless applications," *IEEE Transactions on Communications*, vol. 60, pp. 799–809, March 2012.

[159] D. J. F. Barros, S. K. Wilson, and J. M. Kahn, "Comparison of orthogonal frequency-division multiplexing and pulse-amplitude modulation in indoor optical wireless links," *IEEE Transactions on Communications*, vol. 60, pp. 153–163, December 2012.

[160] R. Zhang and L. Hanzo, "Multi-layer modulation for intensity-modulated direct-detection optical OFDM," *IEEE/OSA Journal of Optical Communications and Networking*, vol. 5, pp. 1402–1412, December 2013.

[161] S. D. Dissanayake and J. Armstrong, "Comparison of ACO-OFDM, DCO-OFDM and ADO-OFDM in IM/DD systems," *IEEE Transactions on Communications*, vol. 31, pp. 1063–1072, January 2013.

[162] B. Ranjha and M. Kavehrad, "Hybrid asymmetrically clipped OFDM-based IM/DD optical wireless system," *IEEE/OSA Journal of Optical Communications and Networking*, vol. 6, pp. 387–396, May 2014.

[163] J. Jiang, P. Zhang, R. Zhang, S. Chen, and L. Hanzo, "Aperture selection for ACO-OFDM in free-space optical turbulence channel," *IEEE Transactions on Vehicular Technology*, vol. (Early Access), 2015.

[164] W. Popoola, E. Poves, and H. Haas, "Generalised space shift keying for visible light communications," in *8th International Symposium on Communication Systems, Networks Digital Signal Processing (CSNDSP)*, (Pozana, Poland), pp. 1–4, July 2012.

[165] W. O. Popoola, E. Poves, and H. Haas, "Error performance of generalised space shift keying for indoor visible light communications," *IEEE Transactions on Communications*, vol. 61, pp. 1968–1976, March 2013.

[166] L. Zeng, D. O'Brien, and H. Minh, "Improvement of date rate by using equalisation in an indoor visible light communication system," in *IEEE International Conference on Circuits and Systems for Communications*, pp. 678–682, 2008.

[167] T. Komine, J. H. Lee, and S. Haruyama, "Adaptive equalization system for visible light wireless communication utilizing multiple white LED lighting equipment," *IEEE Transactions on Wireless Communications*, vol. 8, pp. 2892–2009, June 2009.

[168] K. Fan, T. Komine, Y. Tanaka, and M. Nakagawa, "The effect of reflection on indoor visible-light communication system utilizing white LEDs," in *International Symposium on Wireless Personal Multimedia Communications*, pp. 611–615, 2002.

[169] P. Chvojka, S. Zvanovec, P. A. Haigh, and Z. Ghassemlooy, "Channel characteristics of visible light communications with dynamic indoor environment," *IEEE Journal of Lightwave Technology*, vol. 33, pp. 1719–1725, February 2015.

[170] L. Zeng, D. C. O'Brien, H. L. Minh, G. E. Faulkner, K. Lee, D. Jung, Y. Oh, and E. T. Won, "High data rate multiple input multiple output (MIMO) optical wireless communications using white LED lighting," *IEEE Journals on Selected Areas in Communications*, vol. 27, pp. 1654–1662, December 2009.

[171] A. H. Azhar, T. Tran, and D. O'Brien, "A gigabit/s indoor wireless transmission using MIMO-OFDM visible light communications," *IEEE Photonics Technology Letters*, vol. 25, pp. 1041–1135, January 2013.

[172] T. Q. Wang, Y. A. Sekercioglu, and J. Armstrong, "Analysis of an optical wireless receiver using a hemispherical lens with application in MIMO visible light communications," *IEEE Journal of Lightwave Technology*, vol. 31, pp. 1744–1754, April 2013.

[173] Y. Hong, J. Chen, Z. Wang, and C. Yu, "Performance of a precoding MIMO system for decentralized multiuser indoor visible light communications," *IEEE Photonics Journal*, vol. 5, August 2013.

[174] K.-H. Park, Y.-C. Ko, and M. Alouini, "On the power and offset allocation for rate adaptation of spatial multiplexing in optical wireless MIMO channels," *IEEE Transactions on Communications*, vol. 61, pp. 1535–1543, February 2013.

[175] T. Fath and H. Haas, "Performance comparison of MIMO techniques for optical wireless communications in indoor environments," *IEEE Transactions of Communications*, vol. 61, pp. 733–742, February 2013.

[176] Y. Wang and N. Chi, "Demonstration of high-speed 2-by-2 non-imaging MIMO nyquist single carrier visible light communication with frequency domain equalization," *IEEE Journal of Lightwave Technology*, vol. 32, pp. 2087–2093, June 2014.

[177] T. Chen, L. Liu, B. Tu, Z. Zheng, and W. Hu, "High-spatial-diversity imaging receiver using fisheye lens for indoor MIMO VLCs," *IEEE Photonics Technology Letters*, vol. 26, pp. 2260–2263, October 2014.

[178] A. H. Azhar, T. Tran, and D. O'Brien, "Demonstration of high-speed data transmission using MIMO-OFDM visible light communications," in *IEEE Globecom Workshops 2010*, pp. 1052–1056, December 2010.

[179] K. D. Dambul, D. O'Brien, and G. Faulkner, "Indoor optical wireless MIMO system with an imaging receiver," *IEEE Photonics Technology Letters*, vol. 23, pp. 97–99, January 2010.

[180] V. N. H. Silva, A. P. L. Barbero, and R. M. Ribeiro, "A new triangulation-like technique for the evaluation of the refractive index structure constant in free-space optical links," *IEEE Journal of Lightwave Technology*, vol. 29, pp. 3603–3610, December 2011.

[181] M. Karimi and M. Nasiri-Kenari, "Free space optical communications via optical amplify-and-forward relaying," *IEEE Journal of Lightwave Technology*, vol. 29, pp. 242–248, January 2011.

[182] S. Sanayei, , and A. Norsratinia, "Antenna selection in MIMO systems," *IEEE Communications Magazine*, vol. 42, pp. 521–524, October 2004.

[183] R. Rajasheka, K, S, Hari, and L. Hanzo, "Antenna selection in spatial modulation systems," *IEEE Communications Letters*, vol. 17, pp. 521–524, March 2013.

[184] W. H. Chung and C. Y. Hung, "Multi-antenna selection in spatial using space shift keying in MIMO systems," in *Vehicular Technology Conference 2012 Spring*, (Yokohama, Japan), pp. 1–5, 6-9 May 2012.

[185] S. Kim, M. Shin, and C. Lee, "Transmit antenna selection scheme for iterative receivers in MIMO systems," *IEEE Signal Processing Letters*, vol. 14, pp. 916–919, December 2007.

[186] A. S. Hiwale, A. A. Ghatol, and S. D. Bhad, "Performance analysis of space-time trellis codes with receive antenna selection," in *Proceeding of Wireless Communication and Sensor Network 2008*, (Allahabad, India), pp. 148–152, 27-29 December 2008.

[187] D. Liu and D. K. C. So, "Performance based receive antennas selection for V-BLAST systems," *IEEE Transactions on Wireless Communications*, vol. 8, pp. 214–225, January 2009.

[188] Z. Xu, S. Sfar, and R. S. Blum, "Analysis of MIMO systems with receive antenna selection in spatially correlated Rayleigh fading channel," *IEEE Transactions on Vehicular Technology*, vol. 58, pp. 251–262, January 2009.

[189] W. A. Al-Husaibi and F. F. Ali, "Receive antenna selection for uplink multiuser MIMO systems over correlated Rayleigh fading channels," in *Proceeding of 14th International Symposium Wireless Personal Multimedia Communications*, (Brest, FRA), pp. 1–5, October 2011.

[190] R. S. Blum, Z. Xu, and S. Sfar, "A near optimal joint transmit and receive antenna selection algorithm for MIMO systems," in *Proceeding of Radio and Wireless Symposium*, (San Diego, USA), pp. 554–557, January 2009.

[191] T. Gucluoglu and T. M. Duman, "Space-time coded systems with joint transmit and receive antenna selection," in *Proceeding of International Conference on Communications*, (Glasgow, UK), pp. 5305–5310, June 2007.

[192] H. S. Kim and Y. S. Byum, "Near-optimal selection of joint transmit-receive antennas for MIMO channel based on maximizing channel capacity," in *Proceeding of Asia-Pacific Conference on Communications*, (Busan, Korea), pp. 1–5, August 2006.

[193] M. Naeem and D. C. Lee, "Near-optimal joint selection of transmit and receive antennas for MIMO systems," in *Proceeding of International Symposium on Communications and Information Technology*, (Incheon, Korea), pp. 572–577, September 2009.

[194] T. R. Wei and M. Z. Wang, "Capacity-based efficient joint transmit and receive antenna selection schemes in MIMO systems," in *Proceeding of International Conference on Information and Communication Technology: From Theory to Applications*, (Damascus, Syria), pp. 2125–2129, April 2006.

[195] S. Sanayei and A. Nostatinia, "Capacity maximizing algorithms for joint transmit-receive antenna selection," in *Proceeding of 38th Asiloma Conference on Signals, Systems and Computers*, (California, USA), pp. 1773–1776, November 2004.

[196] A. Yilmaz and O. Kucur, "Error performance of joint transmit and receive antenna selection in two hop amplify-and-forward relay system over Nakagami-M fading channels," in *Proceeding of 21th International Symposium on Personal Indoor and Mobile Radio Communications*, (Istanbul, Turkey), pp. 2198–2203, September 2010.

[197] T. Gucluoglu and T. M. Duman, "Performance analysis of transmit and receive antenna selection over flat fading channels," *IEEE Transactions on Wireless Communications*, vol. 7, pp. 3056–3065, August 2008.

[198] M. Gharavi-Alkhansari and A. B. Gershman, "Fast antenna subset selection in MIMO systems," *IEEE Transactions on Wireless Communications*, vol. 52, pp. 339–347, February 2004.

[199] P. Zhang, S. Chen, and L. Hanzo, "Norm-based joint transmit/receive antenna selection aided and two-tier channel estimation assisted STSK systems," in *IEEE International Conference on Communications*, (Sydney, Australia), pp. 5049–5054, June 2014.

[200] H. Moradi, H. H. Refai, and P. G. LoPresti, "Circular MIMO nodes with transmit selection and receive generalized selection diversity," *IEEE Transactions on Vehicular Technology*, vol. 61, pp. 1583–1589, May 2012.

[201] A. Sevincer, *Transceiver Selection for Multi-Element Free-Space-Optical Communications*. University of Nevada, 2013.

[202] N. D. Chatzidiamantis, D. S. Michalopoulos, E. E. Kriezis, G. K. Karagiannidis, and R. Schober, "Relay selection protocols for relay-assisted free-space optical systems," *IEEE/OSA Journal of Optical Communications and Networking*, vol. 5, pp. 92–103, January 2013.

[203] A. Goldsmith, *Wireless Communications*. Cambridge University Press, 2005.

[204] S. Sugiura, S. Chen, and L. Hanzo, "A universal space-time architecture for multiple-antenna aided systems," *IEEE Communications Surveys and Tutorials*, vol. 14, pp. 401–420, January 2012.

[205] S. Sugiura, S. Chen, and L. Hanzo, "Generalized space-time shift keying designed for flexible diversity-, multiplexing- and complexity-tradeoffs," *IEEE Transactions on Wireless Communications*, vol. 10, pp. 1144–1533, April 2011.

[206] S. Sugiura, "Dispersion matrix optimization for space-time shift keying," *IEEE Communications Letters*, vol. 15, pp. 1152–1155, November 2011.

[207] S. Sugiura, S. Chen, H. Haas, P. M. Grant, and L. Hanzo, "Coherent versus non-coherent decode-and-forward relaying aided cooperative space-time shift keying," *IEEE Transactions on Communications*, vol. 59, pp. 1707–1719, June 2011.

[208] S. Sugiura, C. Xu, S. X. Ng, and L. Hanzo, "Reduced-complexity coherent versus non-coherent QAM-aided space-time shift keying," *IEEE Transactions on Communications*, vol. 59, pp. 3090–3101, November 2011.

[209] N. Fernando, H. Yi, and E. Viterbo, "Flip-OFDM for unipolar communication systems," *IEEE Transactions on Communications*, vol. 60, pp. 3726–3733, December 2012.

[210] I. Djordjevic, B. Vasic, and M. A. Neifeld, "LDPC-coded OFDM for optical communication systems with direct detection," *IEEE Journal of Selected Topics in Quantum Electronics*, vol. 13, pp. 1446–1454, September 2007.

[211] I. Djordjevic and H. G. Batshon, "LDPC-coded OFDM for heterogeneous access optical networks," *IEEE Photonics Journal*, vol. 2, pp. 611–619, August 2010.

[212] C. Chen, W. D. Zhong, X. Li, and D. Wu, "MDPSK-based nonequalization OFDM for coherent free-space optical communication," *IEEE Photonics Technology Letters*, vol. 26, pp. 1617–1620, June 2014.

[213] L. Hanzo, O. Alamri, M. El-Hajjar, and N. Wu, *Near Capacity Multi-functional MIMO Systems*. John Wiley and Sons, 2009.

[214] G. J. Foschini and M. Gans, "On limits of wireless communication in a fading environment when using multiple antennas," *Wireless Personal Communications*, vol. 6, pp. 311–335, March 1998.

[215] P. Zhang, S. Chen, and L. Hanzo, "Two-tier channel estimation aided near-capacity MIMO transceiver relying on norm-based joint transmit and receive antenna selection," *IEEE Transactions on Wireless Communications*, vol. 14, pp. 122–137, January 2015.

[216] L. Hanzo, T. H. Liew, B. L. Yeap, R. Y. S. Tee, and S. X. Ng, *Turbo Coding and Turbo Equalisation and Space-Time Coding: EIXT-Chart-Aided Near-Capacity Designs for Wireless Channels, 2nd Edition*. John Wiley and Sons, Inc., 2011.

[217] M. El-Hajjar and L. Hanzo, "EXIT charts for system design and analysis," *IEEE Communications Survey and Tutorials,*, vol. PP, pp. 1–27, May 2013.

[218] J. Wang, S. X. Ng, A. Wolfgang, L. L. Yang, S. Chen, and L.Hanzo, "Near-capacity three-stage MMSE Turbo equalization using irregular convolutional codes," in *Proceedings International ITG-Conference on Source and Channel Coding, International Symposium on Turbo Codes and Related Topics*, (Munich, Germany), pp. 1–6, April 2006.

[219] R. G. Maunder and L. Hanzo, "Iterative decoding convergence and termination of serially concatenated codes," *IEEE Transactions on Vehicular Technology*, vol. 59, pp. 216–224, January 2010.

[220] A. Ashikhmin, G. Kramer, and S. ten Brink, "Extrinsic information transfer functions: Model and erasure channel properties," *IEEE Transactions on Information Theory*, vol. 50, pp. 2657–2673, November 2004.

[221] C. Lin, C. Rowell, S. Han, G. Li, and Z. Pan, "Toward green and soft: A 5G perspective," *IEEE Communications Magazine*, vol. 52, pp. 66–73, February 2014.

[222] E. Dahlman, G. Mildh, S. Parkvall, J. Peisa, J. Sachs, Y. Selén, and J. Sköld, "5G wireless access: Requirements and realization," *IEEE Communications Magazine*, vol. 52, pp. 42–47, December 2014.

[223] J. G. Andrews, S. Buzzi, W. Choi, S. V. Hanly, A. Lozano, A. C. K. Soong, and J. C. Zhang, "What will 5G be?," *IEEE Journal on Selected Areas in Communications*, vol. 32, pp. 1065–1082, June 2014.

[224] D. Tsonev, S. Videc, and H. Haas, "Light fidelity (Li-Fi): Towards all-optical networking," in *SPIE Proceedings on Broadband Access Communication Technologies VIII*, (San Francisco, CA), pp. 900 702–1–900 702–10, February 2014.

[225] D. Jurca and P. Frossard, "Video packet selection and scheduling for multipath streaming," *IEEE Transactions on Multimedia*, vol. 9, pp. 629–641, April 2007.

[226] P. Pahalawatta, R. Berry, T. Pappas, and A. Katsaggelos, "Conten-Aware resource allocation and packet scheduling for video transmission over wireless networks," *IEEE Journal on Selected Areas in Communications*, vol. 25, pp. 749–759, May 2007.

[227] Y. Li, Z. Li, M. Chiang, and A. R. Calderbank, "Content-aware distortion-fair video streaming in congested networks," *IEEE Transactions on Multimedia*, vol. 11, pp. 1182–1193, September 2009.

[228] F. Fu and M. van der Schaar, "Structural solutions for dynamic scheduling in wireless multimedia transmission," *IEEE Transactions on Circuits and Systems for Video Technology*, vol. 22, pp. 727–739, May 2012.

[229] K. Pandi, A. Ghosh, D. Ghosal, and M. Chiang, "Content-aware optimization for video delivery over WCDMA," *EURASIP Journal of Wireless Communication and Networking*, July 2012.

[230] M. Ismail, W. Zhuang, and S. Elhedhli, "Energy and content aware multi-homing video transmission in heterogeneous networks," *IEEE Transactions on Wireless Communications*, vol. 12, pp. 3600–3610, July 2013.

[231] M. van der Schaar and D. S. Turaga, "Cross-layer packetization and retransmission strategies for delay-sensitive wireless multimedia transmission," *IEEE Transactions on Multimedia*, vol. 9, pp. 185–197, January 2007.

[232] C. Chen, N. Serafimovski, and H. Haas, "Fractional frequency reuse in optical wireless cellular networks," in *IEEE 24th International Symposium on PIMRC*, (London), pp. 3594–3598, September 2013.

[233] C. Chen, N. Serafimovski, and H. Haas, "Joint transmission in indoor visible light communication downlink cellular networks," in *IEEE Globecom Workshops*, (Atlanta, GA), pp. 1127–1132, December 2013.

[234] X. Li, R. Zhang, and L. Hanzo, "Cooperative load balancing in hybrid visible light communications and WiFi," *IEEE Transactions on Communications*, vol. 63, pp. 1319–1329, April 2015.

[235] M. Shreedhar and G. Varghese, "Efficient fair queuing using deficit round-robin," *IEEE/ACM Transactions on Networking*, vol. 4, pp. 375–385, June 1996.

[236] ITU-T, *H.264: Advanced Video Coding*, February 2014.

[237] ITU-T, *H.265: High Efficiency Video Coding for Generic Audiovisual Services*, April 2015.

[238] L. Hanzo, P. Cherriman, and J. Streit, *Wireless Video Communications: Second to Third Generation Systems and Beyond*. Wiley and Sons, 2001.

[239] S. Le Digabel, "Algorithm 909: Nomad: Nolinear optimization with the mads algorithm," *ACM Transactions on Mathematical Software*, vol. 37, pp. 44:1–44:15, February 2011.

[240] A. Ghosh, N. Mangalvedhe, R. Ratasuk, B, Mondal, M. Cudak, E. Visotsky, T. A. Thomas, H. G. Andrews, P. Xia, H. S. Jo, H. Dhillon, and T. D. Novlan, "Heterogeneous cellular networks: from theory to practice," *IEEE Communications Magazine*, vol. 50, pp. 54–64, June 2012.

[241] T. S. Rappaport, S. Sun, R. Mayzus, H. Zhao, Y. Azar, K. Wang, G. N. Wong, J. K. Schulz, M. Samimi, and F. Gutierrez, "Millimeter wave mobile communications for 5G cellular: It will work!," *IEEE Access*, vol. 1, pp. 335–349, 2013.

[242] W. O. Popoola, E. Poves, and H. Haas, "Error performance of generalised space shift keying for indoor visible light communications," *IEEE Transactions of Communications*, vol. 61, pp. 1968–1976, May 2013.

[243] S. Rajagopal, R. D. Roberts, and S.-K. Lim, "IEEE 802.15.7 visible light communication: Modulation schemes and dimming support," *IEEE Communications Magazine*, vol. 50, pp. 72–82, March 2012.

[244] J. Vucic, C. Kottke, S. Nerreter, K.-D. Langer, and J. W. Walewski, "513 Mbit/s visible light communications link based on dmt-modulation of a white LED," *IEEE Journal of Lightwave Technology*, vol. 28, pp. 3512–3518, December 2010.

[245] A. Ghosh, R. Ratasuk, B. Mondal, N. Mangalvedhe, and T. Thomas, "LTE-advanced: Next-generation wireless broadband technology," *IEEE Wireless Communications*, vol. 17, pp. 1536–1284, June 2010.

[246] R. Mesleh, H. Elgala, and H. Haas, "On the performance of different OFDM based optical wireless communications systems," *IEEE/OSA Journal of Optical Communications and Networking*, vol. 3, pp. 620–628, August 2011.

[247] R. J. Drost and B. M. Sadler, "Constellation design for channel precompensation in multi-wavelength visible light communications," *IEEE Transactions on Communications*, vol. 62, pp. 1995–2005, June 2014.

[248] E. Monterio and S. Hranilovic, "Design and implementation of color-shift keying for visible light communications," *IEEE Journal of Lightwave Technology*, vol. 32, pp. 2053–2060, May 2014.

[249] E. Monterio and S. Hranilovic, "Constellation design for color-shift keying using Interior point methods," in *IEEE Globecom Workshop on Optical Wireless Communications*, (Anaheim, CA), pp. 1224–1228, December 2012.

[250] R. Singh, T. O'Farrell, and J. David, "An enhanced color shift keying modulation scheme for high speed wireless visible light communications," *IEEE Journal of Lightwave Technology*, vol. 32, pp. 2582–2592, June 2014.

[251] J. M. Luna-Rivera, R. Perez-Jimenez, J. Rabadan-Borjes, J. Rufo-Torres, V. Guerra, and C. Suarez-Rodriguez, "Multiuser CSK scheme for indoor visible light communications," *Optics Express*, vol. 22, pp. 24256–24267, October 2014.

[252] S. Pergoloni, M. Biagi, S. Rinauro, S. Colonnese, R. Cusani, and G. Scarano, "Merging color shift keying and complementary pulse position modulation for visible light illumination and communication," *IEEE Journal of Lightwave Technology*, vol. 33, pp. 192–200, December 2014.

[253] S. ten Brink, "Convergence behavior of iteratively decoded parallel concatenated codes," *IEEE Transactions on Communications*, vol. 49, pp. 1727–1737, October 2001.

[254] X. Qi, S. Zhou, M. Zhao, and J. Wang, "Design of constellation labeling maps for iteratively demapped modulation schemes based on the assumption of hard-decision virtual channels," *IEEE Proceedings of Communications*, vol. 152, pp. 1139–1148, December 2005.

[255] Commission Internationale de lEclairage Proceeding, *CIE*, 1931.

[256] IEEE Computer Society, *Project: IEEE P802.15 Working Group for Wireless Personal Area Networks (WPANs)*, February 2011.

[257] B. Bai, Q. He, Z. Xu, and Y. Fan, "The color shift key modulation with non-uniform signalling for visible light communication," in *IEEE International Conference on Communications in China*, (Beijing), pp. 37–42, August 2012.

[258] M. K. Simon and M.-S. Alouini, *Digital Communication over Fading Channel*. John Wiley & Sons, Inc., 2005.

[259] X. Wang and H. V. Poor, "Iterative (Turbo) soft interference cancellation and decoding for coded CDMA," *IEEE Transactions on Communications*, vol. 47, pp. 1046–1061, July 1999.

[260] R. Zhang and L. Hanzo, "Three design aspects of multicarrier interleave division multiple access," *IEEE Transactions on Vehicular Technology*, vol. 57, pp. 3607–3617, November 2008.

[261] M. Tüchler and J. Hagenauer, "Design of serially concatenated system depending on the block length," *IEEE Transactions on Communications*, vol. 52, pp. 209–218, February 2004.

[262] M. Tüchler and J. Hagenauer, "EXIT charts of irregular codes," in *Proceedings of Conference Information Sciences and Systems*, (Princeton, NJ), March 2002.

[263] A. Chindapol and J. A. Ritcey, "Design, analysis, and performance evaluation for BICM-ID with square QAM constellations in Rayleigh fading channels," *IEEE Journal on Selected Areas in Communications*, vol. 19, pp. 944–957, May 2001.

[264] A. C. X. Li and J. A. Ritcey, "Bit-interleaved coded modulation with iterative decoding and 8PSK signaling," *IEEE Transactions on Communications*, vol. 50, pp. 1250–1257, August 2002.

[265] N. H. Tran and H. H. Nguyen, "Signal mapping of 8-ary constellations for bit interleaved coded modulation with iterative decoding," *IEEE Transactions on Broadcasting*, vol. 52, pp. 92–99, March 2006.

[266] V. Buttigieg and P. G. Farrell, "Variable-length error-correcting codes," *IEE Proceedings on Communications*, vol. 147, pp. 211–215, August 2000.

[267] R. G. Maunder, J. Kliewer, and L. Hanzo, "Iterative decoding convergence conditions for variable length error correcting codes and for their relatives," *(Eprint: users.ecs.soton.ac.uk/rm/wp-content/freedist2.pdf)*.

[268] L. Hanzo, C. H. Wong, and M. S. Yee, *Adaptive Wireless Transceivers: Turbo-Coded, Space-Time Coded TDMA, CDMA and OFDM Systems*. Wiley, 2002.

[269] K. Zhen, L. Zhao, J. Mei, B. Shao, W. Xiang, and L. Hanzo, "Survey of large-scale MIMO systems," *IEEE Communications Surveys and Tutorials*, vol. 17, pp. 1738–1760, August 2015.

[270] S. Yang and L. Hanzo, "Fifty years of MIMO detection: The road to large-scale MIMOs," *IEEE Communications Surveys and Tutorials*, vol. (Early access), 2015.

[271] W. Yao, S. Chen, and L. Hanzo, "A transceiver design based on uniform channel decomposition and MBER vector perturbation," *IEEE Transactions on Vehicular Technology*, vol. 59, pp. 3153–3159, July 2010.

[272] X. Zhu, X. Zhang, R. Zhang, and L. Hanzo, "Chip-interleaved optical code division multiple access relying on a photon-counting iterative successive interference canceller for free-space optical channel," *Optics Express*, vol. 21, pp. 15926–15937, May 2013.

[273] P. Botsinis, S. X. Ng, and L. Hanzo, "Quantum search algorithms, quantum wireless, and a low-complexity maximum likelihood iterative quantum multi-user detector design," *IEEE Access*, vol. 1, pp. 94–122, May 2013.

List of Figures

List of Tables

Subject Index

F

G

H

I

J

L

Q

R

S

T

U

V

W

Z

Author Index

C

D

E

F

G

H

I

J

K

L

M

N

O

P

Q

R

S

X

Y

Z